Vibrational spectroscopy studies of interdiffusion in polymer laminates and diffusion of water into polymer membranes.

HAJATDOOST, Sohail.

Vibrational Spectroscopy Studies of Interdiffusion in Polymer Laminates and Diffusion of Water into Polymer Membranes

by

Sohail Hajatdoost

A thesis submitted in part fulfilment of the requirements of Sheffield Hallam University for the degree of Doctor of Philosophy

October 1996

ABSTRACT

Confocal Raman microspectroscopy has been used to study the interdiffusion in polymer laminates at the interfacial region between the constituent polymer layers. The effects of the polymer molecular weight, annealing temperature, and annealing time have been studied. Three different laminates with various PMMA molecular weights have been examined, with a view to studying the hydrogen bonding interaction between the alcohol and ester groups of PVOH and PMMA layers. It has been found that ν(C=O) band shows no apparent frequency shift due to hydrogen bonding. However, considerable broadening of the ν(C=O) band has been observed at the interfacial region. In order to study the effect of annealing temperature, a PAN/PVOH laminate has been chosen. It has been shown that the degree of hydrogen bonding is reduced if the polymer laminate is annealed at a higher temperature than the glass transition temperature of both of the constituent polymers. No significant change has been observed after annealing the laminate for various lengths of time.

It has been shown that Raman imaging and Raman microscopy can provide invaluable information about the molecular distribution and chemical interactions of various phases in polymer blends.

The diffusion of pure water and also water from some ionic solutions into sulphonated polyetherethersulphone/polyethersulphone, SPEES/PES has been studied using Fourier transform infrared-attenuated total reflectance, FTIR-ATR spectroscopy. The effects of sulphonation level, annealing temperature, ionic concentration, and presence of some ionic species on diffusion of water into SPEES/PES has been examined. In addition the sorption and desorption processes, and diffusion into a laminate of SPEES/PES-PVOH has also been studied. It was found that the above diffusion processes are not Fickian nor Case II and is best described by a dual-mode sorption model.

The diffusion coefficient for H_2O in various cationic solutions into SPEES/PES has a descending order of $Li^+ > Cs^+ > Na^+ > K^+$. Increasing the ionic concentration results in a decrease in the water diffusion coefficient. It was found that an increase in annealing temperature caused the diffusion curve to become more sigmoidal in shape with a decreases in diffusion coefficient.

CONTENTS

Chapter 1

Chapter 2

Chapter 3

Chapter 4

Chapter 5

Chapter 6

'How resplendent the luminaries of knowledge that shine in an atom, and how vast the oceans of wisdom that surge within a drop!'

Bahá'u'lláh

DECLARATION

The work described in this thesis was carried out by the author in the Materials Research Institute, Sheffield Hallam University, between September 1993 and October 1996. The author declares that this work has not been submitted for any other degree. The work is original except where acknowledged by reference.

Author:

(Sohail Hajatdoost)

Supervisor:

(Professor Jack Yarwood)

ACKNOWLEDGEMENTS

My sincere and special thanks go to my supervisor Professor Jack Yarwood who has made indescribable contributions. His enthusiasm, interest and patience will be remembered for many years. It has been an honour for me to learn from his many skills throughout the past three years.

I would further like to acknowledge Dr Peter Cardew, Dr Steven Spells, Dr Neil Everall, Professor Julia Higgins and Professor D. E. Irish for their help and advice. The collaboration work with Maurien Olsthoorn is appreciated. I must also thank Sheffield Hallam University and NWW Acumem Limited for their financial support for my project.

The encouragement, patience and real support of my dear parents throughout the final months of the project is always remembered and the hospitality, kindness and generosity of Mena is truly appreciated.

All my friends within the group, Nigel, Reena, Bryan, Evangelos, Chris, Jason, Francis, Delphine, Peter, Carine, and Claudia will be remembered.

CHAPTER 1

Introduction
Molecular vibrations
Anharmonicity
Normal modes of vibration
Fourier Transform Infrared Spectrometry and Interferometry
Advantages of FTIR spectroscopy
Attenuated Total Reflectance

1.1. Introduction to infrared spectroscopy

Infrared, IR, radiation is electromagnetic radiation, in the wavelength range that is adjacent to and of lower energy than visible radiation. This region is divided in to smaller regions according to energetic proximity to the visible spectral region. This is summarised in table 1.1.

IR region	approximate range (cm^{-1})	vibrational and/or rotational changes
near-IR	14,000 - 4,000	Some low-energy electron transitions as well as changes in vibrational and rotational levels
mid-IR	4,000 - 400	Changes in fundamental vibrational levels of most molecules and thus it is of most use for chemical analysis
far-IR	400 - 20	rotational changes occur in this region

***Table 1.1:** Summary of various regions of infrared radiation*

In infrared spectroscopy, the observation time for a single vibrator is between 10^{-13} to 10^{-15} seconds. This is important, because it controls the sort of information which can be obtained from this branch of spectroscopy as compared with some other spectroscopic

techniques. A summary of infrared spectroscopy theory is given in sub-sections of this chapter.

1.2. Molecular vibrations

Figure 1.1 shows a typical potential energy curve for a diatomic molecule. In regions close to r_e, at the minimum of the curve, the potential energy can be approximated by a parabola.

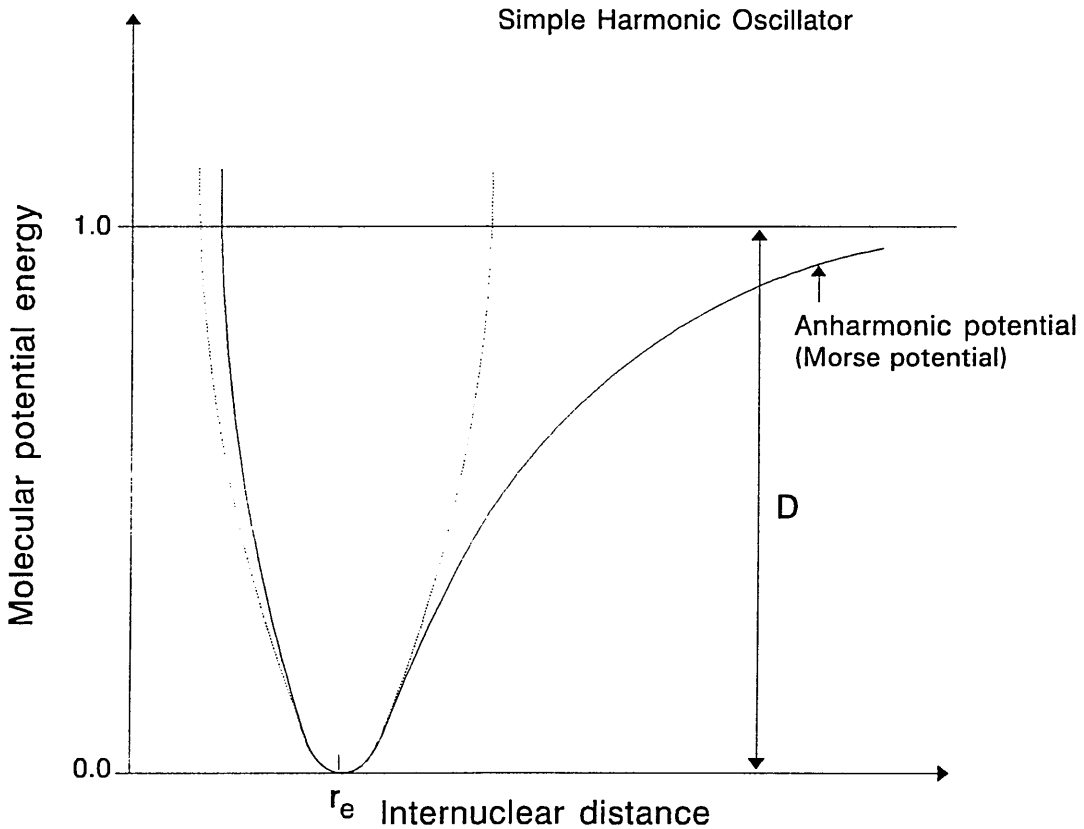

Figure 1.1: *The molecular potential energy curve can be approximated by a parabola near the bottom of the well. The parabolic potential leads to harmonic oscillations. At high excitation energies the parabolic approximation is poor, and is totally wrong near the dissociation limit*

The potential energy, V can be written as

$$\mathbf{V} = \frac{1}{2}\mathbf{k}(\mathbf{r} - \mathbf{r}_e)^2 \qquad (1.1)$$

Where k is the force constant of the bond. The Schrödinger equation [1.1] for the motion of two atoms after simplification is

$$\mathbf{E}\Psi = -(\frac{\mathbf{h}^2}{2\mu})(\frac{\delta^2\Psi}{\delta\mathbf{r}^2}) + \mathbf{V}\Psi \qquad (1.2)$$

The Schrödinger equation (eqn 1.2) is that for a particle of mass μ undergoing harmonic motion. Using this equation the permitted vibrational energy levels are

$$\mathbf{E}_\upsilon = (\upsilon + \frac{1}{2})\mathbf{h}\omega \qquad (1.3)$$

Where $\omega_e = (\frac{\mathbf{k}}{\mu})^{\frac{1}{2}}$

$\upsilon = 0, 1, 2, ...$

1.3. Anharmonicity

Equation 1.3 describes the vibrational energy level for simple harmonic motion. The Hookes law is obeyed and only one transition energy is predicted ($\Delta\upsilon = \pm 1$). However, Hookes law is not obeyed by chemical bonds and as a result, anharmonicity arises. The energy levels given in equation 1.3 are based on the parabolic approximation to the actual

potential energy curve. At high vibrational excitations the motion of the atoms (i.e. the spread of wavefunction) allows the molecule to explore regions of the curve where the parabolic approximation is poor. The motion then becomes anharmonic.

In order to calculate the energy levels over a wider range, it is better to use a function that resembles the true potential energy more closely. The Morse potential energy is

$$\mathbf{V} = \mathbf{D_e}\left[1 - \mathbf{e}^{-\mathbf{a}(\mathbf{r}-\mathbf{r_e})}\right]^2 \qquad (1.4)$$

Where D_e is the depth of the potential minimum and $a = (\mu/2D_e)^{0.5}\omega$. Figure 1.1 shows the shape of the Morse curve. The Schrödinger equation can be solved with this form of V, and the permitted energy levels are

$$\mathbf{E}_\upsilon = (\upsilon + \frac{1}{2})\mathbf{h}\omega - \mathbf{h}\omega\mathbf{x_e}(\upsilon + \frac{1}{2})^2 \qquad (1.5)$$

Where x_e is called the anharmonicity constant and $\mathbf{x_e} = \dfrac{\mathbf{a}^2\mathbf{h}}{2\mu\omega}$

In practice the more general expression for the energy levels is used to fit the experimental data and to find the dissociation energy of the molecule.

$$\mathbf{E}_\upsilon = (\upsilon + \frac{1}{2})\mathbf{h}\omega - \mathbf{h}\omega\mathbf{x_e}(\upsilon + \frac{1}{2})^2 + \mathbf{h}\omega\mathbf{y_e}(\upsilon + \frac{1}{2})^3 + \ldots \qquad (1.6)$$

Figure 1.2 shows the lower energy levels of vibration of the water molecule. The lowest energy level, is called the ground level, for which all the quantum numbers (n_1, n_2, n_3) are zero. This energy is called zero-point energy of the molecule. The fundamental levels are those energy levels for which all quantum numbers are zero except one, which has the value unity. However, if only one quantum is different from zero and it is greater than one then the energy levels are called overtone levels. Combination levels correspond to those energy levels for which two or more quantum numbers have non zero values.

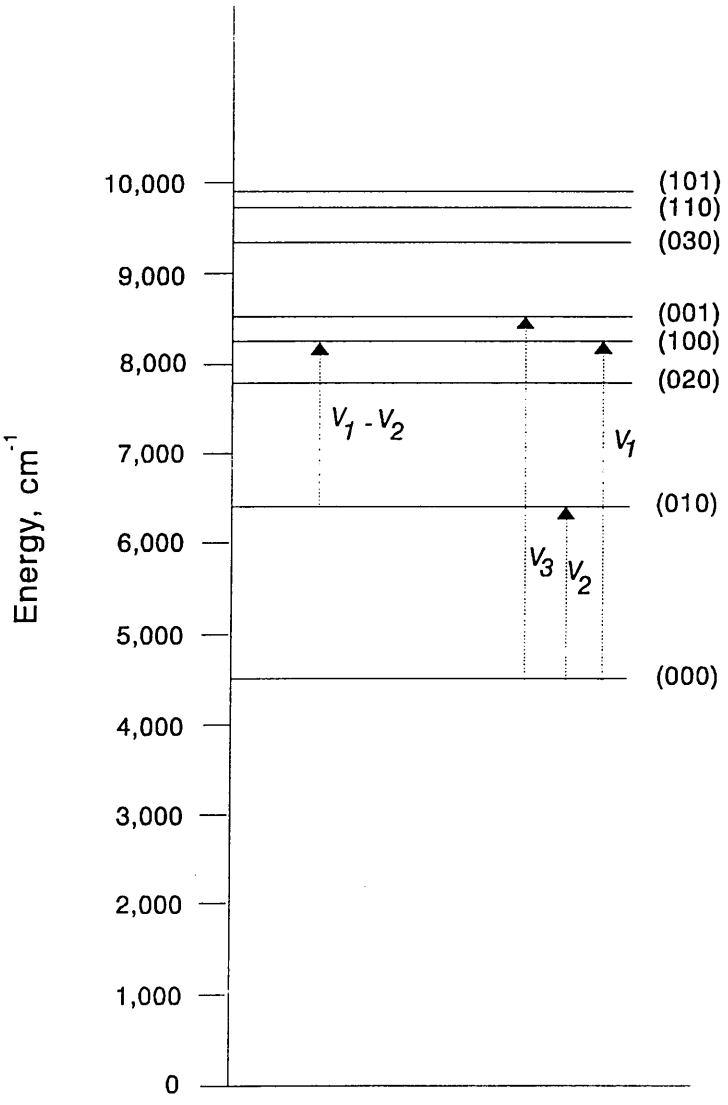

Figure 1.2: *Lower levels of vibration of water molecule. Levels are indexed by the quantum numbers (n_1, n_2, n_3)*

1.4. Normal modes of vibration

All motions of the atoms in a molecule relative to each other are a superposition of so-called normal vibrations. in which all atoms are vibrating with the same phase and normal frequency [1.2]. However their amplitude may be, and usually is, different for each coordinate. The frequency of a normal vibration is known as a normal, or fundamental, frequency of the molecule. Polyatomic molecules with n atoms posses 3n-6 normal vibrations (linear molecules have 3n-5 vibrations), which define their vibrational spectra.

Figure 1.3 shows the three normal modes of vibration of water molecule. The relative displacements of the atoms is represented by the arrows in a mass-weighted coordinate system , when the molecule is vibrating in the particular mode of vibration.

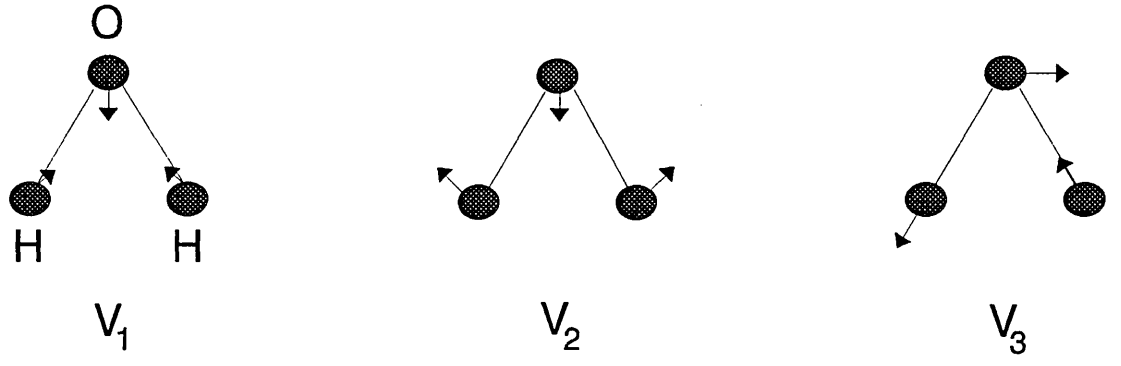

Figure 1.3: *The normal modes of vibration of water molecule*

1.5. Intensity

The intensity of a vibration in infrared spectroscopy depends on three factors, which are the properties of the molecule. These include:

1- Selection rule: This factor determines a transition whether is "allowed" or "forbidden". The normal vibrations of a molecule may only absorb infrared radiation if they modulate the molecular dipole moment μ_k (which is a vector with the components μ_x, μ_y, and μ_z):

$$\mu_{\mathrm{k}} = \mu_0 + \left(\frac{\partial \mu}{\partial \mathbf{Q}}\right)_0 \mathbf{Q} + \frac{1}{2}\left(\frac{\partial^2 \mu}{\partial \mathbf{Q}^2}\right)_0 \mathbf{Q}^2 + \ldots \qquad (1.7)$$

In infrared spectroscopy, the intensity of the transition is proportional to the square of the transition dipole moment. i.e.,

$$\mathbf{I} \propto \left(\frac{\partial \mu}{\partial \mathbf{Q}}\right)^2 \qquad (1.8)$$

2- Population of initial state at thermal equilibrium: The intensity of a line resulting from the transition of a molecule from a level of energy E depends on the population of the level (the number of molecules possessing that energy). When the sample of N molecules is at a temperature T the number with energy E is given by the Boltzmann distribution:

$$\frac{\mathbf{N_i}}{\mathbf{N_0}} = \frac{\mathbf{g_i}}{\mathbf{g_0}} \exp\left(-\frac{\Delta \mathbf{E}}{\mathbf{kT}}\right) \qquad (1.9)$$

Where *g* is the degeneracy of the level (i.e. the number of states corresponding to that energy).

3- Number of molecules in the sample: In absorption spectroscopy, including IR, the relation between the intensities of the incident and the transmitted radiation (I_0 and I) and the concentration c is referred to as the Beer-Lambert law, expressed as

$$\mathbf{I} = \mathbf{I}_0 \exp(-\varepsilon \mathbf{c} \mathbf{l}) \qquad (1.10)$$

or in its logarithmic form

$$\log\left(\frac{\mathbf{I}_0}{\mathbf{I}}\right) = \varepsilon \mathbf{c} \mathbf{l} \qquad (1.11)$$

Where c is concentration, l is cell thickness and ε is extinction coefficient.

1.6. Fourier Transform Infrared Spectrometry and Interferometry

Fourier transform infrared (FTIR) spectrometers consist of several parts. In most instruments an interferometer such as the one designed by Michelson (1891) is used.

The Michelson interferometer (figure 1.4) functions in the following manner. Radiation from a polychromatic source, for example a mercury lamp, is directed towards a beam splitter. Half of the radiation is reflected by the beam splitter to a mirror that reflects the radiation back towards the beam splitter. The remaining portion of the radiation passes through the beam splitter and strikes a mirror that is continuously moved back and forth. After striking the moving mirror, the radiation is reflected back to the beam splitter. A portion of the radiation that was reflected from the stationary mirror and a portion of the radiation that was reflected from the moving mirror combine at the beam splitter and pass through the cell. After passage through the cell the radiation is focused on the detector.

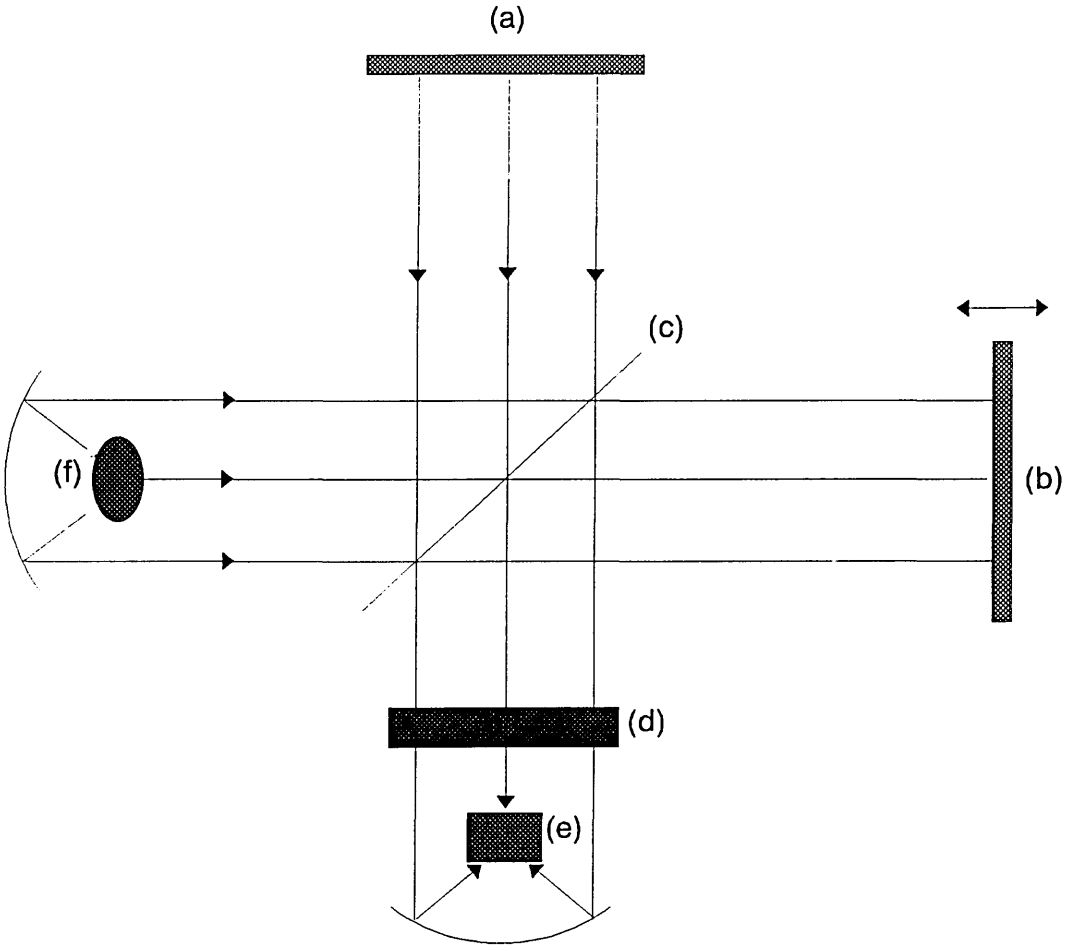

Figure 1.4: *An optical diagram of a Michelson interferometer as used for FTIR spectroscopy. The arrows indicate the direction of radiative travel and the direction of mirror motion. (a) Stationary mirror, (b) moving mirror, (c) beam splitter, (d) cell, (e) detector, and (f) light source.*

If the distance through which the radiation travels between the beam splitter and the stationary mirror is identical to the round-trip distance between the beam splitter and the moving mirror, the radiation from the two mirrors arrives in-phase at the beam splitter, the cell, and the detector. As the moving mirror changes position, however, the distances between the mirrors and the beam splitter are no longer identical and radiation of a single

wavelength will only arrive in-phase at the cell and detector when the distance between the moving mirror and the beam splitter is equal to the distance between the stationary mirror and the beam splitter plus or minus a whole-number multiple of the wavelength of the radiation.

If the moving mirror moves away from the equidistant point by a factor of $\lambda/4$, distance is altered by $\lambda/2$ and the reflected radiation is out-of-phase with that from the stationary mirror and destructively interferes. If the moving mirror is $\lambda/2$ from the equidistant point, the radiation is in-phase with that from the stationary mirror and constructively interferes. As the distance changes, different wavelengths of radiation become in-phase and out-of-phase at a frequency that is dependent upon the wavelength of the incident radiation and the rate at which the mirror moves. By controlling the rate of mirror motion, a series of simultaneous signals that oscillate at frequencies that are directly proportional to the frequency of the EMR arrive at the detector and oscillate sufficiently slowly for the detector to measure.

In a Fourier transform infrared spectrometer, the source emits a polychromatic radiation. This means that several discrete spectral lines or continuous radiation is emitted by the source. In this case the interferogram equation is more complex and the computation of the Fourier transform procedure needs a digital computer to handle the time consuming computations very rapidly.

The signal at the detector is seen to vary sinusoidally providing velocity of movement of mirror is constant. Each time that the optical path difference, x (retardation) is an integral multiple of λ, a maximum is registered. The intensity of the beam at the detector, I'(x) at

any point where $x = n\lambda$ is equal to the intensity of the source $I(\bar{\nu})$. The intensity of the beam at the detector at other values of x is given by

$$\mathbf{I'(x) = \frac{1}{2} I(\bar{\nu})\left[1 + \cos 2\pi \bar{\nu} x\right]} \qquad (1.12)$$

From equation (1.12) it is clear that I'(x) has a constant component equal to $0.5I(\bar{\nu})$ and a modulated component equal to $0.5I(\bar{\nu})\cos 2\pi \bar{\nu} x$. The modulated component is called the interferogram and is important in spectrometric measurements. Equation (1.13) describes the interferogram for a monochromatic source measured with an ideal interferometer.

$$\mathbf{I(x) = \frac{1}{2} I(\bar{\nu}) \cos 2\pi \bar{\nu} x} \qquad (1.13)$$

However it should be noted that several factors related to the instrument will affect the amplitude of the interferogram after detection and amplification. These include (a) beamsplitter efficiency, (b) intensity of the source, (c) detector response, and (d) amplifier characteristics [1.3]. However, all the above factors are constant apart from intensity of the source $I(\bar{\nu})$. In order to take account of the above factors, a single wavenumber-dependent correction factor, $\mathbf{H}(\bar{\nu})$ is added to equation (1.13) to give

$$\mathbf{I(x) = \frac{1}{2} H(\bar{\nu}) I(\bar{\nu}) \cos 2\pi \bar{\nu} x} \qquad (1.14)$$

or

$$\mathbf{I(x) = S(\bar{\nu}) \cos 2\pi \bar{\nu} x} \qquad (1.15)$$

Where $\mathbf{S}(\bar{\nu}) = \frac{1}{2}\mathbf{H}(\bar{\nu})\mathbf{I}(\bar{\nu})$.

The final stage is to compute the cosine Fourier transform of I(x) in order to calculate the spectrum. The interferogram for a polychromatic source is expressed as

$$\mathbf{I}(\mathbf{x}) = \int_{-\infty}^{+\infty} \mathbf{S}(\bar{\nu}) \cos 2\pi \bar{\nu}\mathbf{x}.\mathbf{d}\bar{\nu} \qquad (1.16)$$

which is one-half of a cosine Fourier transform pair, the other being [1.3]

$$\mathbf{S}(\bar{\nu}) = \int_{-\infty}^{+\infty} \mathbf{I}(\mathbf{x}) \cos 2\pi \bar{\nu}\mathbf{x}.\mathbf{dx} \qquad (1.17)$$

Since $\mathbf{I}(\mathbf{x})$ is an even function, equation 1.17 may be rewritten as

$$\mathbf{S}(\bar{\nu}) = 2\int_{0}^{+\infty} \mathbf{I}(\mathbf{x}) \cos 2\pi \bar{\nu}\mathbf{x}.\mathbf{dx}$$

1.6.1. Advantages of FTIR spectroscopy

(a) Fellgett (multiplex) advantage: The signal-to-noise ratio, SNR of a spectrum in FTIR is greater than that of a spectrum measured on a grating spectrometer with the same parameters by a factor of square root of the number of resolution elements, $\sqrt{M}$. This advantage arises from the fact that the detector sees all spectral elements at the same time.

i.e.

$$(\mathbf{SNR})_{\mathbf{G}} \propto \frac{\tau^{\frac{1}{2}}}{\mathbf{N}^{\frac{1}{2}}}$$

$$(\mathbf{SNR})_{\mathbf{FT}} \propto \tau^{\frac{1}{2}}$$

Where τ is the total time, and N is the number of elements. Therefore the SNR gain is $N^{\frac{1}{2}}$. In addition to sensitivity advantage, the time advantage of a Fourier spectrometer is important, and is directly proportional to M.

(b) Jacquinot advantage: Interferograms have a higher optical conductance than prism or grating spectrometers. Spectral optical conductance of a grating instrument can be expressed by:

$$\mathbf{G}_{\tilde{\nu}}^{\mathbf{G}} = \frac{\mathbf{h}.\mathbf{H}}{\mathbf{f}.\tilde{\nu}}.\mathbf{R}_0 \qquad (1.18)$$

Where $G_{\tilde{\nu}}^{G}$ is the optical conductance per wavenumber of grating spectrometers, H is the height of the beam at the grating or prism, h is the length of the entrance slit, f the focal length of the collimator, and R_0 is the theoretical resolving power. In order to compare this equation with that of interferometer equation for the spectral optical conductance, the beam area of the interferometer F_1 is chosen to be equal to the beam area at the grating H^2. Thus the relation for interferometer is

$$\mathbf{G}_{\tilde{\nu}}^{\mathbf{I}} = \frac{2\pi\mathbf{H}^2}{\tilde{\nu}} \qquad (1.19)$$

Thus the ration of the spectral optical conductance of an interferometer and that of a grating spectrometer is

$$\frac{G^{I}_{\tilde{\nu}}}{G^{G}_{\tilde{\nu}}} \approx \frac{2\pi f}{h} \qquad (1.20)$$

This ratio for using a common interferometer is of the order of 100.

(c) Connes advantage: In FTIR spectroscopy, since the 'sampling' is controlled by a laser whose wavelength is 'fixed', control of spectral wavelength can be achieved with greater accuracy.

(d) In addition to the above advantages, it is possible to perform spectral subtraction.

1.7. Attenuated Total Reflectance

Attenuated total reflectance (ATR) is a method used for the infrared analysis of substances that cannot be easily assayed by using other techniques in infrared spectroscopy such as the transmittance technique. It is particularly useful for polymeric substances.

The technique is based upon the fact that totally reflected radiation at an interface with a rarer medium slightly penetrates the surface from which it is reflected. This penetrated radiation is called the evanescent wave and is characterised by an electric field magnitude which decays exponentially with distance from the interface (Fig 1.3). The rate of decay

is dependent on (a) the refractive indices of the denser and the rarer media, (b) the angle of incidence, and (c) the wavelength of the light.

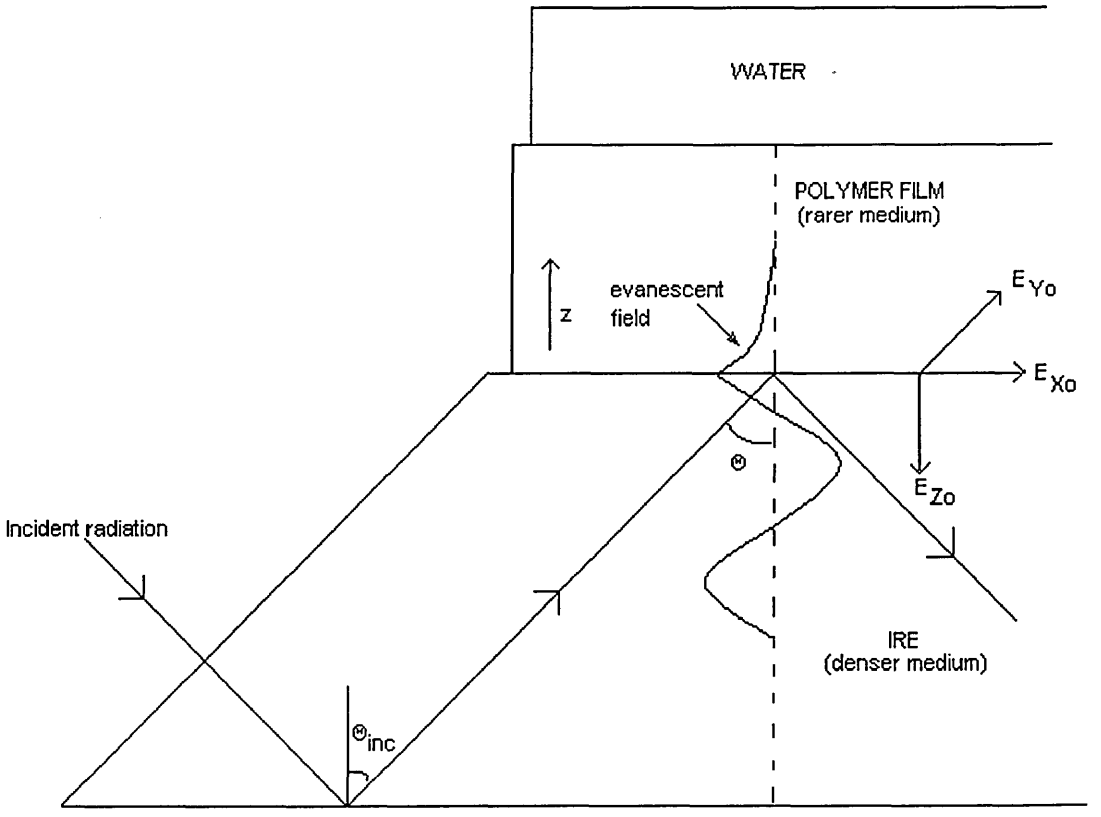

Figure 1.5: *Principle of internal reflection spectroscopy*

Snell's law can be used to calculate the angle of reflection when radiation passes from one medium to another:

$$n_1 \sin a = n_2 \sin b \qquad (1.21)$$

In the above expression, n_1 and n_2 are the refractive indices of the rarer and propagating media, a is the angle of incident radiation as measured from the perpendicular to the

surface between the two media, and *b* is the angle at which the radiation is refracted in the second medium.

From equation 1.21 it is apparent that the as angle of incidence increases, the angle of refraction also increases. If n_2 is less than n_1, an angle *a* exists for which angle *b* is 90^o, that is, for which the radiation is completely reflected. That angle is the *critical angle* θ_c. Incident radiation that strikes the surface between the two media at an angle that is greater than the critical angle is completely reflected from the surface. The value of the critical angle can be calculated from equation 1.21 by substituting 90^o for *b* and θ_c for *a*. Thus equation 1.21 will become:

$$n_1 \sin \theta_c = n_2 \sin 90^o$$

$$\theta_c = \sin^{-1} n_2/n_1 \qquad (1.22)$$

At incident angles greater than the critical angle, total reflection occurs at the surface. Incident radiation is not lost during the reflection although radiation can be lost due to absorption by the prism material. The critical angle is dependent upon a ratio in the refractive index of the two media. Consequently, it is necessary to select an ATR prism material that both has a high refractive index and that is greater than that of the sample and also transmits radiation. Some common materials that are used to construct the prism include, ZnSe (670 - 20,000 cm-1) and KRS-5 (250 - 17,000 cm-1).

The change in the electric field, E, as a result of exponential decay of the evanescent field after reflection of light at interface is given by [1.4, 1.5]:

$$E = E_0 e^{-\gamma z} \qquad (1.23)$$

Where γ is the evanescent field decay coefficient, and is defined as:

$$\gamma = \frac{2n_2\pi\sqrt{\sin^2\theta - \left(\frac{n_1^2}{n_2^2}\right)}}{\lambda} \qquad (1.24)$$

Where λ is the wavelength of the light in vacuum. Figure 1.6 shows a plot of intensity $(E/E_0)^2$ as a function of distance from interface Z for various values of γ.

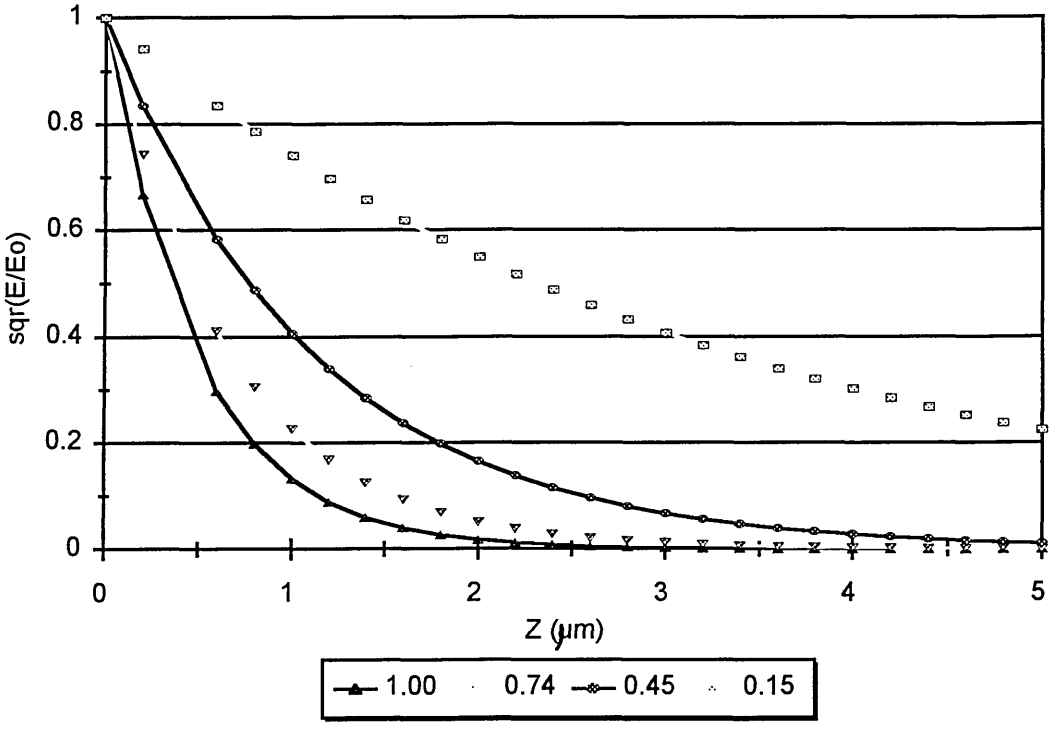

Figure 1.6: *Plot of the intensity of the electric field as a function of depth for various values of gamma, $\gamma(\mu m^{-1})$*

The reciprocal of γ is called the depth of penetration dp. This is defined as the distance at which the electric field decays to a value of E_0 exp [-1] of its value at the interface [1.5]. This parameter (dp) is often used as a measure of depth that is sampled in the IRE experiment. However, it should be noted that E is not zero at dp. The maximum depth sampled is about three times dp.

The energy is removed from the reflected light if the rarer medium is capable of absorbing light at some frequency present in the evanescent wave. This absorbtion can be detected by (a) measuring light emitted in the adjacent medium and thus the technique is called fluorescence spectroscopy or (b) by measuring a decrease in the intensity of the reflected wave and thus the technique is called absorption spectroscopy.

The intensity of the radiation, $(E/E_0)^2$ is equal to the square of the electric field magnitude, and is related to the absorbtion of light. Figure 1.7 shows a plot of the exponential decay of the electric field amplitude (E/E_0) and the intensity $(E/E_0)^2$ as a function of depth into the surface Z. The denser medium used is a ZnSe ATR prism and the rarer medium is a film of sulphonated polyetherethersulfone/polyethersulfone (SPEES/PES) which has been used in this work as a polymeric membrane.

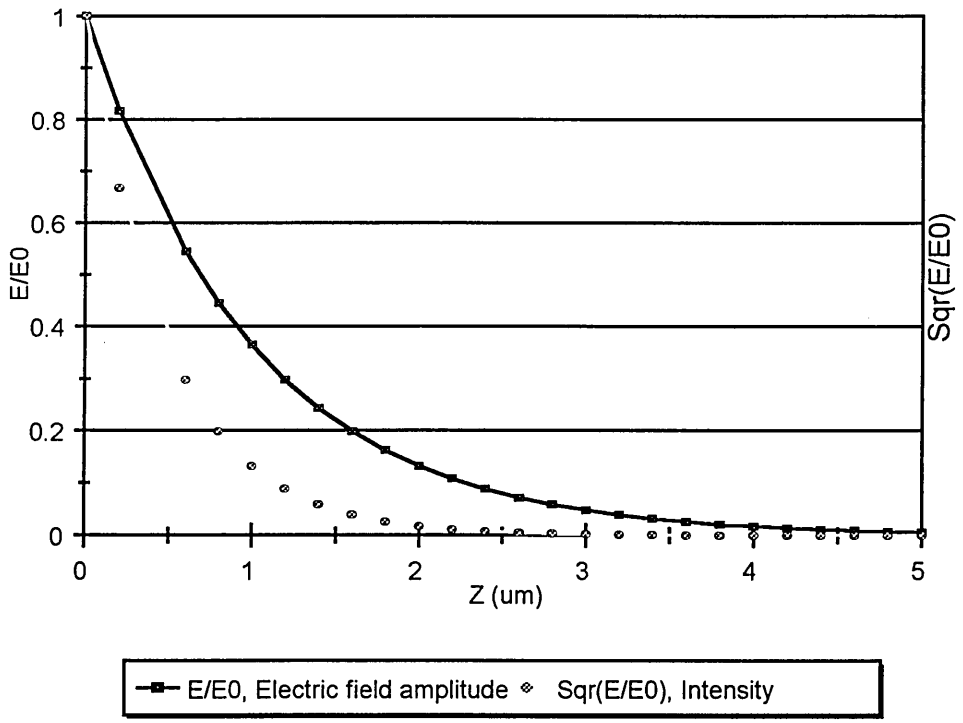

Figure 1.7: *Plot of E/E_0 vs distance(z) and $(E/E_0)^2$ (Intensity) vs distance (z)*

In order to be able to make a comparison between transmission technique and IRS, it is necessary to know the effective thickness, d_e in the IRS experiment. The effective thickness can also provide a basis for calculating the theoretical upper limit on the absorbance for a weak absorber. It is defined as the thickness of a film of the sample material that would give the same absorbance for transmission at normal incidence as that obtained in the IRS. It is necessary to utilise expressions for the electric field amplitudes at the surface of the rarer medium in order to be able to calculate the effective thickness. As can be seen in figure 1.5 there are two polarisations: (a) the one perpendicular to the plane of incidence and is called transverse electric (TE) and (b) the one parallel to the

plane of incidence and is called transverse magnetic (TM). The interface plane between the denser and the rarer media is perpendicular to the plane of incident radiation.

There are three electric field amplitude at the surface of the rarer medium. i.e. E_{Xo}, E_{Yo}, and E_{Zo} (fig 1.3). E_{Zo} is parallel to the plane of incidence and perpendicular to the plane of surface and E_{Xo} is parallel to both planes of incidence and surface. These two electric field amplitudes are associated with the TM wave which is elliptically polarised at the surface as a result of the oblique angle of incidence with the rarer medium. E_{Yo} is perpendicular to the plane of incidence and parallel to the plane of surface and is associated with the TE wave.

The thickness of the rarer medium has effects on the properties of the evanescent field. On this basis, all the cases will fall into two distinct categories. These are (a) the thin film case in which the electric field amplitude remains constant over the thickness, t of the film, such that $t << 1/\gamma$. Therefore it has no controlling effect on the evanescent field and the field decays in medium 3 (ref index = n_3). The other case is (b) the semi-infinite case. This is when the electric field amplitude falls to a very low value within the thickness of the rarer medium t, such that $t >> 1/\gamma$. The following expressions define the amplitude of electric fields in X, Y, and Z directions at the surface of the rarer medium (Z = 0).

For the thin case ($t << 1/\gamma$):

$$\mathbf{E}_{\perp} = \frac{2\cos\theta}{\sqrt{(1-\mathbf{n}_{31}^2)}} \qquad (1.25)$$

$$\mathbf{E}_{\parallel} = \frac{2\cos\theta\sqrt{\left(1+\mathbf{n}_{32}^{4}\right)\sin^{2}\theta-\mathbf{n}_{31}^{2}}}{\sqrt{\left(1-\mathbf{n}_{31}^{2}\right)}\sqrt{\left(1+\mathbf{n}_{31}^{2}\right)\sin^{2}\theta-\mathbf{n}_{31}^{2}}} \qquad (1.26)$$

Where $\mathbf{n}_{31} = \frac{\mathbf{n}_3}{\mathbf{n}_1}$ and $\mathbf{n}_{32} = \frac{\mathbf{n}_3}{\mathbf{n}_2}$

For the semi-infinite bulk case ($t >> 1/\gamma$)

TM wave where $\mathbf{E}_{\parallel} = \left(\left|\mathbf{E}_{\mathrm{Xo}}\right|^{2} + \left|\mathbf{E}_{\mathrm{Zo}}\right|^{2}\right)^{0.5}$

$$\mathbf{E}_{\mathrm{Xo}} = \frac{2\cos\theta\sqrt{\left(\sin^{2}\theta-\mathbf{n}_{21}^{2}\right)}}{\sqrt{1-\mathbf{n}_{21}^{2}}\sqrt{\left(1+\mathbf{n}_{21}^{2}\right)\sin^{2}\theta-\mathbf{n}_{21}^{2}}} \qquad (1.27)$$

$$\mathbf{E}_{\mathrm{Zo}} = \frac{2\sin\theta\cos\theta}{\sqrt{1-\mathbf{n}_{21}^{2}}\sqrt{\left(1+\mathbf{n}_{21}^{2}\right)\sin^{2}\theta-\mathbf{n}_{21}^{2}}} \qquad (1.28)$$

TE wave $$\mathbf{E}_{\perp} = \mathbf{E}_{\mathrm{Yo}} = \frac{2\cos\theta}{\sqrt{1-\mathbf{n}_{21}^{2}}} \qquad (1.29)$$

Where $\mathbf{n}_{21} = \frac{\mathbf{n}_2}{\mathbf{n}_1}$

Figure 1.8 shows the curves corresponding to the magnitude of E fields as a function of

angle of incidence for the ZnSe-SPEES/PES interface

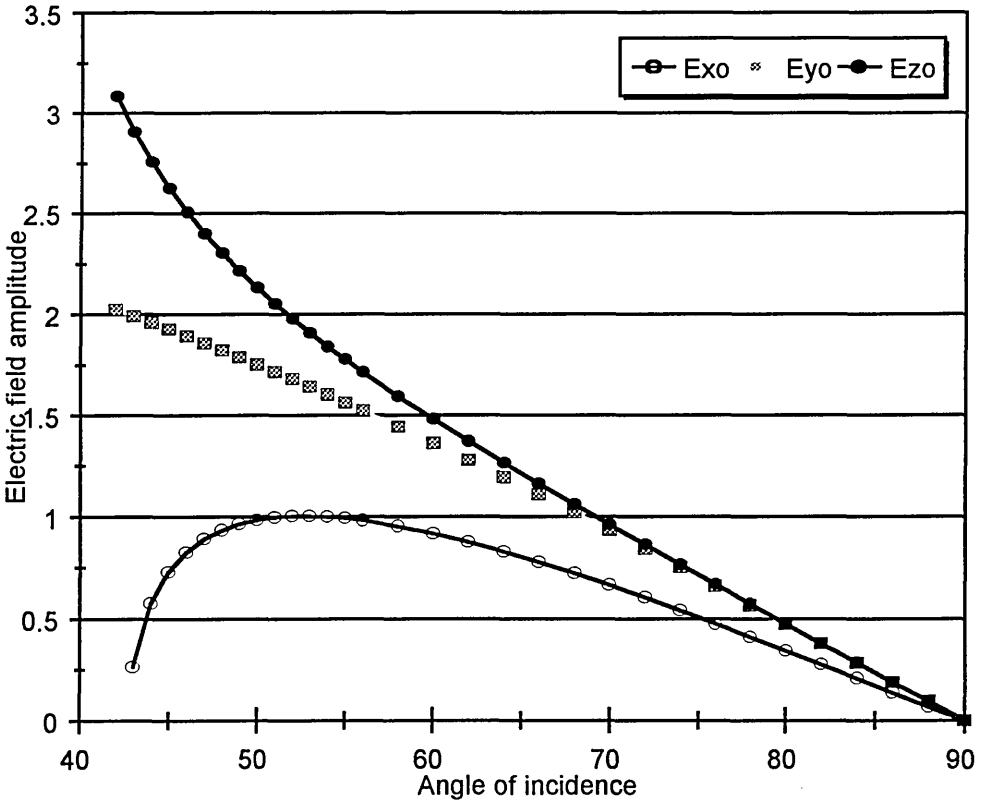

Figure 1.8: *Calculated electric field amplitudes for polarised radiation and their variations with angle of incidence for ZnSe-SPEES/PES interface*

Figure 1.8 shows that the E values all increase away from the grazing angle (90°). E_{xo} decreases abruptly near the critical angle and falls to zero at θc, while E_{Yo} and E_{Zo} both reach maxima at the critical angle.

CHAPTER 2

2.1. Introduction

The Raman effect, one of the most significant advances in spectroscopy was predicted by Smekal in 1923, but it took another five years until observed for the first time by Sir Chandrasekhara V. Raman in 1928 [2.1].He used focused sunlight and filters and visually observed colour changes in the scattered light for his first experiments. Later, using a spectrograph and a mercury lamp, he obtained Raman spectra of many liquids including carbon tetrachloride and benzene. However, he needed to use about 600 ml of sample and 24 hours exposure time in order to record a measurable spectrum. Because of such practical difficulties the Raman effect was not an easy technique to use. The introduction of the Toronto arc source in 1952 improved the technique but the modern Raman renaissance took place some three decades later in early sixties by using visible laser radiation.

Today Raman spectroscopy is one of the most powerful analytical techniques utilising high quality optics, very sensitive detectors, a variety of intense laser light, and digital data acquisition and processing with fast computers. For this reason it is not surprising

that for many samples the Raman spectra can be recorded in seconds and thus the technique is easily and routinely used in academic or industrial environments.

2.2. Theory

The Raman theory has been described by two approaches known as classical theory and quantum theory. These theories have been described in detail by many researchers [2.2-2.5]. When an intense monochromatic beam of light impinges on a sample, about 99.9% of the light is scattered with the same frequency (elastic scattering) and only about 0.1% of the scattered light (inelastic scattering) contains photons which have frequencies greater or lower than that of incident light. In the other words interaction of a molecule with a photon of visible light with a specific energy can cause the photon to be scattered in one of the following ways: (a) the same frequency and retaining its energy (Rayleigh scattering), (b) lower frequency and lower energy (Stokes scattering) and (c) higher frequency and higher energy (anti-Stokes scattering). This has been shown in figure 2.1.

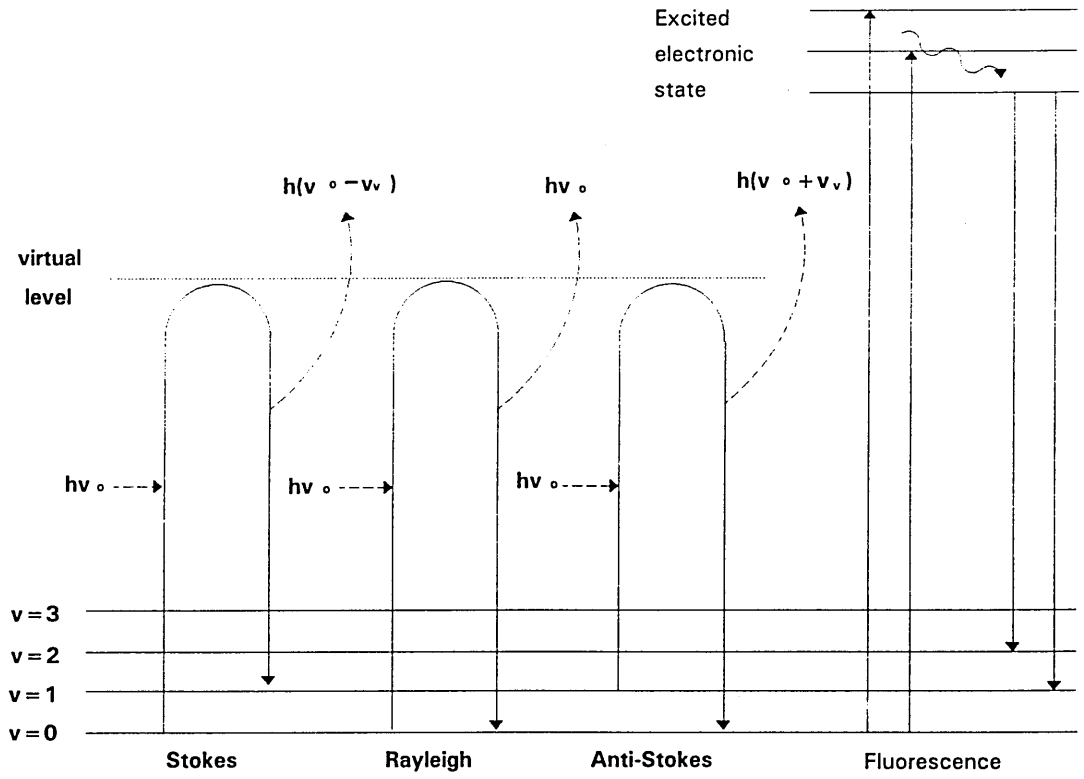

Figure 2.1: Rayleigh and Raman scattering model according to quantum theory

The intensity of Stokes and anti-Stokes scattering is dependent on the vibrational energy level of the molecule just before the collision. As can be seen in figure 2.1 the Stokes lines arise from transition of the molecules from the ground state vibrational energy level to a higher energy level and the anti-Stokes lines arise from the transition of the molecules in an excited energy level to a lower energy level. Since most molecular vibrations at room temperature are in the ground level hence the Stokes scattering is more intense. For this reason the Stokes scattering is usually recorded in most cases and is studied by spectroscopists. Figure 2.2 shows the Raman spectrum of silicon with Stokes and anti-Stokes bands.

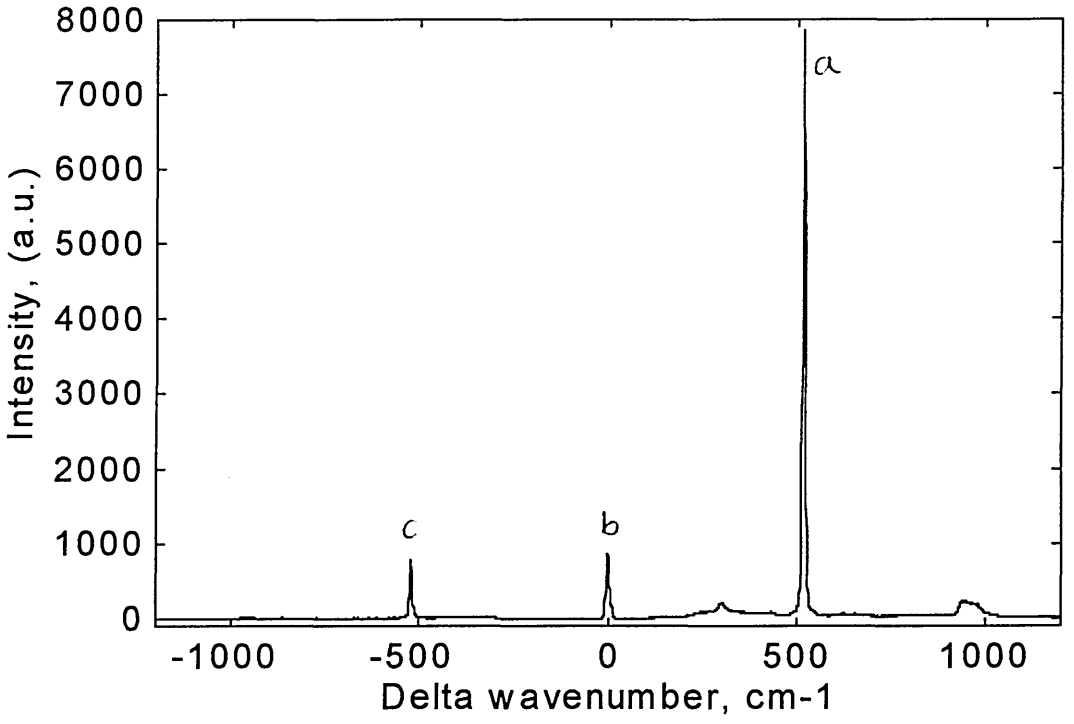

Figure 2.2: *Raman spectrum of silicon where (a) is the Stokes band, (b) is the residual Rayleigh scattered light (it should be noted that this band is only the Rayleigh scattered light after being filtered out by the holographic notch filter) and (c) is the anti-Stokes band*

2.3. Sample fluorescence

One of the problems which is observed commonly in the Raman spectrum of many samples is a background fluorescence spectrum. The exact source of such fluorescence is not understood but one possible explanation for this phenomenon is the existence of trace amounts of "luminescing" sample impurities [2.6]. Fluorescently scattered light also undergoes a Stokes shift.. See figure 2.1.

Although there is no complete cure for this problem, the background fluorescence can be reduced in several ways: (a) Application of Raman microscopy. Indeed one of the advantages of the use of Raman microscopy is the reduction of fluorescence. A possible

reason for such reduction is "bleaching" or "burning out" of impurities by the relatively high power density laser on the small area of the sample.

(b) Choosing a laser beam with excitation wavelength (e.g. 1.06 μm) away from the excitation spectrum of the fluorophore. [2.7].

(c) Using phase-sensitive detection technique: [2.8] In this method Raman signals are separated from those of the fluorescence based by the fact that Raman scattering is an instantaneous process whereas in fluorescence, excited state lifetimes (see fig 2.1) are often in the order of nanoseconds.

2.4. Raman microscopy

The idea of the possibility of extension of laser-excited scattering to the analysis of micrometer and sub-micrometer size particles was first suggested by Tomas Hirschfeld as early as 1969. In his abstract [2.9] he outlined some basic requirements for Raman microprobe spectrometers. Rosasco et al [2.10, 2.11] reported the first successful measurement of the Raman spectrum of individual micrometer and (sub micrometer) sized particles at the IVth International Conference on Raman Spectroscopy in 1974. Delhaye et al [2.12, 2.13], at the same conference reported the realisation of a Raman microscope. This led to the development of the first Raman microprobe at the US National Bureau of Standards [2.14] for particle analysis and at the Université des Sciences et Techniques de Lille, [2.15-2.17] which was later commercially available as the MOLE [2.18].

Since then, Raman microscopy has progressed and today incorporates the latest development in confocal microscopy (see section 2.4.2) which is the most efficient method for Raman mapping and microprobing.

In this thesis applications of Raman microscopy have been described later in detail under two sections of confocal Raman microspectroscopy and Raman imaging and mapping.

2.4.1. Sample heating in Raman microscopy

In Raman microscopy the laser beam may cause damage to the sample. This is due to focusing the laser beam to a very small area on the sample and thus relatively high laser power density at the sample. For polymers, moderate heating may cause damage in structure, composition and morphology. Some researchers have reported such damage on application of Raman microscopy to carbon fibers [2.19-2.23]. However it should be noted that carbon fibers are black and thus absorb a considerable amount of visible light, and hence causing substantial sample heating. In general distribution of generated heat is greatly influenced by the thermal conductivity of the sample [2.24]. Opaque inclusions or a non-uniform distribution of energy density within the sample can cause localised absorption.

2.4.2. Confocal Raman Microscopy

Marvin Minskey, who is well known as the father of artificial intelligence was also the author of another important achievement [2.25]. He built a revolutionary light microscope in the 1950s as a postdoctoral fellow at Harvard University. This instrument enabled him to view successively deeper layers in a specimen with astonishing clarity, without the laborious task of sample preparation in the form of thin sections. He patented the

microscope as " double-focusing stage-scanning microscope " in 1961 but during the 17-years life of the patent no microscopes of similar design were manufactured. Disappointed with the lack of appreciation for his foray in the optics, he left the prototype to rust in a corner of his basement and moved on to other challenges.

To day his approach otherwise known as confocal microscopy is widely used in optical microscopy. It provides one of the significant advances in optical microscopy in the last few decades. A variety of microscopes for different purposes have been built which take advantage of this approach including confocal Raman microscopy.

The confocal setup of a Raman microscope can provide the means for "optical sectioning". This means that it has the ability to discriminate between parts of the sample which are not at the same depth and only allow the detection of scattered Raman light from molecular vibrations of a particular depth. This also provides a valuable way in Raman spectroscopy to almost eliminate the stray light (background, fluorescence) coming from outside the focal volume.

However, it should be noted that the use of the confocal method can also have some disadvantages. Since the laser light is focused on a very small point on the sample, the laser intensity is very high in that region and thus in some cases can damage the sample even at laser powers below 1 mW. This damage becomes visible under a light microscope in the form of a black spot or a "paling" of the sample at the site of the laser focus. The choice of the laser wavelength used for excitation is found to be crucial. In many cases such damage has not been observed with the use of a 632.8 nm laser. Photochemical effects may be the most plausible cause of the sample degradation at 514.5 nm. Foote [2.26] shows that DNA bases and a number of amino acids can be degraded in "photodynamical" processes requiring the presence of light, a sensitiser and oxygen. In

such a process laser excitation brings the sensitiser via the singlet state in a long-lived triplet state. It can then react with oxygen to form reactive oxygen species that could cause the observed radiation damage through oxidation of the DNA bases or amino acids leading to lesions in these molecules.

Confocal Raman microspectrometry has been employed in many areas of science and technology. Some teams of researchers have reported the design of a new instrument or have developed the existing Raman microscopes in order to use the instrument in confocal mode for various applications [2.27-2.33]. The use of fiber-optics in some of the new instruments has been reported [2.34-2.38]. It provides remote capabilities for the microscope and the ability to use multiple excitation sources and detection schemes. Biological applications of the technique include: cell biology and chromosomes [2.39-2.45], DNA-protein complexes [2.47-2.53] and other biological applications [2.54-2.61]. The use of this technique in materials [2.62-2.66] and polymer [2.67-2.74] science has also been reported.

2.4.2.1. Theory

Raman microscopy with spatial resolution of 1 μm in the lateral plane (x, y) has been used for many years to provide information about molecular vibrations of small area of samples. However for some samples a good spatial resolution along the optical axis, z is desirable. The signal intensity recorded by the detector for a given Raman line at the wavelength λ is expressed by: [2.75]

$$\text{signal} \sim I_0 \, \sigma_\lambda \, N \, \theta \, T_\lambda \, s_\lambda \qquad (2.1)$$

Where I_0 = laser irradiance at the sample (watts unit area^{-1})

$\sigma\lambda$ = differential cross-section for the analysed Raman line (cm^2 . sterad^{-1} . molecule^{-1})

N = number of molecules in the probed volume, V

θ = angle of collection of the Raman light

$T\lambda$ = througthput of the instrument at the wavelength λ

$s\lambda$ = sensitivity of the detector at the wavelength λ

As a result of using the confocal approach a small volume of the sample is to be examined and thus, to compensate for the large reduction in the number of the molecules N in the probed volume, only I_0 and θ may be modified. For this reason the best way to decrease sampling volume while increasing laser irradiance and the collection angle is to use microscope objectives. Such objectives are used for both illuminating the sample and collecting the Raman scattered light. The numerical aperture (N. A.) of an objective determines the distribution of the laser field around the focus. The numerical aperture is the sine of half the angular aperture. i. e.,

$$\mathbf{N.A.} = \mathbf{Sin}\left(\frac{\theta}{2}\right) \qquad (2.2)$$

Where, N. A. = Numerical aperture with maxium value of 1.

θ = Angle of entrance.

Thus, microscope objectives with high-numerical aperture (NA) optics are able to focus the laser beam into a very small volume and to collect, under a wide angle, the Raman light scattered by this volume. See figure 2.3.

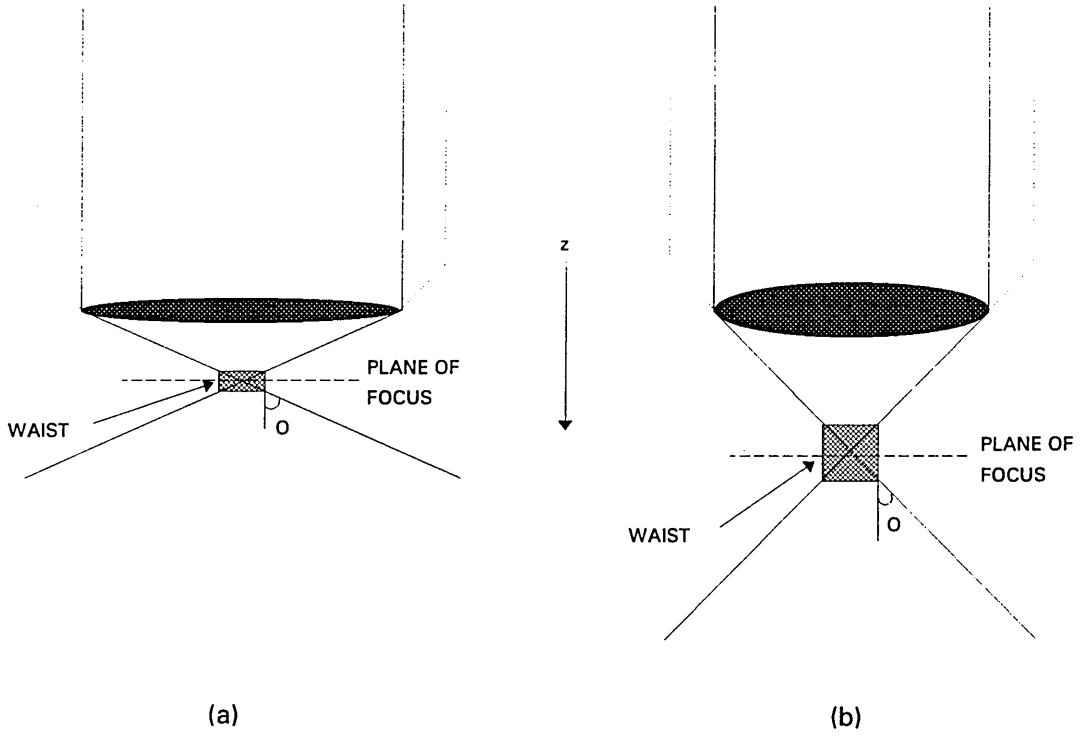

Figure 2.3: *Schematic diagram of the distribution of laser light near focus using a microscope objective with (a) high NA, (b) low NA*

Table 2.1 shows the calculated values of such a relationship for the objectives which have been used for the studies in this thesis.

Objective	**NA**	**1/2 angle, θ (deg)**	**Depth of focus, ω (μm)**
100x	0.95	71.8	0.1
50x	0.80	53.13	0.4
20x	0.46	27.39	2.4
20x (long)	0.40	23.58	3.3
10x	0.30	17.46	6.4

Table 2.1: *Calculated values for the depth of focus, ω for various microscope objectives*

When a pinhole is placed in the back focal plane of a microscope, light from planes higher or lower than focal plane are blocked by the opaque regions around the pinhole and in this way the depth resolution of the microscope can be enhanced enormously. Figure 2.4 shows the principle of confocal microscopy.

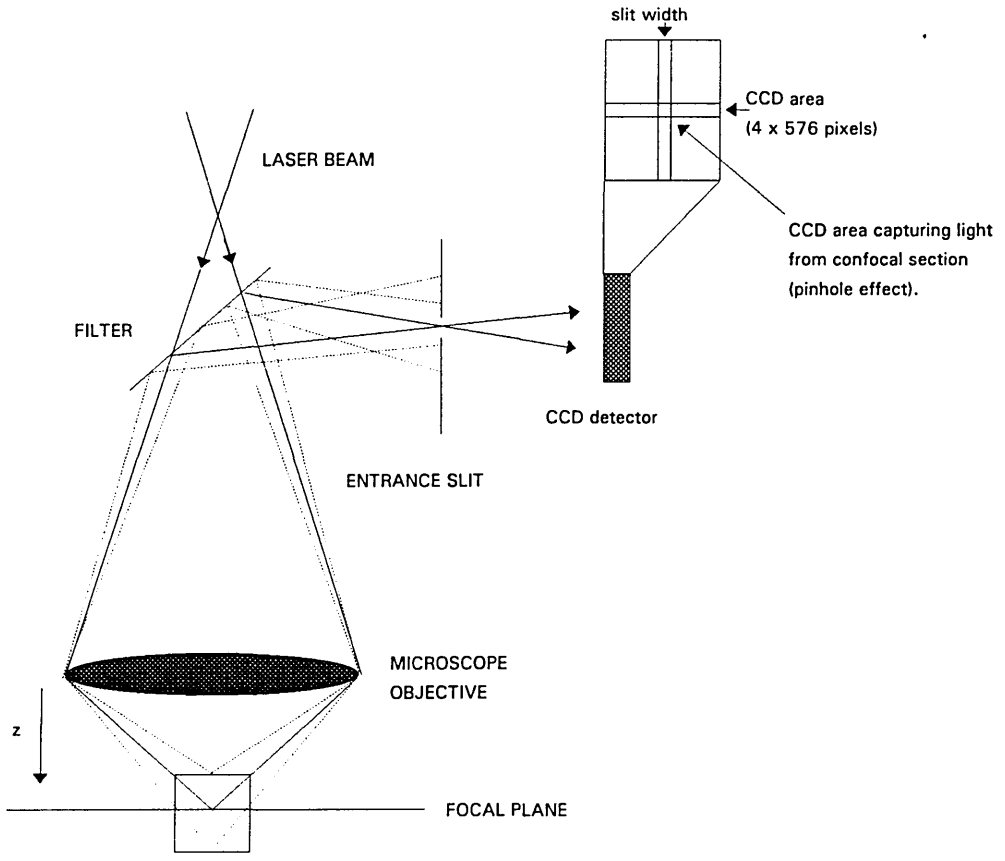

Figure 2.4: *Schematic diagram of the principle of confocal Raman microspectroscopy*

Some researchers [2.73,2.42] have used pinholes with dimensions 100 and 300 μm. The pinhole has been aligned in the optical axis and along the optical axis with the aid of micrometer adjustments. The process of such optical alignment can be difficult and time-consuming. In order to reduce such difficulties Williams et al describe the use of a CCD

detector with a stigmatic Raman spectrograph [2.74]. In this way the long axis of the CCD detector (576 pixels) is used to describe the spectral dimension, while the shorter axis (384 pixels) describes the image height. By using only a few pixels in the spatial direction of the detector (four pixels represent an image of 100 μm) and the spectrometer slit with width of approximately 15 μm (used to provide the primary aperture in the system), the "pinhole effect" as a small area on the CCD detector is created. This is shown in figure 2.4.

The role of the pinhole can be explained by geometrical reasoning and, and in order to keep the model for explaining this role simple, diffraction effects at the pinhole are ignored. This is a good approximation since a pinhole of greater than 100 μm has been used in these studies and thus diffraction effects at the pinhole are small [2.73]. In addition the influence of refraction, scattering, and absorption at the sample surface has been disregarded. Figure 2.5 shows the schematic of a light microscope coupled to a spectrograph. This is similar to the Renishaw Ramascope used for these studies.

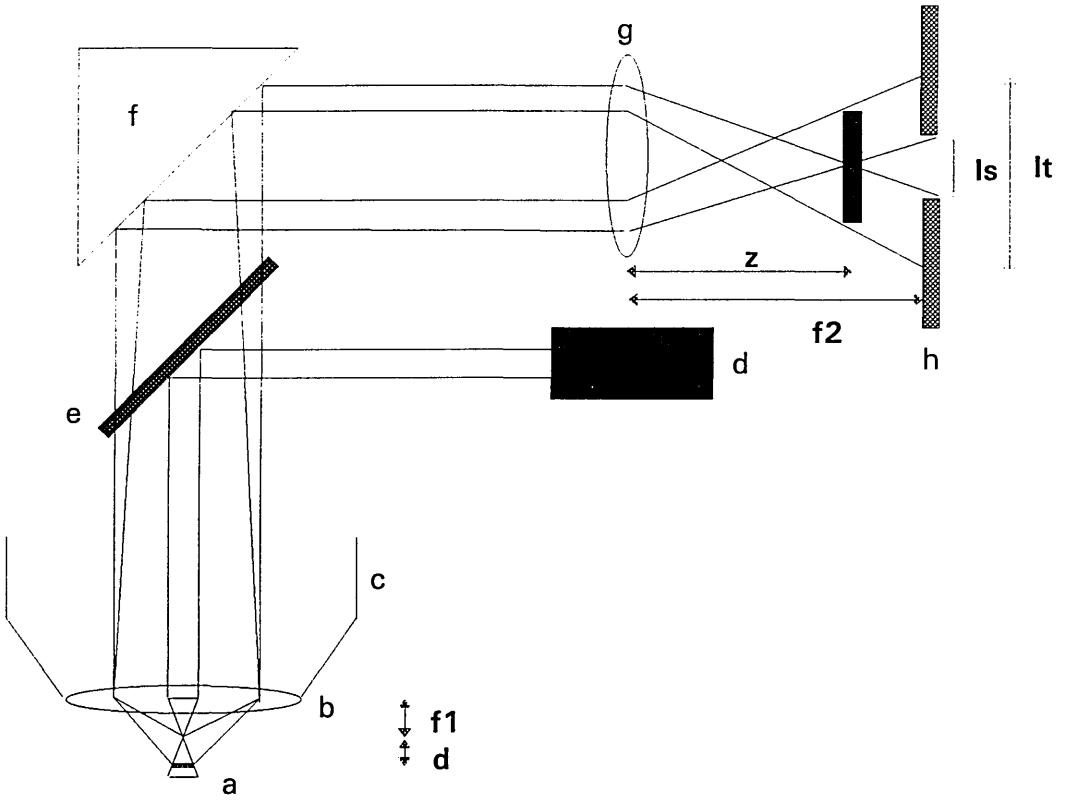

Figure 2.5: *The schematic diagram of the optics in the Raman microscope with confocal setup (similar to Renishaw Ramascope). (a) sample plane, (b) objective lens, (c) microscope objective, (d) laser source, (e) beam splitter, (f) mirror reflecting the Raman light to the spectrometer, (g) slit focusing lens, (h) pinhole, f_1 and f_2 are the focal length of the objective and slit focusing lenses respectively, d is the distance from the focal plane of the objective lens, I_S is the diameter of pinhole and I_t is the diameter of the image of the projected laser spot*

The objective lens and the slit focusing lens are designated as L_1 and L_2 respectively. The smallest diameter of the laser beam is in the focal plane of the objective lens, L1 [2.76] and this diameter remains approximately constant up to a certain distance from the focal plane. This is known as the waist, ω (see fig 2.3). Equation 2.3 can be used to determine depth of waist which is known as depth of the focus [2.77].

$$\omega = 6.4.\left(\frac{\lambda}{2\pi}\right).\left(\frac{1}{\tan\theta}\right)^2$$

or

$$\omega \approx \lambda.\left(\frac{1}{\tan\theta}\right)^2 \qquad (2.3)$$

Where λ = wavelength of the laser light

θ = entrance half-angle

The calculated depth of focus for the objectives used in these studies are shown in table 2.1. The size of the laser spot can be expressed by s(f1 ± d) where f1 is focal length of the objective lens and d is distance from in-focus plane and thus the following equations can be used to determine the diameter of the laser light around the focus;

$$\mathbf{s(f_1 \pm d) = s(f_1)} \qquad \text{for} \quad \left(\mathbf{d} < \frac{\omega}{2}\right) \qquad 2.4$$

$$\mathbf{s(f_1 \pm d) = s(f_1) + 2\left(d - \frac{\omega}{2}\right)\tan\theta} \qquad \text{for} \quad \left(\mathbf{d} > \frac{\omega}{2}\right) \qquad 2.5$$

In a confocal arrangement a slit is placed at the back image of the microscope and an out-of-focus laser spot with size s.(f_1 ± d) will be imaged outside of back focal plane at a distance Z_2 from the slit focusing lens, L_2.(see fig 2.5). i.e.,

$$Z_2 = \left\{ \frac{1}{f_2} - \frac{1}{f_2 - \left(\frac{1}{f_1} - \frac{1}{f_1 \pm d} \right)^{-1}} \right\}^{-1} \qquad (2.6)$$

Where f_2 is the focal length of the slit focusing lens, L2

This image is projected on the back image plane of the microscope which is bigger than the laser spot image lying on the focal plane. The diameter of the out-of-focus projection , I_t on the image plane f_2 can be calculated [2.73] by:

$$I_t = \frac{f_2 . M . [s . (f_1 \pm d)]}{z_2} \qquad (2.7)$$

Where M is the magnification power of the objective. Since the out-of-focus projection, I_t is larger than in-focus one (see fig 2.5), by placing a pinhole with a diameter, I_s less than that of I_t, it is possible to block most of the light coming from the regions below and above than the focal plane and allow only the light from the focal plane to reach the detector of the instrument. Equation 2.7 shows that microscope objectives with a high numerical aperture (and thus with a wide half angle of collection) can ensure (1) a very divergent beam out side the focal plane and (2) a short waist. In this way the projection, I_t (see eqn 2.7) is enlarged from the out-of-focus laser at the back image plane and thus enhances the efficiency of the pinhole.

Figure 2.6 shows a comparison between curves obtained with confocal and conventional Raman microscopy. In this figure intensity distribution has been represented as a function of distance from the object focal plane.

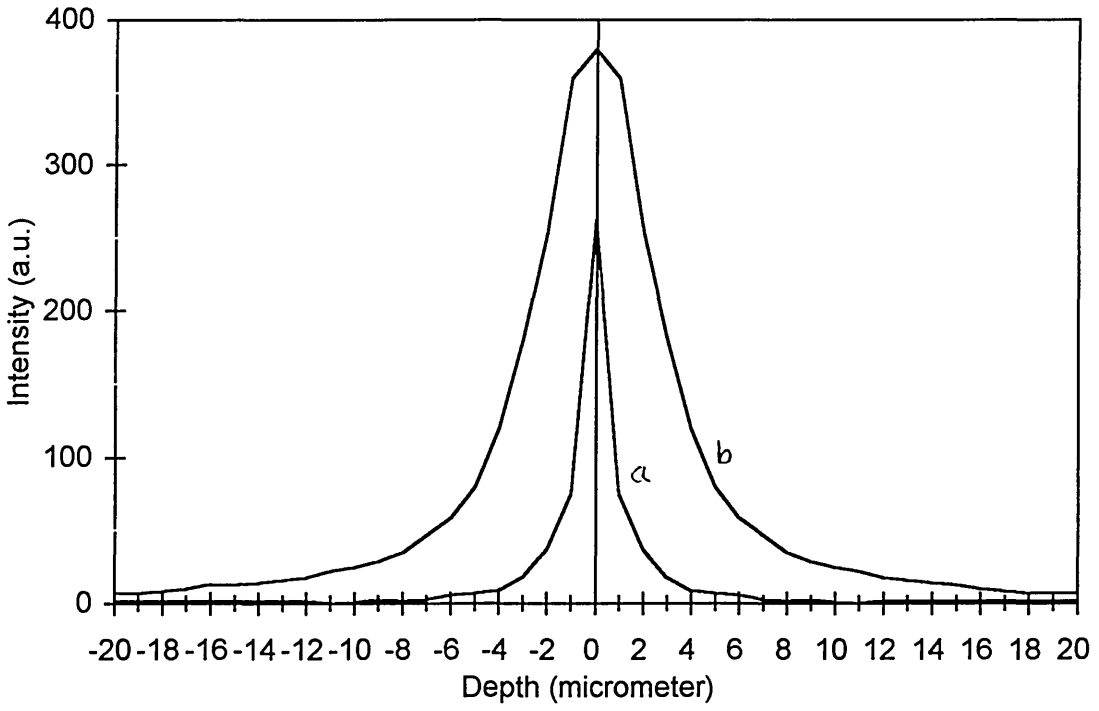

Figure 2.6: *Comparison of (a) confocal Raman microscopy, and (b) conventional Raman spectroscopy*

In order to show the effect of microscope objectives with various magnification power and numerical aperture on confocal Raman microscopy, a simple experiment was performed [2.67]. In this test the focus of the laser was stepwise (1 μm) scanned away from the surface of a silicon wafer, and the signal intensity of the fundamental vibration at 519 cm^{-1} was recorded. Figure 2.7 shows a plot of Raman intensity as a function of distance away

from silicon surface. From this experiment the depth resolution using different microscope objectives could be determined. The depth resolution was thus determined for the 100x objective as 2.0 ± 0.3 μm and for the 50x objective as about 5 ± 1 μm using FWHM criterion. However, it is clear from figure 2.7 that about 90% of the scattered light is contributed from a 2 μm (with a 100x objective) from below and above the plane of focus, but it should be noted that significant Raman scattering light is still contributed from the regions further above and below this region.

The data for the curves in figure 2.7 have been collected experimentally using the above test and thus these curves show the response of the Raman confocal microscope in practice. However it is possible to determine the theoretical response of the system and thus compare the experimental and theoretical performance of the Raman confocal microscope.

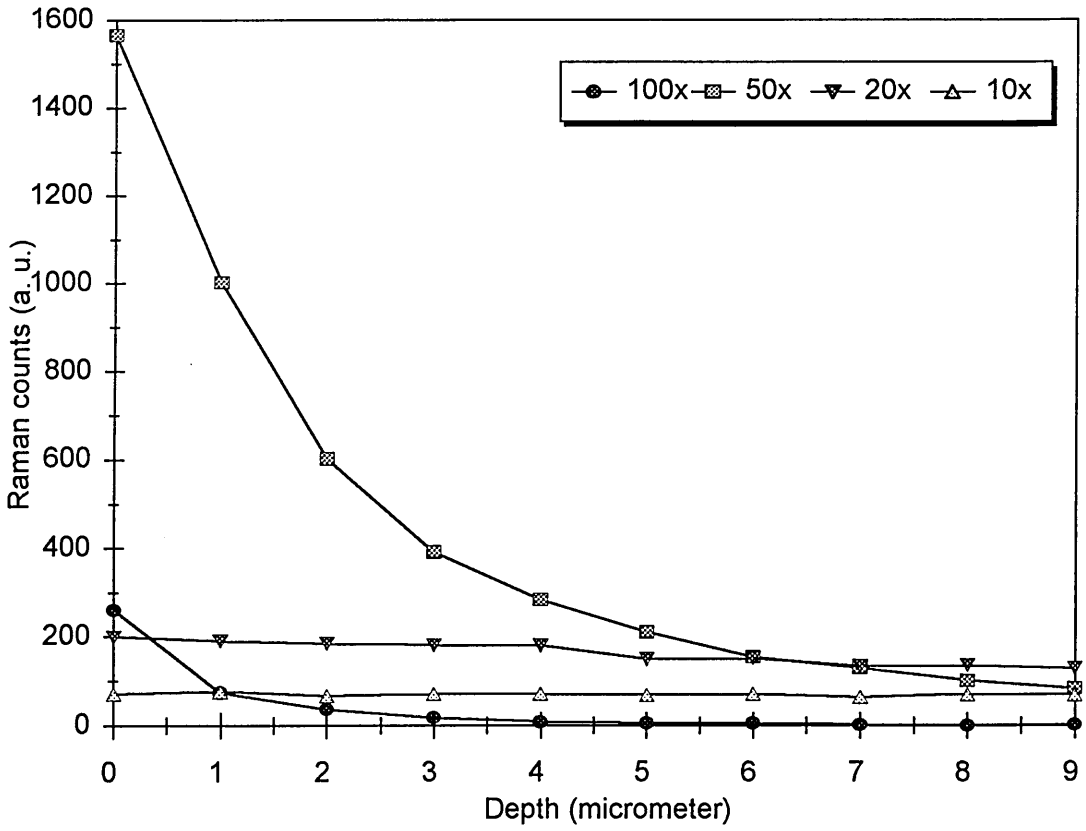

Figure 2.7: *Effect of use of various microscope objectives is shown as a plot of intensity of the 519 cm^{-1} band of silicon (Raman counts) as a function of distance from the focal plane of the objective lens*

The total amount of scattered light (I_t^2)from the infinitely thin plane of sample can be determined by combining equations 2.2 or 2.4 with 2.7 for each depth at a distance d from the front focal plane of the objective lens. Thus the ratio of the scattered light reaching the detector (I_S^2) through the pinhole with diameter I_S and the total scattered light from the sample (I_t^2) with image projection diameter of I_t can be determined. This ratio (I_S^2/I_t^2) is the theoretical response of the Raman microscope with a confocal setup for the infinitely thin plane of the sample. Figure 2.8 shows a comparison of a plot of the theoretical

response of the confocal system used in these studies with a 200 μm pinhole with the experimental response mentioned earlier. In figure 2.8 the intensity of scattered Raman light at the surface of the sample is assumed to be 100%.

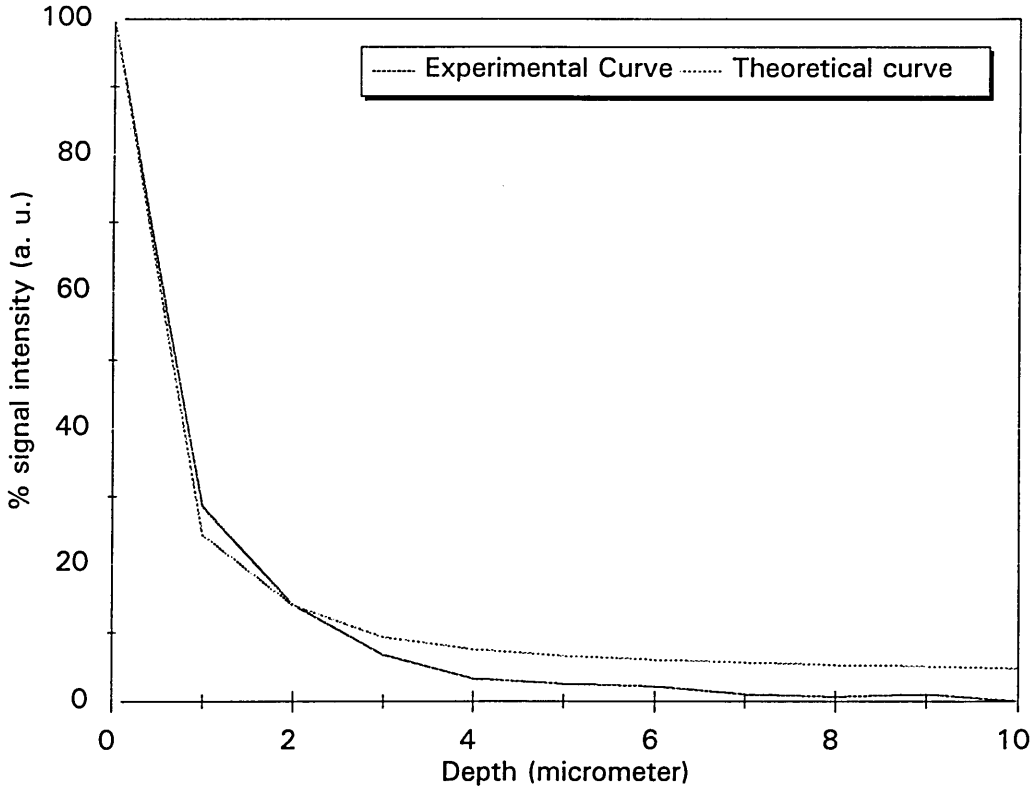

Figure 2.8: *Comparison of the theoretical response of the confocal Raman microscope (Ratio of the intensity of the Raman-scattered light transmitted through the pinhole and the total light intensity, I_S^2/I_t^2) with the experimental response*

2.4.3. Raman imaging and mapping

In recent years different Raman imaging techniques have been developed. One way to categorise them is by the way that the sample is illuminated with laser beam.

a) Global illumination:

This is employed in MOLE (Molecular Optical Laser Examiner) which provides the only way for direct real-time imaging. In this technique a large area of the sample is uniformly irradiated with monochromatic radiation of frequency ν_0. A filter such as a grating monochromator or optical filter tuned to a given characteristic Raman line of one component of the inhomogeneous sample transmits a monochromatic image of this to a two dimensional multi-channel detector.

One of the major advantages of this type of imaging is the relatively short time taken to analyse a surface area of a (large) dimension up to 200 μm^2. It also (unlike mapping) does not require the acquisition of many spectra followed by data manipulation to create the image.

The new designs [2.78] have improved the field of direct Raman imaging. Such systems benefit from three technological developments: (a) the use of the low noise, cooled CCD detector which provides an electronic photographic image of very high quantum efficiency, (b) the use of multilayer dielectric filters with high selectivity and (c) the use of a PC allows control of the tuneable filter and enables processing of the image reflected on the detector. The tunable filters can provide an increase in light throughput and reduction in optical complexity, without loss of ability for light rejection. The filters have a resolution of 2 cm^{-1} for Raman spectra and 20 cm^{-1} for Raman imaging [2.79] and are tuned by rotating the filter with respect to the incident beam.

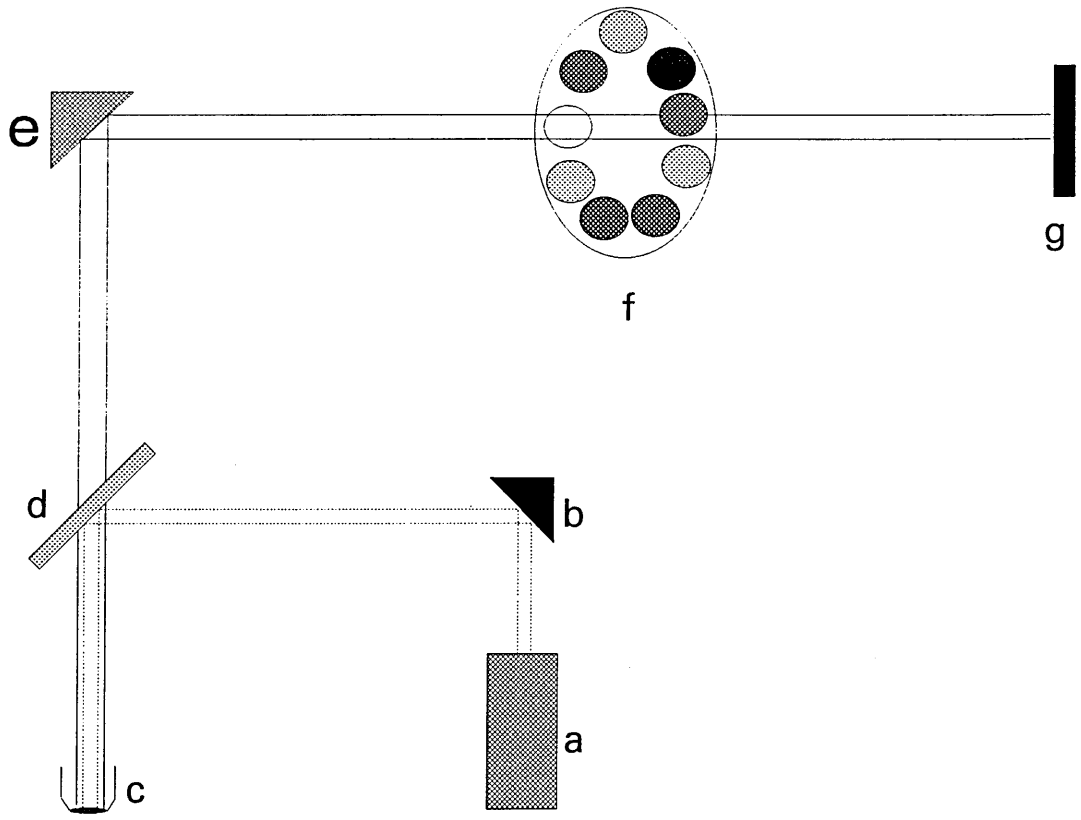

Figure 2.9: *Schematic diagram of the Raman microscope in imaging,(a) laser source, (b) mirror, (c) microscope objective, (d) beam splitter, (e) mirror, (f) filters and (g) CCD detector*

The centre wavelength of the filter pass-band is given by

$$\frac{\lambda(\theta)}{\lambda(0)} = \left(\frac{\mathbf{n}_r^{\,2} - \sin^2\theta}{\mathbf{n}_r^{\,2}} \right)^{\frac{1}{2}} \qquad (2.8)$$

where θ= the angle of incidence (to the normal)

n_r= refractive index of the filter

$\lambda(0)$= centre wavelength at normal incidence

$\lambda(\theta)$= centre wave'ength at angle θ

Equation 2.8 shows that as the angle of incidence is increased, the central wavelength shifts to the lower wavelengths. This is shown in figure 2.10, which is a plot of centre wavelength at angle θ as a function of angle of incidence by using a filter with refractive index of 2, centred at 700 nm for normal incidence. In a Raman microscope such as the Renishaw Ramascope a few of these filters with varying angle of incidence are used to cover the 200 to 4000 cm^{-1} range of Raman frequencies.

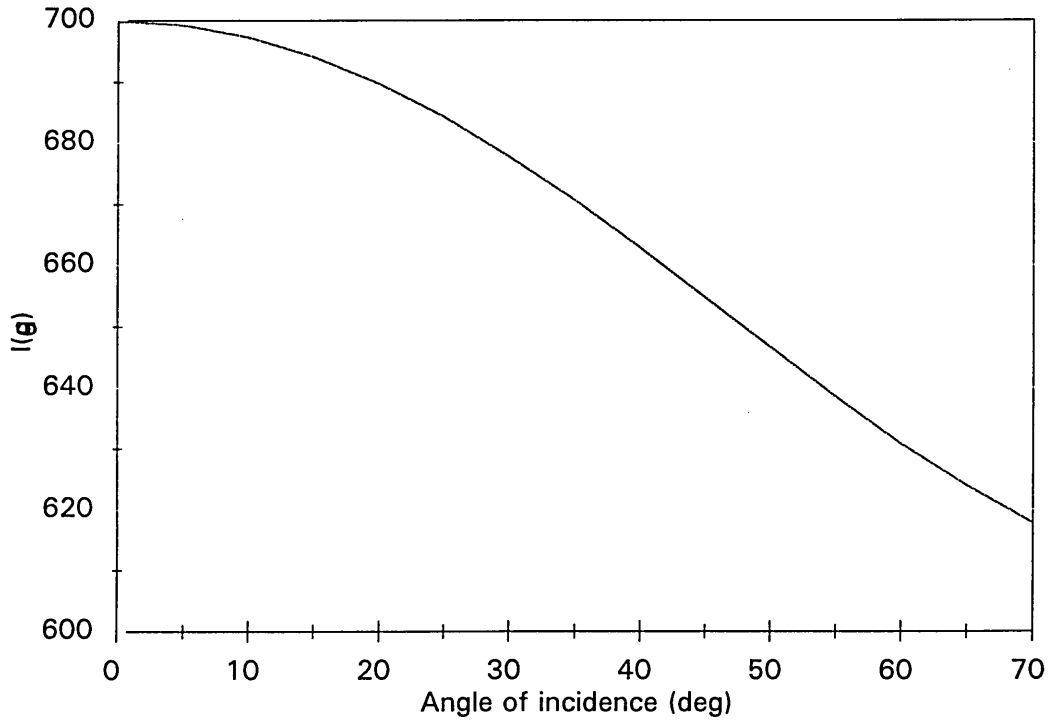

Figure 2.10: *Plot of centre wavelength at angle of incidence, θ as a function of the angle*

However, dielectric bandpass filters suffer from a number of anomalous effects at angles greater than that of normal incidence. These include: (a) scattered Raman light from various sections of the illuminated area passes the filter at slightly different angle, θ.

Thus different parts of the illuminated area undergo different wavelength shifts, (b) for angles greater than normal incidence the transmission bands for p and s-polarised light undergo divergence. This means that p and s-polarisation which are coincident in normal incidence, in non-normal angles of incidence cause separation of the centre wavelength for s and p-polarisation. This effect is more prominent at angles greater than 30^{o}. In order to avoid such anomalous effects Puppels et al [2.80] have developed a new arrangement.

Instead of narrow-band interference filter some researchers have used tunable acousto-optic (AOTF) or liquid crystal (LCTF) filters for direct imaging [2.81-2.82]. AOTFs are solid-state birefringent crystals that provide an electronically tunable spectral notch passband in response to an applied acoustic field. LCTFs can also give a notch passband which is controllable by incorporating liquid crystal waveplate retarders within a Lyot birefringent filter.

Another imaging technique which illuminates the sample globally is known as Hadamard transform Raman microscopy and it has been reported by Treado et al [2.82-2.85] and Liu et al [2.86]. Hadamard mask encoding allows medium to high spatial resolution imaging with global illumination. A laser beam is imaged on the sample through a series of masks. The spatially encoded signals from each of n masks, each containing n resolution elements, are measured. The spatial distribution of the signal is recovered by Hadamard transformation of the matrix of encoded signals.

b) Line illumination:

In this technique both spectral and spatial information can be collected simultaneously and thus a better use of a 2D array detector (e.g. CCD) may be achieved. Spatial distribution of molecular components within the illuminated line of the sample is defined by the data along the slit direction and spectral information is defined by the data

perpendicular to the slit. Dhamelincourt et al [2.75] have patented a special optical device based on line illumination that benefits from advantages of the confocal Raman microscopy.

c) Point illumination:

In this technique the laser beam is focused on a very small area (~ 1 μm^2) of the sample. The Raman scattered light then is passed through a pinhole and then recorded by a two dimensional array detector (CCD). Thus this technique uses the advantages of the confocal microscopy (see section 2.52). Then the focussed laser 'spot' on the sample is changed to another area by using an automated microscope stage controlled by a computer. A new spectrum is then obtained. This procedure is repeated for a desired area of the sample. The Raman map (image) then can be constructed by inputting the Raman data (e.g. band intensity) into a suitable software.

The main advantage of this technique is the high resolution of the image due to the use of confocal microscopy. This technique can also provide additional information about the variation of band shape due to possible interactions between different components of the sample. However, it should be noted that although the mapping process in recent years has been more efficient by using CCD detectors, the major disadvantages associated with this technique are (a) the long time required for collection of the data from many sample points and (b) the subsequent computer data processing.

2.4.3.1. 3-D Raman mapping

The confocal microscope is a popular tool for obtaining three-dimensional images of various materials [2.87-2.88]. A three-dimensional map can be constructed by raster-scanning the optical system across the various planes of the object and then stacking the

resultant maps of the planes at different depths. However, three-dimensional micro Raman imaging is not readily achievable by direct imaging techniques owing to the poor axial resolution of the conventional microscope, which does not allow optical sectioning.

Govil et al [2.89-2.90] have described an alternative to confocal microscopy for three-dimensional microscopic Raman imaging. They have reported the use of Hadamard transform microscopy to acquire the Raman images from different sections of sample. Image-restoration is then achieved by using a nearest neighbour deblurring technique to reject the out-of-focus information and sharpen the images. This type of image restoration is relatively unsophisticated. It does not require calculation of 2D Fourier transforms and a personal computer can handle the procedure. However, one of the disadvantages of this technique is that the sharpening of the image of the plane of focus is at the expense of the signal-to-noise ratio.

2.4.3.2. Applications

Raman microscopy is an important tool in a variety of scientific areas. In materials science it has been applied to semiconductors [2.91] to characterise such devices [2.92] and their microstructure [2.93], analysis of gallium arsenide defects and misorientations [2.79,2.94,2.95], strain mapping of the surface [2.96] and other applications to semiconductors[2.97-2.99]. Carbon composites [2.100], graphitic materials [2.101] and diamond films [2.78, 2.102] have also been studied using Raman microscopy.

This technique has been utilized in order to study inclusions by many groups. Examples of such applications include: identification of catalyst residues as contaminants of finished products, the analysis of defects and bubbles in glass [2.103] in the metallurgical industry [2.104], in the analysis of bubbles in fibres in the fibre optics industry [2.105], *insitu*

analysis of fluid inclusions in minerals[2.106-2.111], inclusions in eclogites [2.112] and feldspars[2.113].

Raman imaging and mapping has been applied to a variety of polymeric materials. Jawhari et al [2.114] have employed micro-Raman mapping to study changes in crystalline structure in PVF_2 when this polymer is subjected to stress. Batchelder et al [2.115] have demonstrated the use of Raman imaging to films of urethane/acrylate polymer which contain PTFE particles. Markwort et al [2.116] have compared global versus point illumination. They have compared three polymeric systems, i.e., (a) polystyrene beads in a matrix of polyacrylate, (b) a polyethene fiber/epoxide composite and (c) a ternary polymer blend. Garton et al [2.117] have examined three examples of polymer blends. These include: (a) a rubber-toughened epoxy resin, (b) polyethlene/polypropylene blends with a range of compositions and (c) a poly(ethylene terephthalate)/poly(butylene terephthalate) blend. Williams et al [2.11] have reported an image of the Raman band of an inhomogenous PTFE coating. Schaeberle et al [2.118] have described Raman imaging of a polypropylene/polyurethane blend employing a solid-state acousto-optic electronically tunable imaging spectrometer integrated with a microscope. Liu et al [2.86] have employed the Hadamard transform Raman microscope to polymer samples. Evans et al [2.69] have demonstrated the use of Raman imaging and Raman confocal mapping for a number of polymeric and non-polymeric materials.

Raman microscopy apart from imaging and mapping has been applied to many other polymeric material. including polymer fibers such as polyacetylene and aramid [2.119, 2.120], poly(p-phenylene benzobisthiazole) [2.121], poly(p-phenylene benzobisoxazole, PBO) [2.122], polyoxymethylene [2.123] and polyethylene [2.124-2.130]. The following systems have been studied as fiber/epoxy composites: polydiacetylene fibers in epoxy matrices [2.131,2.32], single crystals of polydiacetylene embedded in a bisphenyl-urethane

matrix [2.133], single-fiber composites of aramid/epoxy [2.134,2.135] and high modulus polyethylene fibers embedded in an epoxy matrix [2.124, 2.136]. Other applications of the micro-Raman technique to polymeric materials include: the measurement of local stress in a model lubricant polyphenylether [2.137], the study of rigid glassy diacetylene-containing copolyurethane [2.138], study of deformed polymeric materials [2.139-2.141] and measurement of local molecular orientation around a notch in a polycarbonate test sample [2.142].

As well as the above applications, Raman microscopy has also been used for characterisation of zirconia morphology [2.143-2.145], historical and works of art [2.146], biological tissues [2.147-2.149], corrosion [2.150, 2.151] and environmental studies [2.152].

CHAPTER 3

3.1. Introduction

Polymer laminates, formed by the combination of several polymers to form multilayer structures are used, for instance, as food packaging materials and are important in connection with areas such as biocompatibility [3.1, 3.2], adhesion [3.3] and diffusion [3.4-3.8]. Such laminates may be a combination of two or more layers. The properties of these polymeric layers at interface are affected by polymer/polymer interdiffusion and, in all applications, the properties of the polymer are determined by the concentration profile of the two polymers across the interface.

A number of techniques have been used to study the polymer laminates. These techniques include waveguide Raman spectroscopy [3.9], external reflection and attenuated total reflection infrared spectroscopy (FTIR-ATR) [3.10, 3.11], scanning electron microscopy combined with energy-dispersive spectroscopy (SEM/EDS) [3.12], transmission electron microscopy (TEM) [3.13, 3.14] and transmission electron microscopy combined with energy-dispersive spectroscopy (TEM/EDS) [3.15]. Furthermore, several techniques have been utilised to measure the concentration profile across the interface. These include Rutherford backscattering spectroscopy (RBS) [3.16], small angle X-ray scattering

(SAXS) [3.17], small angle neutron scattering (SANS) [3.18], secondary ion mass spectrometry (SIMS) [3.19], IR microdensitometry [3.20] and neutron reflectometry [3.21].

In this work, confocal Raman microspectroscopy has been used to study the variations in the interfacial region in model polymer laminates as a function of (a) polymer molecular weight and (b) annealing temperature. This technique does not provide the information on as small a scale as in neutron total reflection or TEM but it does have advantages; for example (a) little sample preparation is required, (b) the non-destructive nature of the technique, and (c) ease of use of the technique. The theoretical background of confocal Raman microspectroscopy has been described in detail in section 2.4.2.

The polymer laminate used to study the effect of molecular weight was a two-layered model sample consisting of a top layer of poly (vinyl alcohol), PVOH and a base layer of poly (methyl methacrylate), PMMA. Figure 3.1 shows the schematic diagram of the deposited polymer laminate on a quartz slide. In order to study the effect of annealing temperature, a laminate consisting of a top layer of PVOH and a base layer of polyacrylonitrile, PAN was used.

This experimental systems were chosen for two reasons, (a) it was possible to find a solvent that dissolves the PVOH but not the PMMA, and (b) it is not unreasonable to expect interfacial interactions by hydrogen bonding between the two polymer layers.

Pereira et al [3.11] have used FTIR-ATR spectroscopy with the barrier film technique to obtain a depth profile of a PMMA/PVOH laminate. However this technique requires preparation of many laminates with PMMA layers of different thicknesses. Tait et al [3.9] have used waveguide Raman spectroscopy to obtain a depth profile of a PVOH/PMMA laminate. This technique is limited by difficulties found in achieving a viable waveguide.

3.2. Experimental

3.2.1. Polymer laminate preparation:

Poly(vinyl alcohol), PVOH, polyacrlylonitrile, PAN and poly(acrylic acid), PAA were purchased from Aldrich Chemical Company Ltd, Poly(methyl methacrylate), PMMA(I) and PMMA (II) were obtained from ICI (Wilton) and PMMA(III) from Fluka Chemicals Ltd. Table 3.1 shows the various characteristics of these polymers.

Polymer	MW	T_g (°C)	molecular formula	solvent
PMMA(I)	800,000	~100	$[-CH_2C(CH_3)(CO_2CH_3)-]_n$	DCM†
PMMA(II)	120,000	~114	$[-CH_2C(CH_3)(CO_2CH_3)-]_n$	DCM†
PMMA(III)	34,000	~115	$[-CH_2C(CH_3)(CO_2CH_3)-]_n$	DCM†
PVOH	50,000	75-85	$[-CH_2CH(OH)-]_n$	water‡
PAA	2,000	~106	$[-CH_2-CH(COOH)-]_n$	DMF§
PAN	15,000	~85	$[-CH_2-CH(C\equiv N)H-]_n$	water‡

Table 3.1: *Characteristic parameters of the polymer compounds used in this thesis.*

†: *dichloromethane, spectroscopic grade from Aldrich Chemical Company Ltd*
‡: *pure water, Millipore*
§: *N,N-dimethylformamide, spectroscopic grade from Aldrich Chemical Company Ltd*

The PMMA layer (bottom layer) of laminate films was deposited onto a quartz slide from DCM using the dip coating procedure [3.22].

In this technique, thickness of each polymer film can be controlled with speed of dipping and the solution concentration. A PVOH film was then deposited onto the PMMA layer as a 'coating' by the same technique with water as solvent, to produce a laminate. At each stage samples were dried in the oven at 70 °C (other temperatures were used for investigation of the effect of annealing temperature) for 24 hours. Figure 3.1 shows a

schematic diagram of such polymer laminates. The thickness of PMMA and PVOH layers were determined within 1% and 5 % accuracy, respectively, with the use of a surface profiler (Laser Form Talysurf).

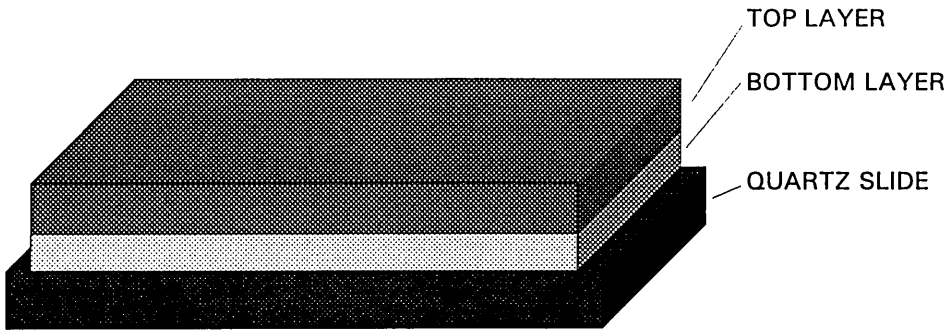

Figure 3.1: *The quartz slide and deposited polymer laminate*

PVOH/PAN or PAA/PAN laminates were prepared by depositing PAN films onto quartz slides from N,N-dimethylformamide, DMF as a solvent using the dip coating technique. In order to form a PVOH/PAN laminate, a PVOH film was then deposited onto the PAN layer from water as a solvent using the dip coating procedure. The PAA/PAN laminate was produced by depositing a PAA film onto the PAN layer from water as a solvent using a casting technique to obtain a thicker PAA film. At each stage polymer films were dried in the oven. The annealing time and temperatures used for preparation of these laminates are summarised in table 3.2.

In order to determine that after drying there is no residual solvent (DMF) present in the PAN layer, the Raman spectrum of this film was obtained and the presence of the characteristic bands corresponding to DMF was examined. The thicknesses of the PAN, PVOH and PAA layers were determined within 2%, 5% and 4% accuracy respectively using a surface profiler (Laser Form Talysurf).

Laminate	Bottom layer (PAN)		Top layer (PVOH or PAA)	
	Temp (°C)	Time (hrs)	Temp (°C)	Time (hrs)
PAN/PVOH (I)	65	24	65	21
PAN/PVOH (II)	75	43	75	20
PAN/PVOH (III)	65	43	90	24
PAN/PAA	85	25	65	45

TABLE 3.2: Annealing temperature and time used for preparation of the laminates

3.2.2. Confocal Raman microspectroscopy procedure

The polymer films were deposited on the quartz slides using a dipping instrument which is capable of carring out the dipping procedure with various reproducible speeds.

Raman spectra were recorded on a Renishaw Ramascope spectrometer (system 2000). Figure 3.2 shows the schematic diagram of this instrument. It is equipped with a Peltier cooled CCD detector, a holographic grating (1800 grooves/mm) and two Raman holographic edge filters which prevent the back scattered laser radiation from entering the spectrograph. The stigmatic single spectrograph is attached to an Olympus BH2 microscope.

The Ramascope was set up in confocal mode using a 100x short-working-length objective (N.A. value of 0.95), a slit width of about 15 μm and a CCD area of 4 x 576 pixels. The long axis (576 pixels) defines the spectral dimension and the short axis describes the height of the image. The arrangement of the CCD and the slit width acts as the pinhole for

blocking out-of-focus signals. This confocal arrangement provides the depth resolution of about 2.5 ± 0.3 μm. Before each depth profiling experiment, the resolution of the confocal arrangement was determined with depth profiling of a silicon wafer as the standard material. The details of this experiment has been described in section 2.4.2. The Raman spectra were recorded using the 632.8 nm line of a He-Ne laser.

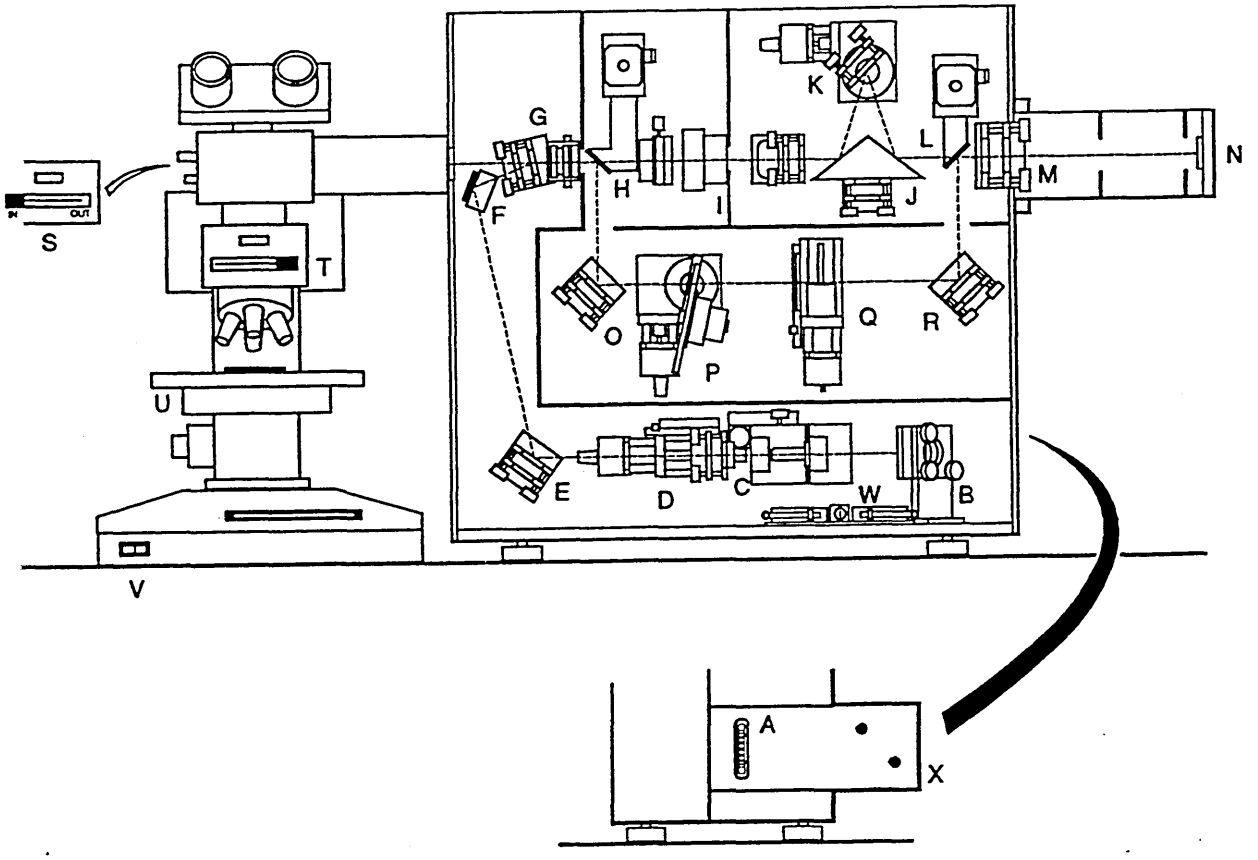

Figure 3.2: *Schematic diagram of the Renishaw Ramascope, system 2000. (A) laser attenuation filter wheel, (B) laser alignment mirror, (C) objective lens and 300 μm pinhole, (D) spot focus adjustment lens (x4 objective), (E) adjustable lens, (F) fixed mirror, (G) dichroic beam splitter (holographic notch filter) and polariser, (H) wedge mirror, (I) spatial filter, (J) isosceles triangular mirror, (K) grating, L wedge mirror, (M) focusing lens, (N) CCD chip, (O) adjustable mirror, (P) filter disc and drive motors, (Q) Fabry-Perot etalon filter, (R) adjustable mirror, (S) laser light mirror control, (T) white light 50:50 beam splitter control, (U) mechanical stage, (V) on/off switch for white light, (W) interlock switches and defeat key-switch and (X) delivery optics tube containing alignment mirror [2.32]*

A depth profile of each laminate was then obtained by focusing the microscope stepwise (1 μm) through the polymer laminate and recording a spectrum at each step. The position, area and the full width at half height (FWHH) of the important bands were determined as a function of the depth using the Renishaw curve-fitting programme.

3.3. Results and discussions

3.3.1. Effect of molecular weight

PMMA/PVOH laminates prepared with various molecular weights of PMMA were used for these experiments. See table 3.1. The thickness of the PMMA and PVOH layers were 4.5 ± 0.5 μm and 9.5 ± 0.5 μm respectively. This system was selected to examine interactions at the interfacial region due to possible hydrogen bonding between the carbonyl group of PMMA and the hydroxyl group of PVOH. Another advantage of this system is that, we can deposit the PVOH layer from water on a PMMA substrate, since PMMA is not soluble in water. Spectra of the pure individual films are shown in figures 3.3 and 3.4.

In order to obtain a depth profile of each laminate, the 550 - 1100 cm^{-1} region of the spectrum was recorded. Figure 3.5 shows the spectra recorded as a function of depth for the PMMA(III)-PVOH laminate.

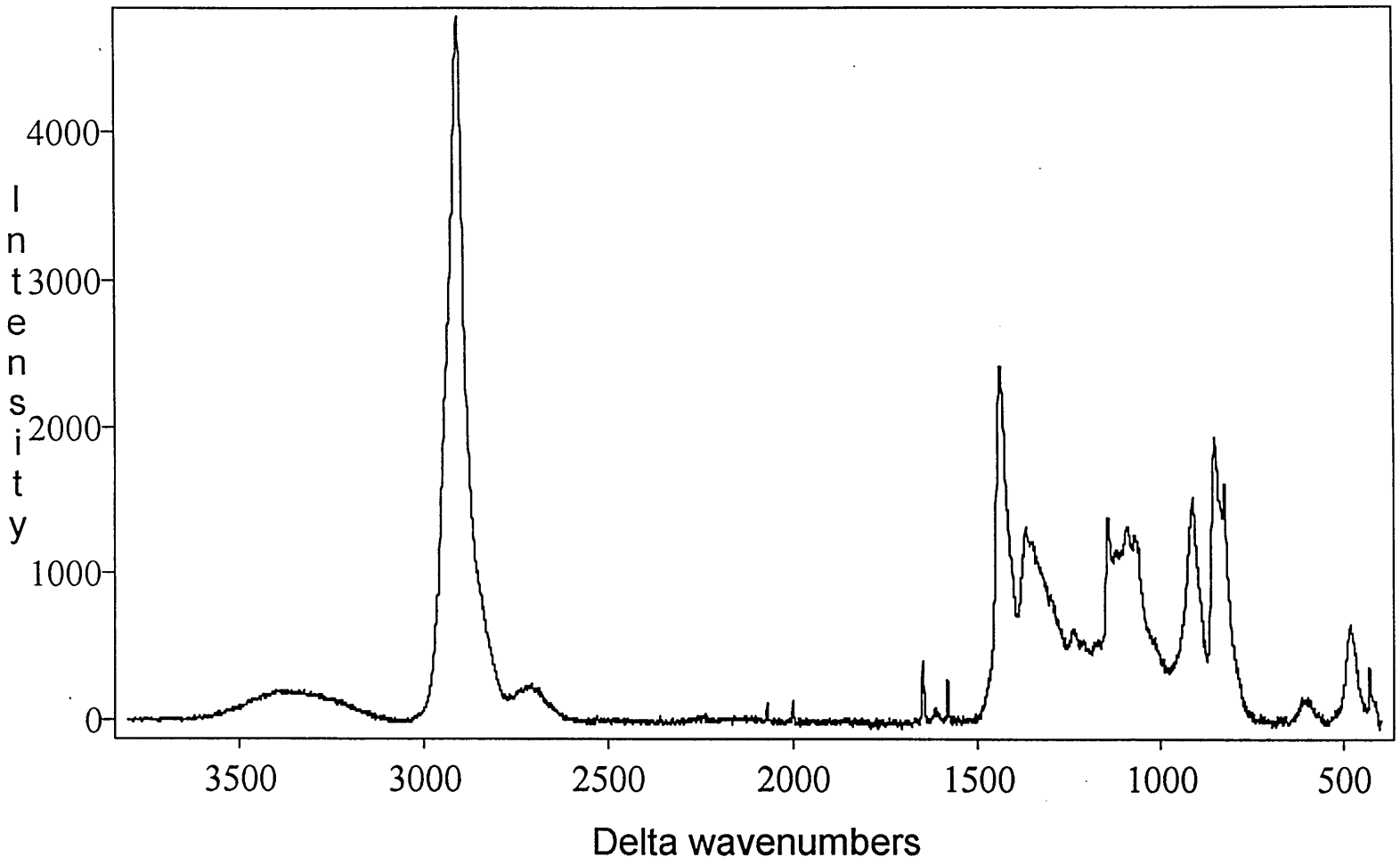

Figure 3.3: Raman spectrum of a pure PVOH film.

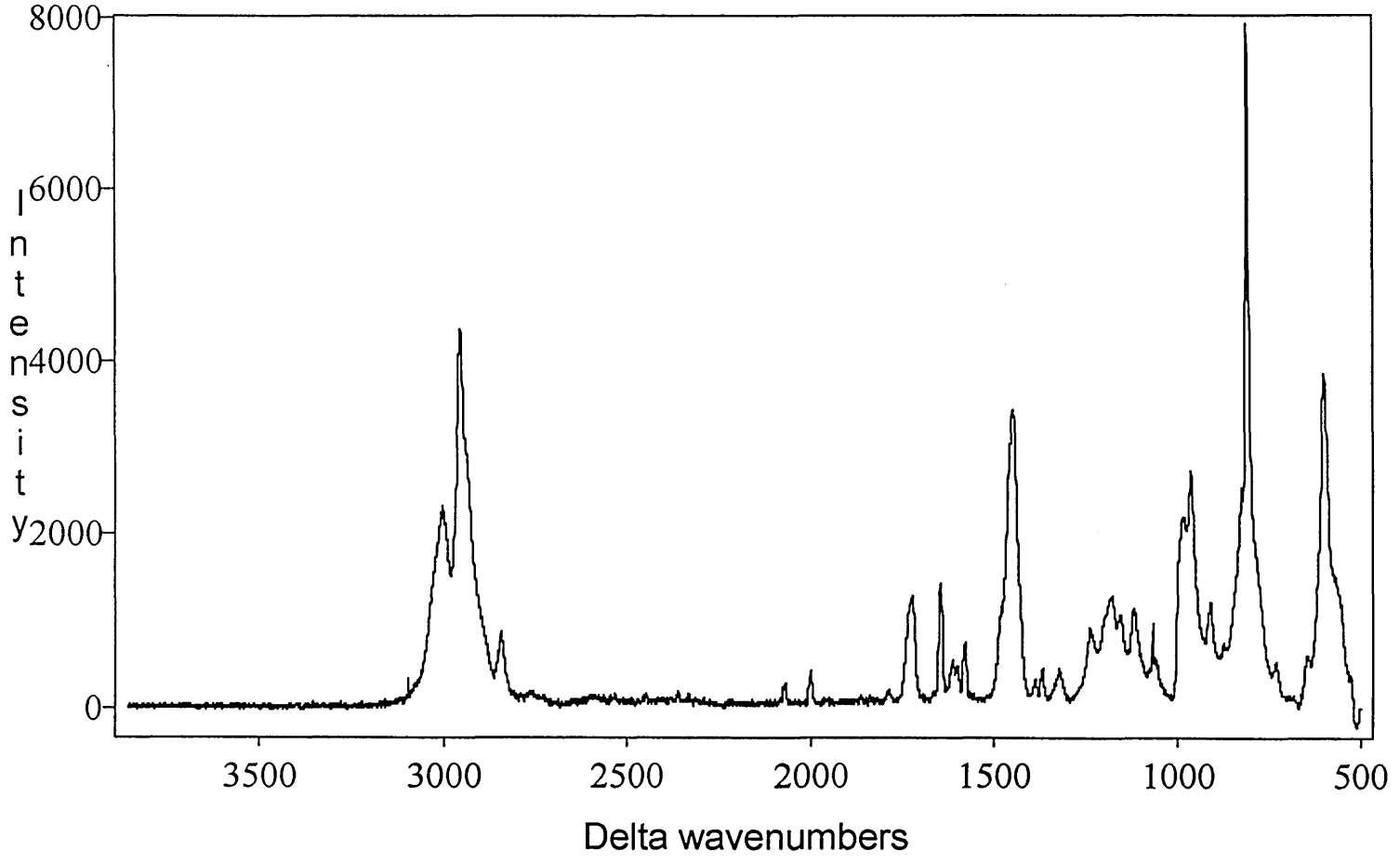

Figure 3.4: Raman spectrum of a pure PMMA film.

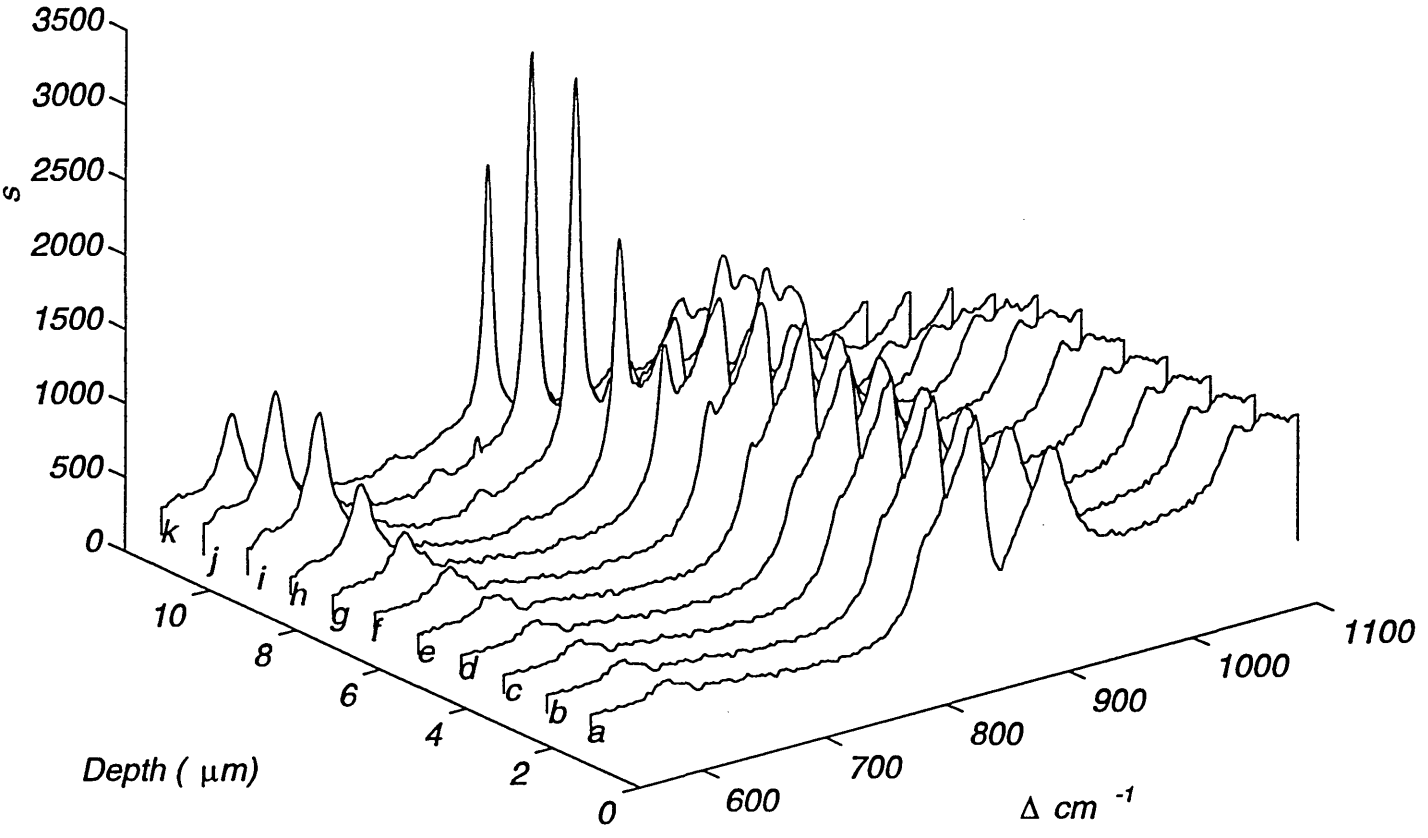

Figure 3.5: *3-D representation of the depth profile of the ν(C=O) band of PVOH/PMMA laminate obtained by focusing the microscope stepwise (1 μm) through the laminate*

As expected, the initial spectra show no bands corresponding to PMMA and only PVOH bands at 854 and 917 cm^{-1} (Figs 3.5a - d). The subsequent spectra (Figs 3.5e - j) indicate the presence of PMMA with bands at 813 and 601 cm^{-1} as well as PVOH bands. The important feature of this region, which in this thesis is referred to as the interfacial region, is that as we continue recording the spectra through the depth of the laminate, the intensities of the PMMA bands increase as the intensities of the PVOH bands decrease.

This is expected, since by focusing at the deeper parts of the laminate, spectra are collected closer to the PMMA layer and further away from PVOH layer. It is this region which is expected to show some hydrogen bonding interaction between the ester and alcohol groups of the PMMA and PVOH layers respectively. Finally, the last spectrum (Fig 3.5k) shows only bands corresponding to the pure PMMA. However, the intensity of the PMMA bands show a decrease on moving into the pure PMMA layer. This phenomenon has been observed for all the three cases. The loss of intensity of PMMA band in the lower regions is probably due to the effects of absorption, scattering and mismatch of refractive index of the two polymers at the interface.

It is clear from figure 3.5 that the bands corresponding to both PMMA and PVOH layers appear in some of the spectra. Since both polymers have Raman bands in the 500-1100 cm^{-1} region, the method of spectral subtraction was utilised to distinguish spectra corresponding to the PVOH and PMMA layers. Thus a spectrum of pure PVOH (see fig 3.3) film was first obtained and this spectrum was used for spectral subtraction without any intensity weighting. Then the spectrum of pure PVOH film was subtracted from each spectrum. However, in order to remove all the bands corresponding to PVOH layer, it was necessary to add scale and offset values to each of the input files before they were subtracted. Figure 3.6 shows the results of the spectral subtraction.

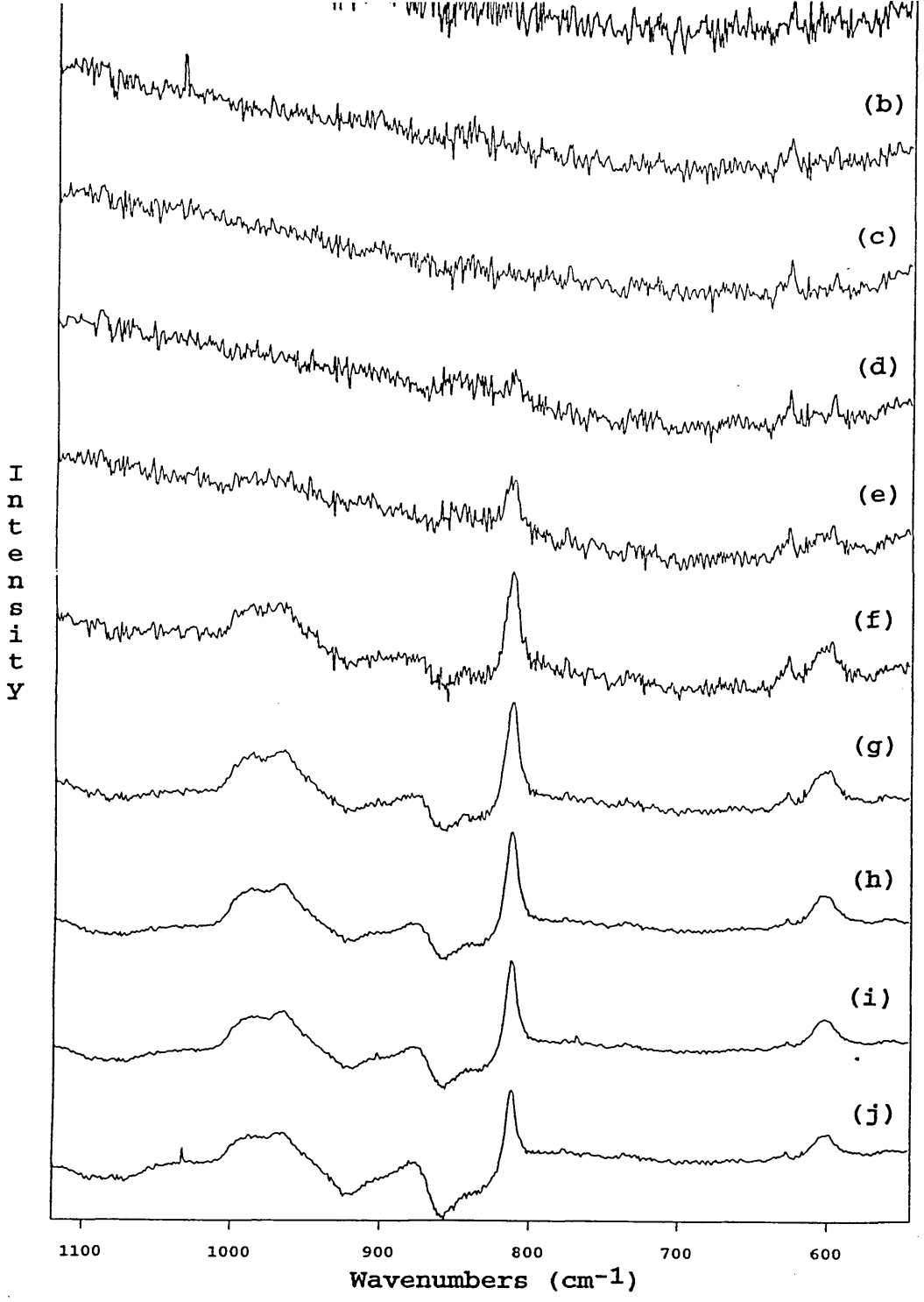

Figure 3.6: Raman data obtained by subtraction of a pure PVOH film from each of spectra recorded in the depth of the PMMA(III)/PVOH laminate

It can be seen that the first detectable sign of PMMA band at 813 cm^{-1} has appeared in the plane of focus about 4 μm below the top surface of the upper layer in the PVOH/PMMA(III) laminate. However, it should be noted that this does not indicate the position of upper boundary of the interfacial region. The reason for this is that as mentioned earlier (fig 2.7) although approximately 90% of the scattered light is collected from about 2.5 μm below and above the plane of focus, but significant Raman signals may be contributed by PMMA in the lower regions.

The spectral subtraction method was repeated as above to determine the last spectrum which shows any bands corresponding to the upper layer (PVOH). Hence, a spectrum of a pure PMMA film (fig 3.4) was first collected and then this was used for subtraction without adjusting the intensity. As mentioned earlier, scale and offset values were added to each of the input files before they were subtracted. Figure 3.7 shows the results of the subtraction.

It is clear that the last detectable sign of the bands corresponding to PVOH at 917 and 854 cm^{-1} appear in the spectrum of the plane of focus about 10 μm below the top surface. For the reasons mentioned above, it should be noted that this does not necessarily define the position of the lower boundary of the interfacial region.

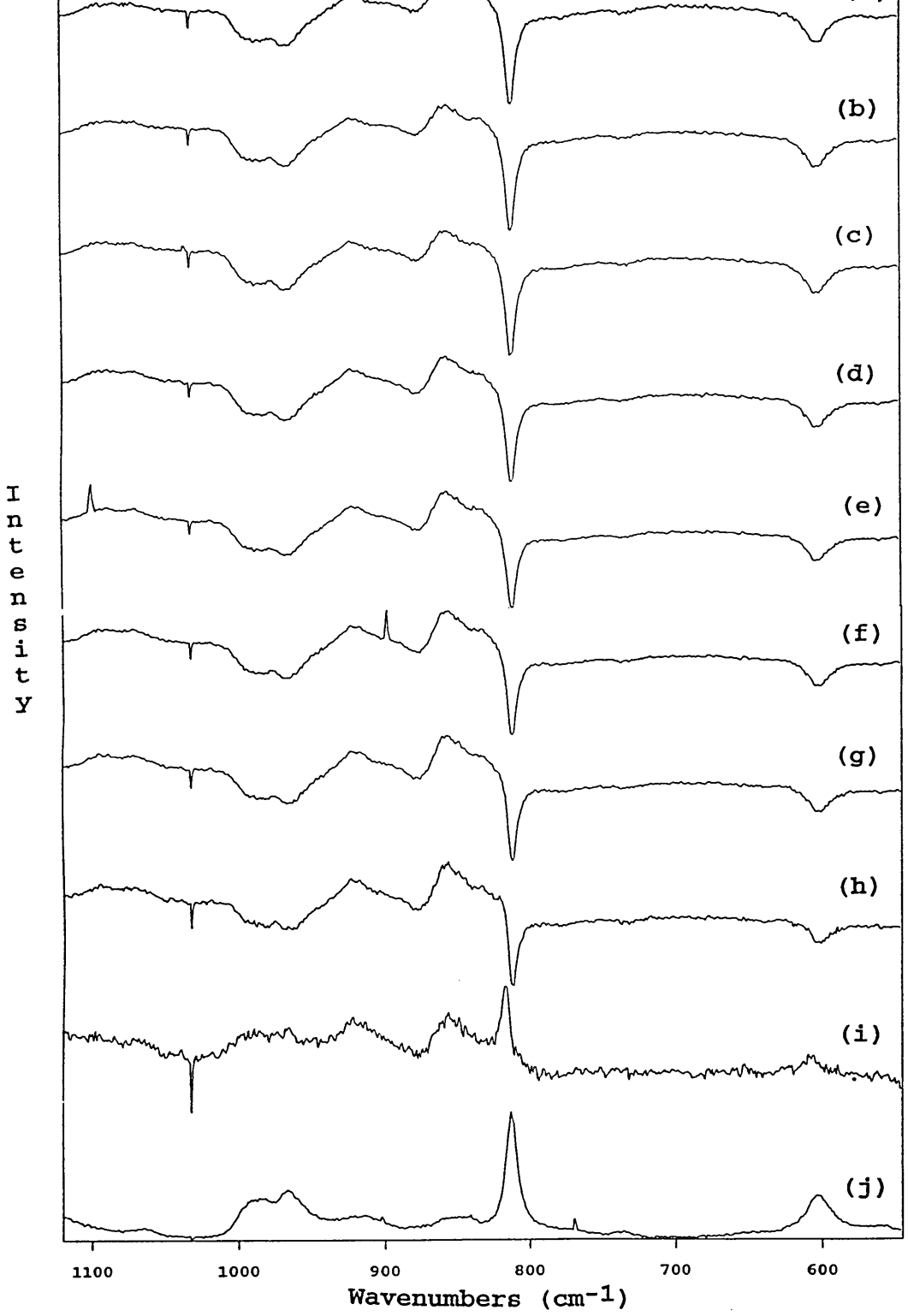

Figure 3.7: Raman data obtained by subtraction of a pure PMMA film from each of spectra recorded in the depth of the PMMA(III)/PVOH laminate

In order to determine whether the depth of penetration is related to the molecular weight of the PMMA film, we performed the same experiment and obtained the depth profiles for the PVOH/PMMA(II) and PVOH/PMMA(I) laminates with PMMA molecular weights of 120,000 and 800,000 respectively. Figure 3.8 shows the plot of intensity as Raman counts for total exposure time as a function of depth for the all the three different PVOH/PMMA systems. It should be noted, however, that in view of the depth resolution of the confocal microscope, we can not determine the exact upper and lower boundaries of the interfacial region. In addition to this it should be noted that unlike infrared techniques in a Raman experiment the value of intensity (Raman counts) in a fixed time scale may vary slightly due to the effect of various factors such as slight changes in laser intensity or dust particles and so on. Thus this degree of uncertainty has been corrected by adding error bars to each intensity value.

It is clear from figure 3.8 that the degree of interpenetration is not the same in all the three systems. Indeed, although it is difficult to determine the exact position of the interfacial region, it can be seen that the interfacial region is broader for the laminates with lower PMMA molecular weight.

One possible explanation for the relationship between molecular weight and the degree of interpenetration of PMMA is the effect of molecular weight on the mobility of the polymer chains at a limited annealing time. Boven et al [3.10], using infrared spectroscopy have shown that the rate of the interdiffusion is dependent on the molecular weight of the polymers used.

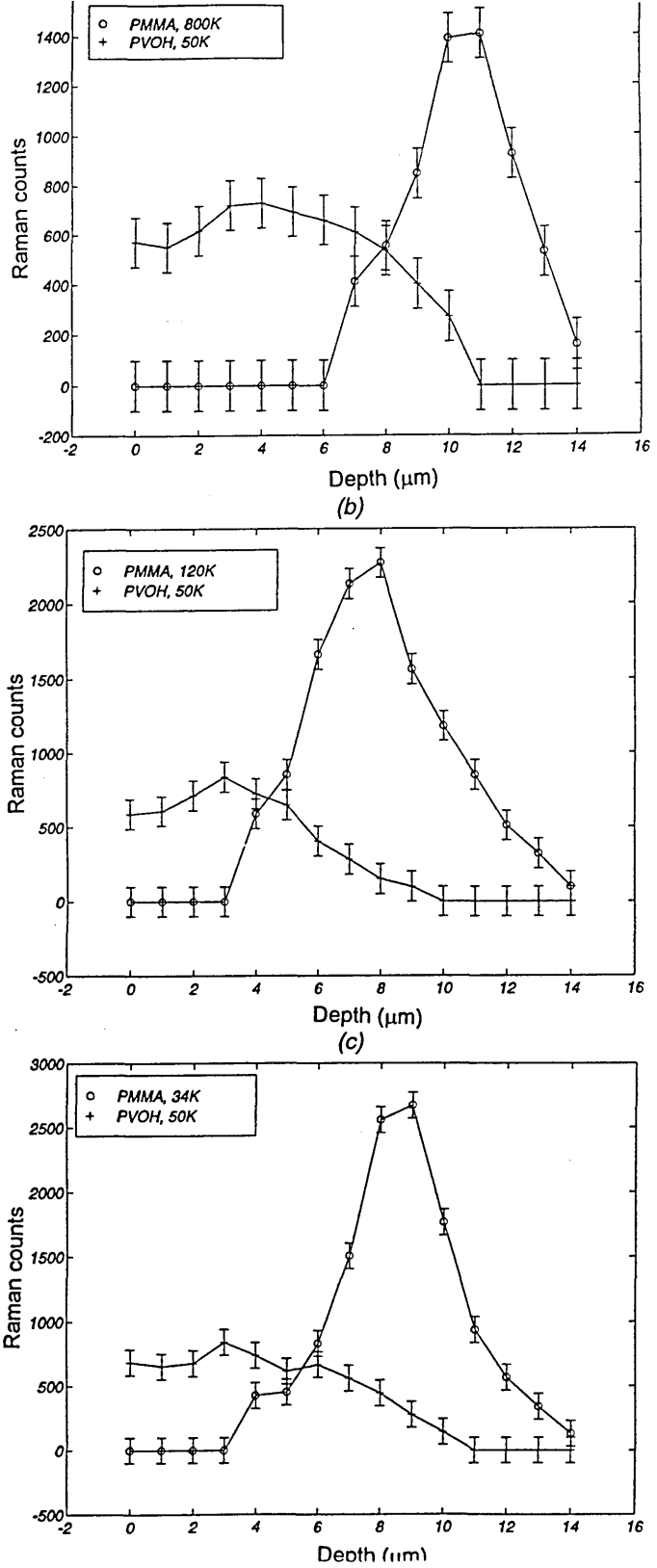

Figure 3.8: *Plot of the intensity (Raman counts for total exposure time) as a function of depth for (a) PVOH/PMMA(I) laminate, (b) PVOH/PMMa(II) laminate, and (c) PVOH/PMMA(III) laminate*

This means that the polymers with the lower molecular weight reach a completely mixed (equilibrium) system faster than the polymers with higher molecular weight. Thus, it is reasonable to expect that the PVOH/PMMA(III) laminate with lower PMMA molecular weight has reached closer to the completely mixed system than the PVOH/PMMA(I) laminate with much higher PMMA molecular weight. This study indicates the potential power of the confocal Raman microspectroscopy to study the extent and rate of interdiffusion in polymer laminates.

3.3.1.1. Interfacial Effects

So far it has been shown that the two polymers interpenetrate towards each other at the interfacial region. In this region, the existence of some degree of hydrogen bonding interaction between PMMA and PVOH films might be expected. It is well known [3.23] in vibrational spectroscopy that hydrogen bonding is manifested by frequency shifts, band broadening and intensity changes in the carbonyl, ν(C=O) and hydroxyl, ν(O-H) bands of the ester and alcohol groups of the polymers. Unfortunately the ν(O-H) band (at about 3400 cm^{-1}), which is very strong in the infrared spectrum, does not have a very high Raman cross section (fig 3.3). However, the ν(C=O) band is clearly visible in the Raman spectrum and the possible changes in this band at the interfacial region can be studied. Figure 3.9 shows the Raman spectra recorded at the 1600-1900 cm^{-1} region for the various depths of the PVOH/PMMA(III) laminate.

It is clear that the carbonyl band is broader near the upper part of the interfacial region (fig 3.9a) than in the PMMA layer (fig 3.9c) even allowing for relatively low signal to noise ratio.

Since the PVOH film has been deposited on the PMMA film from a water solution, one should consider whether hydrogen bonding between the hydroxyl group of water and the carbonyl group of the ester (PMMA) may be responsible for the υ(C=O) band broadening. In order to check this, a pure PMMA film was coated with a water layer and then was dried in an oven for the same drying temperature and time (70 ^{o}C, 24 hours) as for the laminates. A comparison of the spectra of the PMMA film before and after a few hours of exposure to water shows a υ(C=O) band broadening. However, spectrum of PMMA after complete drying shows no υ(C=O) band broadening. This indicates that all the hydrogen bonding due to water-PMMA association has been removed after complete drying. Thus it can be concluded that the υ(C=O) band broadening in the laminate after complete drying is due to hydrogen bonding between hydroxyl group of PVOH and carbonyl group of PMMA.

Figure 3.10 shows a plot of full width at half-height (FWHH) of the υ(C=O) band as a function of the distance, Z, from the top surface focal plane of the laminate. The error bars have been determined on the basis of uncertainty caused by the noise level in the spectra for measuring the exact FWHH.

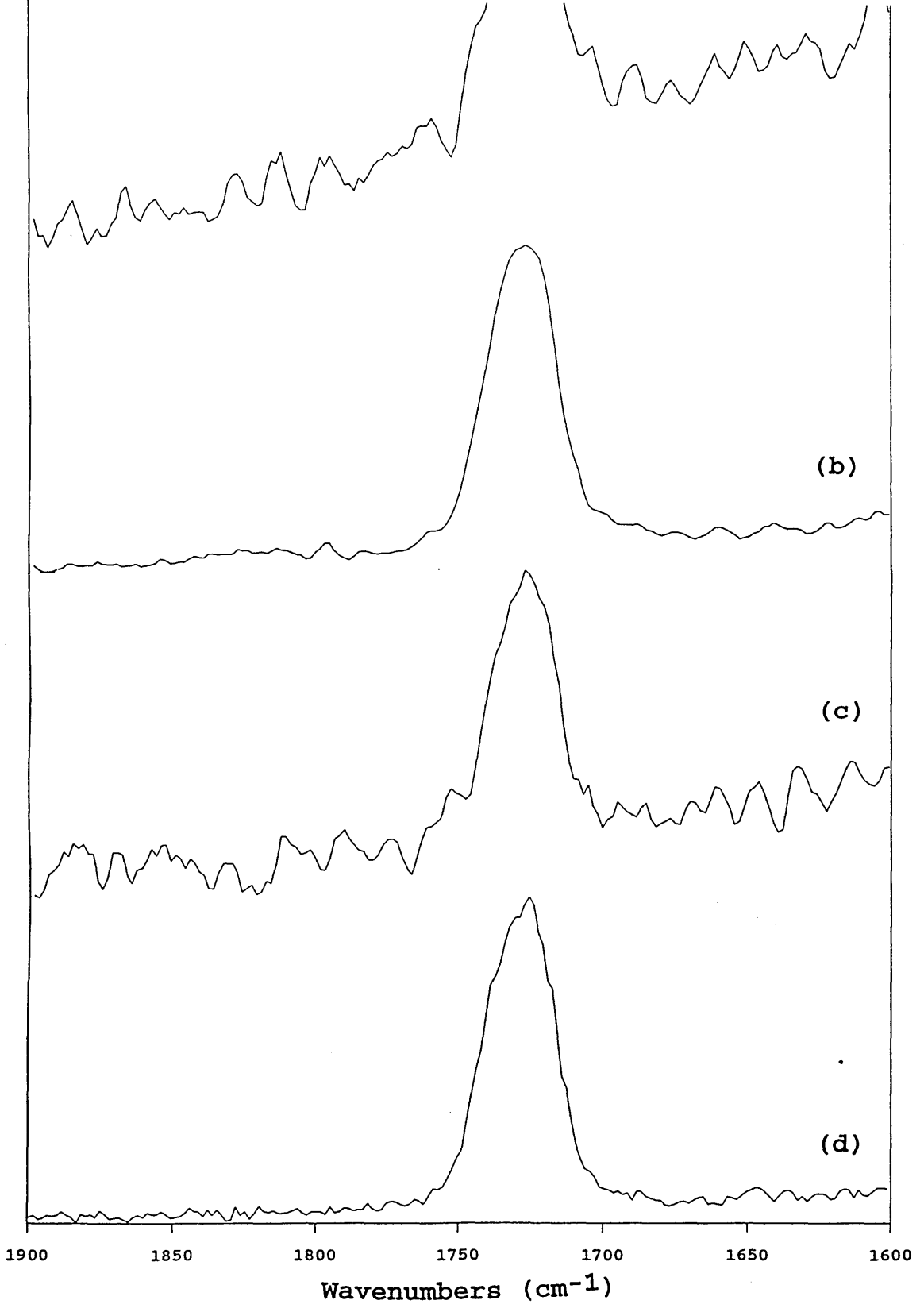

Figure 3.9: *Raman spectra of ν(C=O) band of PVOH/PMMA (III) laminate. The carbonyl band corresponding to (a) upper part of the interfacial region, (b) middle of the interfacial region; (c) PMMa layer, and (d) a pure PMMa film*

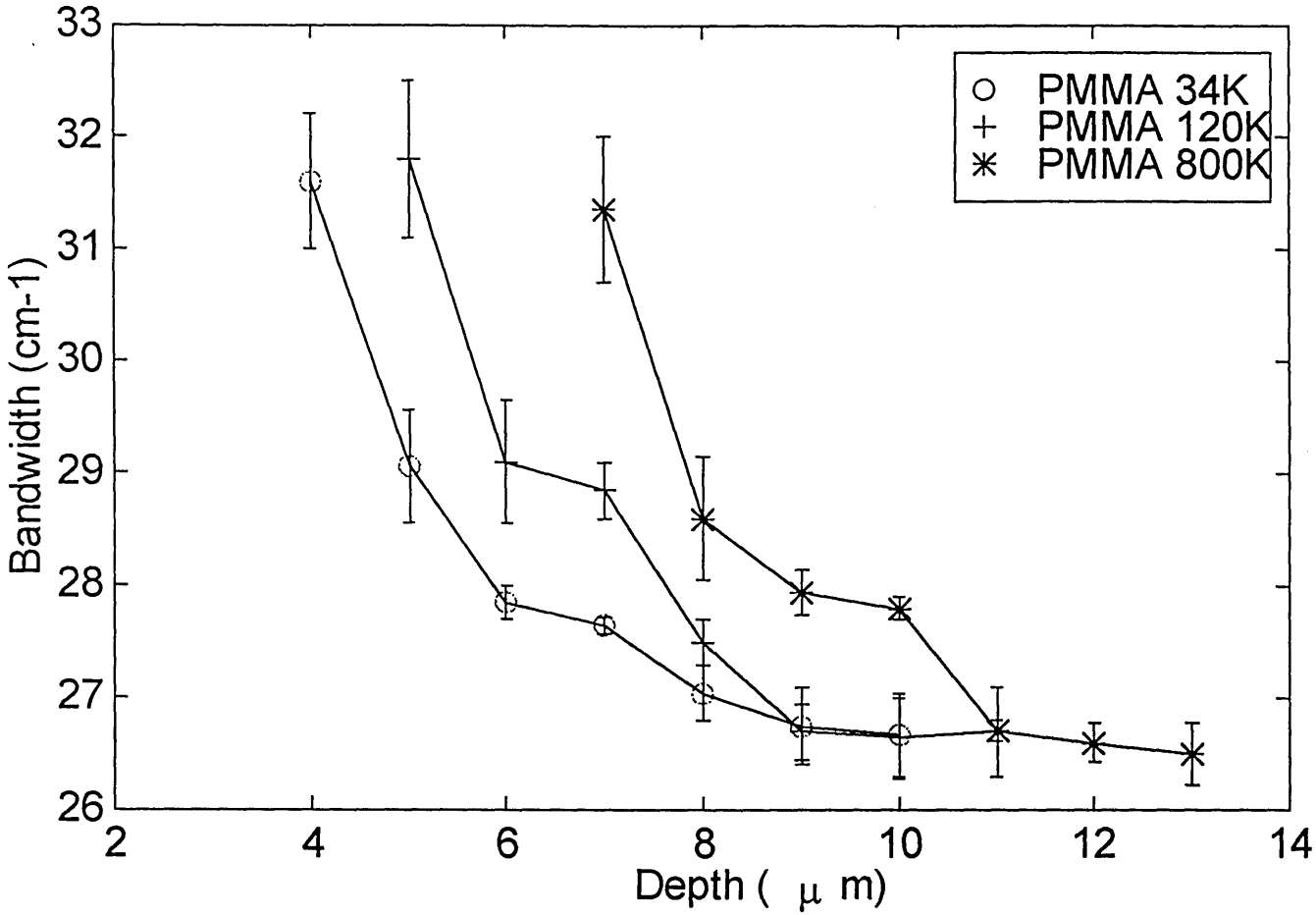

Figure 3.10: *Plot of the intensity (Raman counts for total exposure time) as a function of depth for (a) PMMA(I)/PVOH laminate, (b) PMMA(II)/PVOH laminate, and (c) PMMA(III)/PVOH laminate.*

As expected, for hydrogen bonding interaction, the band width is much broader at the interfacial region and decreases as it approaches the PMMA layer. Indeed the band width measured for the υ(C=O) band of the pure PMMA region (fig 3.9c) of the laminate is in good agreement with that measured for a PMMA film (fig 3.9d). However, there was no obvious shift of the υ(C=O) band as might also be expected for a hydrogen bonded interaction.

One possible explanation for this is the effect of the dilution phenomena in the interfacial region. In this region the PMMA carbonyl group may interact via dipolar interaction with other PMMA carbonyls or via hydrogen bonding with surrounding PVOH molecules. Shelley et al [3.24] have explored the variation in Raman isotropic υ(C=O) band position and half-width (FWHH) for DMF as a function of concentration in carbon tetrachloride, CCl_4. They have shown that the
υ(C=O) band shifts to higher frequency with band broadening as the mole fraction of DMF decreases. It is also known [3.25-3.27] that the υ(C=O) band shifts to lower frequency with band broadening due to intermolecular hydrogen bonding. A close examination of the spectra of PMMA/PVOH laminates, shows that the concentration of PMMA decreases from the pure PMMA layer to the upper sections of the interfacial region.

It is expected that there are more PMMA carbonyl dipolar interactions with other PMMA carbonyls in the PMMA layer compared to the interfacial region. This dilution effect is expected to lead to a blue shift with band broadening of the υ(C=O) mode in the interfacial layer. On the other hand, the degree of hydrogen bonding interaction between PMMA and PVOH molecules is higher in the interfacial region compared with that in pure PMMA. This is expected to lead to a red shift with band broadening of the υ(C=O) band. Thus, the overall result of these two effects on the υ(C=O) band is expected to be a little

or no frequency shift with band broadening. In this sense our observations may be rationalised.

3.3.2. Effect of annealing temperature

PAN/PVOH laminates prepared under different annealing temperatures were used for these experiments. See table 3.2. This laminate was selected for these experiments due to having the desired requirements. These include (a) both polymers have the functional groups which are expected to show some degree of chemical interactions such as hydrogen bonding at the interfacial region, (b) both polymers have well separated characteristic bands in their Raman spectra.

The PAN polymer with an intense $\upsilon(C\equiv N)$ band in its Raman spectrum provides the possibility of examining the band width, position and area of this band for any possible interactions and (c) The polymers are soluble in different solvents. This means that it is possible to deposit the top layer (PVOH) from water on a PAN substrate, since PAN is not soluble in water [3.28].

In order to ensure that the PAN sample used for these studies is not soluble in water as the solvent of the top layer, the following experiment was carried out. A mixture of PAN in water (0.27 g in 15 ml) was stirred and heated for approximately five hours and then transferred into an oven and heated at 65 ^{o}C for further five hours. After precipitation of the PAN particles, the water sample was examined for the presence of PAN using Raman microspectroscopy. The absence of the PAN characteristic bands in the Raman spectrum indicates that PAN is not soluble in detectable amounts in water.

The Raman spectra of pure PAN and PVOH films are shown in figures 3.11 and 3.3 respectively. The Raman spectrum of PAN (fig 3.10a) shows an intense band at 2244 cm^{-1}, corresponding to the nitrile stretching vibration, $\nu(C\equiv N)$. This band is known to be sensitive to hydrogen bonding [3.29]. The FWHH of this band for a pure PAN film was determined as 10.5 ± 0.2 cm^{-1}. In addition to the nitrile band, $\nu(C\equiv N)$, another two characteristic bands corresponding to PVOH film at 917 and 854 cm^{-1} in the Raman spectrum were examined. These two bands are well resolved and do not over lap with PAN characteristic bands in this region.

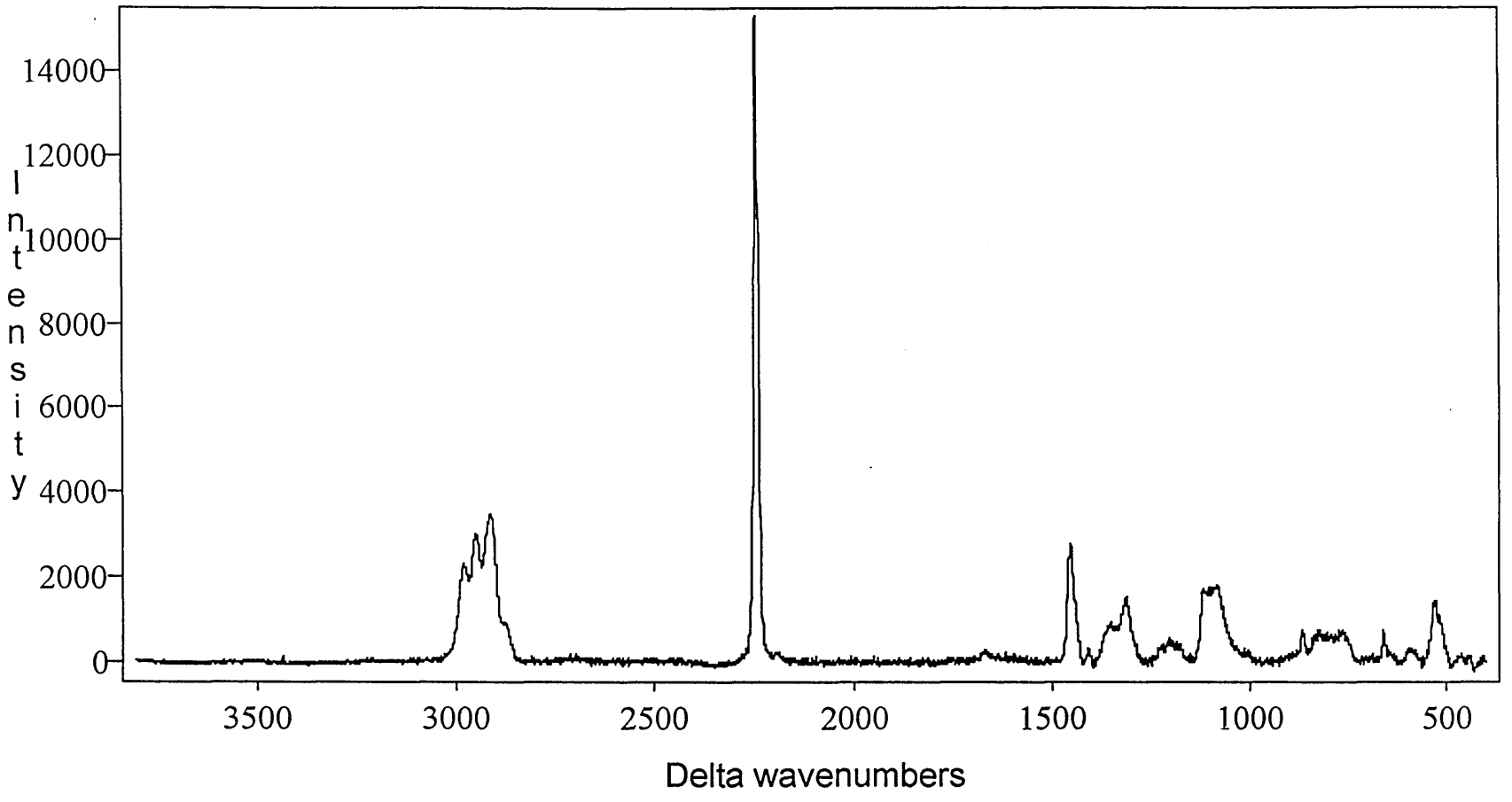

Figure 3.11: Raman spectrum of a pure PAN film.

3.3.2.1. Annealing temperature of 65 °C

A PAN/PVOH laminate was annealed at 65 °C for 21 hours. The thicknesses of the PAN and PVOH layers at the point where the depth profiling was carried out were approximately 13 μm and 20 μm respectively. In order to examine the changes in the nitrile band, ν(C≡N) of PAN a series of Raman spectra as a function of depth was obtained for 1960-2420 cm^{-1} region in 1 μm steps with 300 seconds exposure time for each spectra. Figure 3.12 shows the three dimensional representation of these spectra.

In addition, a series of Raman spectra at the same point in the laminate were recorded for the 550-1120 cm^{-1} region in 1 μm steps with 1800 seconds exposure time. The reason for the greater exposure time for the 550-1120 cm^{-1} region is due to existence of less intense Raman bands corresponding to PAN and PVOH films in this region.

In order to examine the changes in the ν(C≡N) band, a curve fitting procedure was carried out (see fig 3.13) twice with at least twenty iterations each time using a Renishaw curve fitting programme. Figure 3.14 shows the plot of the mean FWHH and integrated area of the ν(C≡N) band as a function of depth.

The plot of integrated area of the υ(C≡N) band as a function of depth in figure 3.14 shows a broad curve with FWHH of approximately 10 cm^{-1} with the highest point at about 15 μm from the top surface of the laminate. On the other hand, a determination of changes in intensity of the PVOH bands at 854 and 917 cm^{-1} shows that at a depth of 19 μm still the top layer is still present although in small amount. These results indicate that the PAN (bottom) layer has been shifted into the PVOH layer.

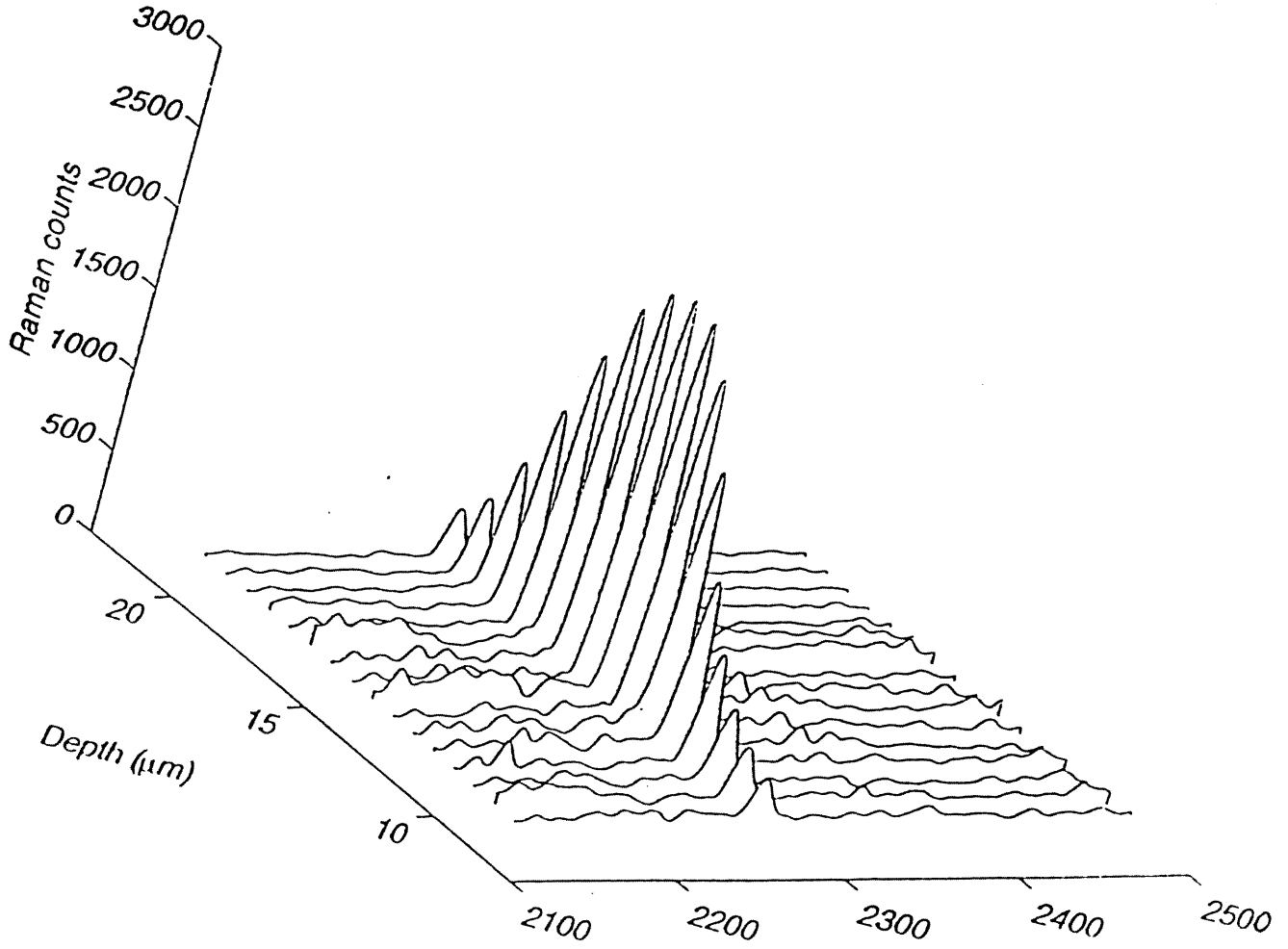

Figure 3.12: *3-D representation of the depth profile of the ν(C≡N) band of PVOH/PAN laminate obtained by focusing the microscope stepwise (1 μm) through the laminate*

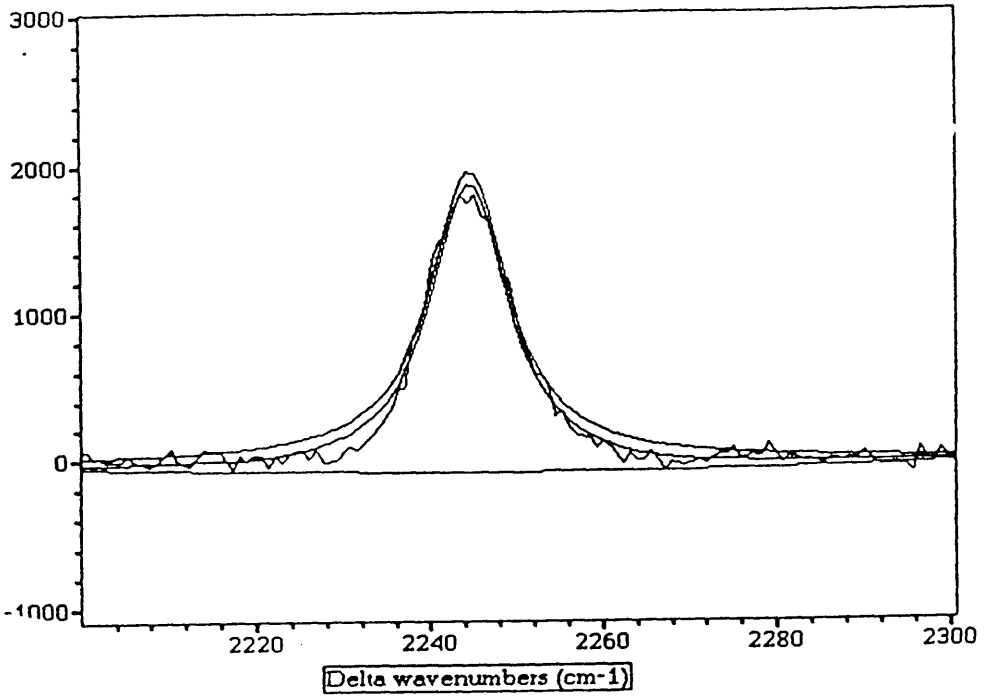

Figure 3.13: *Curve fitting (after background correction) of nitrile band from PAN at a depth of 18 μm in the PAN/PVOH laminate annealed at 65 ^{o}C*

However, as was discussed in section 2.4.2.1. with the confocal arrangement, a resolution of about 2 μm along the optical axis is attainable, but still it should be noted that some Raman scattered light is contributed from up to about 5 μm from the focal plane. See figure 2.8.

From figure 3.14, it may appear that the PVOH layer has not interdiffused into the PAN layer and this may be contrary to expectations that both polymers should show some degree of interdiffusion. One reason for this anomaly appears to be the use of the surface profiler. This instrument which has ideally been developed for surface profiling of hard materials measures the thickness of the polymer films by moving a stylus across the polymer film.

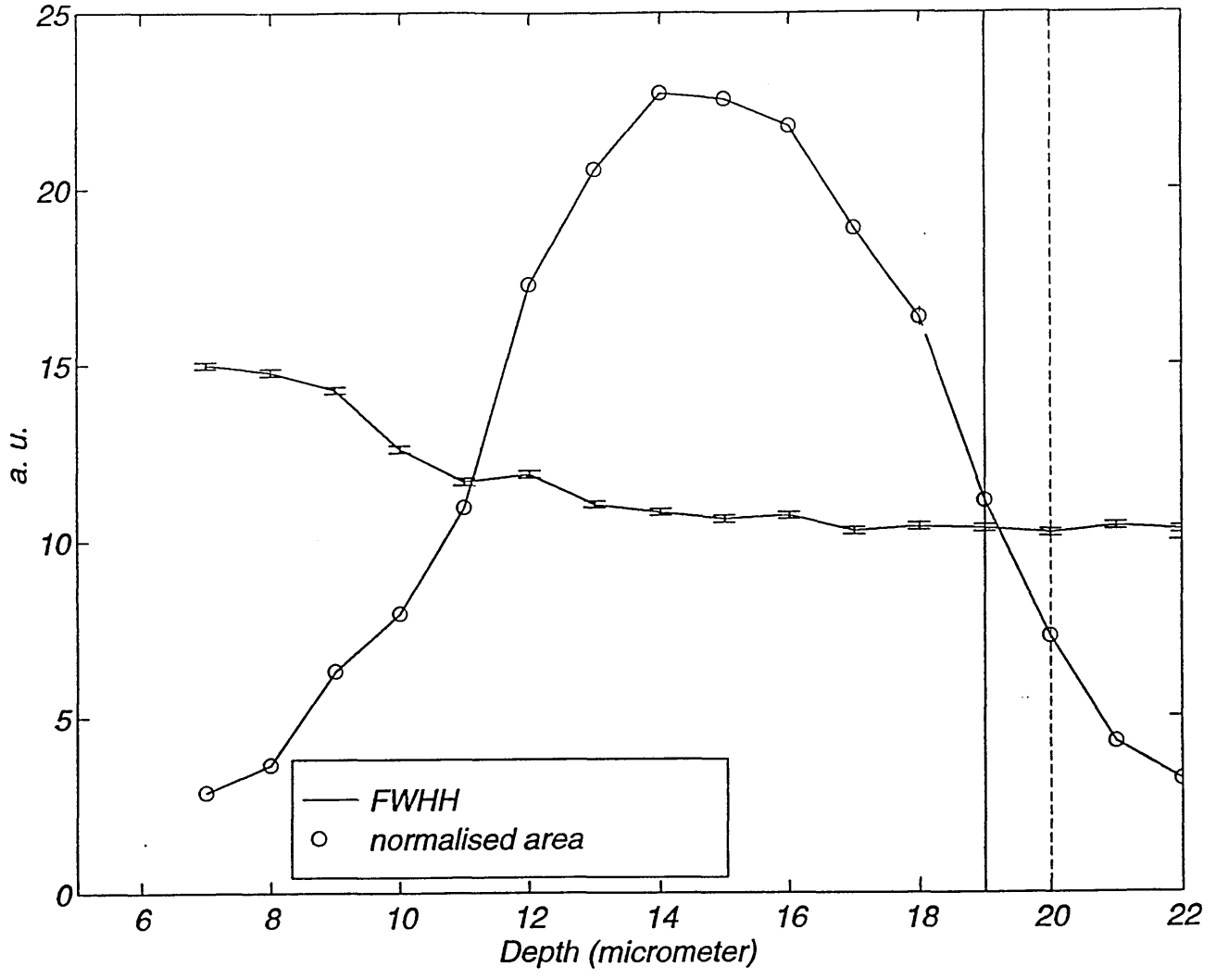

Figure 3.14: *Plot of FWHH and integrated area of nitrile band of PVOH/PAN laminate, annealed at 65 °C. Solid line indicates the approximate position of interface determined by surface profiler and dotted line indicates the end of top layer determined by evaluation of the Raman intensity of the band corresponding to PVOH (top) layer*

During such a procedure, if the polymer film after complete drying still is soft, the stylus may groove the surface and the depth of the grooves depend on the degree of softness of the film. On this basis, the polymer films which were treated with the surface profiler were examined under an optical microscope. It was found that PAN and PMMA films which were used as the bottom layer in the PVOH/PAN and PVOH/PMMA laminates, show such damages by the stylus. This has been shown in figure 3.15 which is an optical image of a PMMA film.

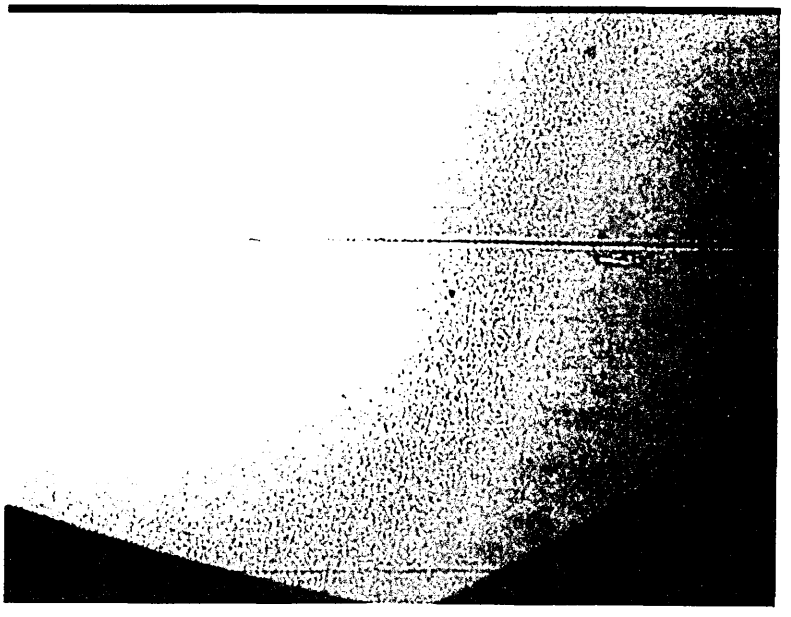

Figure 3.15: *An optical image of a PMMA film showing the grooves created along the line of the movement of the stylus used to measure the thickness of the film*

The depth of each groove was determined using an optical microscope. This is done first focusing on the bottom of the groove and then by focusing the microscope on the edges of the groove, and using the microscope stage micrometer, it is possible to determine the depth of the groove. On the other hand the PVOH layer which comprises the top layer in the both laminates, i.e. PVOH/PMMA and PVOH/PAN appears to be harder after

complete drying and examination of this film with an optical microscope shows no sign of grooves along the line of movement of stylus. Since the Raman depth profiling experiments have been carried out in a region other than the line along the grooves, it is clear that the top layer (PVOH) will be thinner than that measured by the surface profiler. This has been shown in figure 3.16.

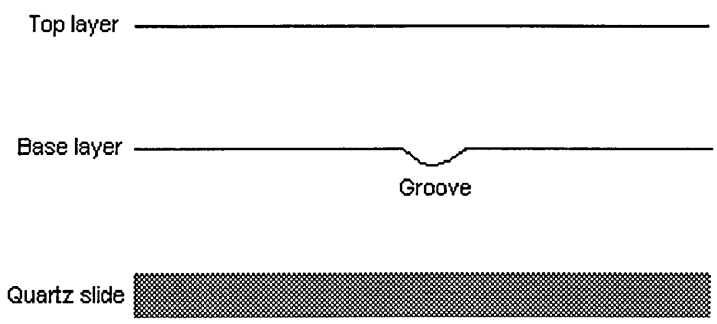

Figure 3.16: *Diagram showing the effect of grooves created by stylus during the thickness measurement with a surface profiler (Laser Form Talysurf). It is clear that as a result of such damage, the bottom layer may appear thinner than the actual thickness*

Thus, on this basis, figure 3.14 has been corrected. See figure 3.17. Another factor which may cause inaccuracy in depth profiling of a PVOH/PAN or PVOH/PMMA laminate is the absence of any intense sharp band in the Raman spectrum of PVOH. The PVOH Raman bands used in these experiments are at 854 and 917 cm^{-1}. The measurement of intensity or integrated area of these bands becomes increasingly difficult in the lower parts of the laminates. On the other hand the changes in parameters of the intense and sharp nitrile band of PAN film at 2244 cm^{-1} can be determined with greater accuracy.

The measurement of the FWHH of the $\upsilon(C\equiv N)$ band at the interfacial region for this laminate shows a significant increase to 15 cm^{-1} at a depth of 7 μm. This is a band broadening of 4.5 cm^{-1} in comparison with the $\upsilon(C\equiv N)$ band of a pure PAN film.

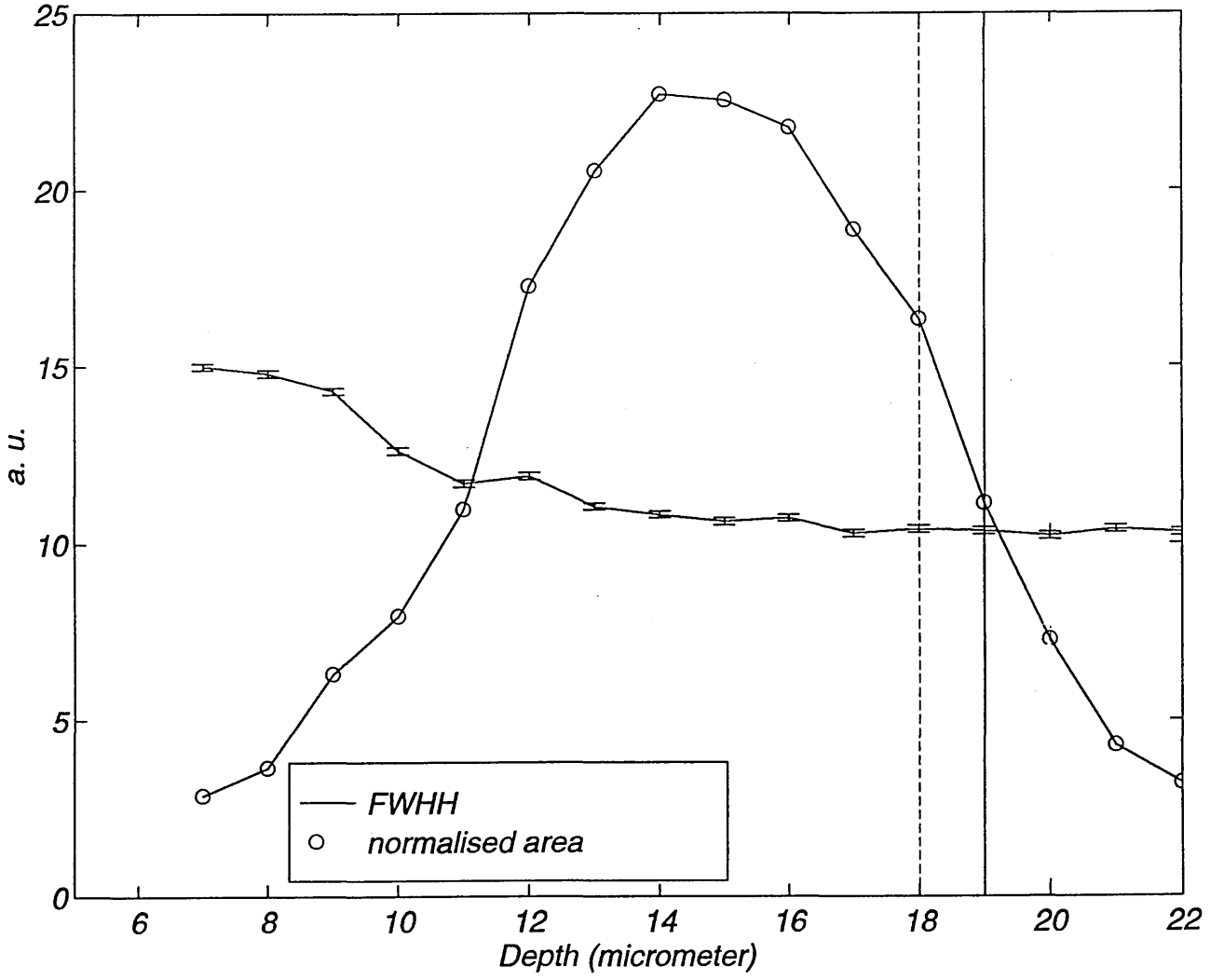

Figure 3.17: *Plot of FWHH and integrated area of nitrile band of PVOH/PAN laminate, annealed at 65 °C. Solid line indicates the approximate position of interface determined by surface profiler and dotted line indicates the end of top layer determined by evaluation of the Raman intensity of the band corresponding to PVOH (top) layer*

One possible explanation for this band broadening is the influence of hydrogen bonding between the nitrile group of PAN film with the hydroxyl group of PVOH film at the interface. As was explained earlier the effect of the dilution phenomena in the interfacial region should be considered. In this region the PAN nitrile group may interact via dipolar interaction with other PAN nitriles or via hydrogen bonding with surrounding PVOH molecules. A close examination of the spectra of PVOH/PAN laminates, shows that the concentration of PAN decreases from the pure PAN layer to the upper sections of the interfacial region.

It is expected that there are more PAN nitrile dipolar interactions with other PAN nitriles in the PAN layer compared to interfacial region. This dilution effect is expected to lead to a blue shift with band broadening of the $\upsilon(C\equiv N)$ mode in the interfacial layer. On the other hand, the degree of hydrogen bonding interaction between PAN and PVOH molecules is higher in the interfacial region compared with that in pure PAN. This is expected to lead to a red shift with band broadening of the $\upsilon(C\equiv N)$ band. Thus, the overall result of these two effects on the $\upsilon(C\equiv N)$ band is expected to be a little or no frequency shift with band broadening. In this sense our observations may be rationalised.

3.3.2.2. Annealing temperature of 75 °C

In addition to the annealing temperature of 65 °C, the depth profiling experiment was also carried out on the PVOH/PAN laminate with annealing temperatures of 75 and 90 °C. The aim of this study was to determine whether the interactions at the interfacial region are affected by the annealing temperature. Figure 3.18 shows the plot of FWHH and integrated area of the $\upsilon(C\equiv N)$ band of the PAN film in the PVOH/PAN laminate. In this figure the effect of grooves created by the stylus on measurement of the thickness of the layers has again been taken into account. See section 3.3.2.1.

The exposure time for each spectrum was 600 seconds. Although this exposure time is sufficient for obtaining good Raman spectra of the nitrile band at the 2244 cm^{-1} region, it is not sufficient to give good Raman spectra of the PVOH bands at 854 and 917 cm^{-1} region and the S/N ratio is poor. However, the longer exposure time will increase the background fluorescence significantly and as such it will be extremely difficult to obtain the Raman bands with high intensity. It appears that annealing the laminates at high temperatures, causes a significant increase in background fluorescence. The exact source of such a background fluorescence is not fully understood. See section 2.3.

The depth profiling procedure of this laminate was the same as the laminate annealed at 65 ^{o}C. From figure 3.18, it is evident that the FWHH of the $\upsilon(C\equiv N)$ band shows an increase to 15.5 cm^{-1}. This is a band broadening of approximately 5 cm^{-1} compared with FWHH of the same band in the pure PAN film and is a greater increase than that of PVOH/PAN laminate annealed at 65 ^{o}C. This may suggest an increase in the hydrogen bonding interaction due to greater mobility of the polymer chains at the interfacial region at the higher temperatures.

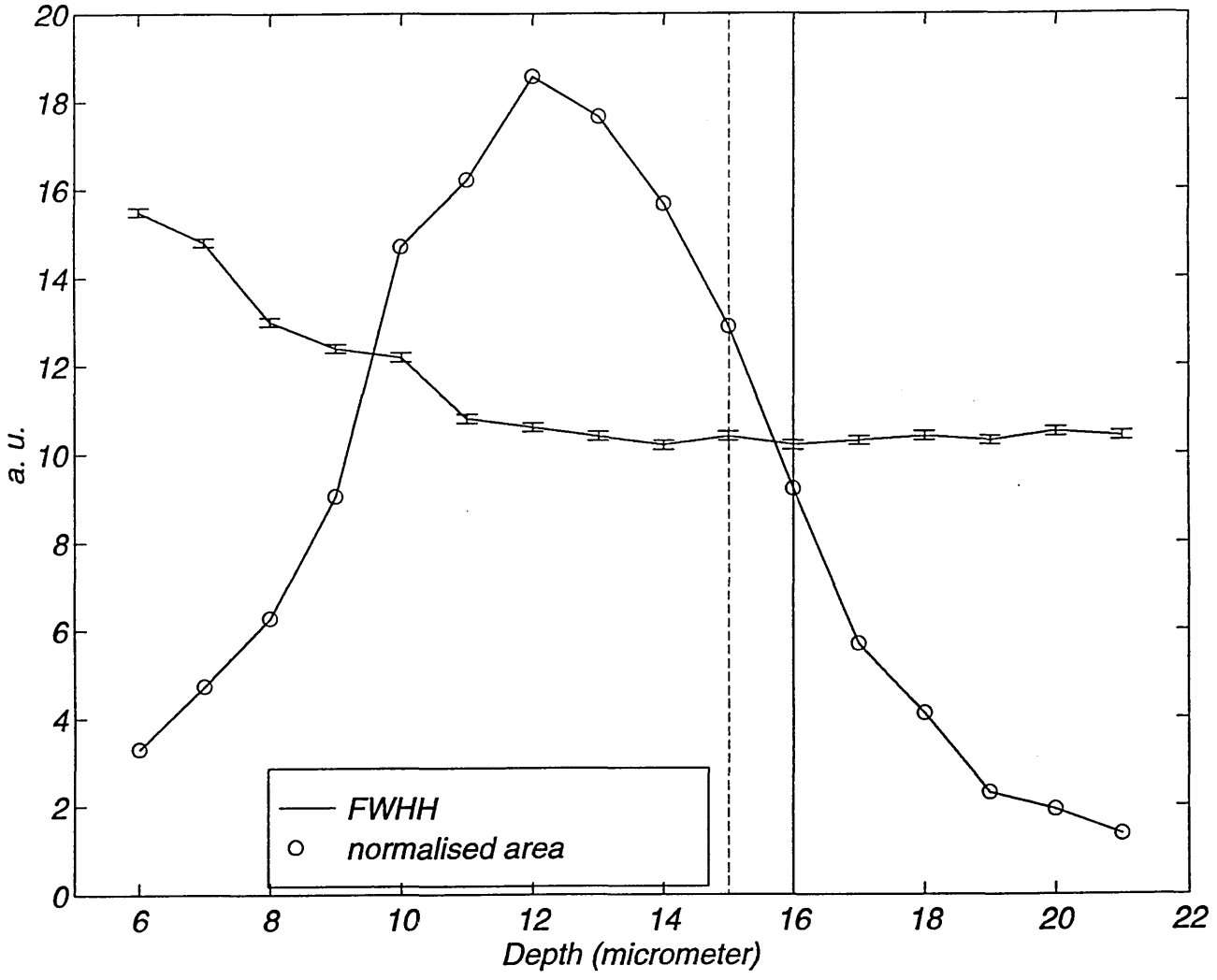

Figure 3.18: Plot of FWHH and integrated area of nitrile band of PVOH/PAN laminate, annealed at 75 °C. Solid line indicates the approximate position of interface determined by surface profiler and dotted line indicates the end of top layer determined by evaluation of the Raman intensity of the band corresponding to PVOH (top) layer

3.3.2.3. Annealing temperature of 90 °C

In order to study the effect of the annealing temperature at temperatures greater than the Tg of both polymers, a PVOH/PAN laminate was annealed at 90 °C. The depth profiling procedure was carried out in the same way as before.

The Raman spectra of the laminate annealed at 90 °C showed a significant increase in background fluorescence even greater than that of laminate annealed at 75 °C. This may indicate an evidence for chemical degradation. The increased fluorescence made the collection of the Raman spectra with good S/N ratio extremely difficult. In order to obtain the Raman spectra without saturating the CCD detector, it was necessary to minimise the exposure time to 200 seconds for each spectrum. Figure 3.19 shows a Raman spectrum of the 2000-2600 cm^{-1} region. The horizontal line in the spectrum is due to saturation of the CCD detector.

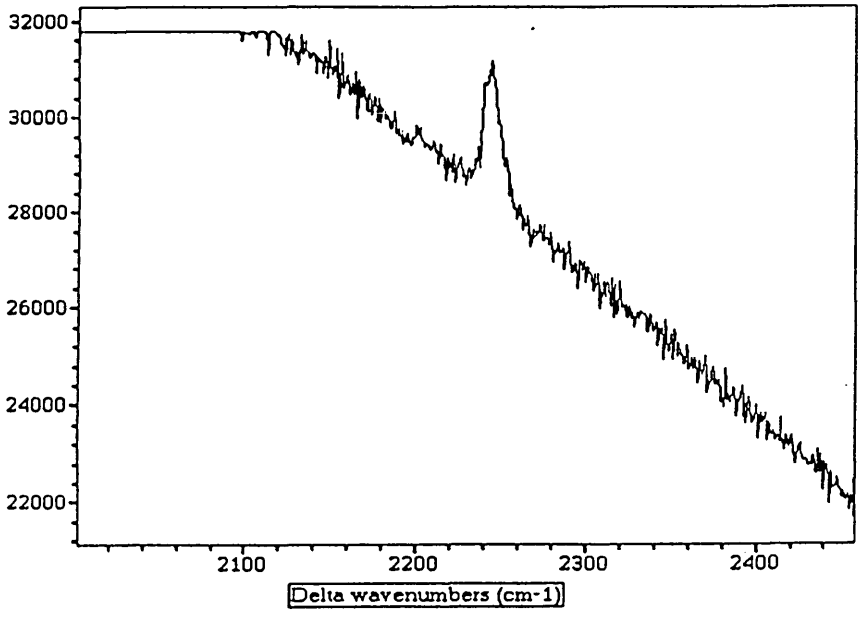

***Figure 3.19:** partly saturated Raman spectrum of the PAN nitrile band at a depth of 12 μm*

Table 3.3 shows the intensity of the background fluorescence level of the laminates annealed at various temperatures.

Annealing temperature (°C)	Background fluorescence (Raman counts)
65	3200
75	4400
90	24000

Table 3.3: *Background fluorescence level of the laminates annealed at different temperatures*

The FWHH and integrated area of the ν(C≡N) band was determined and plotted as a function of the depth. This is shown in figure 3.20. The FWHH in this laminate is increased compare to that of pure PAN film by approximately 3 cm^{-1}. From figure 3.20, It appears that the PAN layer in this laminate shows less interdiffusion into the PVOH layer in comparison to laminates annealed at 65 and 75 °C. Furthermore, from figure 3.21, It is clear that the laminate annealed at 90 °C shows less increase in FWHH than that of annealed at 75 °C. This is contrary to expectations, since the laminate annealed at 75 °C shows greater band broadening than the one annealed at 65 °C.

One explanation for this is the effect of annealing the laminate at the a temperature (90 °C) above the glass transition temperature, Tg of both constituent polymers. Zhang et al [3.30] have shown that intermolecular hydrogen bonding is reduced when the annealing temperature is greater than the Tg. Increase in molecular motion is expected to break the hydrogen bonds, resulting in phase separation due to dissociation of intermolecular hydrogen bonds above the Tg of the constituent polymers. Further increase in temperature causes thermal degradation.

3.3.3. PAA/PAN laminate

So far the polymer laminates used in these studies were PVOH/PMMA and PVOH/PAN. In these laminates, PVOH with hydroxyl groups was use as the top layer and it is shown that in contact with PMMA containing the carbonyl group or with PAN containing the nitrile group will show some degree of intermolecular interaction. In order to examine the effect of other polymers with the hydroxyl group in polymer laminates, a PAA/PAN system was utilised. The polymer laminates were deposited on a quartz slide and annealed at 65 °C. The depth profiling procedure was carried out as before using the confocal Raman microspectroscopy technique. The specific characteristics of these polymers are shown in table 3.1.

Figure 3.22 shows a Raman spectrum of a pure PAA film. The Raman spectra at various levels (1 μm steps) were recorded for the 1360-1840 cm^{-1} region to examine the changes in the ν(C=O) band of PAA at about 1700 cm^{-1}. However, this band is broad and relatively weak (see fig 3.22) and as a result it was difficult to examine the exact changes in this band at the interfacial region.

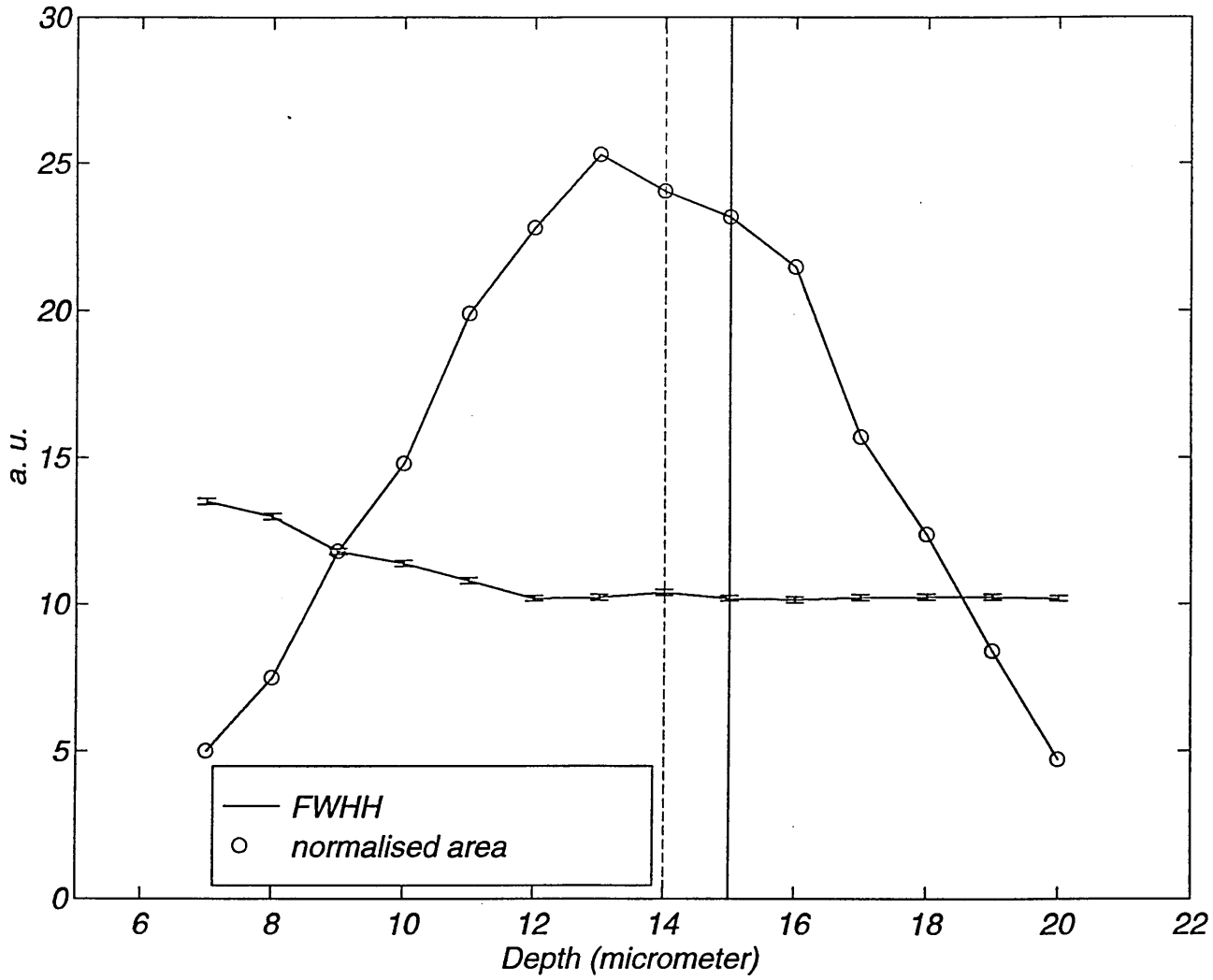

Figure 3.20: *Plot of FWHH and integrated area of nitrile band of PVOH/PAN laminate, annealed at 90 °C. Solid line indicates the approximate position of interface determined by surface profiler and dotted line indicates the end of top layer determined by evaluation of the Raman intensity of the band corresponding to PVOH (top) layer*

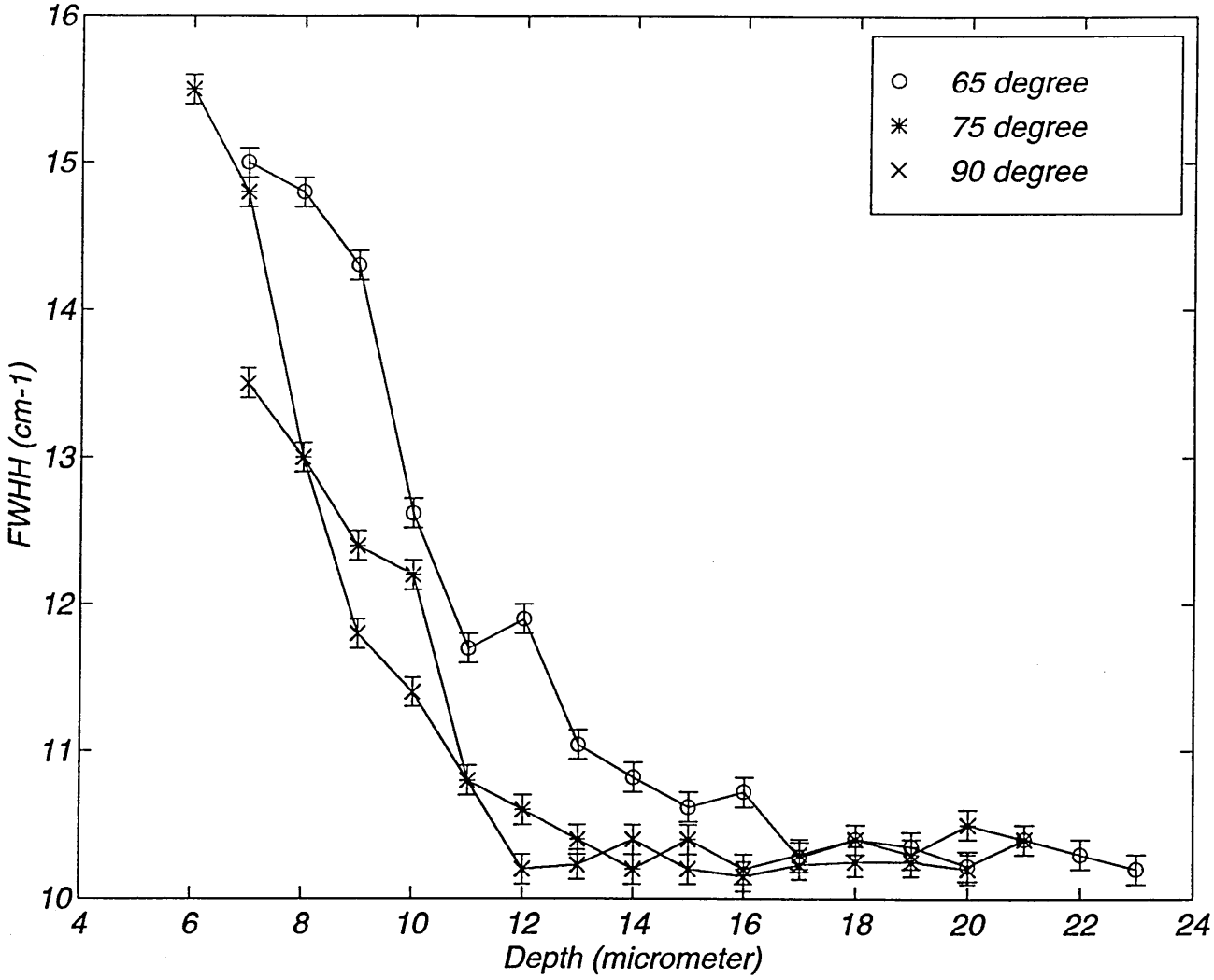

Figure 3.21: *Plot of FWHH of the ν(C≡N) of PAN in PVOH/PAN laminate as a function of depth for the laminates annealed at various temperatures*

However, the changes in the ν(C≡N) band of PAN were examined for comparison with the changes in this band in the PAN/PVOH laminate. Figure 3.24 shows a plot of FWHH and the integrated area of the ν(C≡N) band as a function of depth in PAA/PAN laminate.

Figure 3.23 shows a broader curve corresponding to area in this laminate in comparison to the PVOH/PAN laminate annealed at the same temperature. This suggests a greater degree of interdiffusion. One reason for this is the low molecular weight of PAA polymer (2,000) compared with the relatively higher molecular weight of PVOH (50,000). As a result of this, it is expected that PAA chains with greater mobility interpenetrate further into the PAN layer than PVOH.

However, the FWHH of the ν(C≡N) band remains almost unchanged (see fig 3.23). This is in contrast to significant broadening of this band in PVOH/PMMA and PVOH/PAN laminates at the interfacial region. Figure 3.23 shows a comparison of the changes in band width of the the ν(C≡N) band of PAN in PVOH/PAN and PAA/PAN laminates.

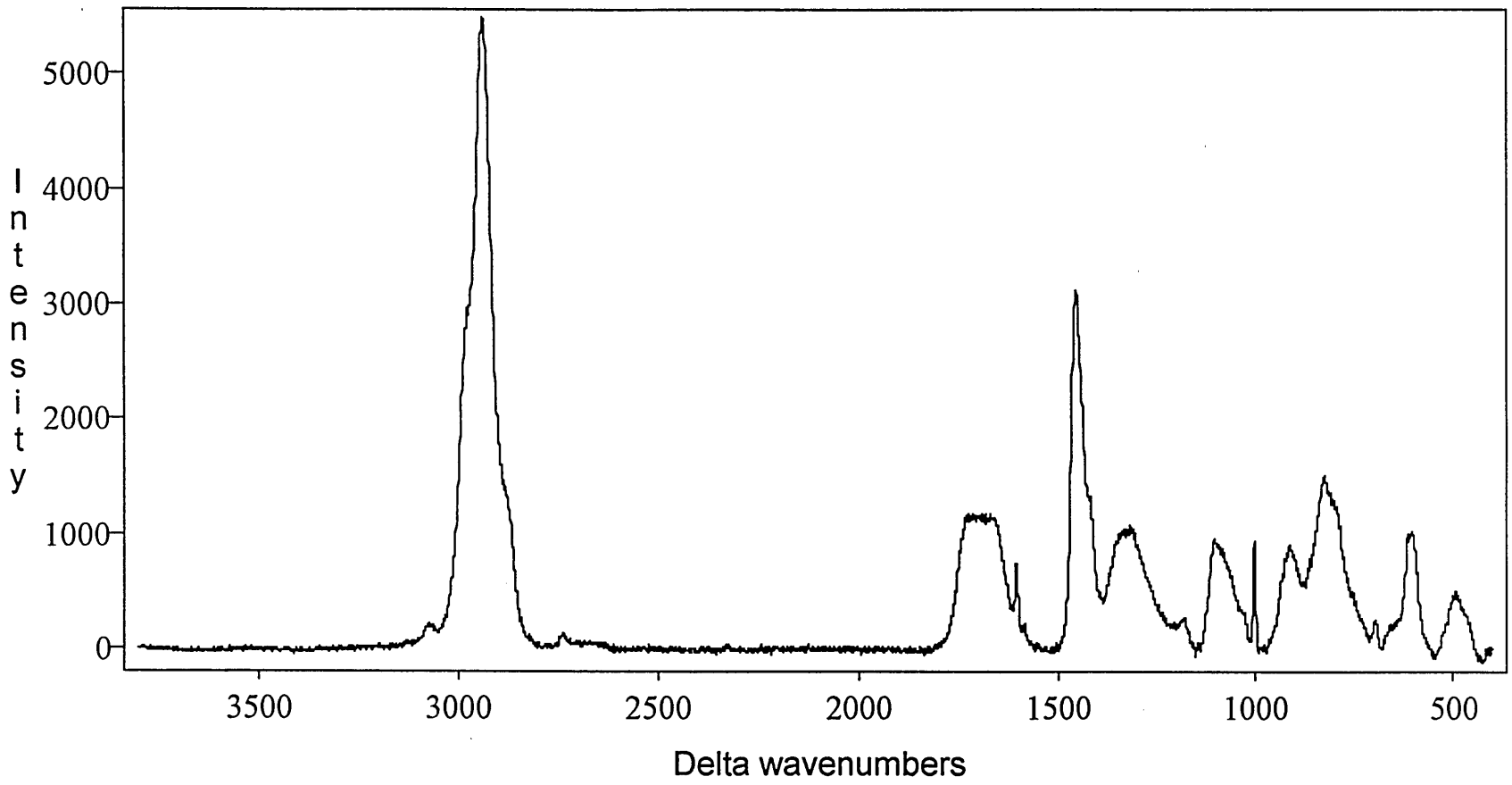

Figure 3.22: The Raman spectrum of a pure PAA film.

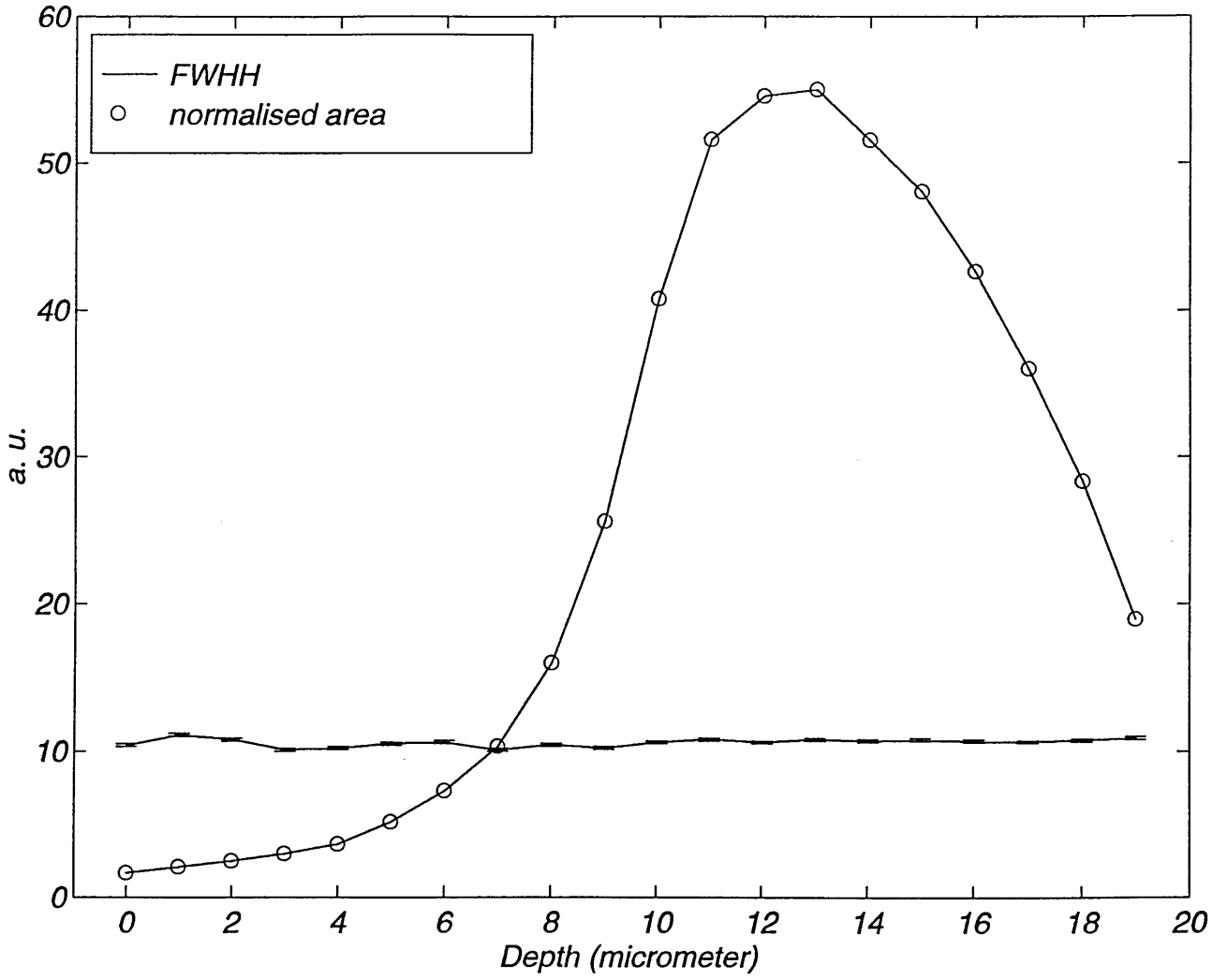

Figure 3.23: *A plot of FWHH and integrated area of the ν(C≡N) band in PAA/PNN laminate. For the ease of comparison the points corresponding to the integrated area have been devided by 2000*

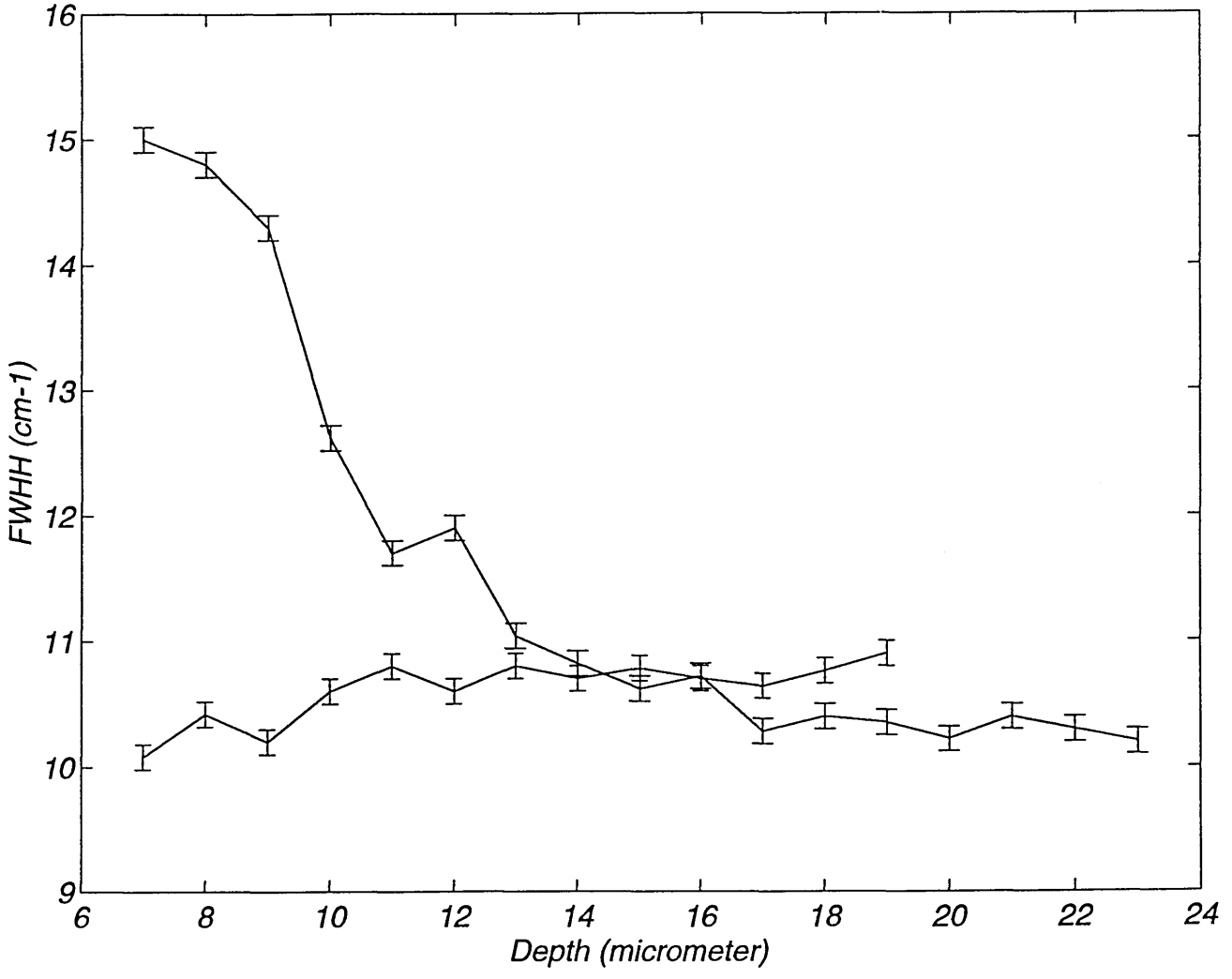

Figure 3.24: A comparison of FWHH of the ν(C≡N) band in PVOH/PAN and PAA/PAN laminates

The fact that there is no significant change in the FWHH of the ν(C≡N) band at the interfacial region of PAA/PAN laminate indicate that there are no significant intermolecular interactions between the constituent polymer layers.

In the first instance this might be surprisinging, since PAA film contains hydroxyl groups which are expected to interact with the nitrile groups of the PAN layer. However, a close examination of the structure of the PAA polymer shows the possibility of the intramolecular interactions in this polymer. Tanaka et al [3.31] have shown the ability of PAA to form cross-linking by hydrogen bonding in aqueous solutions. Indeed, the broad carbonyl band in the Raman spectrum of the PAA is indicative of such intermolecular interactions. Most of these hydrogen bonding interactions are of a 'closed' (cyclic dimer) type in which two carboxyl groups form a ring structure through two hydrogen bonds formed between the oxygen atoms of the carbonyl groups and hydrogen atoms of the hydroxyl groups. Since, the PAA film was deposited onto the PAN film from water as a solvent, this could account for the lack of significant intermolecular interactions between the PAN and the PAA layers. This means that many of the hydroxyl groups of the PAA have already formed intermolecular interactions in the PAA aqueous solution before deposition on the PAN film. Thus, a little or no hydrogen bonding between PAA and PAN films can take place.

3.3.4. Effect of annealing time

One of the parameters which may have an effect on the interaction of the polymers at the interfacial region is the length of time that the laminate has been annealed. In order to examine this, a PVOH/PMMA laminate was prepared by depositing the PMMA film from solution using DCM as a solvent on a quartz slide. This film was cured at 65 ^{o}C for 24 hours. In the second step a PVOH film was deposited on the PMMA film by casting from

a solution using water as a solvent and the whole sample was annealed at 65 °C for 5 hours.

The depth profiling procedure was carried out as before and the changes at the interfacial region was recorded. Then the laminate was annealed for another 24 hours at the same temperature and the depth profiling was carried out at the same point on the sample and the Raman spectra were recorded. Eventually the sample was annealed for another 24 hours at the same temperature and the depth profile Raman spectra of the same point were collected.

A comparison of these depth profiles shows no difference between the data collected corresponding to the laminate annealed at various lengths of time. This may suggest that no significant interdiffusion has occurred after initial annealing time (5 hours) and an equilibrium state has been established. On this basis no significant changes with further annealing at the same temperature (65 °C) is expected. However, it should be noted that the resolution of the Raman confocal microspectroscopy is about 2 μm along the optical axis of the microscope (z) (see section 2.4.2.) and thus small changes after initial annealing time may not be detected.

CHAPTER 4

4.1. Introduction

A polymer blend is defined as a mixture of at least two polymers or copolymers [4.1]. Sometimes the mixture is a single-phase material. An example of this is dissolved plasticizer in polymer materials. However, most of the mixtures are heterogeneous and although such heterogeneities are often very small, they still may result in a degradation of the desirable properties of the material. Figure 4.1 shows an overview of the most common two-phase systems consisting of polymers.

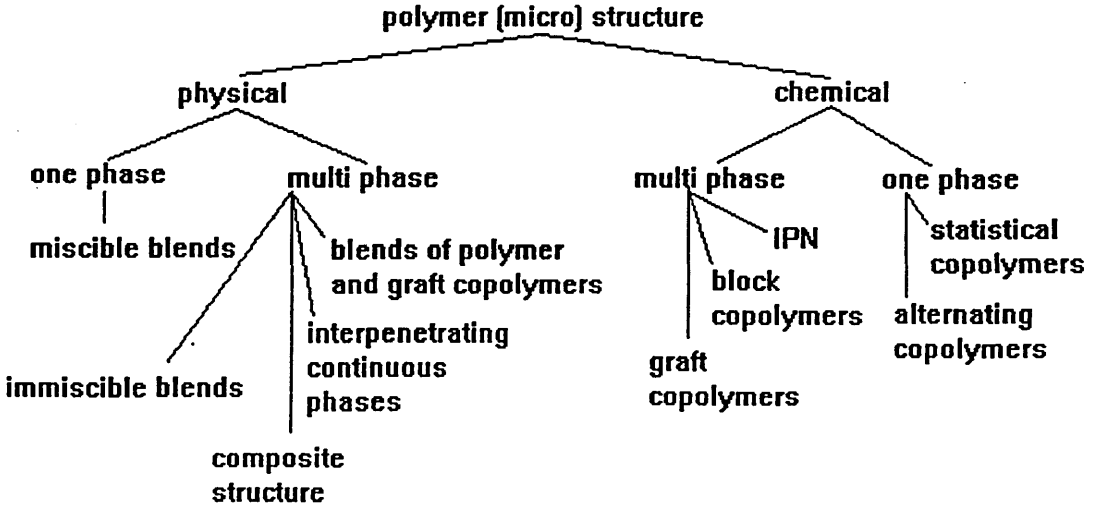

Figure 4.1: Microstructure of polymer blends and alloys (from ref 4.1)

Polymer blends can offer enormous technological and economical advantages and, as a result, have currently captured a high level of interest [4.2, 4.3]. Recycling plastics, for example, is currently an important industrial process of which the end product is a polymer blend. The degree of miscibility, the interaction of phases, phase size and the composition of the phases can all affect the properties and the behaviour of these blends.

A number of optical and electron microscopy techniques have been used to provide information about the morphology of these blends. Light microscopy is one of the most common techniques and has been used for study of imiscible polymer blends. Polarised light microscopy [4.4, 4.5] has been utilised to study polyethylene/ polypropylene blends. These blends have also been studied by fluorescence microscopy [4.6 - 4.8] and phase contrast [4.5]. Scanning electron microscopy, SEM, has been applied to immiscible polymer blends such as PS/EPYM [4.9] and toughened epoxides [4.10]. Transmission electron microscopy, TEM, with very high resolution (1 nm) can provide information on small polymer structures. It has been used to study the microstructure of block copolymers [4.11] and very fine phase dispersion of phases [4.12]. Electron microscopic techniques (with many advantages including high resolution) do however, suffer from some practical and technical disadvantages. These include difficult sample preparation in the case of TEM and electron beam damage [4.13]. Rapid and substantial chemical changes in polymers can occur in the electron microscope as a result of interaction with a highly ionising radiation of the electron beam. Apart from optical and electron microscopy, other techniques have been used to characterise polymer blends. These include: nuclear magnetic resonance, NMR [4.14-4.22], X-ray diffraction, ultraviolet spectroscopy, UV [4.23-4.28], electron spin resonance, ESR [4.29-4.31], X-ray diffraction, XRD [4.32], X-ray photoelectron spectroscopy, XPS [4.33-4.38] and atomic force microscopy, AFM [4.39-4.41]

Vibrational spectroscopic and microscopic techniques can provide invaluable information about the nature of interactions between various phases of a blend. Infrared spectroscopy has been widely used by different researchers for characterisation of polymer blends. These include studies on; blends of polyurethane elastomers and carboxylated nitrile rubber [4.42], on miscibility and specific interactions in blends of poly(2-ethyl-2-xazoline) with hydroxylated polymethacrylates [4.43], on chemical interactions in blends of bisphenol-A polycarbonate with tetraglycidyl-4,4'-diaminodiphenylmethane epoxy [4.44], poly(styrene-graft-ethylene oxide) as a compatibilizer in polystyrene/polyamide blends [4.45], on hydrogen-bonded polymer blends containing poly(4-hydroxystyrene-co-4-methoxystyrene) copolymers [4.46], on phase structures of hexamine cross-linked Novolac blends [4.47], on the compatibility of poly(styrene) poly(vinyl acetate) blends [4.48], molecular structure of compatible polymer blends [4.49], on the surface composition of miscible polymer blends [4.50], on the ionic conductivity and compatibility of blends of poly(methyl methacrylate) and poly(propylene glycol) complexed with $LiCF_3SO_3$ [4.51], on the structure of blends of poly-tert-butyl acrylate with polyacrylic acid [4.27], on the analysis of polycarbonate poly(ethylene terephthalate) blends [4.52], on the mapping of the phase diagram of an aromatic polyamide blend [4.53], on the photodegradation of blends of polycarbonate and poly(methyl methacrylate) [4.28], on surface studies of polymer blends [4.54], on volume contraction on mixing in poly(vinyl ethylene-co-1,4-butadiene) polyisoprene blends [4.55] and many others.

Raman spectroscopy and in particular Raman microscopy, by comparison with infrared techniques, has been little used by researchers for characterisation of the polymer blends. The following have applied Raman spectroscopy to study; effect of annealing time, film thickness and molecular weight on surface enrichment in blends of polystyrene and deuterated polystyrene [4.56] and surface segregation in blends of polystyrene and deuterated polystyrene [4.57].

Schaeberle et al [4.58] have previously described the application of Raman chemical imaging as a routine and noninvasive method for characterisation of materials. They have applied the imaging technique to the visualisation of polypropylene/polyurethane blends. Garton et al [2.72] have employed Raman microscopy to characterise rubber toughened epoxy resin, a polyethylene-polypropylene blend and a polyester (PET/PBT) blend. Markwort et al [2.113] have compared the two alternative methods of Raman imaging for characterisation of the polymer blends. Batchelder et al [2.112] have studied films of a urethane/acrylate polymer which contain PTFE particles.

In this work, Raman imaging and confocal point by point mapping have been applied to polymer blends in order to study the possible interactions between the constituent polymers. These polymer blends include (a) PAN/PMMA and (b) PAN/PVOH.

Raman imaging and mapping via point illumination in combination with confocal light collection and via global (wide-field) illumination have been described in detail in sections 2.4.2 and 2.4.3 respectively. Various applications of these techniques by different researchers have also been reviewed.

4.2. EXPERIMENTAL

Poly (methyl methacrylate), PMMA, polyacrylonitrile, PAN and poly(vinyl alcohol), PVOH polymer samples were purchased from Aldrich Chemical Ltd. Table 4.1 shows the various characteristics of these polymers.

polymer	MW	Tg (^{o}C)	Molecular formula	solvent
PMMA	124,000	114	[-CH2C(CH3)(CO2CH3)-]$_n$	DMF ¤
PAN	15,000	~85	[-CH2-C(C≡N)H-]$_n$	DMF ¤, DMSO §
PVOH	50,000	75-85	[-CH2CH(OH)-]$_n$	DMSO §

Table 4.1: *Characteristic parameters of the polymer compounds used in this thesis.*

¤: dimethyl sulfoxide, DMSO, spectroscopic grade from Aldrich Chemical Company Ltd.
§: N,N-dimethylformamide, DMF, spectroscopic grade from Aldrich Chemical Company Ltd.

The PMMA/PAN blend was prepared by dissolving the two polymers in a 2:1 PAN:PMMA ratio in DMF. The mixture was spread on a quartz slide and cured at 100 ^{o}C for 24 hours. The PAN/PVOH blend was also prepared in the same way by dissolving the two polymers in DMSO.

The Raman imaging and mapping data were obtained using a Renishaw Ramascope©, (System 2000). This instrument consist of a low-powered (25 mW) air cooled HeNe laser, an Olympus microscope, a single spectrograph for spectroscopy mode, a set of angle-tunable bandpass filters (with a resolution of 20 cm^{-1}) for imaging mode and a Peltier-cooled CCD detector (576 x 384 pixels). This instrument is also equipped with a motor driven microscope stage. The details of Raman imaging technique is described in chapter 2.

The Raman mapping was carried out by setting the instrument in confocal mode (see section 2.4.2.) using a x50 objective, slit width of ~12 μm and a CCD area of 4 x 576 pixels. In order to obtain a set of spectra for a chosen area of the sample, the microscope was focused on a point and the Raman spectrum of a region containing a distinctive Raman band corresponding to only one of the constituent polymers was recorded. The sample was then moved by one 1 μm and the second spectrum was acquired. This procedure was continued in a rasterring fashion until a set of spectra corresponding to a desired area on the

sample was collected. Raman imaging was carried out by defocusing the laser beam spot on desired area of the sample using x50 objective. By selecting a distinctive Raman band of one of the components of the polymer blend, the Ramascope selects a suitable filter (see section 2.4.3.) for detection of the desired band.

4.3. Results and discussion

4.3.1. PMMA-PAN blend

A blend of PMMA and PAN was prepared and studied by Raman microscopy. Figure 4.2 shows a white light image of the blend. It is clear from this picture that there are distinctive particles in the blend. However, it is not possible from this picture to determine the composition of these particles, and thus such variation may be due to topological differences.

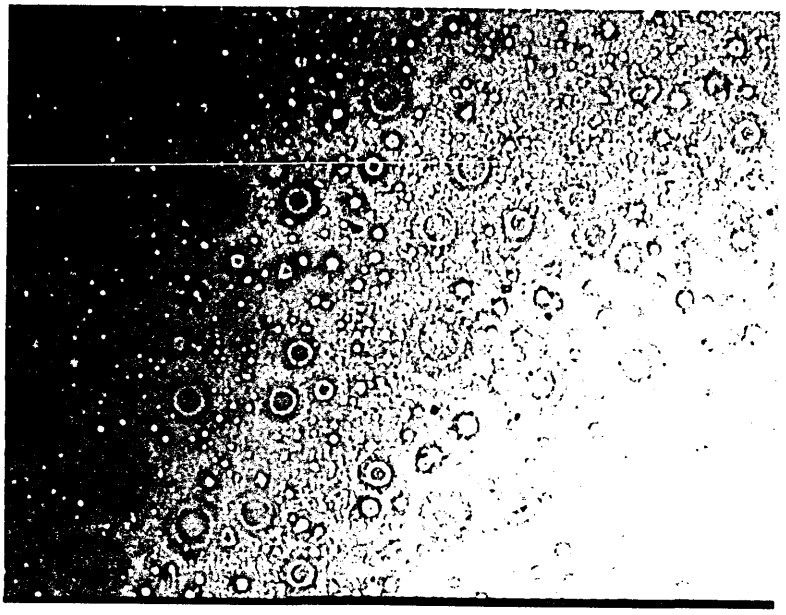

Figure 4.2: *White light image of the surface of a PMMA-PAN blend*

In order to determine the composition and distribution of these phases, Raman confocal microscopy was employed and a point by point map of a chosen area of the blend. A series

of spectra for the 2000-2450 cm^{-1} region containing the $\upsilon(C\equiv N)$ band of PAN were recorded. The intensity, integrated area, position and the band width of the band for each spectrum were determined. In order to construct the map, the Renishaw software was used to plot the data. Figure 4.3 shows a 3-D map of intensity of the $\upsilon(C\equiv N)$ band of PAN at 2244 cm^{-1} for an area of 15 μm^2 on the surface of a the PMMA-PAN blend.

It is clear from figure 4.3 that the levels of high intensity are the areas with greater degree of PAN in the blend and thus the lower region particularly the one at the centre of the map corresponds to absence of PAN particles.

Since the blend consist of two polymers, it is expected that the regions which show a low level of PAN particles, should correspond to the presence of PMMA particles. In order to examine this, a second map of the almost the same area of the surface of the blend was mapped. The mapping procedure was carried out in the same way but now a series of spectra were recorded for the carbonyl band region (1650 - 1800 cm^{-1})of the Raman spectra. The intensity, position, integrated area and the band width of the $\nu(C=O)$ band of PMMA were determined. Figure 4.4 shows a map of intensity of the $\nu(C=O)$ band for the selected area of the blend. A comparison of figures 4.3 and 4.4 shows that these two maps are apparently the reverse of one another.

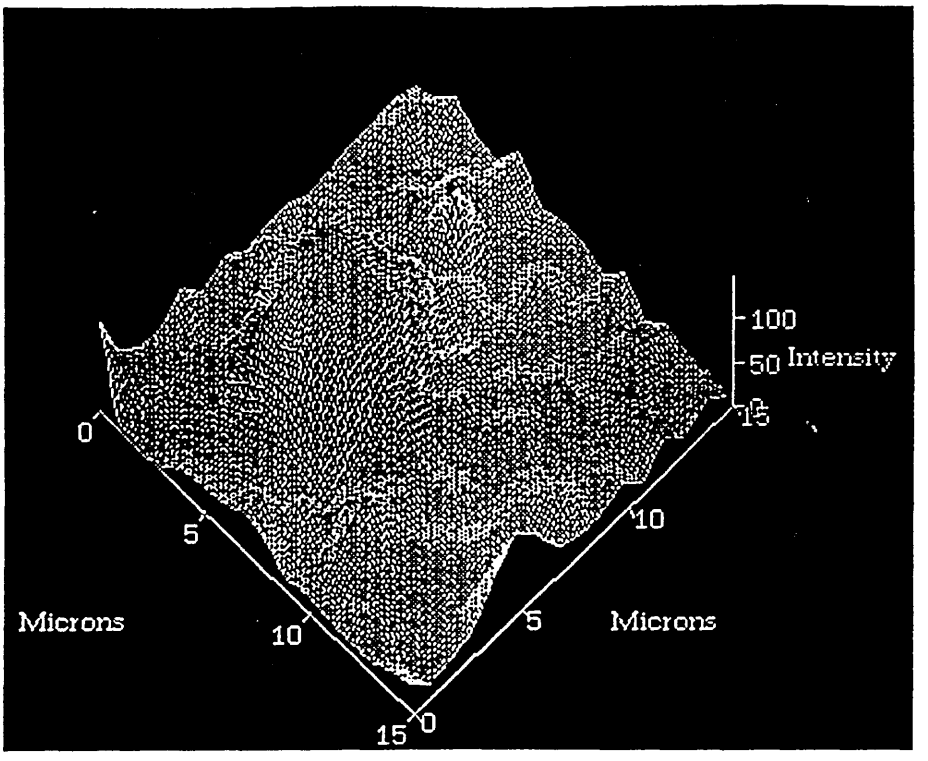

(a)

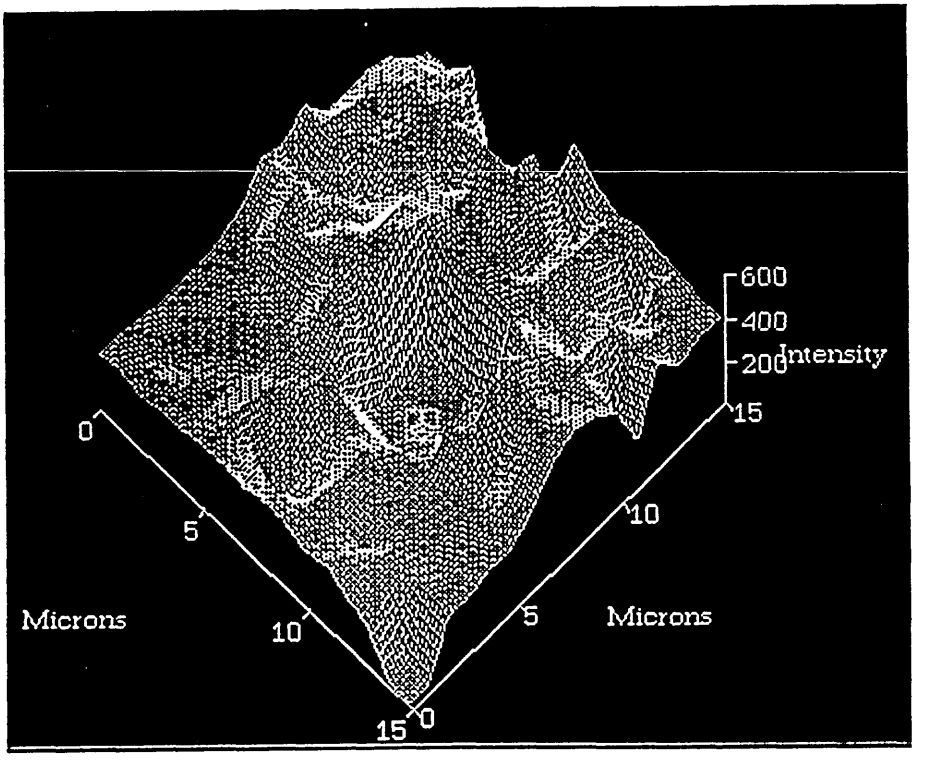

(b)

Figure 4.3: *(a) a 3-D map of intensity of the ν(C≡N) band from a 15 μm and (b) a 3-D map of intensity of the υ(C=O) band from a 15 μm^2 area of the surface of a PMMA-PAN blend.*

It is known [3.23] that chemical interactions, for example hydrogen-bonding changes the width and position of the ν(C=O) band of PMMA and the ν(C≡N) band of PAN. In order to determine possible phase interactions between these two polymers, a map of changes in the band width of the ν(C≡N) band was plotted. Figure 4.4 shows this map.

It is clear from figure 4.4 that there is almost no change in the width of the this band. This is expected, since both PMMA and PAN contain functional groups which are not expected to show chemical interactions such as hydrogen-bonding. Thus no variation in the position and width of these bands.

Clearly, micro Raman mapping could be used to determine the detailed distribution of various phases in the polymer blend with good accuracy. However, one disadvantage of this technique is that it is an extremely time consuming procedure involving the collection and processing of large amounts of data in order to construct the maps shown above.

One way of solving this problem is by the use of Raman imaging as explained in section 2.4.3. In this method, a relatively large area of the PMMA-PAN blend was illuminated by the laser beam. In order to obtain a Raman image of the PAN particles, the nitrile band at 2244 cm^{-1} was chosen. The Ramascope automatically selects the right filter for this region of the spectrum. However, this kind of imaging needs some care in order to make sure that the recorded image is the one corresponding to the selected band and not due to background fluorescence which may not be relevant to the particular polymer particle under analysis. Figure 4.6 shows the Raman spectrum of a PAN sample.

It is clear from figure 4.6 that the bands corresponding to PAN sit on a raised, fluorescence, baseline. A simple Raman image of any of the bands of this polymer without background

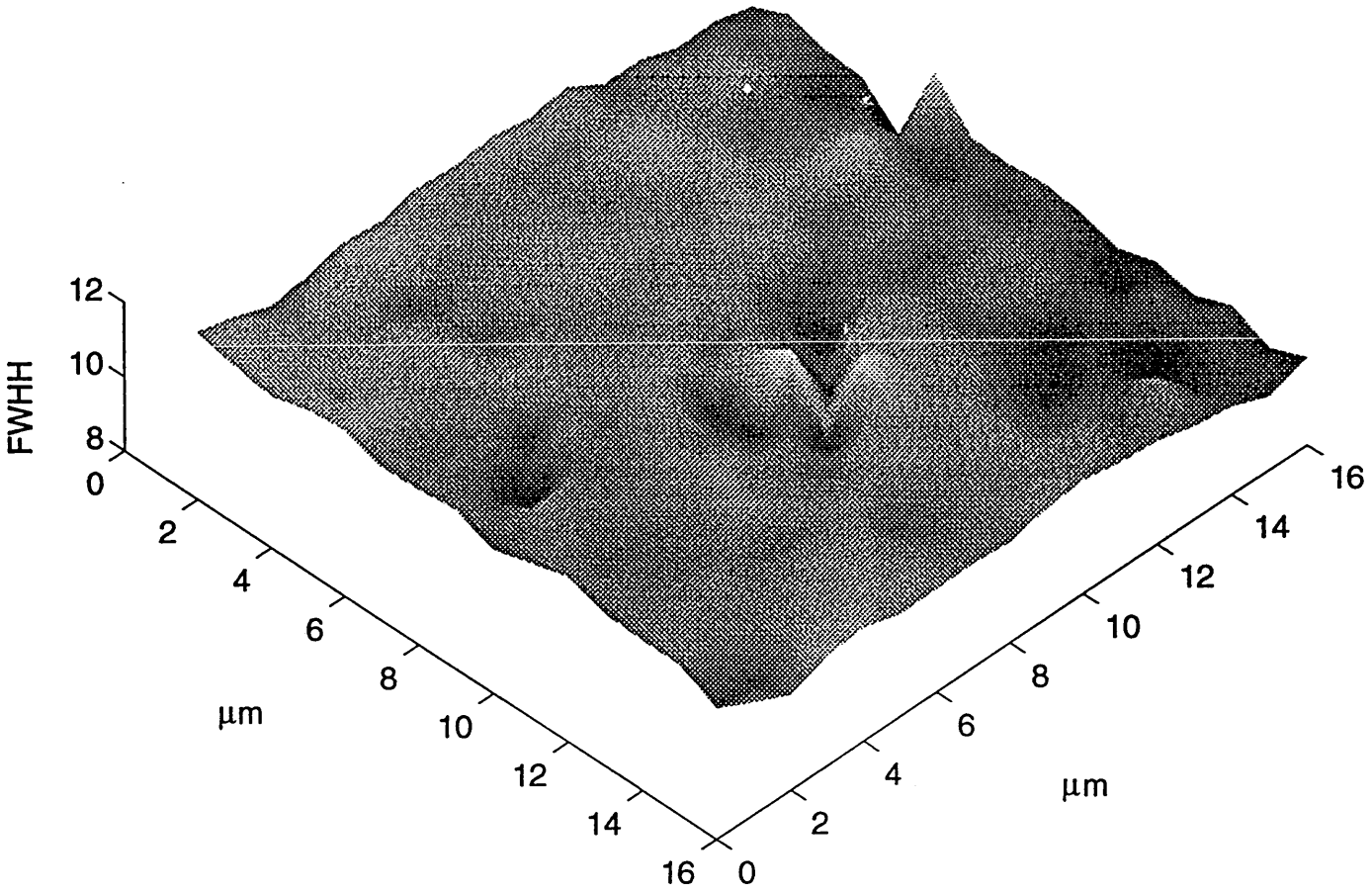

Figure 4.4: A 3-D map of band width of υ(C=O) band in a PMMA/PAN blend.

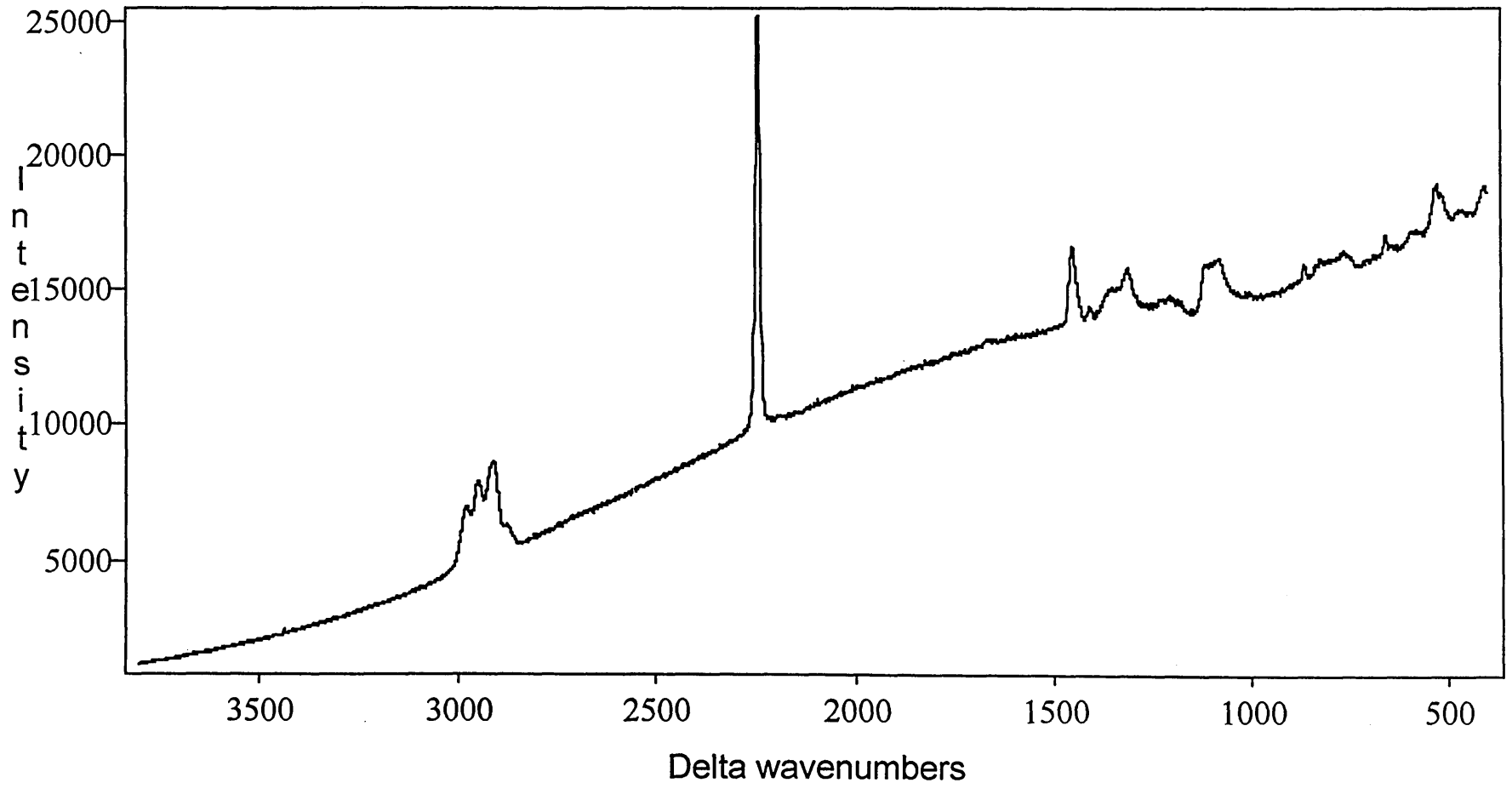

Figure 4.5: Raman spectrum of a PAN film.

subtraction may only result in a very bright spot which is due to saturation of the CCD detector.

In order to remove the contribution from the fluorescence from the Raman image of the $\upsilon(C\equiv N)$ band, first, a background image on either side of the band was recorded. These two images were averaged in order to represent a baseline under the desired band. In the next step, a Raman image of the nitrile band at 2244 cm^{-1} was obtained and finally by data processing, the Raman image was ratioed against the background image. This is called flat fielding and it not only removes the contribution from the fluorescence background, but also compensates for uneven illumination of the sample and topographical effects. Figure 4.6 shows a Raman image of a selected area of the PMMA-PAN blend.

The Raman image in figure 4.6 is shown with a grey scale. The bright areas in the image correspond to the presence of PAN polymer and the dark spots correspond to the absence of PAN. It was already shown before (with confocal mapping) that these regions correspond to PMMA particles sitting on a PAN background.

The Raman image shown in figure 4.6 was collected with an exposure time of 200 seconds. This signifies the main advantage of the Raman imaging with global illumination technique. This means that it can be successfully and routinely performed in order to obtain information about the distribution of various phases in a blend in a relatively short time.

However, it should be noted that there are some limitations associated with this technique. These include: (a) since use has been made of tunable filters with a 20 cm^{-1} band pass, a true Raman image of a particular phase in a blend of materials may only be obtained if the desired constituent material contains at least one intense band which is over 20 cm^{-1}

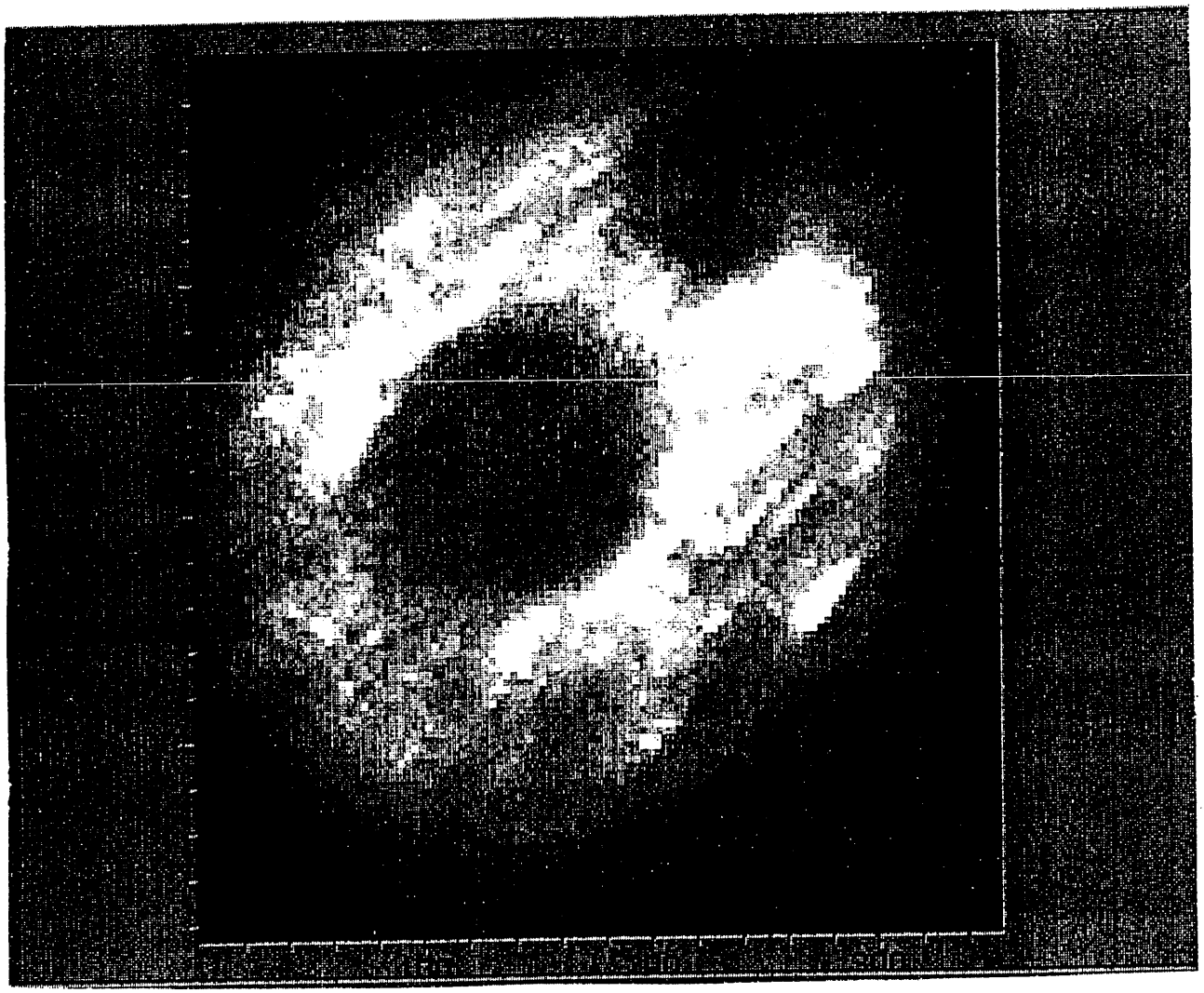

Figure 4.6: *Raman image of a selected area of a PMMA-PAN blend.*

away from the characteristic bands of other constituent materials, (b) due to use of these filters, the resolution of the images is not as high as pictures obtained by confocal mapping. As a result, it is not possible to obtain information about the possible interactions between the phases. Furthermore, these images are not as well resolved as images obtained by white light microscopy. This is due to the nature of Raman spectroscopy. The data collected by the detector in a Raman image is the scattered light from the sample whereas in a light microscope the data collected by the detector is the reflected light from the sample.

4.3.2. PAN-PVOH blend

In the previous chapter, a laminate of these two polymers was studied (see section 3.3.2.). It was shown that these polymers, at the interfacial region, show some chemical interactions. This was manifested in the broadening of the $\upsilon(C\equiv N)$ band at the interface, when spectra were obtained by depth profiling of the PAN/PVOH laminate using Raman confocal microspectroscopy. In order to examine the interfacial region between these two polymers in the lateral (xy) direction (the plane perpendicular to the direction of the laser light), a blend of PAN and PVOH was prepared by spreading a solution of these polymers from DMSO on a quartz slide and curing at 65 ^{o}C for 24 hours. Figure 4.7 shows a white light image of the blend.

The Raman mapping was carried out as in the case of PMMA-PAN blend. A series of Raman spectra from a selected area of the blend were recorded for the region 750-2300 cm^{-1} containing the characteristic bands corresponding to both PAN and PVOH. The intensity, position, width and integrated area of the selected bands of these polymers were determined. Figures 4.8 shows the maps of intensity of the bands corresponding to PAN and PVOH phases

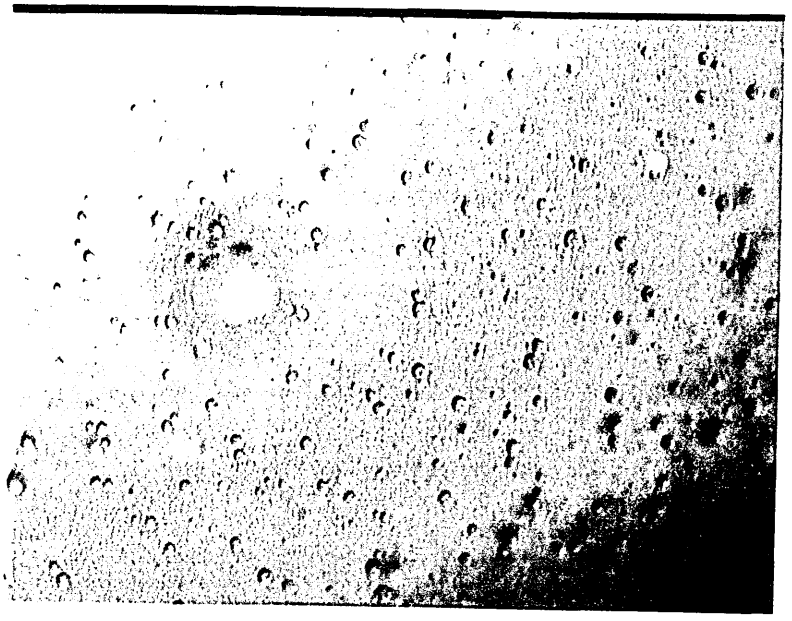

Figure 4.7: *White light image of PAN-PVOH blend*

It is clear from figure 4.8a that a number of regions with high intensity exist in this area of the sample. Since the map shows the intensity of the ν(C≡N) band, this means that PAN is present as individual particles in the polymer matrix. On the other hand, it can be seen from figure 4.8b that the PVOH map shows a more even distribution of this polymer. Furthermore, with a close examination, it is indeed evident that these two maps are almost reverse of each other. This means that where the PAN band has a high intensity, the PVOH band has a low intensity and *vice versa*. From a comparison of these figures with figure 4.7 (the white light image) it is clear that the particles in the white light image correspond to PAN.

However, figure 4.8 does not provide any information about the possible interactions between the phases in the PAN-PVOH blend. In order to examine this a map of the changes in the width of the υ(C≡N) band was plotted. Figure 4.9 shows this map.

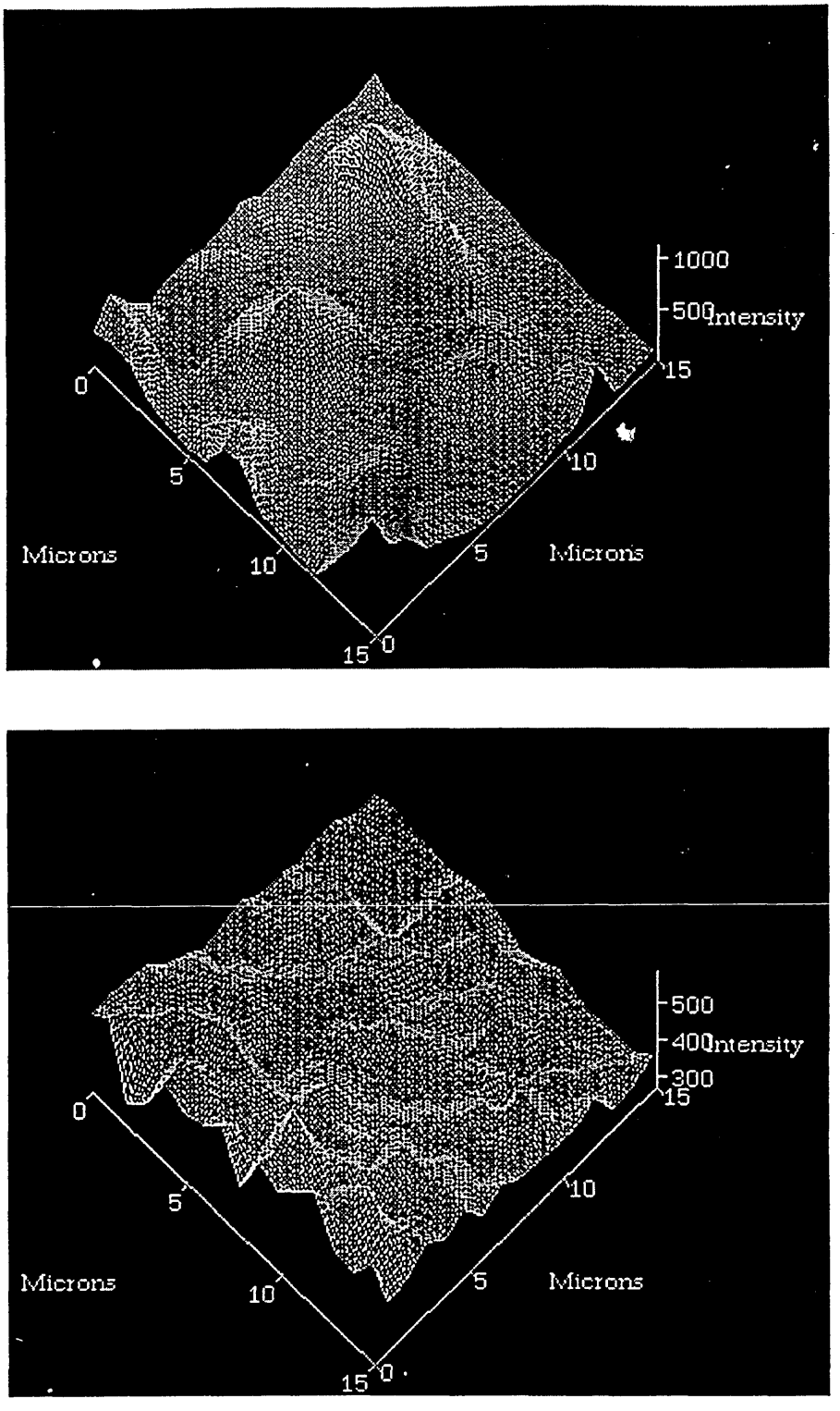

Figure 4.8: *3-D Raman map of (a) intensity of the nitrile band of PAN at 2244 cm^{-1} and (b) intensity of the band corresponding to PVOH at 854 cm^{-1}.*

It is clear from this figure that the maximum change in the band width of the nitrile band is found at the interfacial borders of the PAN particles with PVOH background. This agrees well with broadening of the same band at the interfacial region in the PVOH/PAN laminate which was investigated by depth profiling.

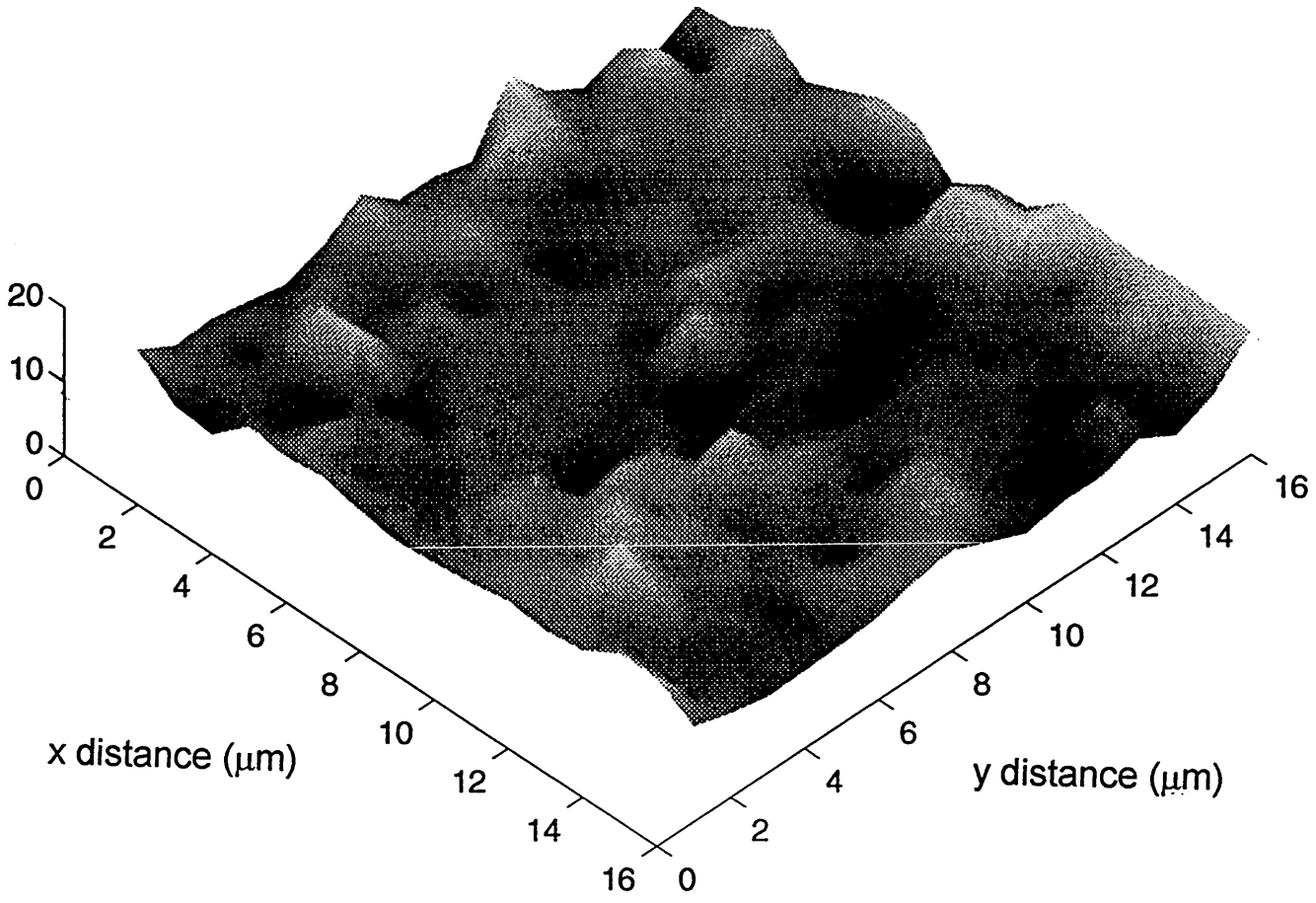

Figure 4.9: 3-D map of changes in the width of υ(C≡N) band in a selected area of PAN-PVOH blend.

4.3.3. Raman Confocal mapping of interfacial region in PMMA/PVOH

In the previous chapter a depth profiling study of PVOH/PMMA laminates using Raman confocal microspectroscopy was described and it was shown that it is possible to determine the interaction at the interfacial region. However, the depth profiling study did not provide any information about the distribution of the constituent polymers at the interfacial plane.

In order to obtain such information, Raman confocal microspectroscopy was applied and a map of the PMMA characteristic band at 813 cm^{-1} was recorded. In order to do this the experiment was carried out in the following steps: (a) the Ramascope was set up in confocal mode and then a depth profile of a PVOH/PMMA laminate was obtained. This determines the position of the interfacial region in the depth of the laminate. (b) the microscope was focused on the interfacial region in order to capture the scattered light only corresponding to this region and, (c) a map of a selected area was obtained as described before. Figure 4.10 shows the map of intensity of PMMA band for the selected area at the interfacial region. This figure shows an even distribution of the PMMA film at the interfacial region. The polymer chains of the constituent films are expected to be in relatively the same environment at this region.

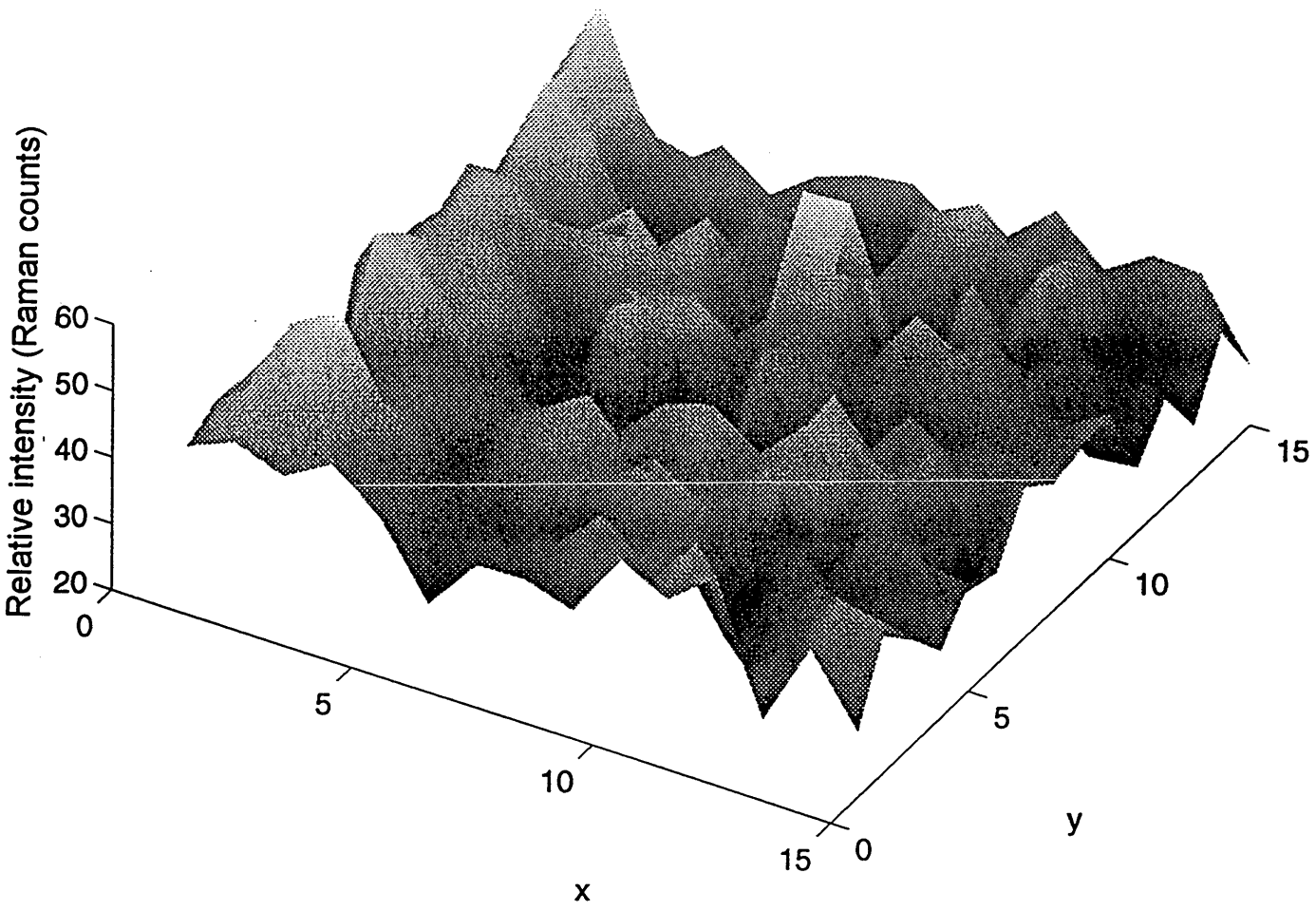

Figure 4.10: 3-D map of intensity of PMMA band at 813 cm^{-1} at a depth of 10 μm corresponding to the interfacial region in a PMMA/PVOH laminate.

CHAPTER 5

5.1. Introduction

Shortage of water in many parts of the world is an increasing threat to many human societies. This problem is certain to become more serious in the next few decades with the overriding need for water in raising the standard of life, in industrialisation and most importantly in the production of food for the increasing world population.

It is known that transport or storage of water is expensive. On this basis, in recent years intensive research has been directed towards obtaining potable water from brackish or sea-water [5.1-5.3] by forcing this through a semi-permeable polymer membrane against the osmotic pressure. The reason for this is due to economic advantages associated with this method of separation in comparison to conventional separation techniques such as centrifugation, extraction and distillation.

5.2. Polymeric membranes

Naturally occurring polymers, such as cellulose have been utilised for many centuries in macrofiltration. However, the history of synthetic polymeric membranes began by

invention of cellulose nitrate by Schönbein in 1846. This was followed by Fick in 1855 utilising cellulose nitrate to perform his *Über Diffusion*. Since than many different synthetic polymeric membranes have been developed and investigated.

Polysulfone (PS) and polyether sulfone (PES) are amongst the most popular synthetic polymeric membranes. Both PS and PES have some properties which qualify them as outstanding polymeric membranes. These include high Tg (PS = 195 ^{o}C and PES = 230 ^{o}C), thermal and oxidative stability, an amorphous glassy state, good strength and flexibility, resistance to extremes of pH, and low creep even at elevated temperatures. These two polymers are Lewis bases and soluble in protic solvents such as chloroform, methyl chloride and formic acid and also soluble in polar solvents including dimethylacetamide (DMAC), 1-methyl-2-pyrrolidonone, (NMP), dimethylformamide (DMF), and dimethylsulfoxide (DMSO).

The chemical and physical structure of the polymeric membranes are important factors in their permeation ability. By chemical structure is meant the combination of steric and polar properties of polymeric membranes at the molecular level. This includes chain segments and functional groups. A number of factors can affect the packing density and hence the permeability of these separation membranes. These include the kinetics of gelation (solidification), physical ageing and so on. Some of these factors are intrinsic to the polymer molecules themselves.

An important example of this is the nature of side groups attached to the polymer backbone which act as spacers. It is known [5.4] that the size and shape of the side groups determine polymer characteristics such as packing density, the rigidity of polymer chain segments and the accessibility, and thus participation of functional groups in membrane-

permeant interaction. On the other hand maximum packing density and crystalline order can occur as a result of the absence of such side groups.

This can be shown by a comparison of polyethersulfone (PES) and polysulfone (PS) [5.4]. In PES monomers are

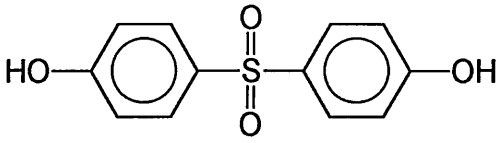

and as a result of this PES has a regular structure

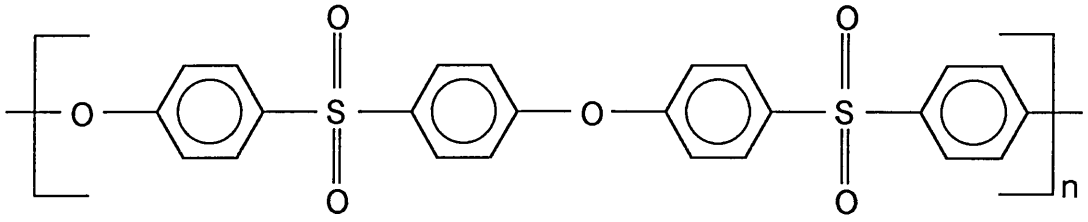

whereas in the case of polysulfone, one monomer is based on the sodium salt of bisphenol A,

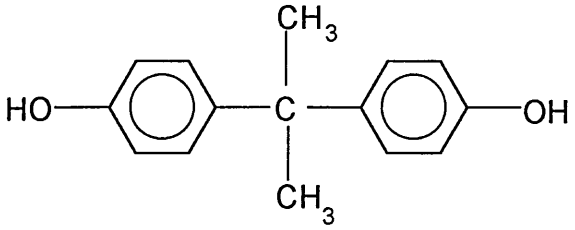

and the other one is the same as that of the monomers of PES. Thus the structure of PS is

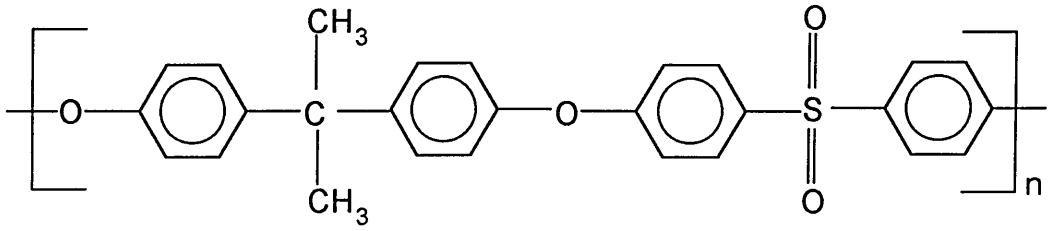

As a result of this PS has less structural regularity than PES. In addition the greater size of aliphatic isopropylidene group [-C(CH_3)$_2$] and its low polarity makes the polymer more mobile than PES. This greater degree of regularity in PES gives it more packing density and as a result this PES contain less free volume in its matrix and thus it shows less permeability.

The high degree of resonance stabilisation in these polymer structures is due to attachment of sulfone groups to phenyl rings in which aromatic ring π electrons can be withdrawn by the sulfone group. As a result of this the polymeric membrane has increased thermal and oxidative resistance property.

The resonance stabilisation has also a planar configuration and increased bond effects which contributes to the rigidity even at elevated temperatures. The toughness of the polymer is a result of the presence of the ether groups in the backbone which make the polymer more flexible. The presence of aromatic moieties make the polymeric membrane more resistant to high-energy irradiation.

As a result of having aromatic rings small amounts of ionic moieties groups can be incorporated into the organic polymer backbone and thus an ionomer is formed. Common functionalities for cation exchange membranes are $-SO_3^-$ and $-COO^-$. These hydrophilic groups are responsible for the swelling of the polymer network on exposure to water. An example of such ionomers is a random copolymer known as sulphonated polyetherethersulfone/polyethersulfone, SPEES/PES with the following structure:

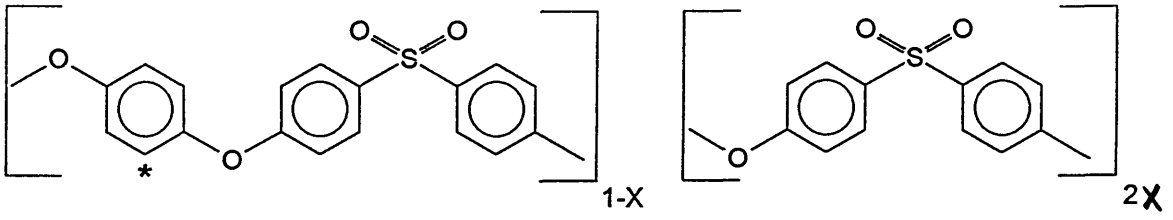

* = Hydroquinone residue where the sulphonation occurs.

X = 0.05 - 0.80

A structural feature of ionomers is that the ionic groups tend to cluster [5.5]. In the first instance ion pairs are formed. At higher concentrations, ion pairs transform into multiplets and then into hydrophilic clusters embedded in the hydrophobic organic phase.

5.3. Water in polymeric membrane

The behaviour of water when incorporated into a host matrix such as a polymer, is significantly different from normal water. Stillinger [5.6] argues that boundaries and interfaces in the host matrix can affect the water phase transitions by reducing the number of degrees of freedom in a way that disrupts the natural order of pure water in the bulk. Furthermore, these spatial constraints also lead to clustering.

Many researchers have noted different types of water in the host matrix. As an example, Haly [5.7] reports eight distinguishably different types of water in one hydrated system. These types of water have been described as 'tightly bound', 'loosely bound', 'free', ' freezable', 'non-freezable', 'intermediate', associated' and 'interfacial' water. Falk [5.8] has investigated the state of water in perfluorosulfonate, Nafion membranes using infrared spectroscopy. Based on this study he concludes that (a) hydrogen bonding of water in fully hydrated Nafion is considerably weaker than in liquid water at the same temperature, (b) a substantial proportion of water molecules have one OH (or occasionally both OH groups) exposed to the fluorocarbon environment, and (c) water absorbed in Nafion appears to be in a state quite unlike the liquid phase and may be expected to have physical properties widely different from those of water in aqueous solution of electrolytes.

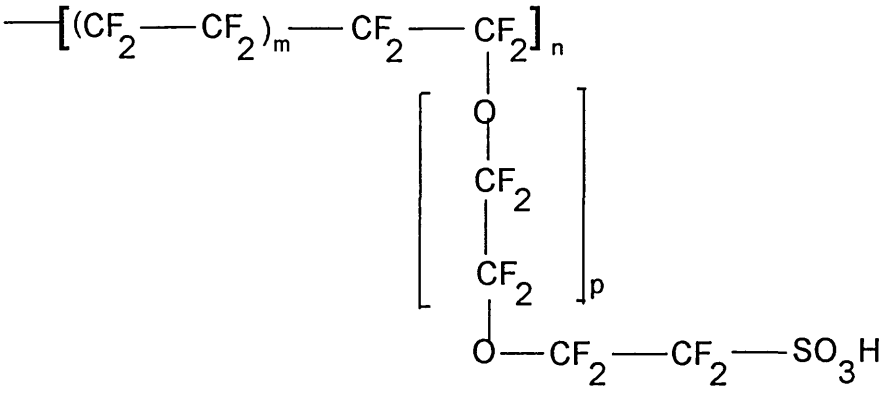

(m=5-13.5, n=~1000, p=1, 2, 3, ...)

Structure of Nafion

Introduction of water into an ion exchange membrane can result in swelling of the polymer matrix. The interaction between the organic polymer backbone and the cations is endothermic and may reduce the rate of swelling. The strongly exothermic tendency of the counterions and ionogenic side chains to hydrate also results in the initially bound water molecules (in ionic solvation shells) causing little or no volume expansion of the network. When the membrane is dry the counterions are strongly bound by electrostatic forces in contact with ion pairs. However, if the water uptake proceeds, it results in moving the association-dissociation equilibrium between bound and unbound counterions and increases the counterion mobility. Additional water has a tendency to dilute the network of polymer and this provides the driving force for swelling of the matrix.

Swelling can be influenced by the nature of the counterions. This is due to (a) increasing hydration capacity of the counterion resulting in increased water uptake. The following order is true for alkali counterions [5.5]:

$$Li^+ > Na^+ > K^+ > Rb^+ > Cs^+$$

In addition, swelling reduces as the valency increases. This is due to the formation of ionic crosslinks and the reduction in hydration capacity by the formation of triplet association such as:

$$—SO_3^-\cdots Ca^{++}\cdots SO_3^-—$$

(b) As the association-dissociation equilibrium between bound and unbound counterions shifts to more dissociation (by allowing for a more complete hydration shell formation), the internal osmotic pressure in the polymer is enhanced.

Water uptake is comparatively less if instead of pure water, an ionic solution is introduced into the polymer. This is due to (a) lower external water activity, a_w (<1), and (b) distribution of the dissolved ions across the membrane-solution interface. Donnan [5.9, 5.10] as early as 1911 explained the overall features of electrolyte uptake by ion exchange membranes.

SPEES/PES or Nafion in the salt form have pendent groups of $—SO_3^- X^+$ in their structure, where X is an exchangeable cation. Mauritz and Lowry [5.11, 5.12] using Fourier transform infrared spectroscopy, FTIR and Komoroski and Mauritz [5.13, 5.14] using nuclear magnetic resonance spectroscopy, NMR have monitored the association of the counterion with the sulfonate moieties in Nafion membranes in the salt form. FTIR studies [5.11] have revealed that the SO_3^- symmetric stretching mode (~ 1060 cm^{-1}) is significantly affected by the H_2O/SO_3^- molar ratio as well as the monovalent counterion radius. It has been observed that this band broadens and shifts to higher frequencies with

decreasing water content, and the magnitudes of the shift diminishes with increasing bare ionic size for the series $Rb^+ \rangle K^+ \rangle Na^+ \rangle Li^+$.

5.4. Diffusion of water into polymer

The process in which matter is transported as a result of random molecular motions from one part of system to another is called diffusion. The motion of a single molecule is random and has no preferred direction of motion. On this basis it is sometimes referred to as the 'random walk'. Although the direction of movement of the molecule cannot be predicted, it is possible to calculate the mean-square distance travelled in a given interval of time. However, the overall observation is that the molecules transfer from regions of higher to that of lower concentrations.

In 1855 Fick noted that transfer of heat by conduction is also due to random molecular motion and by adopting the mathematical equation of heat conduction derived earlier by Fourier (1822) put diffusion on a quantitative basis. He showed that diffusion of an isotropic substance can be described by;

$$\mathbf{F} = -\mathbf{D}\frac{\partial \mathbf{C}}{\partial \mathbf{x}} \qquad (5.1)$$

Where C is the concentration of diffusing substance, F is the rate of transfer per unit area of section, x is the space coordinate measured normal to the section, and D is diffusion coefficient. Based on this equation the rate of transfer of the diffusing molecule through unit area of a section is proportional to the concentration gradient measured normal to the section. It is clear that according to equation 5.1, D has the unit of $(length)^2/time$ (e.g. cm^2s^{-1}) providing the unit for F is considered as mass (e.g. gram) per unit time (e.g.

second) and the unit of C has the same unit of mass to that of F. Since the diffusion occurs in the direction opposite to that of increasing concentration, a negative sign is used. The fundamental differential equation of diffusion can then be drived from equation 5.1 resulting the following equation [6.15].

$$\frac{\partial C}{\partial t} = D\frac{\partial^2 C}{\partial x^2} \qquad (5.2)$$

Equations 5.1 and 5.2 are known as Fick's first and second law respectively. Equation 5.2 shows that the rate of change of concentration is proportional to the curvature (the second derivative) of the concentration with respect to distance. If the curvature is zero, then the concentration is constant in time.

5.5. Diffusion behaviour

The glass transition temperature is described as the temperature that the state of polymer changes from glassy to rubbery state, at a given concentration. The mechanical relaxation times decrease with increasing temperature and concentration of diffusing molecules and motion of the polymer segments are enhanced. When a penetrant diffuses into a rubbery polymer above its glass temperature, a rapid adjustment of the polymer chains occurs, and as a result, a Fickian behaviour is exhibited. However, not all the polymers behave in the same way and they have a broad range of mechanical relaxations associated with structural changes. In general, diffusion can be categorised into three classes [5.16]. (see below)

The amount of the molecules diffused at time t in a plane sheet is described by the following equation;

$$\frac{M_t}{M_\infty} = \frac{4}{L}\left(\frac{Dt}{\pi}\right)^n \qquad (5.3)$$

Equation 5.3 can also be written as;

$$Log\left(\frac{M_t}{M_\infty}\right) = Log\left(\frac{4}{L}\right) + nLog\left(\frac{D}{\pi}\right) + nLog(t) \qquad (5.4)$$

where M_t and M_∞ are the amount of material transported at time t and at equilibrium respectively, L is the film thickness and D is diffusion coefficient.

(a) Case I or Fickian diffusion: The rate of diffusion is much less than that of mechanical relaxation time. Case I is an extreme with respect to the shape of the sorption-time curve with n=0.5. These systems are controlled by the diffusion coefficient and as such behaviour of these systems can be described by a single parameter. The movement of the diffusant is without any interactions and is simply based on a random walk.

The characteristic features of sorption and desorption-time curves for Fickian diffusion can be listed as [5.17]:

(I) In a semi-infinite medium, in the early stages, when diffusion takes place the amount sorbed or desorbed is directly proportional to the square root of time. The linear behaviour is approximately up to 50 per cent of the final equilibrium uptake.

(II) The plot of sorption and desorption against square root of time after initial linear part becomes concave towards the $(time)^{1/2}$ axis, and steadily approach the final equilibrium value.

(III) When the diffusion coefficient increases with increasing concentration throughout the relevant range of concentration, desorption is always slower than sorption, and conversely if D decreases with concentration increasing, desorption is faster.

(b) Case II diffusion: This is the other extreme; i.e. the rate of diffusion is faster than that of the mechanical relaxation process. This system can also be described by a single parameter (equation 5.3) with n=1. In this case, the parameter of interest is the constant velocity of the advancing front of liquid located at the boundary between swollen gel and glassy core. If the mechanical properties of the two stages are sufficiently different, fracture can occur in the glassy core.

In this diffusion mode strong interactions between the diffusant and the polymer may occur. Some of the diffusing molecules are either precipitated or form a new immobile chemical compound in a chemical reaction and, as a result of this they are immobilised and can not diffuse into the polymer matrix. These immobilisation processes are very rapid compared to the rate of diffusion and the regions in which all the sites are occupied or unoccupied respectively are separated by a sharp boundary.

(c) Case III or Non-Fickian or anomalous diffusion: The rates of diffusion and mechanical relaxation are comparable. Two or more parameters are needed to describe this behaviour. The value of n is between 0.5 and 1, or changes sigmoidally from one to another. This system lies between case I and II. In general, all the cases that cannot be described by case I and II are classified as case III.

Changes in polymer structure on solubility and diffusional mobility or internal stresses exerted by one part of the medium on another as diffusion proceeds can be the causes of anomalous behaviour.

Non-Fickian diffusion usually has been observed for so called glassy polymers. Fick's law describes the diffusion behaviour by a concentration-dependent form with constant boundary conditions. However, this is not an adequate description for glassy polymers. One of the reasons for this is the swelling of polymer due to penetration of diffusing species. In contrast to glassyones, 'rubbery polymers' do show Fickian behaviour. This is due to rapid responses of a rubbery polymer to any changes in environment, whereas glassy polymers respond relatively slower to these changes. On this basis it is believed that any response in a glassy polymer is time-dependent.

5.5.1. Effect of surface concentration on diffusion coefficient

Changes in the diffusion coefficient [5.17] are considered to occur in two stages. The increased ease of polymer segmental motion due to increasing the solvent concentration, leads to an immediate increase in the diffusion coefficient. A further stage of diffusion coefficient increase is then thought to occur over a period of time as a result of the relaxation processes, characteristic of the glassy state.

As a consequence of these two effects, the value of the diffusion coefficient in any element of a polymer penetrant system at a given time will be "history dependent", This means that the diffusion coefficient will depend on the concentration history of the element.
The simplest interpretation of the two-stage sorption is that a quasi-equilibrium (approximate equilibrium) is rapidly reached at the polymer surface and this is followed by the establishment of the same equilibrium concentration of diffusing material throughout the polymer sheet by simple diffusion. The second stage of the sorption then results from an increase in surface concentration, which occurs slowly relative to the diffusion rate, and so the concentration throughout the whole of the polymer sheet increases with time at a rate that is independent of the thickness of the polymer sheet.

5.6. SORPTION

5.6.1. Dual mode sorption theory

Gas sorption isotherms for rubbery polymers at modest pressures are linear [Reimers 5.18], however, below the glass-transition temperature, Tg, these isotherms become increasingly non-linear and are convex to the pressure axis. This behaviour was first explained by Barrer et al [5.19] who proposed a dual mode sorption model. Since then many researchers have found that this model can successfully explain their observed data.

As a glassy polymer is cooled through the glass transition temperature, the micro-Brownian motion of at least some fraction of the polymer chains is drastically slowed down. As a result of this a number of gaps will be frozen out in the glassy polymer which are called 'microvoids'. These microcavities have not been seen [5.20], and it is assumed that they must exist only at molecular level. On this basis, glassy polymers are heterogeneous on the molecular scale [5.20]. When small solute molecules are introduced into the system, they spend most of the time rattling about in these cages, till one key polymer segment moves under thermal vibration to let the molecule out. It was originally assumed that these adsorbed molecules are totally immobilised but later Petropoulos [5.21] and Koros et al [5.22, 5.23] showed that these species are only partially immobilised.

The solubility of these adsorbed molecules into relatively immobile sites, which can saturate, is approximately described by a Langmuir isotherm. The following equation describes the Langmuir isotherm for gas molecules dissolved in a glassy polymer at an equilibrium pressure, p.

$$C_H = \frac{C_H' bp}{1+bp} \qquad (5.5)$$

where C_H is the penetrant concentration in microcavities or 'holes' in the polymer matrix, C_H' is the saturation concentration of the penetrant species in the microvoids and b is a 'hole-affinity' constant.

On the other hand the penetrant molecule can be sorbed into a volume region, large enough to accommodate it, surrounded relatively intimately, primarily by chain segments of chains whose micro-Brownian motion is not frozen out. These type of penetrant molecules are much more mobile than those molecules surrounded by segments stemming from chains whose backbone is frozen out.

The solubility of these absorbed and totally mobile species is represented by Henry's law. The dependence of the penetrant concentration in the polymer due to ordinary dissolution, C_D on pressure is given by relation:

$$\mathbf{C_D = k_D P} \qquad (5.6)$$

Where k_D is the solubility coefficient in the Henry's law limit (the reciprocal of Henry's law constant).

The dual sorption model postulates that the total concentration, C of a penetrant gas in a glassy polymer is the sum of the above contributions:

$$\mathbf{C = C_D + C_H} \qquad (5.7)$$

Thus by substituting the values of C_D and C_H from equations (5.5) and (5.6) into equation (5.7) the relation for the total amount of solute sorbed by both mechanisms is given:

$$C = k_D P + \frac{C_H' bp}{1 + bp} \qquad (5.8)$$

It should be noted that a local equilibrium between the absorbed and adsorbed populations is maintained through the polymer matrix [5.24]. The total sorbed concentration tends towards the limit of Henry's law as the pressure increases.

A number of researchers have used the dual mode sorption model to describe the studies of the sorption and equilibrium for CO_2 in a polyamide film for pressures up to 0.78 atm [5.25], the permeability of CO_2 through kapton polyamide for pressures up to 16.3 atm [5.26], sorption of water by an amorphous polyamide [5.27], CO_2 sorption and transport in polycarbonate [5.28, 5.29], the gas sorption behaviour of CO_2, C_2H_6 and CH_4 into polyethersulfone and polyhydroxyether [5.18], the sorption of CO_2, O_2 and N_2 into polyethersulfone [5.30], sorption of CO_2, N_2 and He gases below 1 atm into polyimide films [5.31, 5.32], diffusion of 2,4-dinitroaniline and non-ionic azo dyes in nylon-6 film [5.33], transport of water in poly(acrylonitrile) [5.34], diffusion in glasses [5.35 5.36], diffusion in textile fibers [5.37 5.38] and enzyme membranes [5.39], drug transport in skin [5.40] and water clustering in reverse osmosis [5.41]

5.7. Study of diffusion by experimental techniques

A number of experimental techniques have been devised to study diffusion processes. These include permeation methods [5.42], optical detection of chemical labels, Park [5.43 5.44], sorption and desorption kinetics [5.42], mass label detection using Rutherford backscattering [5.45], concentration-distance curves [5.42] radioactive labels [5.43 - 5.45], nuclear magnetic resonance [5.46], Raman microprobe spectroscopy [5.47], laser interferometry [5.47], capillary column inverse gas chromatography [5.48], mechanical

measurement of thickness changing as a function of swelling [5.49-5.51], birefringence [5.46], UV absorption [5.46], rotating-polariser ellipsometry [5.52], absorbance of thin layers [5.52], and Fourier transform infrared-attenuated total reflection spectroscopy [5.53-5.63].

The method of sorption is one of the most common techniques used to investigate the diffusion of small molecules in polymers. In this method, if the concentrations just within the surface of a plane sheet are maintained constant, the amount of diffusant, M_t taken up by the sheet in a time t, is given by the following equation.

$$\frac{\mathbf{M_t}}{\mathbf{M_\infty}} = 1 - \sum_{n=0}^{\infty} \frac{8}{(2n+1)^2 \pi^2} \exp\left(\frac{-D(2n+1)^2 \pi^2 t}{4L^2}\right) \qquad (5.9)$$

Where L is the thickness of the sheet, M_∞ is the equilibrium sorption attained theoretically after infinite time, and D is diffusion coefficient. For short-times, equation 5.7 can be rewritten as;

$$\frac{\mathbf{M_t}}{\mathbf{M_\infty}} = \frac{2}{L}\left(\frac{D}{\pi}\right)^{0.5} t^{0.5} \qquad (5.10)$$

The thickness of the film in equation 5.10 is 2L and the value of the diffusion coefficient can be deduced by determining the initial gradient of a graph of straight line of M_t/M_∞ as a function of $t^{0.5}$. Using equation 5.10 instead of equation 5.9 results in some error and it is of the order of 0.1 % [5.43]. Equation 5.9 can be rewritten in order to simplify calculation of diffusion coefficient for long-times.

$$\frac{M_t}{M_\infty} = 1 - \frac{8}{\pi^2}\exp\left(\frac{-D\pi^2 t}{4L^2}\right) \qquad (5.11)$$

or

$$\ln\left(1 - \frac{M_t}{M_\infty}\right) = \ln\left(\frac{8}{\pi^2}\right) - \frac{D\pi^2 t}{4L^2} \qquad (5.12)$$

In general, the above techniques can be used to measure the diffusion coefficient of a solute by monitoring either the release from, uptake into, or permeation through a polymer layer. One of disadvantages of some of these techniques is that they require periodic sampling, and subsequent analysis by spectroscopic, chromatographic, or radiometric methods to identify and quantify the concentration of the permeant molecule in a polymer film.

In contrast, Fourier transform infrared attenuated total reflection spectroscopy (FTIR-ATR) can provide a unique method of direct identification and quantification of concentration of the diffusion of permeant molecules into polymer films *in situ*. In addition, this technique can provide information about the diffusion of all the diffusing species simultaneously providing they have detectable and distinguishable infrared bands.

The FTIR-ATR technique has been utilised by a number of researchers to study the mutual diffusion of small molecules in polymer films. Fieldson and Barbari demonstrated the application of this technique to measure diffusion of liquid water in polyacrylonitrile [5.52], and to study acetone-polypropylene, methanol-polystyrene and methanol-poly(methyl methacrylate) systems [5.54], The mutual diffusion of small molecules in

polymer films studied by Hemmelmann and Brandt [5.55, 5.56], Cogan et al [5.57] and Xu et al [5.58] and in gels by Wurster et al [5.59], Pereira and Yarwood studied the diffusion of liquid water in sulphonated polyethersulfone films [5.60], Kuzmenka and Granick investigated kinetics of polymer absorption at the solid-liquid interface[5.61], Rosenberg and Kellner determined diffusion coefficients of diffusion of carbohydratesxin photocrosslinkable polyvinylalcohol [5.62]

5.7.1. Application of FTIR-ATR spectroscopy to diffusion in polymers

Principles and theory of FTIR-ATR spectroscopy have been described in chapter 1. In this section, the use of this technique for obtaining information about diffusion of small molecules in polymers is presented.

As was explained earlier, Fick's second law for diffusion of 1-D diffusion in a layer with a constant diffusion coefficient is as follows;

$$\frac{\partial C}{\partial t} = D\frac{\partial^2 C}{\partial Z^2} \qquad (5.2)$$

The boundary conditions for a region of $-L < x < L$ with an initial uniform concentration, C_0 and a constant concentration at the surface, C_L are:

$$C = 0 \qquad \text{at } t < 0 \; ; \; 0 \leq z \leq L$$

$$C = CL \qquad \text{at } t \geq 0; \; z = L$$

$$\partial C / \partial z \qquad \text{at } t \geq 0; \; z = 0$$

Equation 5.2 can be solved for these boundary conditions giving;

$$\frac{C-C_0}{C_L-C_0}=1-\frac{4}{\pi}\sum_{n=0}^{\infty}\frac{(-1)^n}{2n+1}\exp\left(\frac{-D(2n+1)^2\pi^2 t}{4L^2}\right)\times\cos\left(\frac{(2n+1)\pi z}{2L}\right) \qquad (5.13)$$

The mass of sorbed penetrant in sorption kinetic experiments, is measured as a function of time. The equation 5.13 can be integrated over the thickness of the film to give the sorbed mass. The result of the integration is (equation 5.9):

$$\frac{M_t}{M_\infty}=1-\sum_{n=0}^{\infty}\frac{8}{(2n+1)^2\pi^2}\exp\left(\frac{-D(2n+1)^2\pi^2 t}{4L^2}\right) \qquad (5.9)$$

Where M_t is the mass sorbed at time t, and M_∞ is the mass sorbed at equilibrium.

In FTIR transmission spectroscopy at low absorbances, the relationship between the absorption of electromagnetic waves and the quantity of the absorbing material is expressed by the Beer-Lambert law given by:

$$dI=\alpha I dz=-\varepsilon C I dz \qquad (5.14)$$

Where α is the absorption coefficient, ε is the molar extinction coefficient, I is the light intensity at position z, and C is the concentration of absorbing group. The above equation can be integrated to give:

$$A=-\ln\left\{\frac{I}{I_0}\right\}=\int_{-l}^{l}\varepsilon C dZ \qquad (5.15)$$

Where I_0 is the intensity of the incident light, I is the intensity of the transmitted light, A is the measured absorption, and $2L$ is the thickness over which the absorbing group is present. The absorbances given in equation 5.15 is analogous to the mass uptake in equation 5.9 since it involves an integration of the concentration profile over the film thickness.

However, the major disadvantage of using transmission spectroscopy to measure sorption kinetics in polymer samples with equation 5.15 is that it involves removing the polymer film from the penetrant bath and blotting prior to spectroscopic analysis.

In contrast to the transmission method, FTIR-ATR spectroscopy can provide information about the diffusion kinetics *in situ*. The details of this technique have been described in section 1.3. In ATR spectroscopy, the rarer medium absorbs specific frequencies of light in the evanescent wave, the reflection is frustrated and the reflected wave has a reduced intensity at these wavelenghts, resulting in an absorption spectrum. In order to combine the evanescent field strength equation with the Beer-Lambert law, it is necessary to assume that only weak absorption occurs. With this assumption:

$$\frac{\mathbf{I}}{\mathbf{I_0}} = \mathbf{e}^{-\mathbf{A}} \approx (1-\mathbf{A}) \qquad (5.16)$$

or

$$\mathbf{dI} = -\mathbf{I_0 dA} \qquad (5.17)$$

Substituting equation 5.17 into equation 5.15 and integrating gives:

$$\mathbf{A} = \int_0^{\mathbf{L}} \frac{\boldsymbol{\varepsilon}\mathbf{CI}}{\mathbf{I_0}} \mathbf{dz} \qquad (5.18)$$

Integration is from 0 to L. This is because in the ATR configuration, the diffusing molecule only enters the film from one side. The decay of the evanescent field is given by:

$$\mathbf{E} = \mathbf{E}_0 \exp\left[-\frac{2\mathbf{n}_2\pi\sqrt{\sin^2\theta - \left(\frac{\mathbf{n}_1}{\mathbf{n}_2}\right)^2}}{\lambda}\mathbf{z} \right] \qquad (5.19)$$

where E is the electric field strength at the interface, n_1 is the refractive index of the rarer medium and n_2 is the refractive index of the propagating medium. Since I = E2, the field strength of the evanescent wave (E) can be substituted. Thus rewriting the expression for multiple reflection, N, as:

$$\mathbf{A} = \int_0^L \mathbf{N}\varepsilon^*\mathbf{C}\mathbf{E}_0^2 \exp\left[-\frac{2\mathbf{n}_2\pi\sqrt{\sin^2\theta - \left(\frac{\mathbf{n}_1}{\mathbf{n}_2}\right)^2}}{\lambda}\mathbf{z} \right] \mathbf{dz} \qquad (5.20)$$

Where $\varepsilon^* = \varepsilon/I_0$. Substituting equation 5.13, into equation 5.20 and integrating gives:

$$\frac{\mathbf{A}_t - \mathbf{A}_0}{\mathbf{A}_\infty - \mathbf{A}_0} = 1 - \frac{8\gamma}{\pi\left[1-\exp(-2\gamma\mathbf{L})\right]} \times \sum_{n=0}^{\infty} \left\{ \frac{\exp\left(\frac{-\mathbf{D}(2\mathbf{n}+1)^2\pi^2\mathbf{t}}{4\mathbf{L}^2}\right)\left[\frac{(2\mathbf{n}+1)\pi}{2\mathbf{L}}\exp(-2\gamma\mathbf{L}) + (-1)^n(2\gamma)\right]}{(2\mathbf{n}+1)\left[4\gamma^2 + \left(\frac{(2\mathbf{n}+1)\pi}{2\mathbf{L}}\right)^2\right]} \right\}$$

(5.21)

Where $\gamma = \dfrac{2n_2\pi\sqrt{\sin^2\theta - \left(\dfrac{n_1}{n_2}\right)^2}}{\lambda}$

As was discussed earlier the diffusion process in glassy polymers is best described by a dual mode sorption model (see section 5.6.1.). In this model, it is assumed that one species is totally mobile and can diffuse into the polymer matrix freely and the other species is only partially mobile. Thus the expression for describing this model contains two diffusion coefficients for mobile and partially immobile species. Equation 5.22 describes the Fick's second law for partially mobile molecule when;

$$C_1(0) = x_2 C_0$$

and $$C_1(t=\infty) = x_1 C_\infty$$

$$\frac{\partial C_1}{\partial t} = D_1 \frac{\partial^2 C_1}{\partial z^2} \qquad (5.22)$$

where x_1 is related to the fraction of the partially mobile molecules. For totally mobile species when;

$$C_2(0) = x_2 C_0$$

and $$C_t(t=\infty) = x_2 C_\infty$$

$$\frac{\partial C_1}{\partial t} = D_2 \frac{\partial^2 C_1}{\partial z^2} \qquad (5.23)$$

where x_2 is related to the fraction of the totally mobile molecules and thus $x_1 + x_2 = 1$. The substitution of these boundary conditions into equation 5.21 gives equations 5.24 and 5.25 which are the expressions for the first and second sorption modes respectively [Pereira 5.60].

$$\frac{A_1 - x_1 A_0}{x_1(A_\infty - A_0)} = 1 - \frac{8\gamma}{\pi[1-\exp(-2\gamma L)]} \times \sum_{n=0}^{\infty} \left\{ \frac{\exp\left(\frac{-D_1(2n+1)^2\pi^2 t}{4L^2}\right)\left[\frac{(2n+1)\pi}{2L}\exp(-2\gamma L) + (-1)^n(2\gamma)\right]}{(2n+1)\left[4\gamma^2 + \left(\frac{(2n+1)\pi}{2L}\right)^2\right]} \right\}$$

(5.24)

$$\frac{A_2 - x_2 A_0}{x_2(A_\infty - A_0)} = 1 - \frac{8\gamma}{\pi[1-\exp(-2\gamma L)]} \times \sum_{n=0}^{\infty} \left\{ \frac{\exp\left(\frac{-D_2(2n+1)^2\pi^2 t}{4L^2}\right)\left[\frac{(2n+1)\pi}{2L}\exp(-2\gamma L) + (-1)^n(2\gamma)\right]}{(2n+1)\left[4\gamma^2 + \left(\frac{(2n+1)\pi}{2L}\right)^2\right]} \right\}$$

(5.25)

The total absorbance can be deduced by addition of A_1 and A_2 after rearrangement of equations 5.24 and 5.25. The value of A_∞ can also be determined by the same approach.

Parameters D_1 and D_2 can be calculated using the Levenberg-Marquardt least square method. This method is used when two adjustable parameters are to be determined and has become the standard approach for non-linear squares routines[5.63, 5.64]. In this method through the minimisation of the chi-squared merit function, χ^2, the value of diffusion coefficients and A_∞ are determined.

CHAPTER 6

6.1. Introduction

This chapter describes studies of diffusion of pure water into sulphonated polyetherether sulphone/polyethersulphone, SPEES/PES. This material is a copolymer with ion exchange capacity and is used as a polymeric ion exchange membrane. The characteristics of such materials, which are used as reverse osmosis membranes, have been described in chapter 5.

Fourier transform infrared attenuated total reflection spectroscopy, FTIR-ATR has been utilised to characterise the diffusion process. The main advantage of application of this technique is that the diffusion processes can be studied *in situ*. The theoretical background of this technique has been described in chapter 1.

6.2. Experimental

6.2.1. Chemicals

SPEES/PES was obtained from NWW Acumem Limited. This copolymer is synthesised as follows:

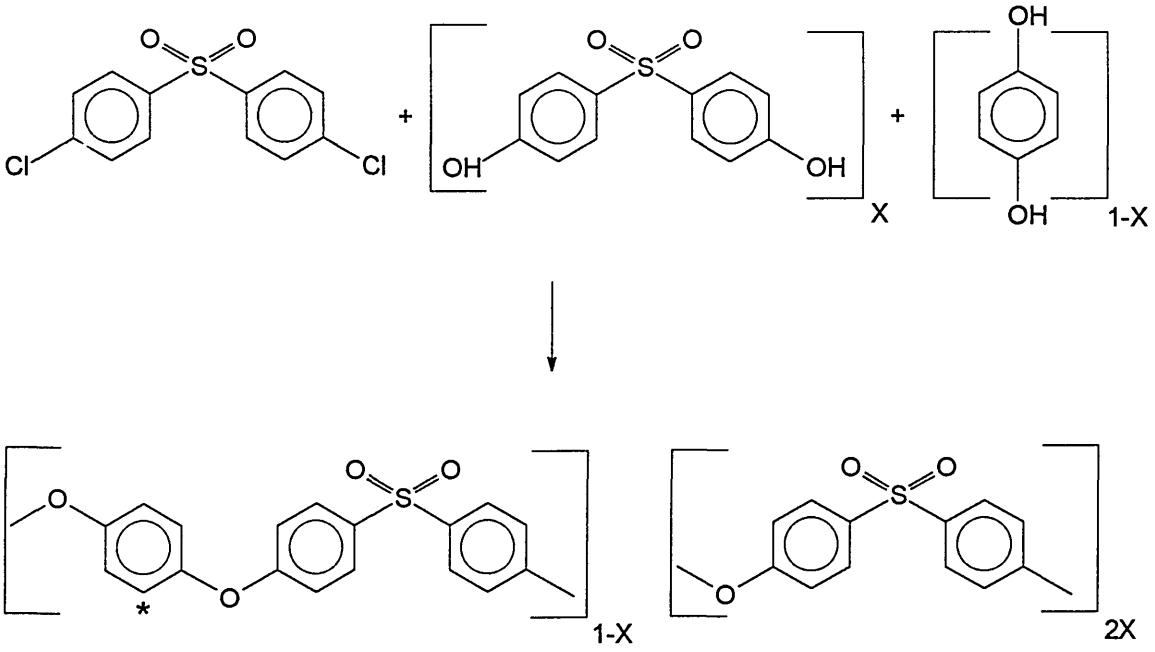

It sulphonates only at hydroquinone residue* so that ion exchange capacity of sulphonated polymer is pre-determined by copolymer composition. Sulphonation occurs in 98% H_2SO_4 without degradation. Degree of sulphonation is characterised by "S - No", Where

$$S = \frac{\text{No. of non-sulphonatable rings}}{\text{No. of sulphonatable rings}} = (2 + 2x)/(1-x)$$

The characteristics of copolymers which were used in this work are summarised in table 6.1.

Polymer (S-No)	Exchange Capacity (Eq/Kg)	Water Uptake (% weight)
S = 20	0.398	5.5
S = 8	0.894	12.7
S = 5	1.297	20.5

Table 6.1: *Characteristics of SPEES/PES copolymers.*

1-methyl-2-pyrrolidonone, NMP (99+%, HPLC grade), Dimethylformamide, DMF (99.9+%, HPLC grade) and polyacrylonitrile, PAN were obtained from Aldrich Chemical company. Deionised water (Millipore) was used for this work.

6.2.2. Sample preparation and spectroscopic measurements

The ATR crystals used in the experiments were polished ZnSe parallelepipeds, obtained from Spectra Tech Inc. The sampling surface of the crystals were 50 mm x 10 mm and they have a thickness of 6 mm. The normal vectors of the optical entry and exit faces were inclined at 45° to the sampling surfaces. The refractive index of ZnSe is 2.4. This material is insoluble in water and most organic solvents. It will, however, etch in both acidic and alkali solutions. The material is prone to oxidation from oxidising agents such as peroxides and hypochlorides to form an infrared absorbing layer of selenium dioxide. This will darken the surface of the crystal, sometimes appearing as a brown or purple film.[1.2]

Before each experiment, the crystals were cleaned by washing with acetone and methanol and then by refluxing in hot 2-propanol for at least 4 hours. The SPEES/PES polymer films were then deposited on ZnSe substrate by casting technique from 7% solution of

SPEES/PES desolved in NMP. The films were annealed at 65 °C for 24 hours. The thickness of each film was determined to be 10 μm within 5% accuracy using a surface profiler (Laser Form Talysurf).

Measurements of the infrared spectra were obtained using a Mattson Polaris Fourier transform infrared spectrometer. This instrument is fitted with a liquid nitrogen-cooled bullseye mercury-cadmium-telluride (MCT) detector. The spectrometer is controlled from a compatible PC running Mattson FIRST® software.

The film-coated crystal was mounted in a flow-through ATR cell obtained from Graseby Specac plc, as shown in figure 6.1. In the ATR cell, the solvent (water) was injected from one side of the cell and the excess of solvent is collected in a reservoir at the other side of the cell. All experiments were carried out at 25 °C. The exposed area of the polymer sample within the liquid cell is 6 mm x 42 mm.

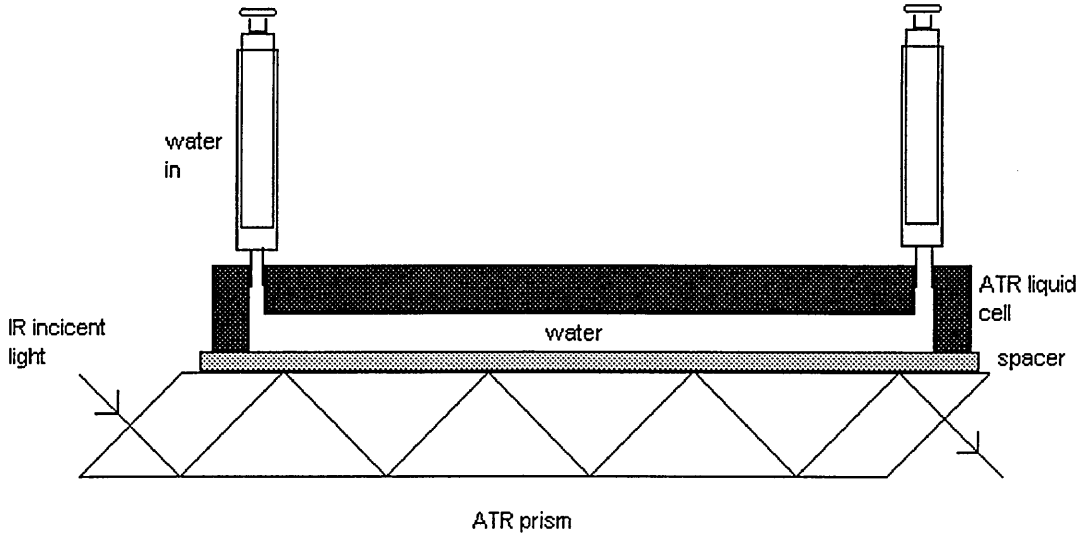

Figure 6.1: *Schematic diagram of side view of ATR cell*

The cell was placed in a variable angle macro ATR accessory. The entire assembly was then mounted in spectrometer sample compartment. The micro ATR was then aligned with rotating the second mirror of the holder and the final alignment was performed by maximising voltage at the MCT detector. In order to collect infrared spectra, first, a background spectrum of the dried film was taken as a reference. The subsequent sample spectra were then obtained using a macro program. In FTIR-spectroscopy, a spectrum with good signal to noise ratio is taken over a period of time which is called the sampling time. In a diffusion experiment, it should be noted that the first experimental data is not taken at time zero, but during the sampling time. In order to take this into account, the mean value of time was used for determining the diffusion coefficients. The parameters for infrared sampling are given in table 6.2

Resolution	4 cm^{-1}
scans per sample	10
signal gain	4
Apodisation	triangular
iris	98 %

Table 6.2: *FTIR spectrometer sampling parameters*

6.3. Results and discussion

6.3.1. Raman surface profile and SEM surface image of SPEES/PES film

The surface of a sample SPEES/PES film prepared by the above method was examined with Raman spectroscopy. Figure 6.2 shows a point by point image of surface of the film using confocal Raman microspectroscopy. The Raman mapping was carried out by setting the instrument in confocal mode (see section 2.4.2.) using a x50 objective, slit width of 12 μm and a CCD area of 4 x 576 pixels. In order to obtain a set of spectra for a chosen area of the sample, the microscope was focused on a point and the Raman spectrum of the

900 - 1200 cm^{-1} region containing the symmetric SO_2 stretching band of SPEES/PES was recorded. The intensity of this band was measured and the Raman map was then constructed. It is clear from the mapping image that the surface of the copolymer film is uniform.

The uniformity of the surface of the films was also examined by scanning electron microscopy, SEM using a 10 kV beam. The polymer film was first coated with a thin carbon layer. Figure 6.3 shows the SEM image of a 2 μm SPEES/PES film on ZnSe ATR prism. It is apparent from this image that in some areas of the film, small clusters of "needle shape" species are present. In order to determine the chemical composition of these clusters, X-ray analysis was employed. Figure 6.4 shows the results of the X-ray analysis. It is clear that one of the main constituent elements of the needle clusters is selenium and one of the main elements present in the polymer matrix background is sulphur from SPEES/PES film. One possible reason for presence of such needle clusters is due to defects in the surface of the ZnSe ATR prism or dissolution of ZnSe.

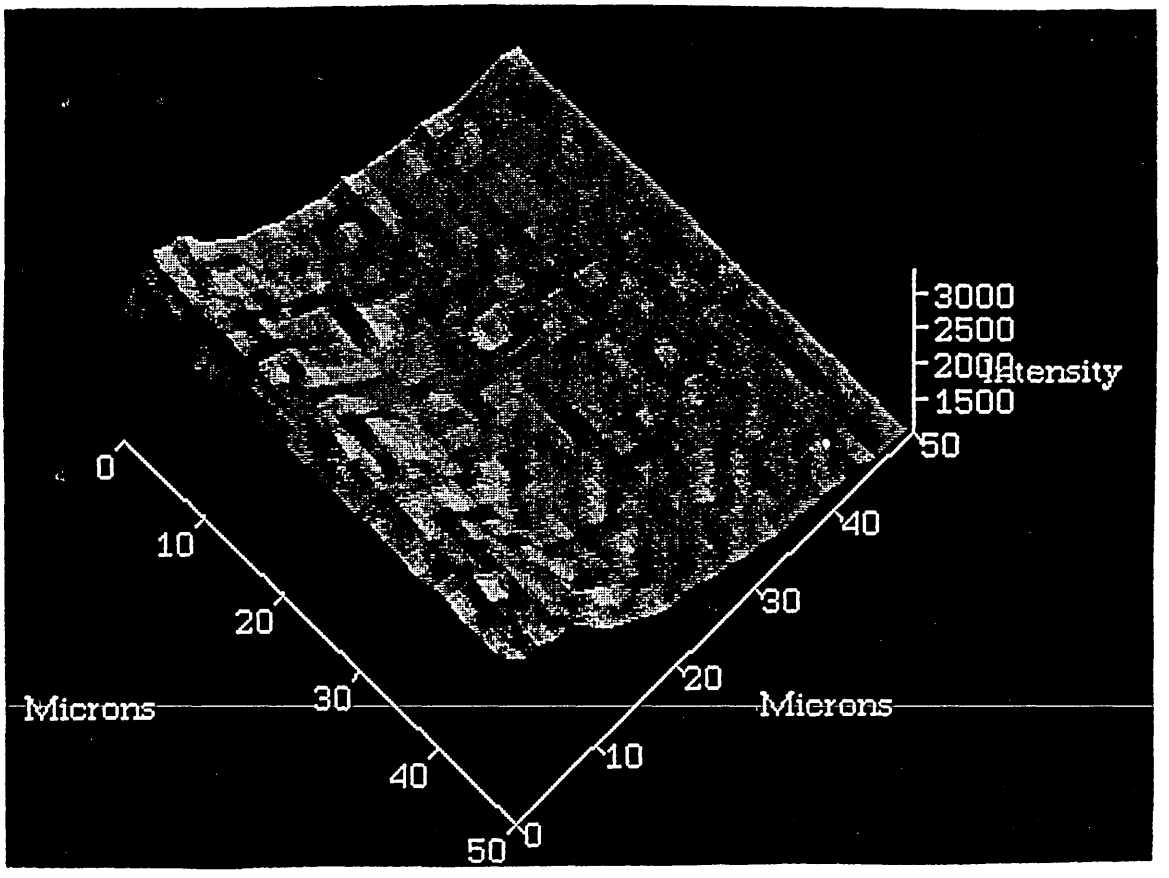

Figure 6.2: A 3-D Raman map of intensity of SPEES/PES band at 1145 cm^{-1}

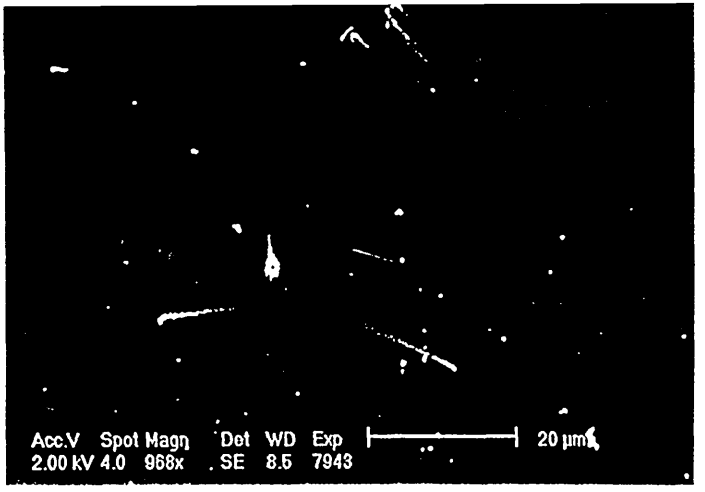

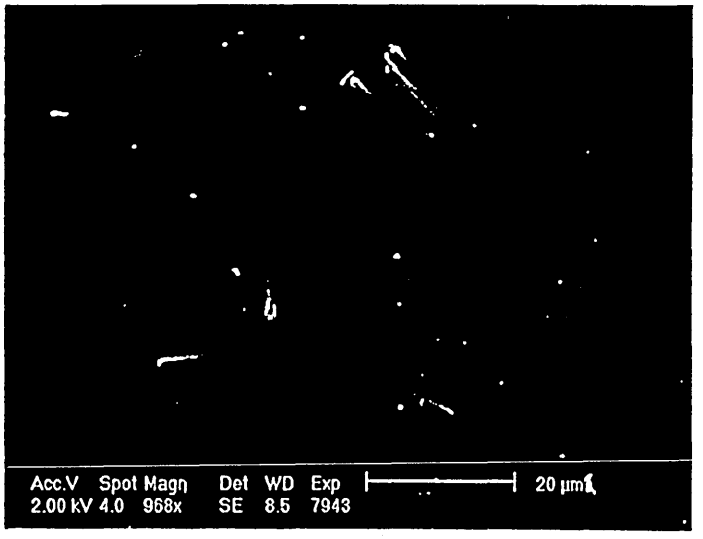

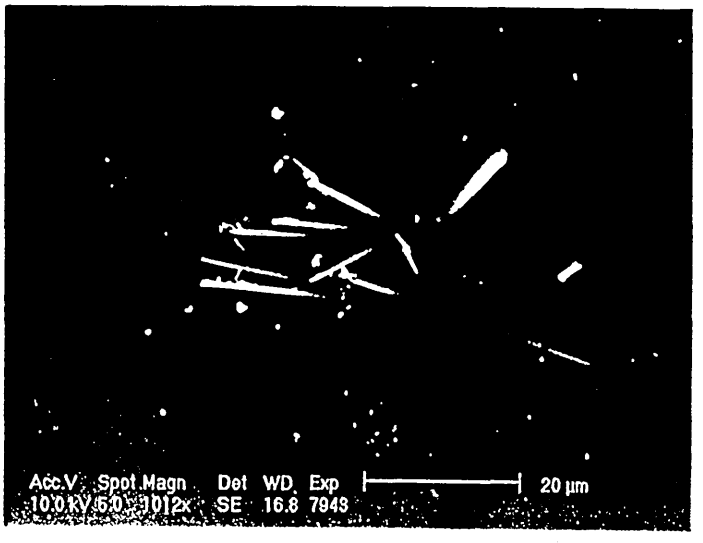

Figure 6.3: SEM image of surface of SPEES/PES film

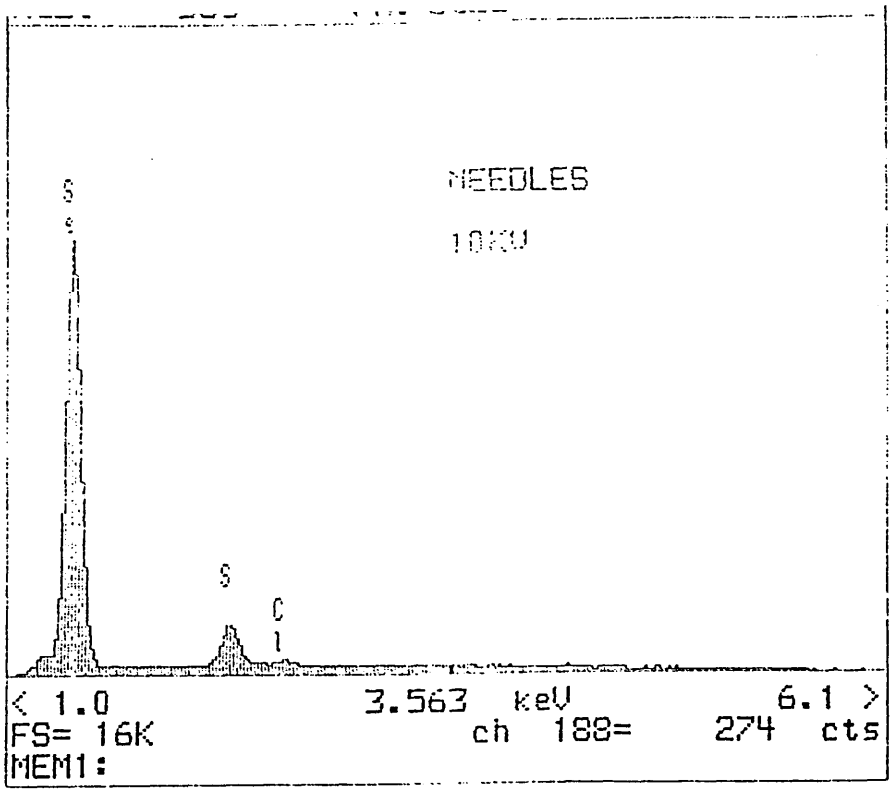

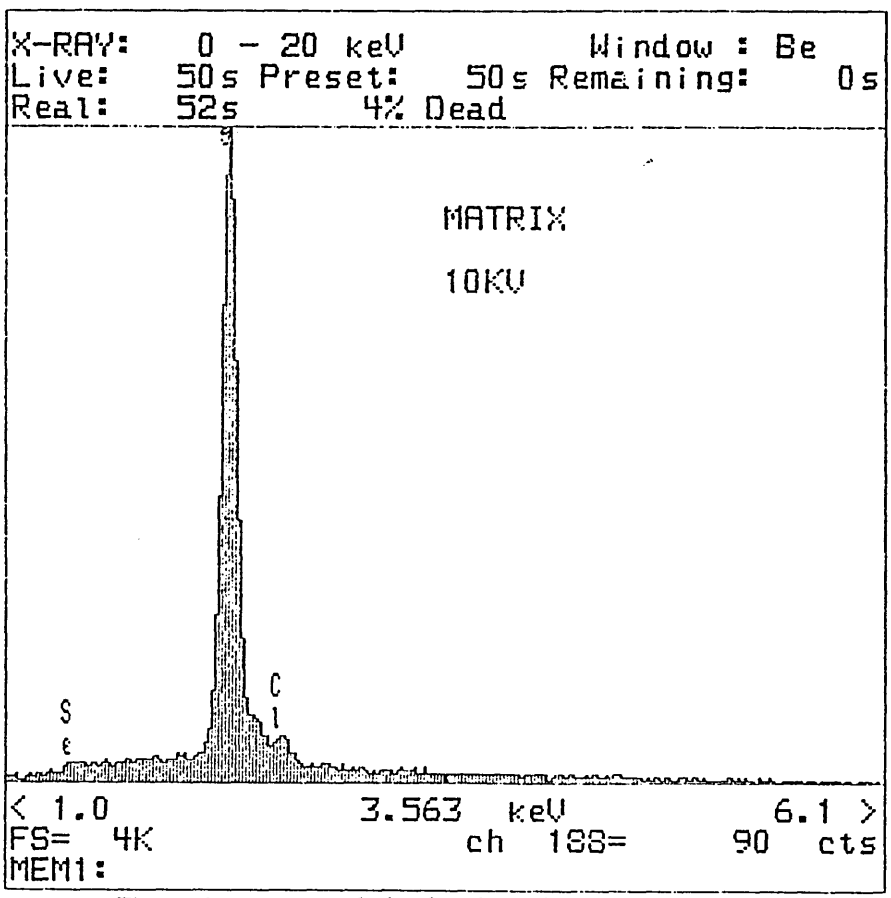

Figure 6.4: X-ray analysis of surface of SPEES/PES film

6.3.2. Comparison of dry and wet SPEES/PES spectra (symmetric SO_2 band)

Figures 6.5 and 6.6 show infrared and Raman spectra of SPEES/PES respectively. The assignments of main infrared bands in the spectrum are given in table 6.3.[6.1-6.4]

Band Position (cm^{-1})	Infrared Assignment
869, 850	Out of plane C-H deformation of isolated H in 1, 2, 4 substituted benzene ring
1010	Ring vibration of p-substituted aryl ether
1023	Symmetric O=S=O stretching of the sulphonate group
1080, 1107	Aromatic ring vibrations
1151	Symmetric O=S=O stretching of sulphone group
1167	Antisymmetric O=S=O stretching of the sulphonate group
1240	Antisymmetric C-O-C stretching of the aryl ether group
1296, 1321	Doublet resulting from antisymmetric O=S=O stretching of the sulphone groups
1408, 1471, 1487, 1579	Aromatic C=C stretching
3068, 3095	Aromatic C-H Stretching

Table 6.3: *Assignment of main infrared bands of SPEES/PES*

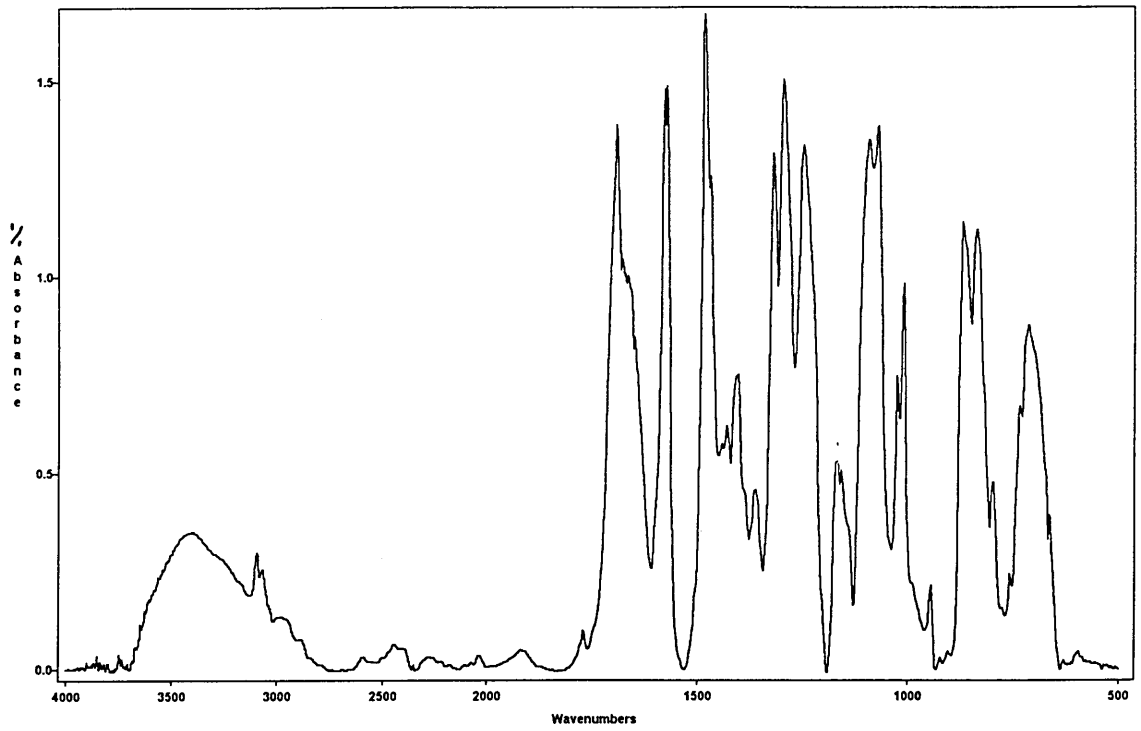

Figure 6.5: *Infrared spectrum of SPEES/PES*

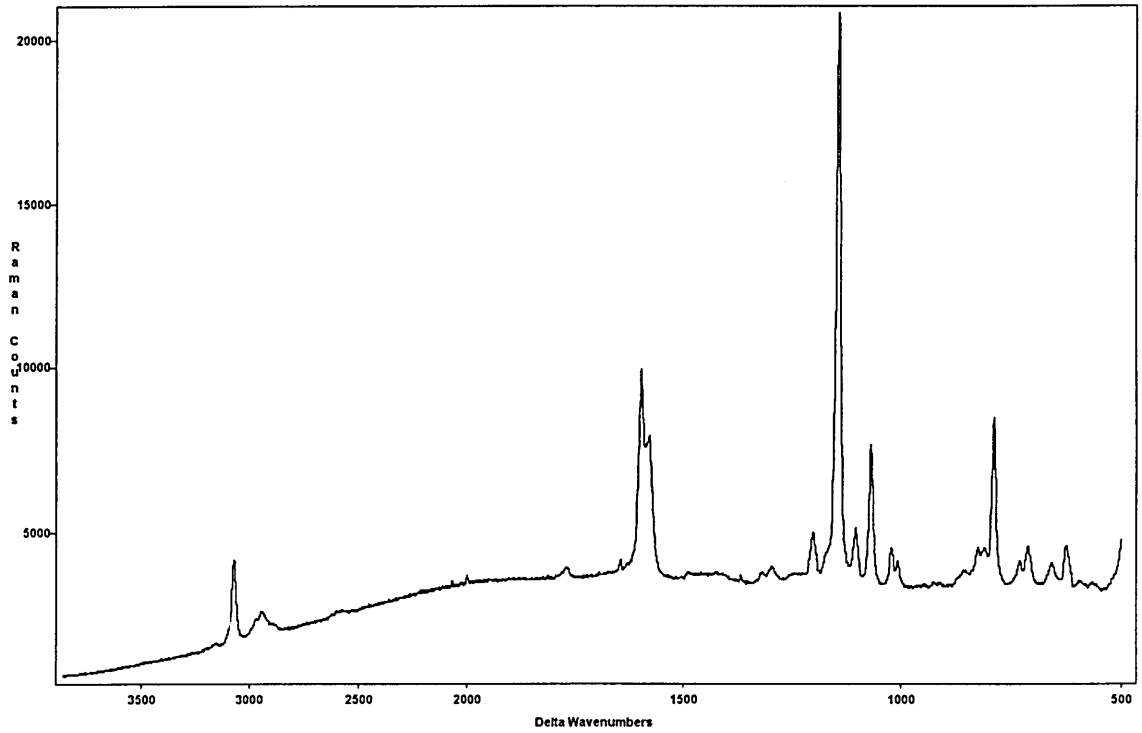

Figure 6.6: *Raman spectrum of SPEES/PES*

Exposing a dry SPEES/PES film to water is expected to induce changes in some of the vibrational modes of the polymer. In order to examine the final spectrum a wet SPEES/PES film after a diffusion experiment was collected and compared with a spectrum of the same sample before exposure to water. Figure 6.7 shows Raman spectra of the polymer film before and after diffusion of water for the 980 - 1120 cm^{-1} range.

Figure 6.7 shows that the band at 1023 cm^{-1} corresponding to symmetric O=S=O stretching of the sulphonate group, ν (SO_3^-) has shifted to higher frequency by 2 cm^{-1} after water has penetrated into the polymer matrix. Such blue shift is due to interaction between the water molecules and the SO_3^- groups of the polymer [6.4]. It was not possible to determine the changes to the infrared spectrum as a result of water diffusion. This was due to the highly absorbing nature of SPEES/PES in the finger printing region of the spectrum. Thus, it is not possible to obtain a good well resolved spectrum even with the use of spectral subtraction.

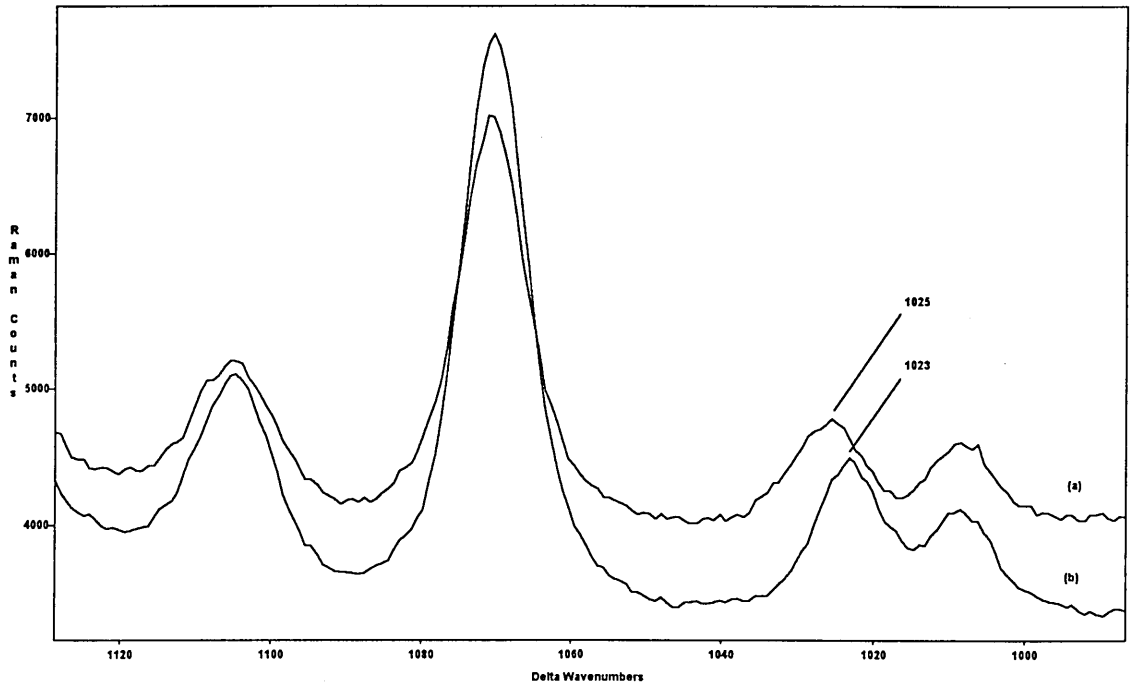

Figure 6.7: *Raman spectra of SPEES/PES (a) after and (b) before exposure to water*

6.3.3. Comparison of shape of water ν(OH) ν(OD) bands in pure water and in polymer matrix

The shape of the ν(OH) band of water is governed by various vibrations in the water molecule. Figure 6.8 shows an infrared spectrum of liquid water. The assignment of the main infrared bands of free and liquid water molecules is given in tables 6.4 and 6.5 respectively [6.4, 6.5].

Band Position (cm^{-1})	Infrared Assignment
1595	bending mode, ν_2
3651	symmetric stretching mode, ν_1
3756	antisymmetric stretching mode, ν_3

Table 6.4: *Assignment of main infrared bands of water molecules*

Band Position (cm^{-1})	Infrared Assignment
1650	bending vibration, ν_2
2110	bending vibration + torsion vibration
3225	overtone of the bending vibration, $2\nu_2$
3400	OH in hydrogen bridges
3615	OH groups

Table 6.5: *Assignment of main infrared bands of liquid water at 20 ^{o}C*

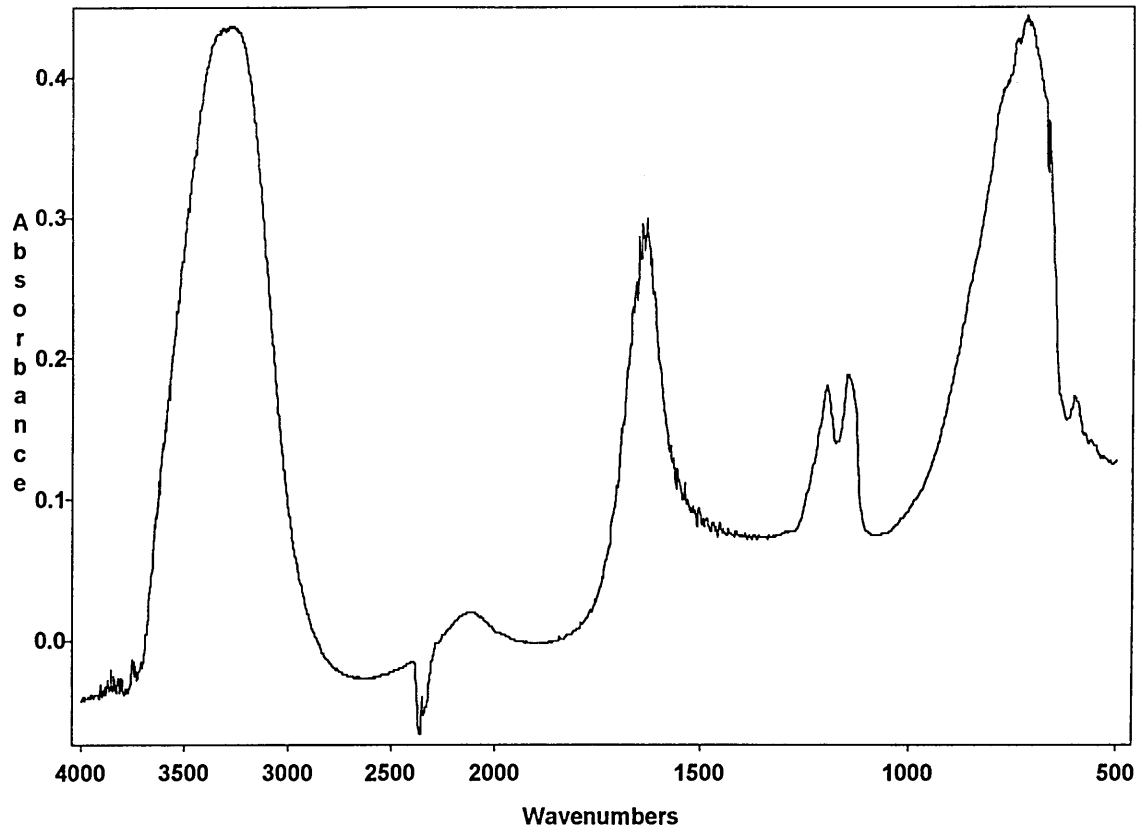

Figure 6.8: Infrared spectrum of liquid water

One of the factors determining the shape of this band is hydrogen bonding between the water molecules. One side of the ν(OH) band is steeper than the other side. The simplest explanation for this is in terms of variation of O-----O-----O and O----H structures. This gives a range of hydrogen bonding energies. The band has high intensity between 3800 and 3000 cm^{-1}, with a spectral density distribution reflecting the whole range of hydrogen bond strengths. The "wing" with higher frequency corresponds to the water vapour and the low frequency "wing" correspond to water in the liquid phase [6.5]. In the liquid there is a fixed free volume. In this free volume, water molecules can form hydrogen bonding but there is a limit to this free volume and beyond that the water molecules cannot form any further hydrogen bonding [6.6]. The structure of the water network in liquid form can be shown as figure 6.9.

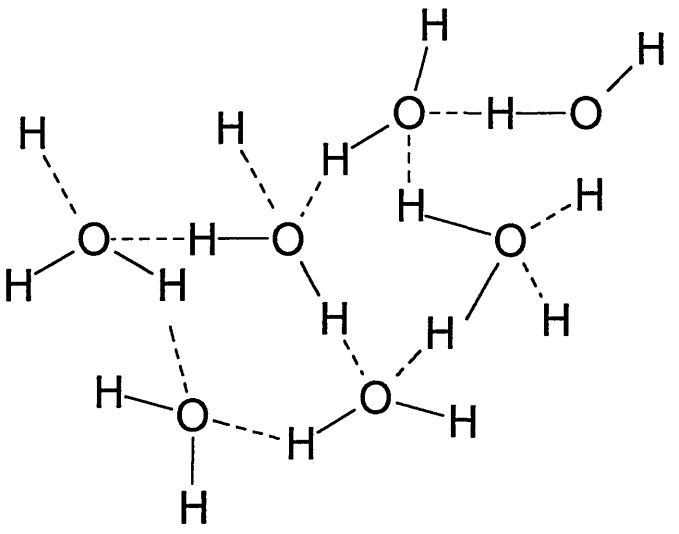

Figure 6.9: Structure of the liquid water network

This means that the average distance between oxygen atoms (O----H-O) in the network (see figure 6.9) will be different depending on the degree of hydrogen bonding. In liquid water, because of limitation of free volume, this distance has a maximum and this is the reason for a sharp fall in the high frequency side of the ν(OH) band. In the vapour phase there is no limitations on free volume, and as result a range of bands corresponding to various degrees of hydrogen bonding are responsible for a shallow "wing" on the high frequency side of the band.

It is expected that, as a result of interaction with the polymer, the vibrations of water molecules undergo some changes resulting in changes in the shape of the ν(OH) band. Figure 6.10 shows a comparison of OH stretching band of water in SPEES/PES after 22 seconds and at equilibrium and in liquid form. Figure 6.11 shows a comparison of water in polyacrylonitrile, PAN film and in the liquid phase. It is clear that there are a number of

differences between the ν(OH) band of water in apolymer matrix in comparison to liquid water.

The ν(OH) band of water in the polymer has apparently shifted to higher frequency. This could be due to a shift in equilibrium between strongly and weakly hydrogen bonded water molecules. This is in accordance with continum theory [6.5]. Kell gave a definition of this theory, describing water as having essentially complete hydrogen bonding, at least at low temperatures, but as having a distribution of angles, distances, and bond energies. Workers favouring continum models have tended to consider water in terms of a continuous distribution of interactions presumed to be spectroscopically indistinguishable. However, there is another type of model for representing water. This is called the " mixture " model, and describes the liquid water as an equilibrium mixture (or solution) of species that are distinguishable in an instantaneous picture.

The ν(OH) band of liquid water is more symmetrical and broader. At shorter diffusion times, there is a smaller number of strongly hydrogen bonded waters. This could be due to the water being 'weakened' as it diffuses into the polymer matrix. At longer time periods the
ν(OH) band profile begins to broaden suggesting that the water in the polymer is gaining more 'pure-water' character.

It should be noted that the environment surrounding each water molecule is important in determining the shape of the band. In the case of water after diffusion it is expected that the environment surrounding the water molecules is different from that in pure liquid water, and possibly these environments are in various phases. It is expected that as an example some of water molecules are (a) trapped in microvoids in the polymer matrix and form a type of water 'clusters', and (b) some of the water molecules may interact with the

polymer and thus forming new hydrogen bonds with the ionic groups of the polymer (SO_3^- in SPEES/PES). In both cases the water network will be 'weakened' and on average there will be fewer strongly hydrogen bonded OH groups.

It is clear from figure 6.11 that, the perturbations in PAN are more dramatic than SPEES/PES. A comparison of the ν(OH) band of PAN with that of water shows that the band has shifted to higher frequency indicating loss of more strongly hydrogen bonded water molecules in comparison with water.

Figure 6.12 shows a comparison of the uncoupled ν(OD) band of D_2O/H_2O (18%) solution in SPEES/PES at equilibrium with that of pure water. It is clear that no significant band shift is apparent. However, the ν(OD) band of the solution in SPEES/PES is broader than that of pure water. By comparison with the ν(OH) band of the H_2O, the ν(OD) band does not show much width change. One possible reason for this is the effect of the environment around the ν(OH) and ν(OD) vibrations. In an 18% solution of D_2O/H_2O, ν (OH) or ν(OD) vibrations are surrounded predominantly by hydrogen atoms and as such OD species are well separated and thus, they oscillate in an OH 'dilute' environment. This results in a narrower range of environments and thus, a narrower ν(OD).

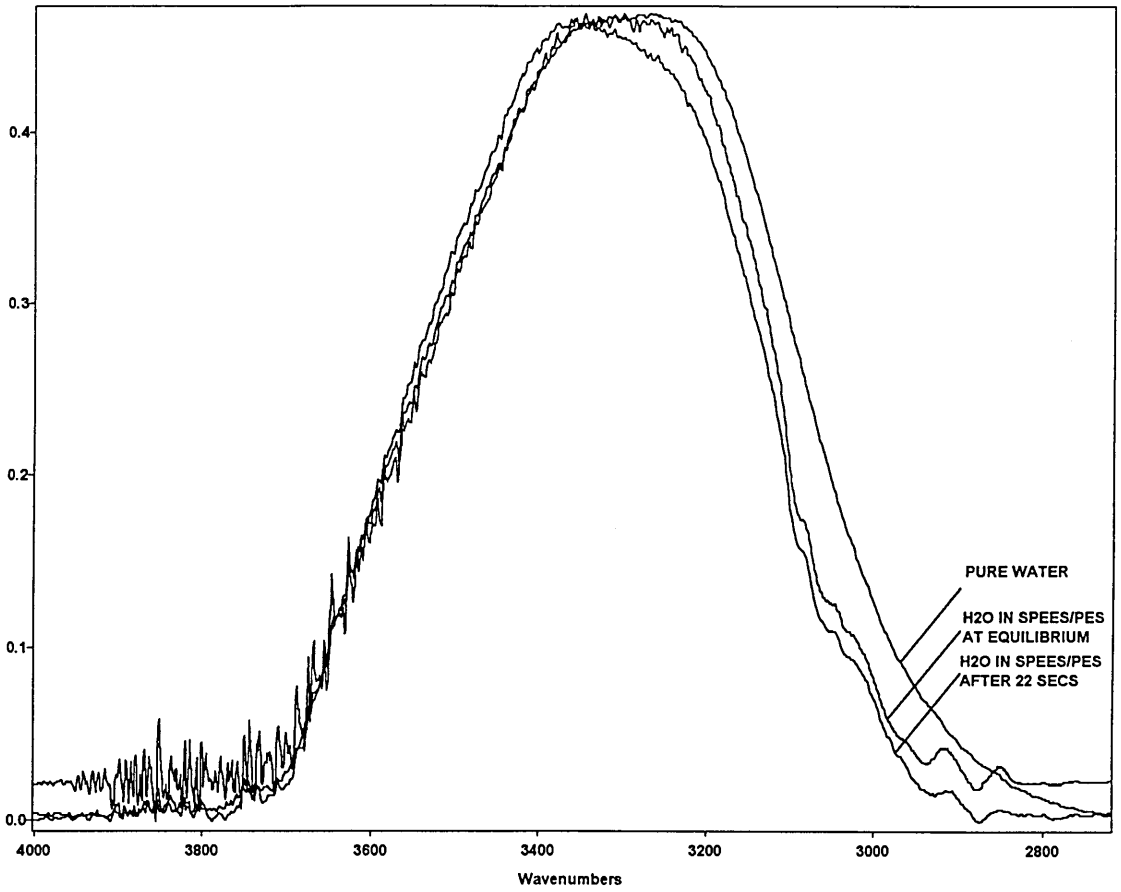

Figure 6.10: *Spectra of ν(OH) band of water in SPEES/PES and in the liquid phase*

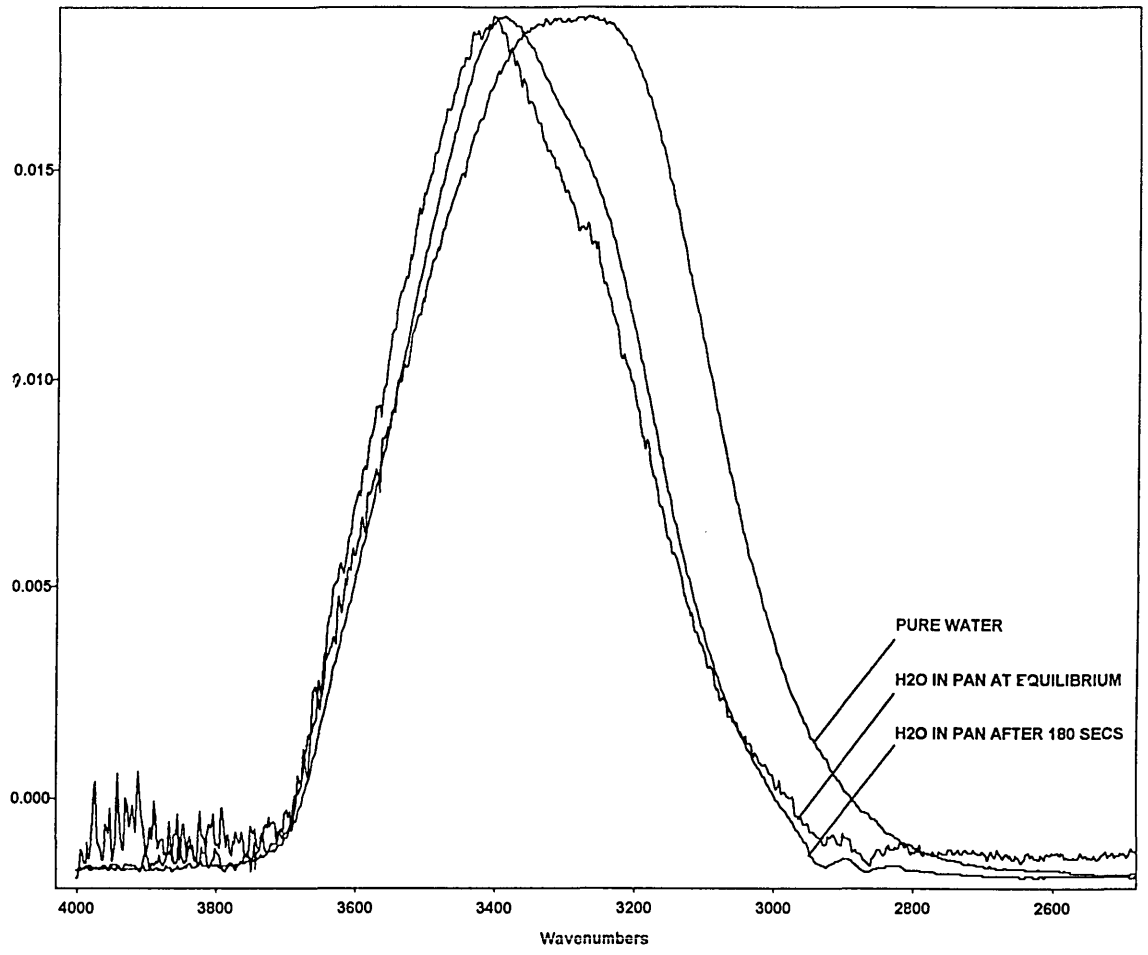

Figure 6.11: *Spectra of ν(OH) band of water in PAN and in the liquid phase*

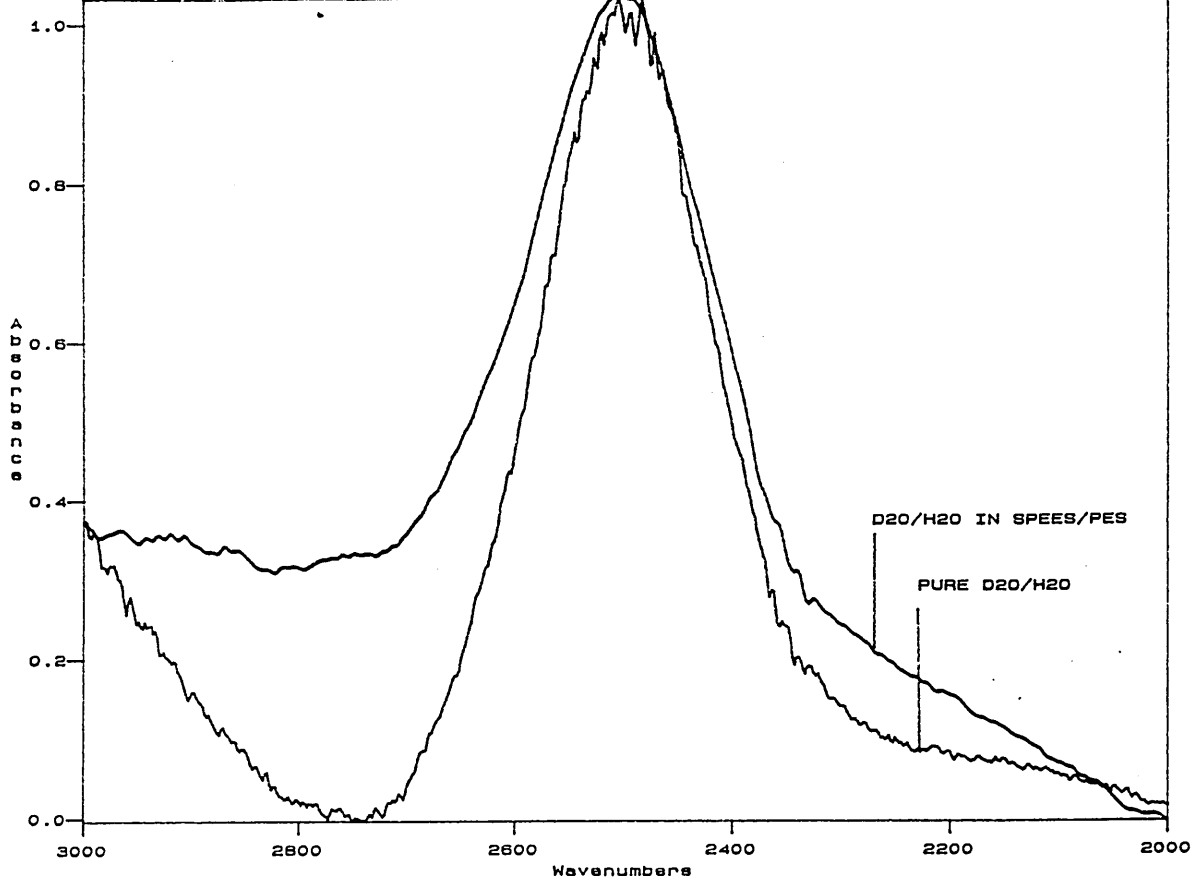

Figure 6.12: Comparison of v(OD) band of D_2O/H_2O and D_2O/H_2O in SPEES/PES

6.3.4. Diffusion of the pure water in SPEES/PES (S8 and S20)

The diffusion of water in the SPEES/PES film was measured by observing the OH stretching peak. The peak was integrated from 2700 to 3800 cm^{-1} to obtain an absorbance at each time. Figure 6.13 shows a series of spectra recorded at constant time intervals for diffusion of water into SPEES/PES. The integrated absorbencies for SPEES/PES (S8 and S20) as a function of time are shown in figure 6.14. The thickness of polymer film in both cases is 10 μm ± 0.5 and is measured with a Talysurf surface profiler.

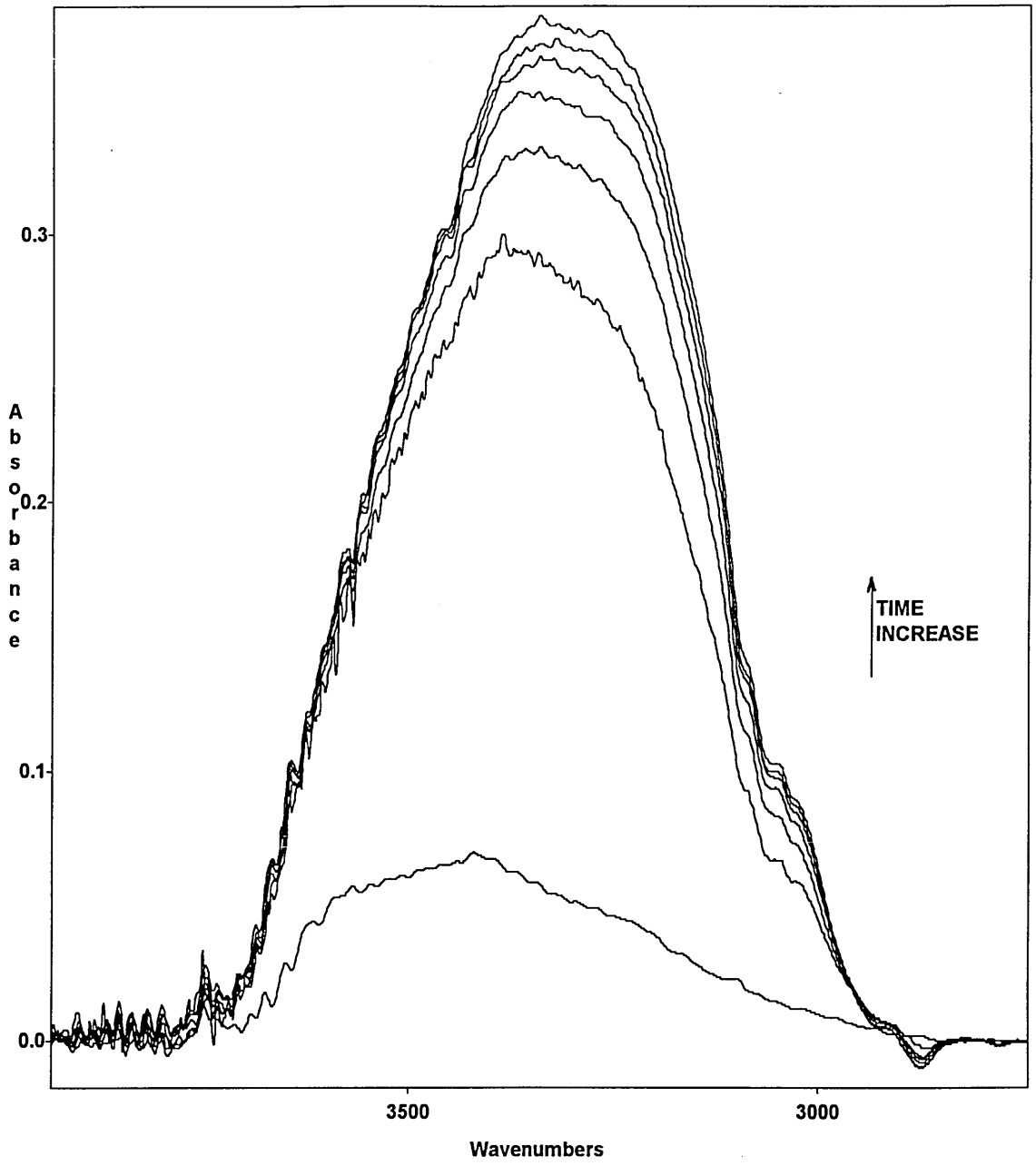

Figure 6.13: *Sequence of time-evolved spectra from SPEES/PES sample*

Figure 6.14 shows that the intensity of the ν(OH) band of diffusing water increases rapidly and reaches an 'equilibrium' level. However, the intensity of water at the equilibrium point is greater in the case of SPEES/PES (S8) than that of S20. In addition, the time taken to reach the equilibrium state is greater for S20 than S8. These observations can be explained

based on differences in the sulphonation level of these two copolymers. In SPEES/PES (S8), approximately 12.5% of the monomers in the polymer chains are sulphonated and thus it has a water uptake capability of 12.5% by weight (see table 6.1) in comparison to 5.5% water uptake of SPEES/PES (S20) in which approximately 5% of the monomers are sulphonated.

The diffusion coefficient of water penetration in the above polymer films can be calculated using equations 5.19 and 5.20 (see section 5.7.1). SPEES/PES is a glassy polymer and as explained earlier (see section 5.6.1) many researchers [5.24-5.40] have shown that the diffusion processes in glassy polymers are best described with a dual mode sorption. Figure 6.15 shows the solution of equations 5.19 and 5.20 to diffusion curve for SPEES/PES (S20). The values of diffusion coefficients for water penetration into SPEES/PES (S5), (S8) and (S20) are shown in table 6.6, where D_1 is the diffusion coefficient for the rapid initial stages of the diffusion which is due to adsorption of the water molecules onto the surface and the ionic sites of the polymer, D_2 is the value of diffusion coefficient for the diffusion of water molecules through the polymer matrix at longer times.

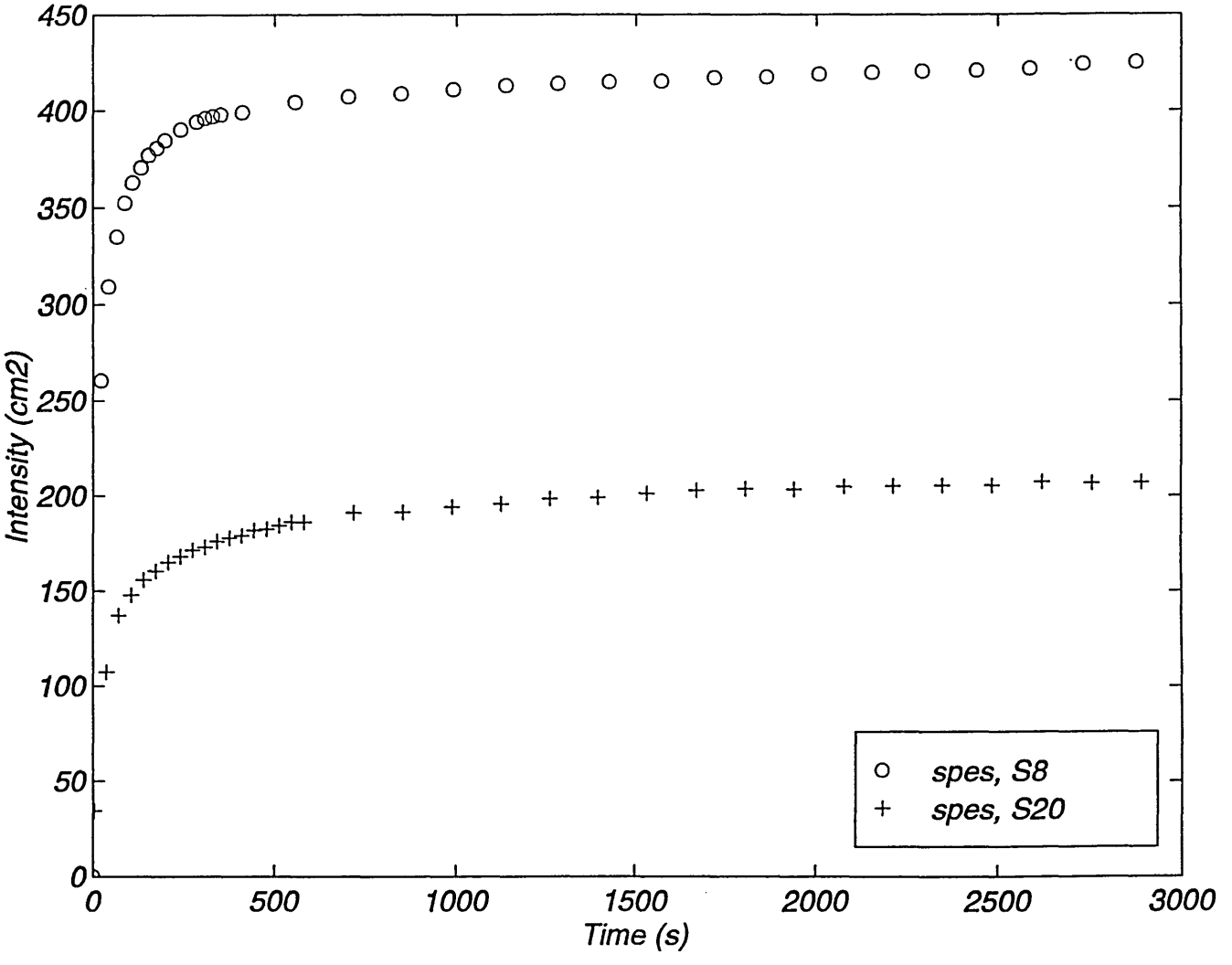

Figure 6.14: Integrated absorbance versus time for water -SPEES/PES (S8 and S20) at 25 °C

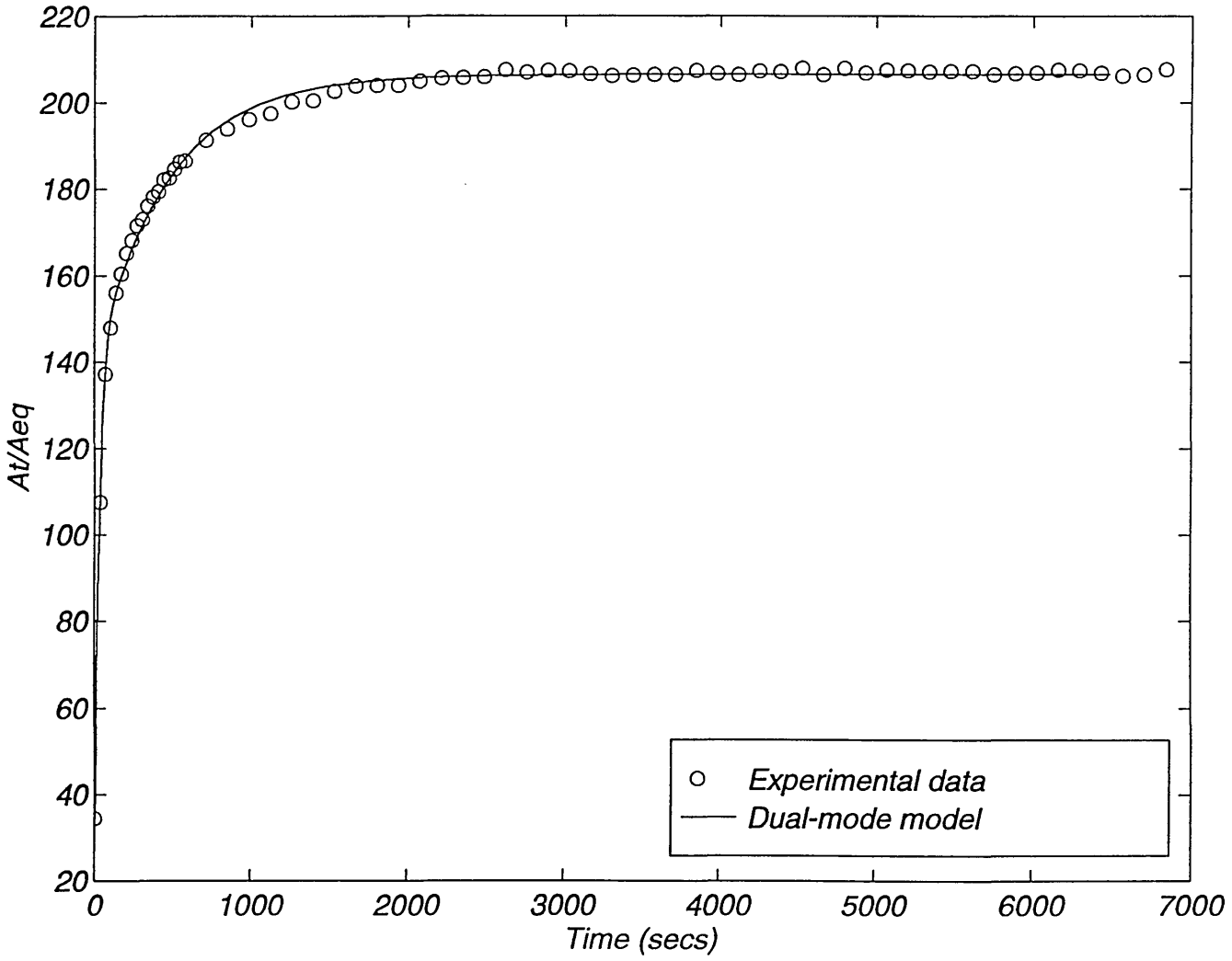

Figure 6.15: *Comparison between experimental data points and the solution to equations describing the dual sorption model for diffusion of water into SPEES/PES (S20)*

SPEES/PES film, S-No	D_1 (cm^2/sec)	D_2 (cm^2/sec)	X_a
S5	$(4.19 \pm 0.22) \times 10^{-8}$	$(3.56 \pm 0.27) \times 10^{-9}$	0.80 ± 0.02
S8	$(1.52 \pm 0.27) \times 10^{-8}$	$(2.16 \pm 0.24) \times 10^{-9}$	0.76 ± 0.03
S20	$(3.42 \pm 0.25) \times 10^{-9}$	$(8.20 \pm 0.28) \times 10^{-10}$	0.68 ± 0.02

Table 6.6: *Diffusion coefficient values of water penetration into SPEES/PES at 25 °C*

It is clear from the values of diffusion coefficients shown in table 6.6 that these values are greater for the SPEES/PES polymers with higher sulphonation level. This means that the diffusion process is faster in the polymer films which are more sulphonated. This is expected since the polymers with higher sulphonation level have greater tendency for absorption of water. This is also expected to have a greater effect on the adsorption of water onto the ionic sites (SO_3^-) of the polymer. In fact, it is clear that the D_1 values which correspond to the adsorption of the penetrating molecules show a greater variation as a result of changes in the sulphonation level of SPEES/PES.

Table 6.6 also shows that the X_a values are different for the three polymer systems and the values are greater for the copolymer with higher sulphonation level. The Xa values represent the fraction of the penetrating molecules which are adsorbed on the specific sites of the polymer matrix and thus partially immobilised (see section 5.6.1.). It also gives some indications of how predominant one mode of the diffusion behaviour is in relation to other. On this basis the greater value of X_a for high sulphonation level polymers can be explained.

The Fickian component of the above diffusion curves in the short term can be determined using equation 5.10. For an ideal Fickian behaviour, plotting the integrated absorbance as a function of square root of time results a straight line in the short time. Figure 6.16 shows a plot of experimental points for diffusion of water in SPEES/PES.

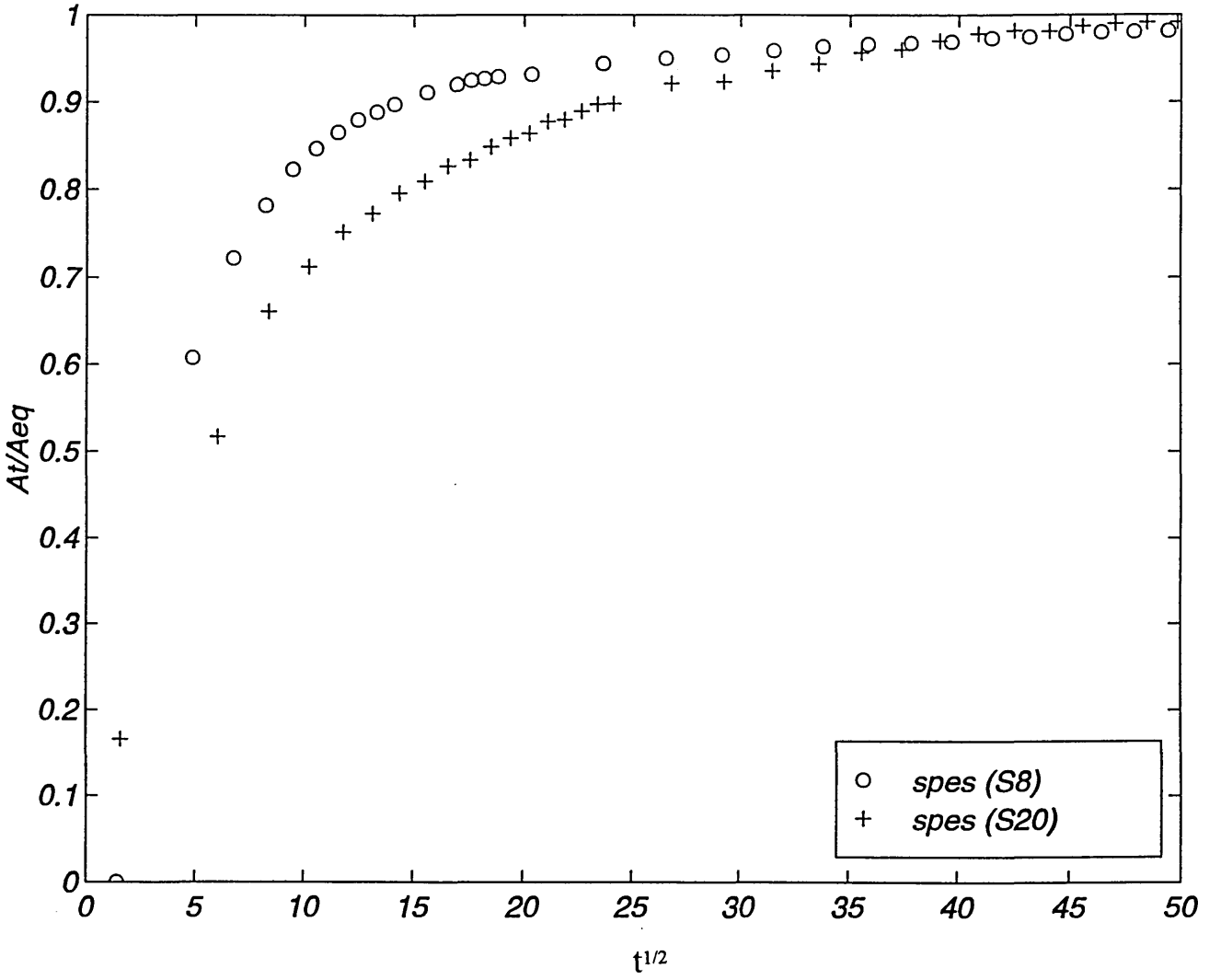

Figure 6.16: Plot of integrated absorbance as a function of square root of time for diffusion of water into SPEES/PES

As described earlier (see section 5.5) an ideal Fickian diffusion plot of intensity versus $t^{1/2}$ is approximately linear up to 50% of the final equilibrium uptake. It is apparent that this is not the case in diffusion of water in SPEES/PES. However, this is a behaviour displayed by rubbery polymers but since SPEES/PES is a glassy polymer, a non-Fickian behaviour is predicted. This is an indication of an anomalous behaviour of the diffusion process in the polymer film.

However, it is possible to draw a straight line through the first few data points on the curve. Although this is arguable, since the number of data points on such straight line is only a few and one might expect more data points to support the linearity in the very beginning period of the diffusion. However, it should be noted that in a FTIR-ATR experiment there are some limitations with the shortest time intervals that the data point can be collected. It was found that the shortest time interval for SPEES/PES system is 25-30 seconds. In fact, this might account for a disadvantage of using this system for studying the diffusion processes. In this work, the experimental parameters have been selected in a way to minimise the time intervals.

The exponent "n" in equation 5.3 (see below) indicates the type of diffusion behaviour.

$$\frac{M_t}{M_\infty} = \frac{4}{L}\left(\frac{Dt}{\pi}\right)^n$$

As an example, for case I or Fickian diffusion, the sorption-time curve has a value of n=0.5. In order to estimate this value for diffusion behaviour in SPEES/PES, the above equation can be rewritten as:

$$Log\left(\frac{M_t}{M_\infty}\right) = Log\left(\frac{4}{L}\right) + nLog\left(\frac{D}{\pi}\right) + nLog(t)$$

By plotting the data points as $\log(A_t/A_{eq})$ versus log(t), it is possible to determine the value of "n" (see figure 6.17).

Although it is difficult to draw a straight line through the data points , the first data points may indicate that the value of "n" is between 0.5 and 1. This shows that the diffusion behaviour is neither case I and case II and thus basically non-Fickian behaviour.

The long term component of the diffusion curve can also be determined using the equation 5.12 (see below).

$$\ln\left(1-\frac{M_t}{M_\infty}\right) = \ln\left(\frac{8}{\pi^2}\right) - \frac{D\pi^2 t}{4L^2}$$

Figure 6.18 shows a plot of the experimental data as $\ln(1-A_t/A_{eq})$ versus time. In the long term the curve become linear and by determining the slope of the line, it is possible to obtain the value of the diffusion coefficient.

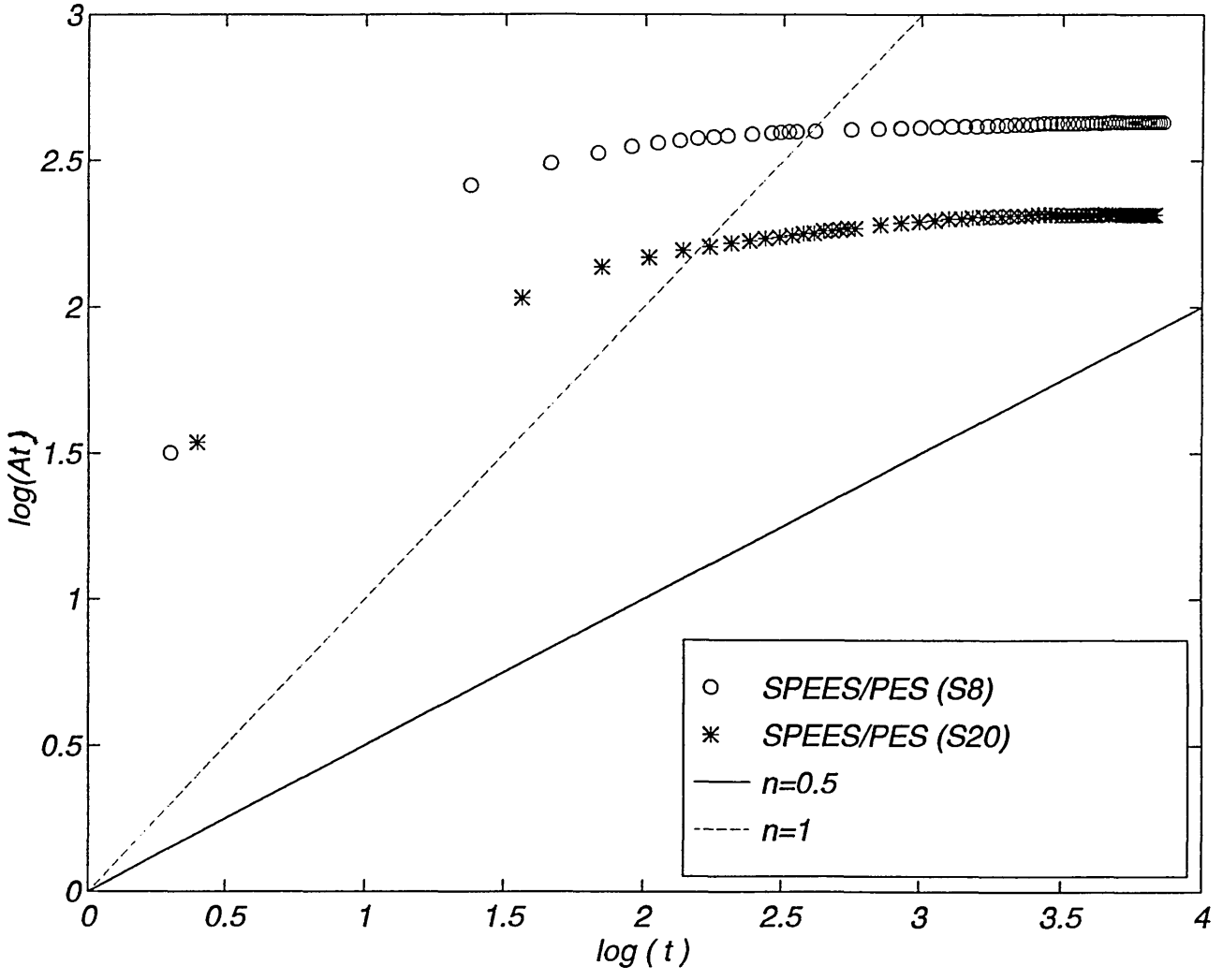

Figure 6.17: Plot of data points of diffusion of water in SPEES/PES

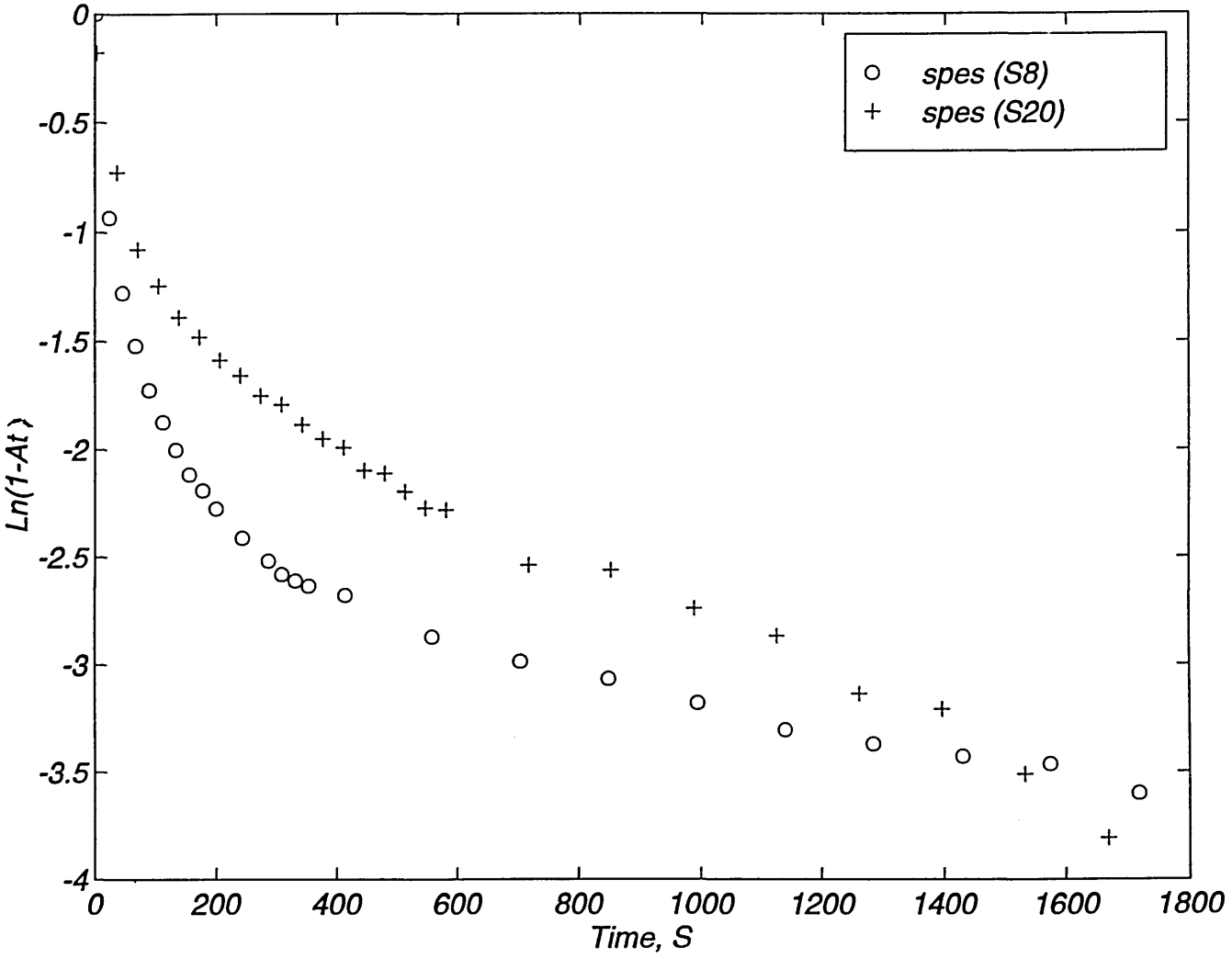

Figure 6.18: Plot of experimental data for diffusion of water into SPEES/PES using equation 5.12

6.3.5. Sorption and desorption

An understanding of sorption and desorption process in polymers is important in membrane-based and/or liquid separation, barrier applications, and polymer impregnation processes [6.7]. Fleming and Koros [6.8] have shown that gas sorption and desorption isotherms in glassy polymers exhibit hysteresis or, a manifestation of the long relaxation times associated with this non-equilibrium state. This is in contrast to the behaviour in rubbery polymers in which the sorption and desorption isotherms coincide. Dé Nevè and Shanahan [6.9] have investigated the effect of water uptake by epoxy resin adhesives. Water ingress has been monitored using gravimetric measurements whilst changes in mechanical properties have been followed using viscoelastometry. They have shown that the absorption of water leads to a decrease in glass transition temperature which induces plasticization of the polymers.

In order to study the sorption and desorption process, a SPEES/PES membrane was casted onto a ZnSe ATR prism and cured at 65 ^{o}C for 24 hours. First the polymer membrane was exposed to pure water and a series of spectra for the sorption process was collected for a known period (approximately 30 minutes). Then, the excess of water was removed from the surface of the polymer film. This was followed by a dry nitrogen gas flow. This causes the sorbed water molecules to desorb from the polymer matrix.

Figures 6.19 and 6.20 show a series of spectra for the ν(OH) band for sorption and desorption of water into and from SPEES/PES respectively. A comparison of the ν(OH) band at equilibrium of the sorption processes shows that the band has shifted to lower frequency for third sorption. It should be noted the water band shown in figure 6.19 is a mixture of various ν(OH) bands corresponding to different water environments. Some are free water molecules which are totally mobile and have no significant interactions with polymer matrix whereas some are strongly interacting with the ionic sites of the

SPEES/PES polymer. Exposing the polymer for the first time into water results in some defects in the material and thus the nature of water molecules in relation to their surroundings will be different. It is expected for example that the polymer swells and thus, the free volume in the polymer matrix increases. On this basis it can be expected that the shape of the ν(OH) band will be influenced by these changes.

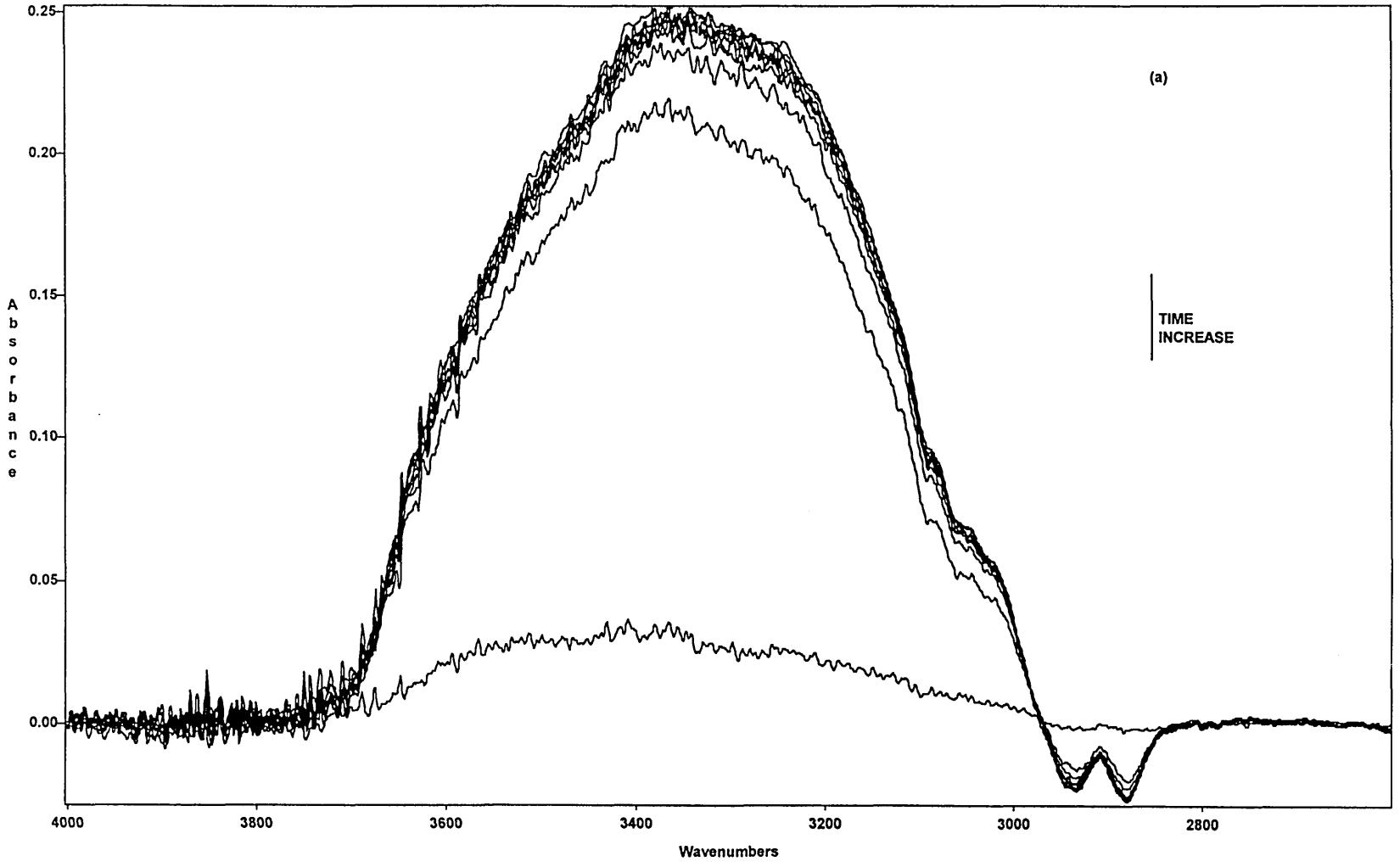

Figure 6.19a: Spectra of ν(OH) band for the first sorption of water into SPEES/PES

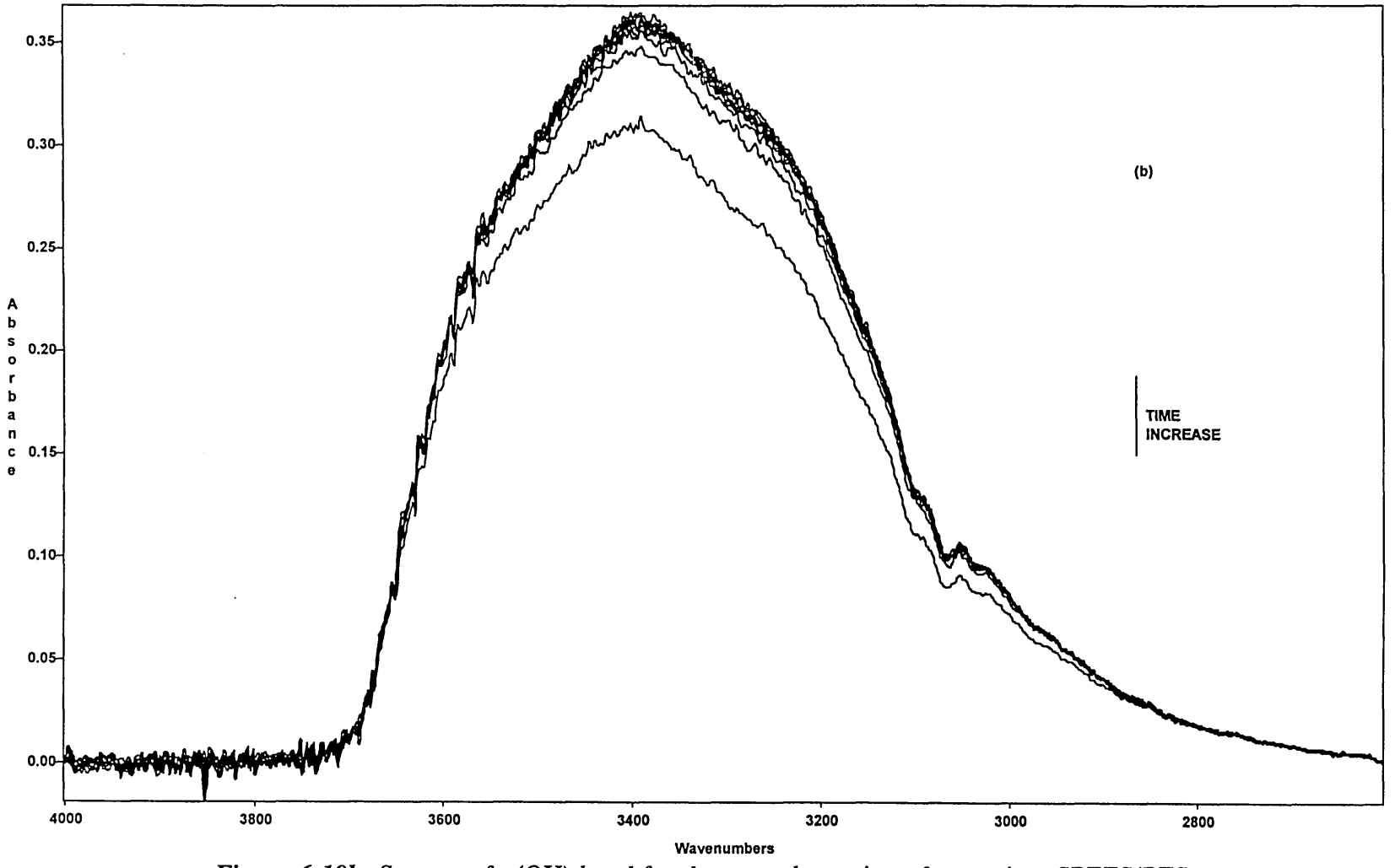

Figure 6.19b: Spectra of ν(OH) band for the second sorption of water into SPEES/PES

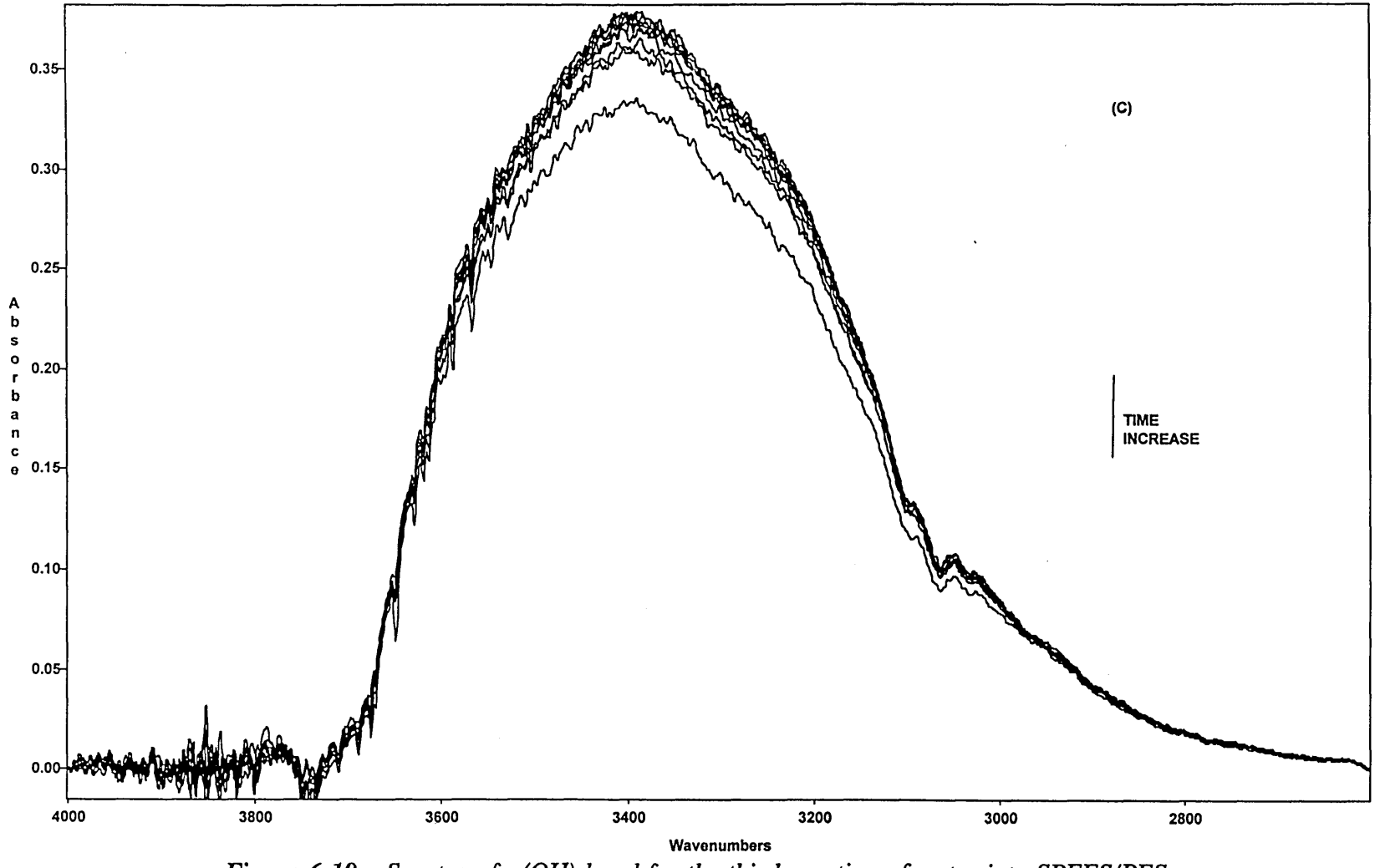

Figure 6.19c: Spectra of ν(OH) band for the third sorption of water into SPEES/PES

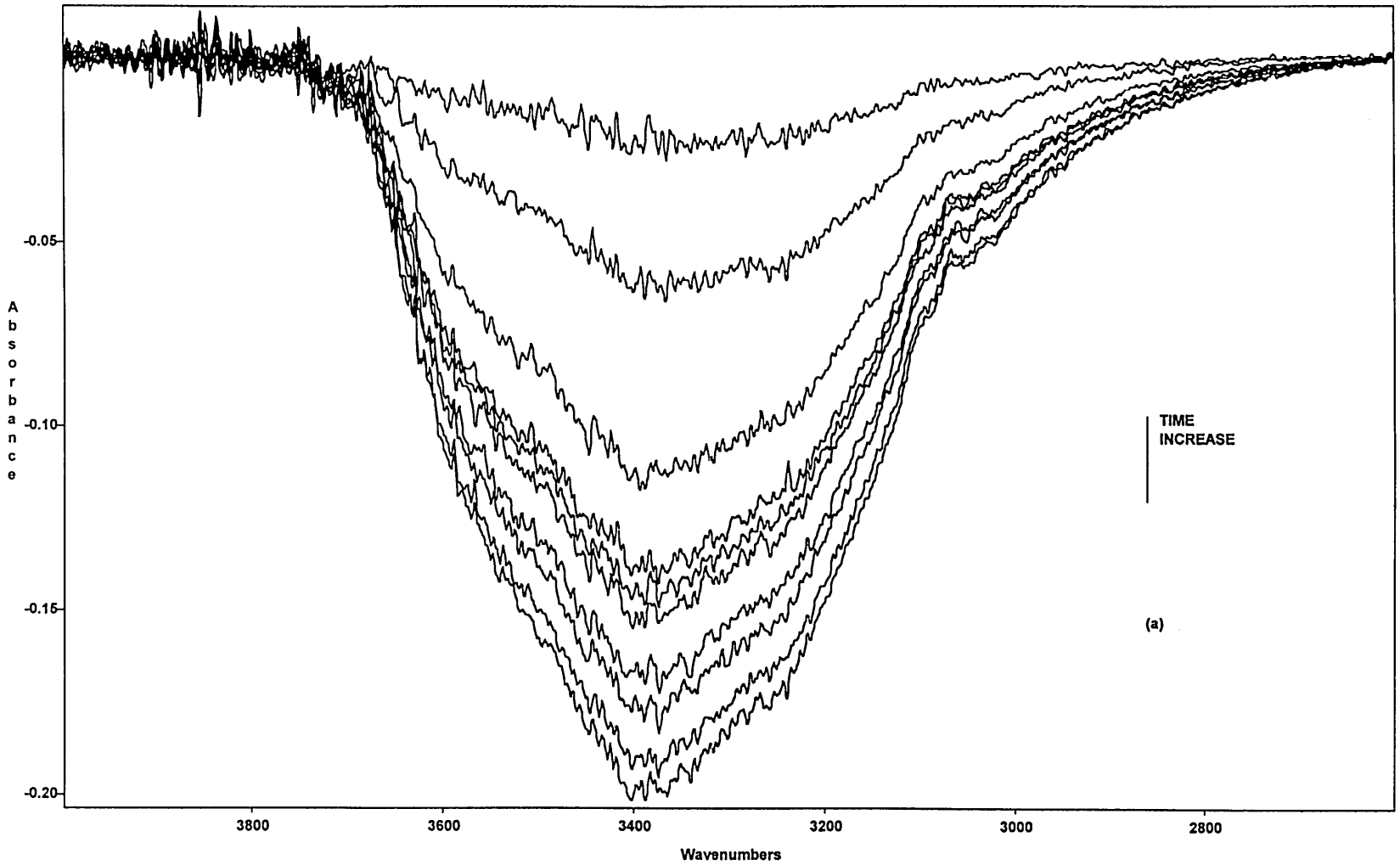

Figure 6.20a: Spectra of ν(OH) band for the first desorption of water from SPEES/PES

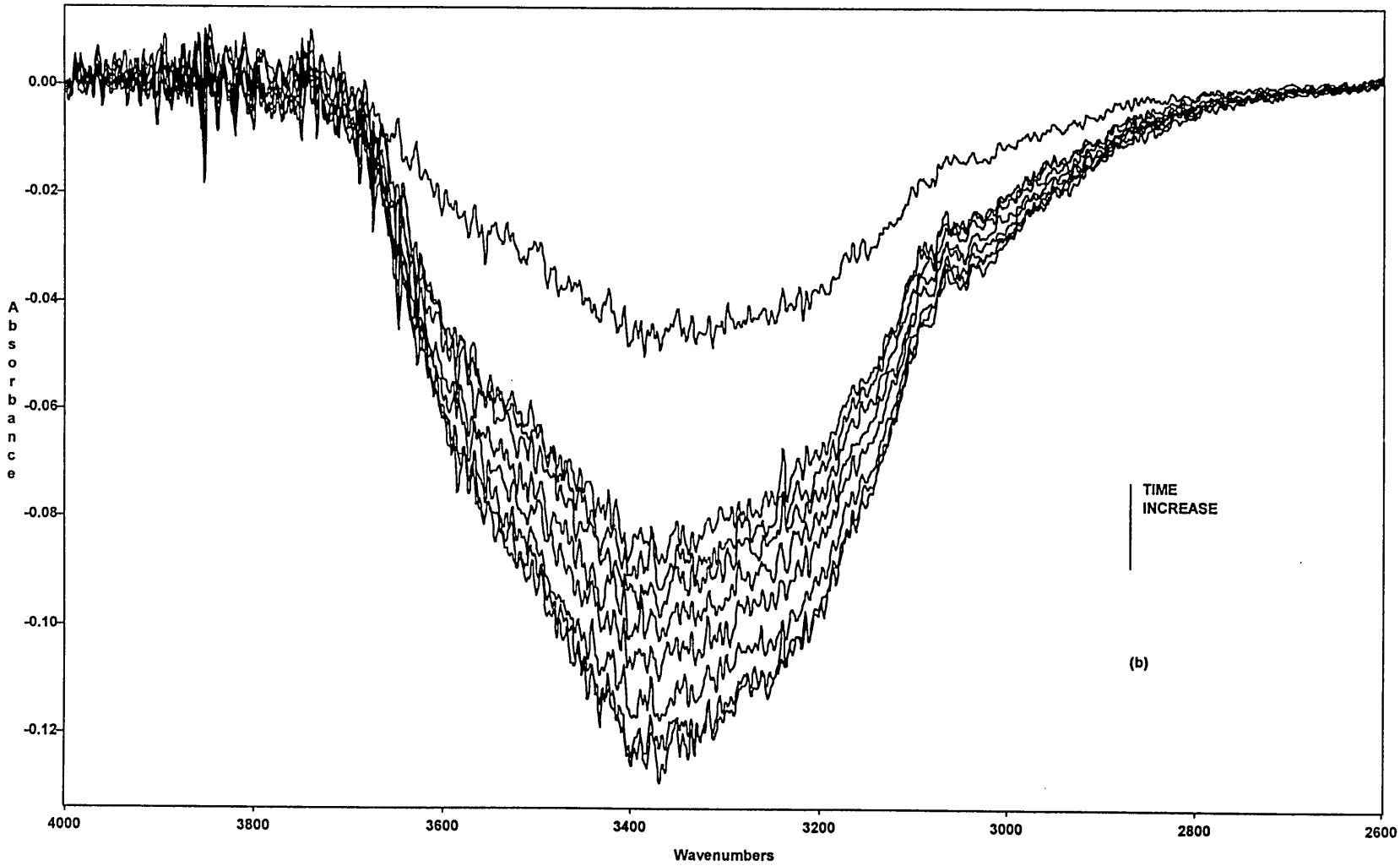

Figure 6.20b: Spectra of ν(OH) band for the second desorption of water from SPEES/PES

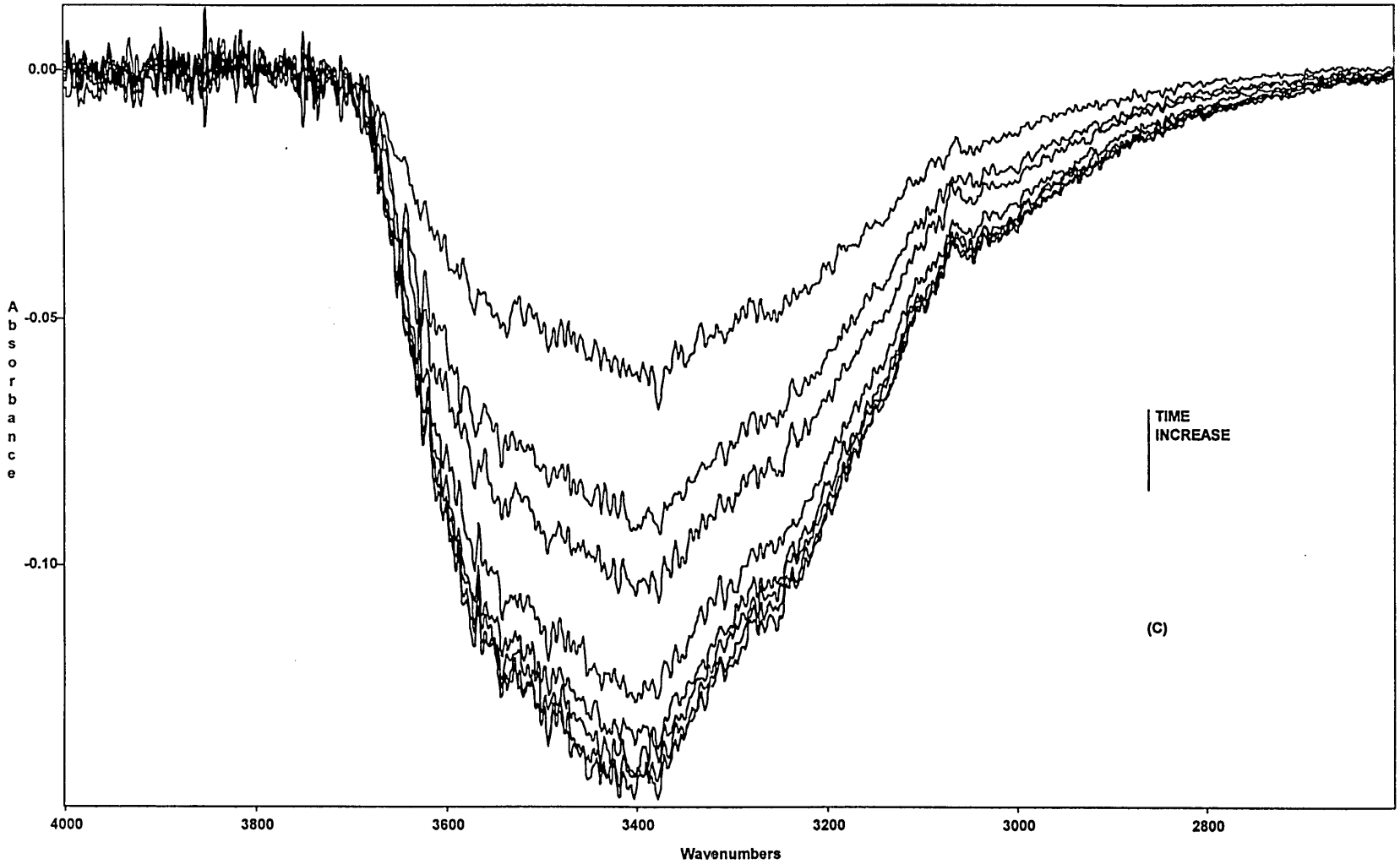

Figure 6.20c: Spectra of ν(OH) band for the third round desorption of water from SPEES/PES

Figures 6.21 and 6.22 show plots of integrated absorbance of experimental data versus time for sorption and desorption processes respectively. It is clear that the absorption level at equilibrium has increased significantly from the first sorption process. In addition the time taken to reach the equilibrium state is very rapid in the first sorption. This means that the first mode of sorption which corresponds to internal adsorption of water onto specific sites on the polymer is very fast. However, it is clear that in the second, and particularly in the third, sorption the time taken to reach equilibrium state is much slower and it seems that the second mode of diffusion behaviour is more dominant.

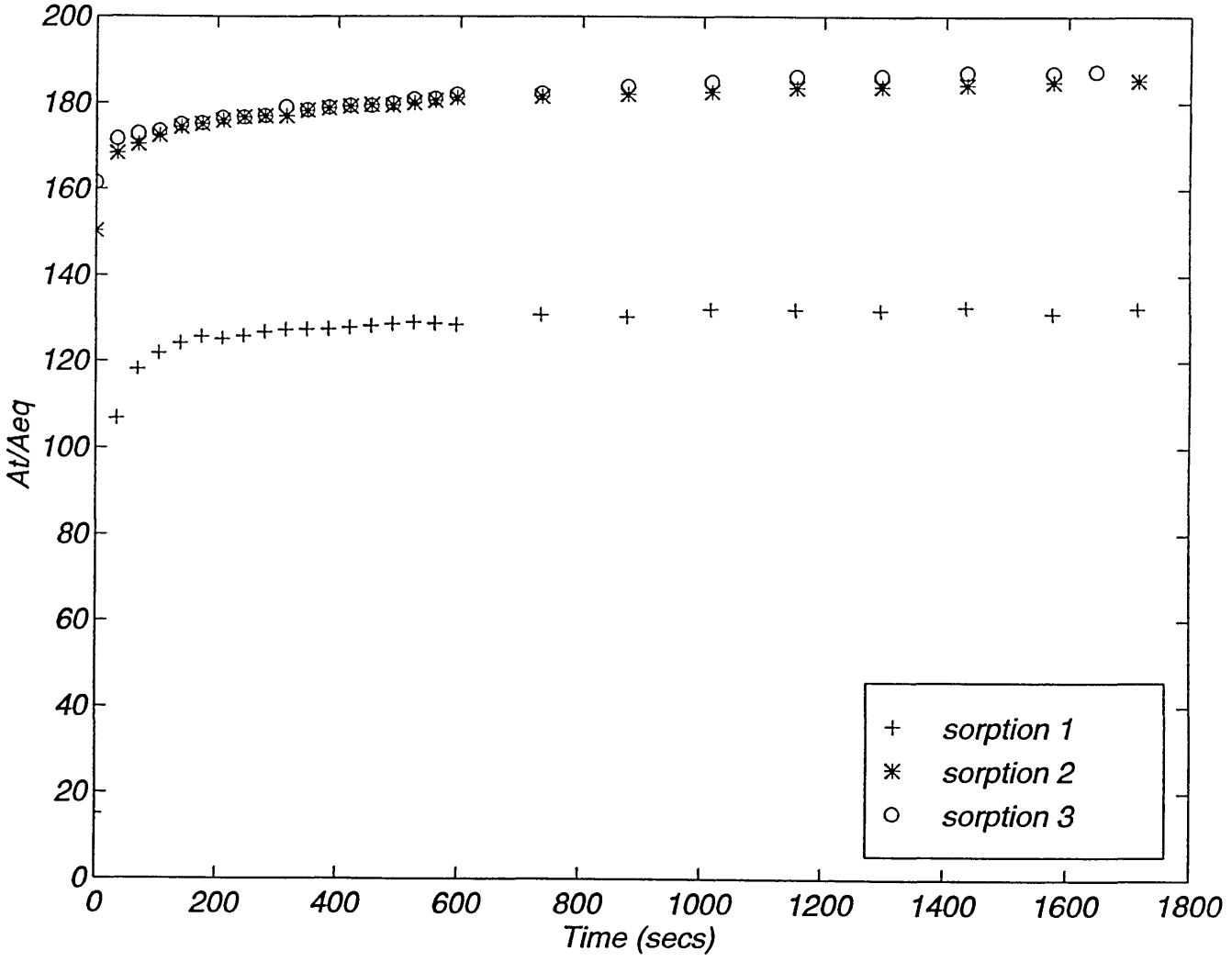

Figure 6.21: A plot of integrated absorbance as a function of time for sorption of water into SPEES/PES

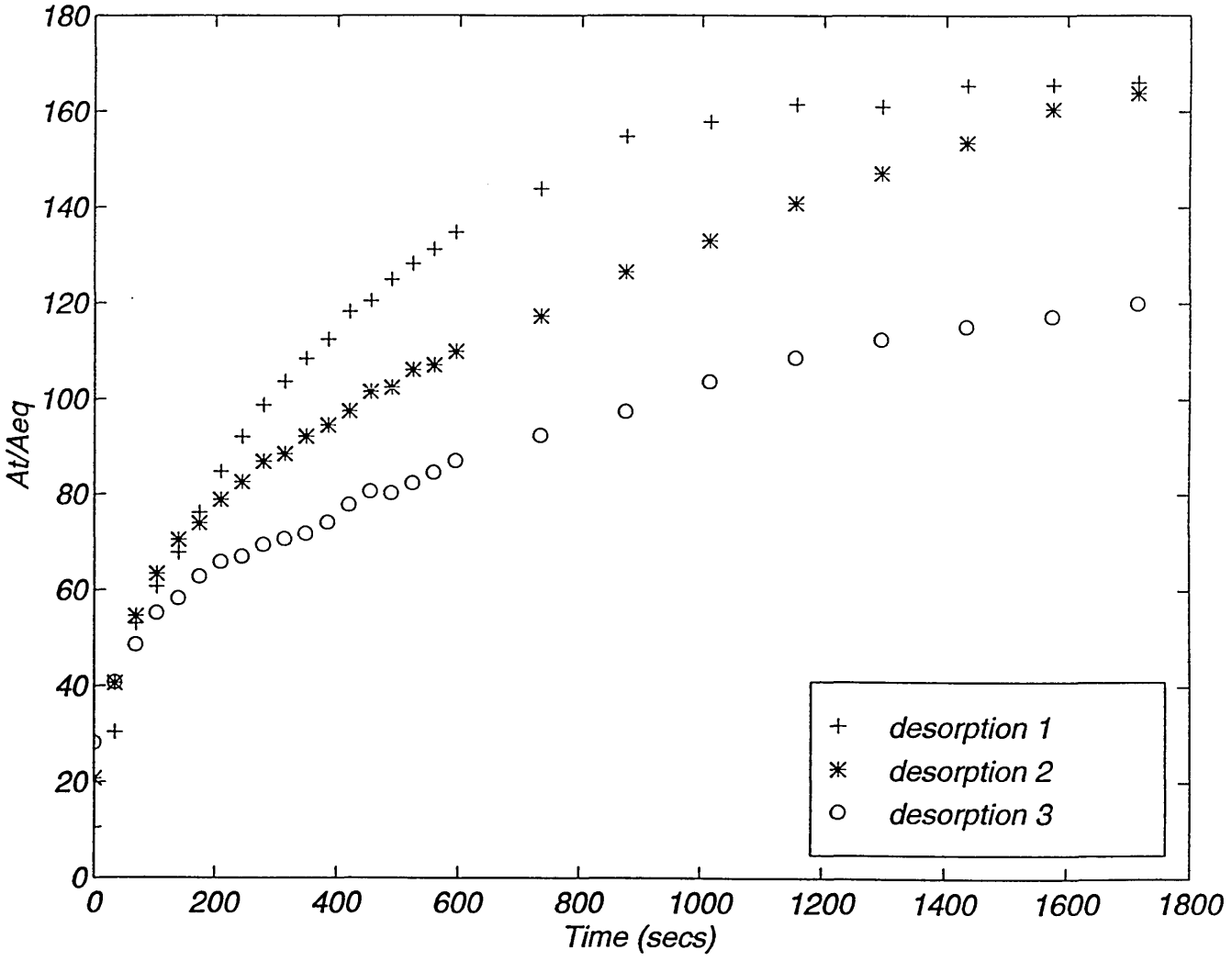

Figure 6.22: A plot of integrated absorbance as a function of time for desorption of water into SPEES/PES

Figure 6.23 shows a comparison of the sorption curve with that of desorption. However, it should be noted the desorption curve in figure 6.23 is inverted in order to ease the comparison between the two processes. It was shown earlier that using equations 5.19 and 5.20 it is possible to describe the diffusion process and the two diffusion coefficients D_1 and D_2 corresponding to adsorption of water molecules on specific sites on the polymer (SO_3^-).

Crank [5.16] has shown that equation 5.9 can be used to describe the sorption process. He has further shown that if free and immobilised solute are considered to be initially in equilibrium everywhere in the sheet, then the mathematical solutions presented for sorption also describe the desorption process, providing M_t is taken to mean the amount of solute leaving the sheet up to time t, and M_∞ the corresponding amount after infinite time. Since equations 5.24 and 5.25 have been drived from equation 5.9, it can be assumed that these equations can also be used to describe desorption. Table 6.7 and 6.8 show the results of curve fitting to experimental data for sorption and desorption of water into and from SPEES/PES (S5) and (S8) respectively.

The results of fitting to the equations describing a double mode diffusion (equations 5.24 and 5.25) is shown in figures 6.24 and 6.25 for sorption and desorption respectively.

Process	D_1 (cm^{-1}/sec)	D_2 (cm^{-1}/sec)	X_a
Sorption 1	$(4.19 \pm 0.08) \times 10^{-8}$	$(3.56 \pm 0.07) \times 10^{-9}$	0.80 ± 0.02
Sorption 2	$(5.00 \pm 0.09) \times 10^{-8}$	$(2.15 \pm 0.06) \times 10^{-9}$	0.65 ± 0.05
Sorption 3	$(5.15 \pm 0.08) \times 10^{-8}$	$(2.03 \pm 0.06) \times 10^{-9}$	0.58 ± 0.04
Desorption 1	$(4.52 \pm 0.07) \times 10^{-8}$	$(1.24 \pm 0.08) \times 10^{-9}$	0.26 ± 0.05
Desorption 2	$(2.17 \pm 0.06) \times 10^{-8}$	$(1.67 \pm 0.07) \times 10^{-9}$	0.28 ± 0.03
Desorption 3	$(1.98 \pm 0.07) \times 10^{-8}$	$(1.43 \pm 0.07) \times 10^{-9}$	0.31 ± 0.04

Table 6.7: *Diffusion coefficients of sorption and desorption of water into and from SPEES/PES (S5)*

Process	D_1 (cm^{-1}/sec)	D_2 (cm^{-1}/sec)	X_a
Sorption 1	$(1.80 \pm 0.07) \times 10^{-8}$	$(2.16 \pm 0.04) \times 10^{-9}$	$0.50. \pm 0.05$
Sorption 2	$(2.61 \pm 0.06) \times 10^{-8}$	$(1.95 \pm 0.05) \times 10^{-9}$	0.73 ± 0.06
Sorption 3	$(3.69 \pm 0.07) \times 10^{-8}$	$(1.52 \pm 0.07) \times 10^{-9}$	0.92 ± 0.04
Desorption 1	$(3.00 \pm 0.08) \times 10^{-8}$	$(6.85 \pm 0.06) \times 10^{-9}$	0.24 ± 0.07
Desorption 2	$(2.78 \pm 0.05) \times 10^{-8}$	$(4.27 \pm 0.07) \times 10^{-9}$	0.36 ± 0.07
Desorption 3	$(1.93 \pm 0.06) \times 10^{-8}$	$(1.41 \pm 0.05) \times 10^{-9}$	0.45 ± 0.05

Table 6.8: *Diffusion coefficients of sorption and desorption of water into and from SPEES/PES (S8)*

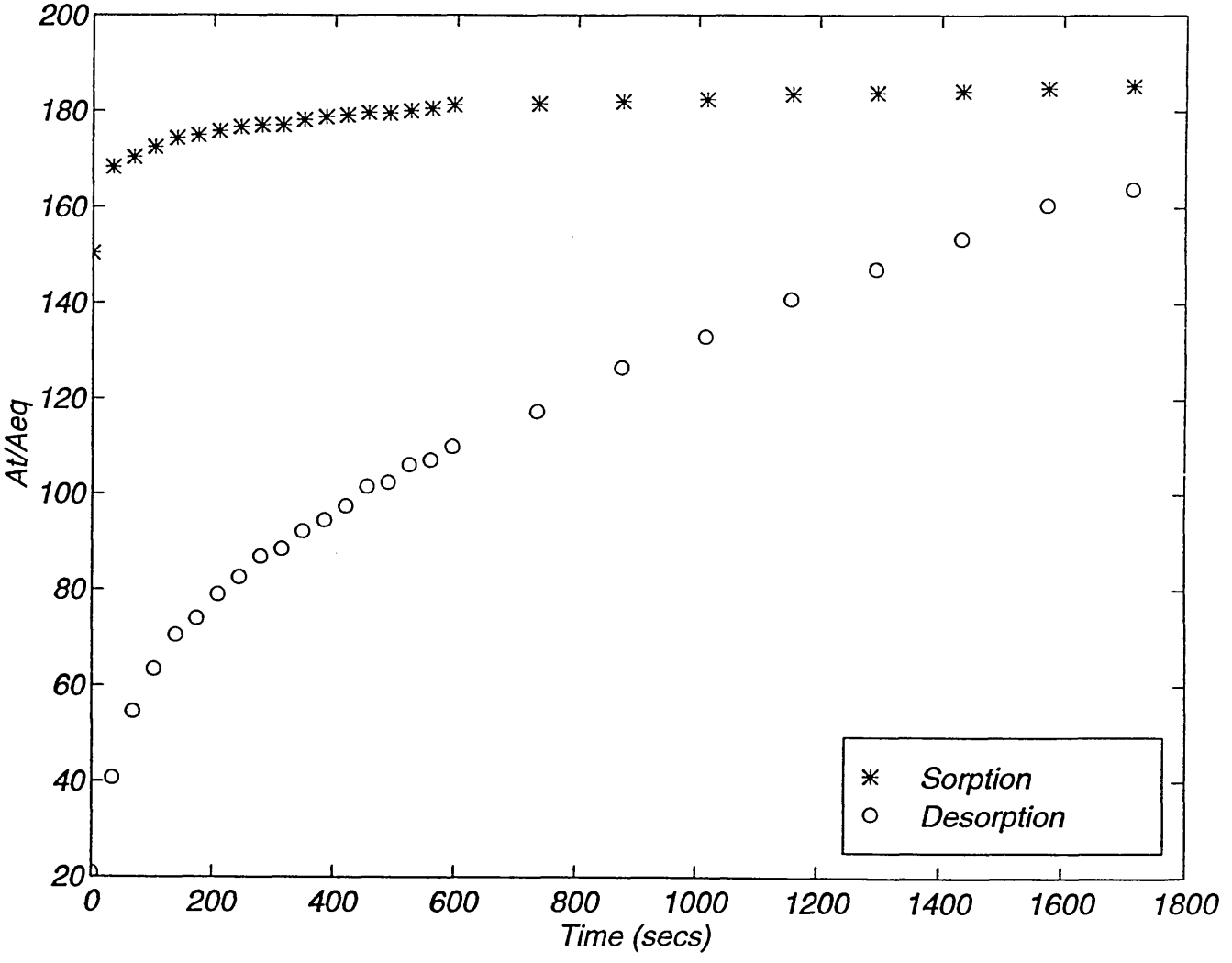

Figure 6.23: A comparison of the sorption curve with that of desorption of Water from SPEES/PES

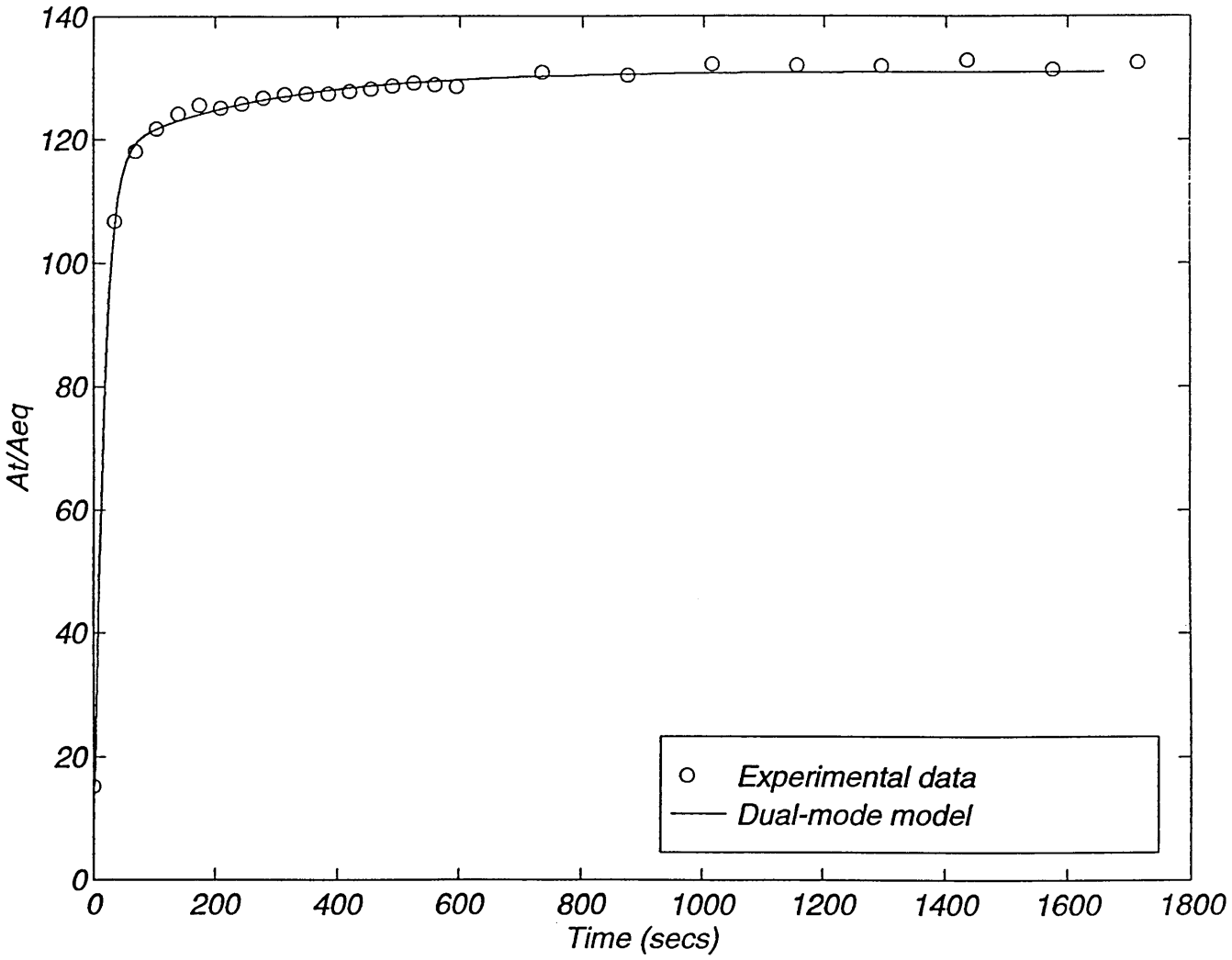

Figure 6.24: *A Comparison of experimental data and solution to equations describing a double mode diffusion for sorption of water into SPEES/PES*

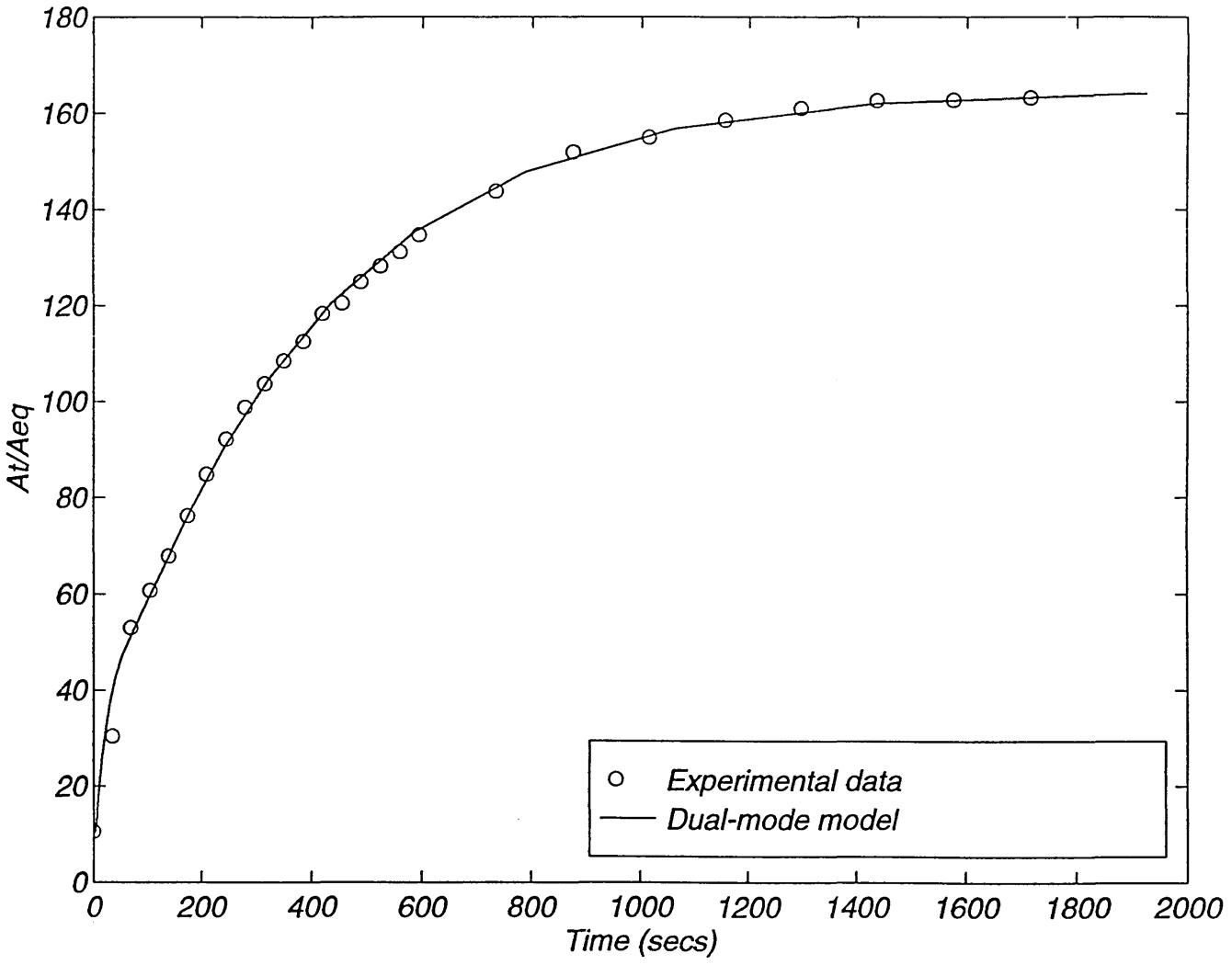

Figure 6.25: A Comparison of experimental data and solution to equations describing a double mode diffusion for desorption of water into SPEES/PES

CHAPTER 7

7.1. Introduction

It is clear that any polymer diffusion consists of at least two parts, i.e., the polymer membrane and the diffusing species. It is expected that the variations in any of these have a possible effect on the diffusion process. In chapter 6, the diffusion of pure water into SPEES/PES film was described. In all of those studies the interfering effects of all ionic species or contaminations on diffusing water molecules were eliminated. All of the polymer films were treated in the same way.

In this chapter the effect of various cations and anions on diffusion of water molecules into SPEES/PES in addition to the effect of annealing temperature on the polymeric film will be described.

7.2. Diffusion of water from ionic aqueous solutions

SPEES/PES can be used as membrane films for desalination of brackish or sea-water. It is known that a number of anions and cations with varying concentrations exist in such water. This section describes the effect of presence of these ions in diffusion of water molecules into SPEES/PES.

7.2.1. Experimental

The solutions used in this study were all ionic aqueous solutions with 0.2 molar concentration. The chloride salts (99+ %) used for preparation of the solutions were obtained from Aldrich Chemical Company. The polymer films were SPEES/PES (S8) and were cast from NMP solution onto a ZnSe ATR prism. Figure7.1 shows the ATR prism with coated polymer film in contact with an ionic solution. The thickness of the films after annealing at 65 °C for 24 hours were 10 ± 0.5 μm as measured with a surface profiler(Laser Form Talysurf). The FTIR-ATR spectroscopy was carried out as described earlier (see section 6.2.2.) using a Mattson Polaris FTIR spectrometer equipped with a bullseye MCT detector. A series of spectra at regular time intervals were collected with the parameters specified in table 6.2. The spectra were manipulated using Mattson FIRST® software.

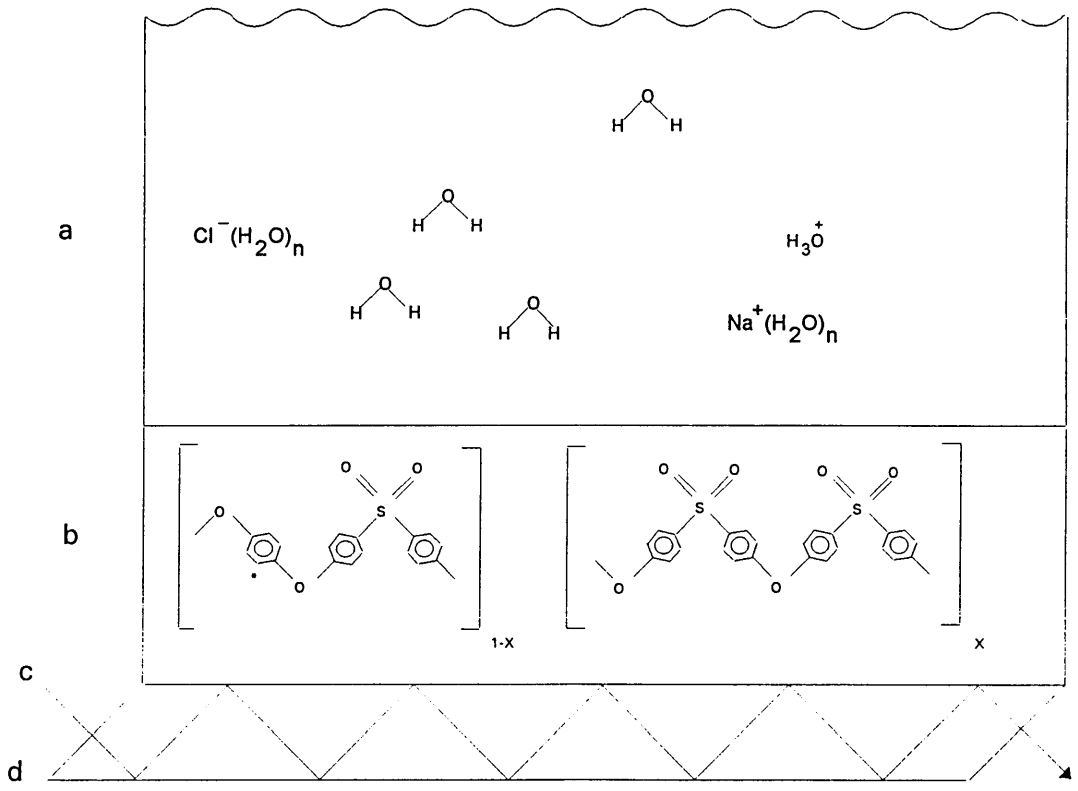

Figure 7.1: Schematic diagram of experimental set up for diffusion of cationic aqueous solutions into SPEES/PES film. (a) diffusing solution, (b) polymer film, (c) incident IR radiation, and (d) ZnSe ATR prism.

7.2.2. Results and Discussion

Figure 7.2 shows a comparison of the ν(OH) band of water in SPEES/PES (S8) after diffusion from various ionic aqueous solutions. It is clear that there is no significant difference in shape of this band between these spectra. This may indicate that the state of water in SPEES/PES is independent of the ions present in the solution.

Figure 7.3 shows the plots of diffusion of water from some ionic aqueous solutions (Li^+, Na^+, K^+, Cs^+) measured by the integrated intensity of the ν(OH) band of diffusing water into SPEES/PES as a function of time. It is clear that the intensity at equilibrium level is different depending on the type of cation present. The order of the equilibrium intensity is: $Li^+ > Cs^+ > Na^+ > K^+$. The diffusion coefficients for the diffusion of these ionic solutions is shown in table 7.1. It is clear that the values of diffusion coefficients also follow the above order.

Ion	D_1 (cm²/sec)	D_2 (cm²/sec)	X_a
Pure Water	$(1.8 \pm 0.27) \times 10^{-8}$	$(2.16 \pm 0.24) \times 10^{-9}$	0.76 ± 0.03
Li^+	$(9.77 \pm 0.1) \times 10^{-9}$	$(15.6 \pm 0.1) \times 10^{-10}$	0.58 ± 0.02
Na^+	$(6.69 \pm 0.1) \times 10^{-9}$	$(5.13 \pm 0.1) \times 10^{-10}$	0.62 ± 0.03
K^+	$(4.27 \pm 0.1) \times 10^{-9}$	$(6.13 \pm 0.1) \times 10^{-10}$	0.53 ± 0.03
Cs^+	$(9.23 \pm 0.1) \times 10^{-9}$	$(7.18 \pm 0.1) \times 10^{-10}$	0.71 ± 0.04
Ca^{++}	$(6.05 \pm 0.1) \times 10^{-9}$	$(4.89 \pm 0.1) \times 10^{-10}$	0.51 ± 0.02

Table 7.1: *Diffusion coefficient of diffusion of water molecules into SPEES/PES (S8) in the presence of cations.*

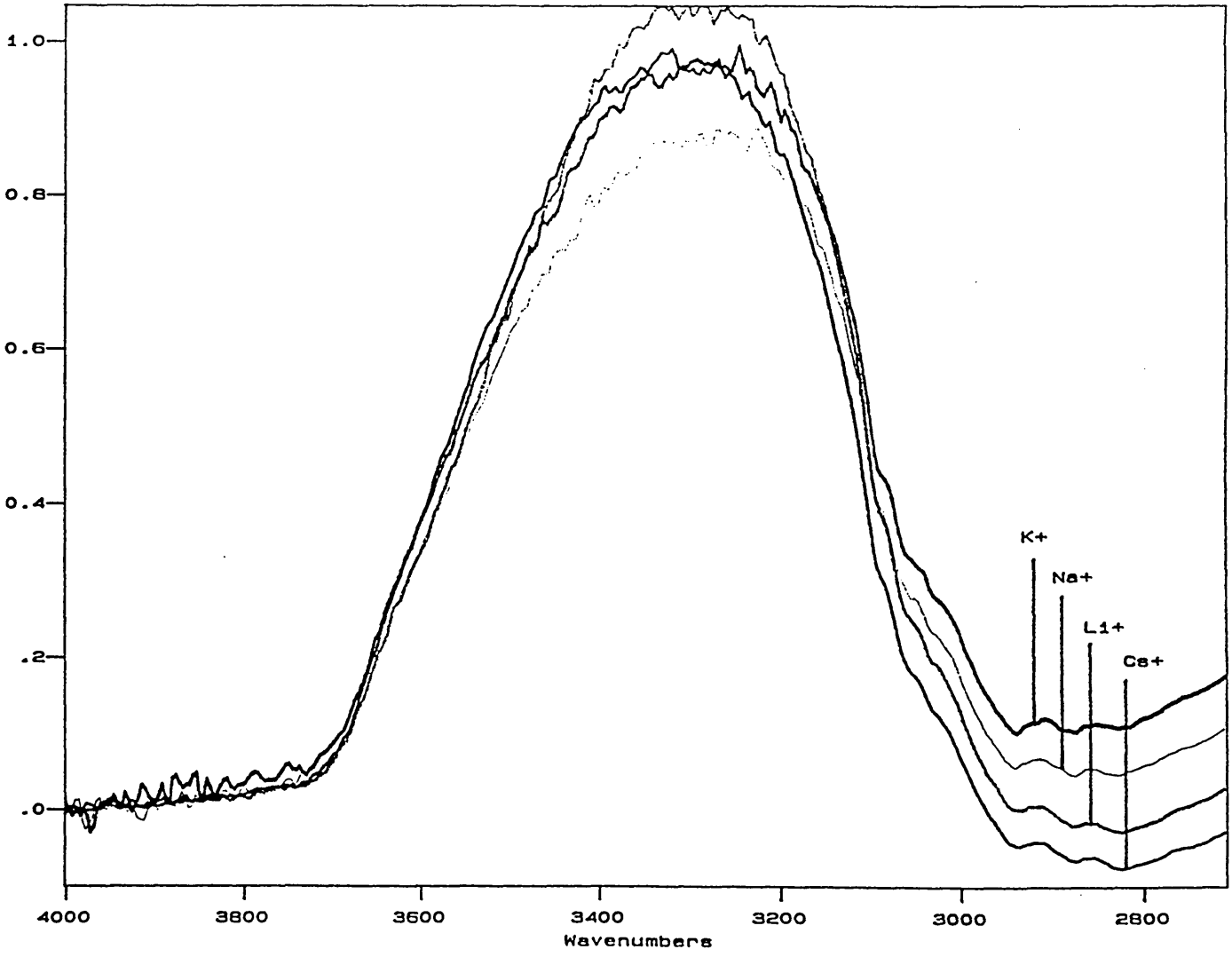

Figure 7.2: A comparison of ν(OH) band of water in SPEES/PES from various ionic aqueous solutions

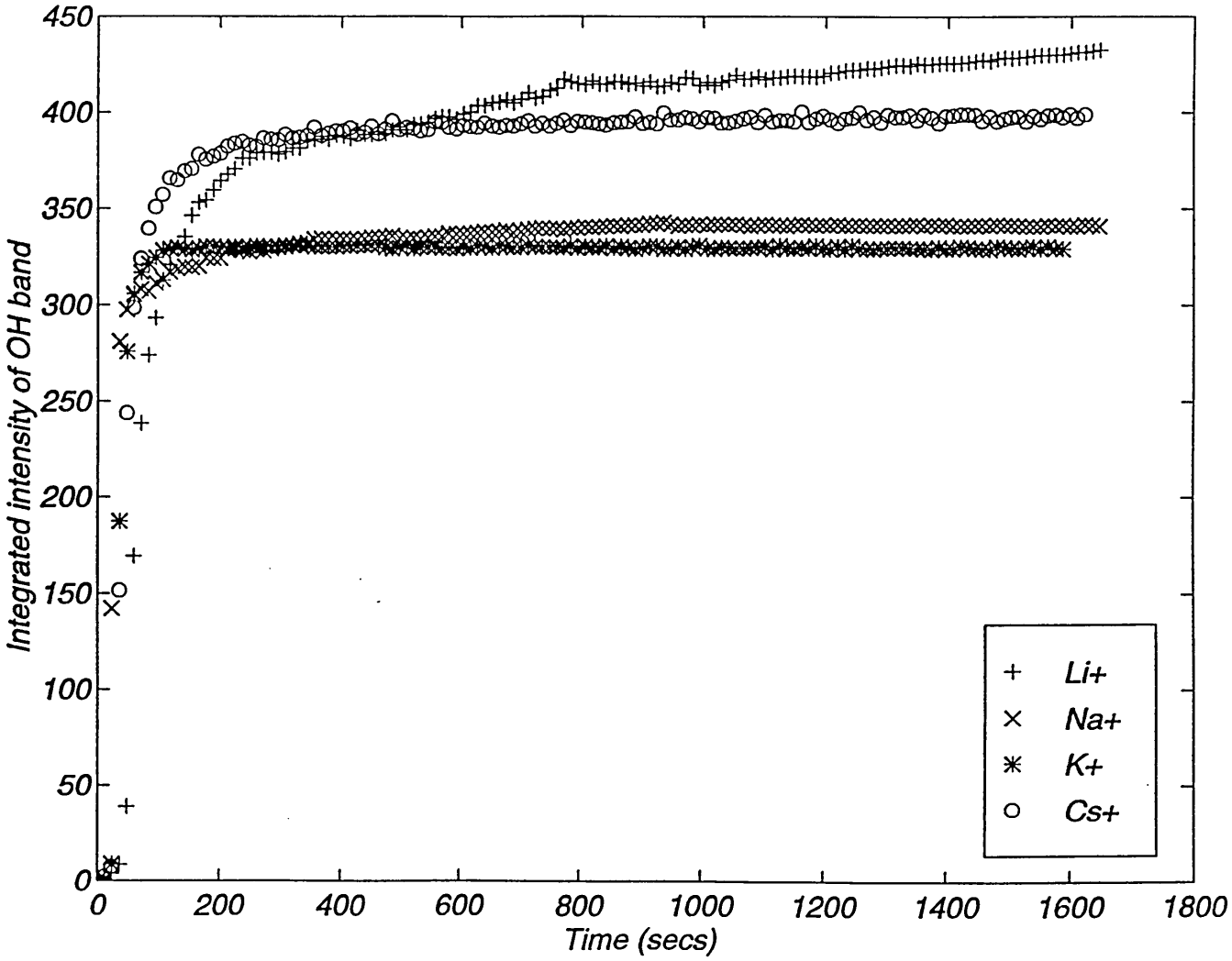

Figure 7.3: Plot of integrated intensity of the ν(OH) band as a function of time for diffusion of water from various aqueous ionic solutions

The above observations can be explained based on a combination of various factors affecting the diffusion of the water molecules into the SPEES/PES membrane. However, it should be noted that, it is difficult to draw a definite conclusion based on these data. In this section we have been tried to discuss a number of factors which are expected to be responsible for the above data. These include (a) the interaction of the polymer with the water molecules and the ionic species at the polymer surface before diffusion of the water molecules takes place, and (b) the effect of the hydrated ionic species on diffusion of water within polymer matrix.

Figure 7.4-7.8 show plots of log (A_t/A_∞) as a function of log (t). It is possible to determine the value of exponent 'n' in the following diffusion equation from the slope of the curves in figures 7.4-7.8.

$$\frac{\mathbf{M_t}}{\mathbf{M_\infty}} = \frac{4}{\mathbf{L}}\left(\frac{\mathbf{Dt}}{\pi}\right)^{\mathbf{n}}$$

or

$$\mathbf{Log}\left(\frac{\mathbf{M_t}}{\mathbf{M_\infty}}\right) = \mathbf{Log}\left(\frac{4}{\mathbf{L}}\right) + \mathbf{nLog}\left(\frac{\mathbf{D}}{\pi}\right) + \mathbf{nLog(t)}$$

The solid line indicates the slope for an exponent n=0.5. This represents case I (Fickian) diffusion. The other extreme is a case II diffusion when n=1. The slope of the curves corresponding to the diffusion of water from aqueous ionic solutions indicates that the exponent 'n' in each case has a value between 0.5 and 1. This indicates an anomalous diffusional behaviour and it is an evidence for need of a 'dual' mode model describing two Fickian behaviours.

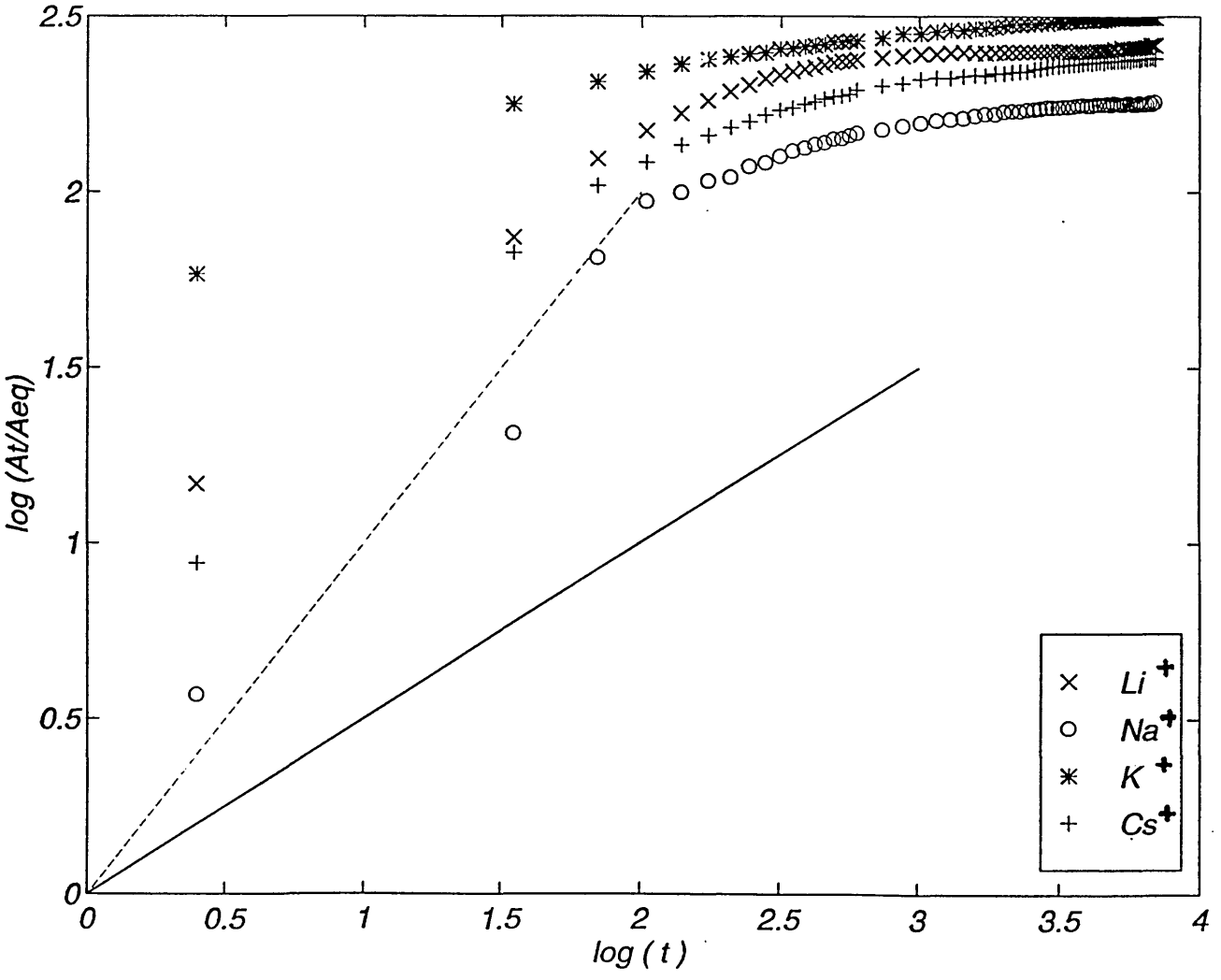

Figure 7.4: Plot of $\log(A_t/A_\infty)$ Versus log(t) for diffusion of water from aqueous ionic solutions into SPEES/PES (S8). Solid line: n=0.5 and dashed line: n=1

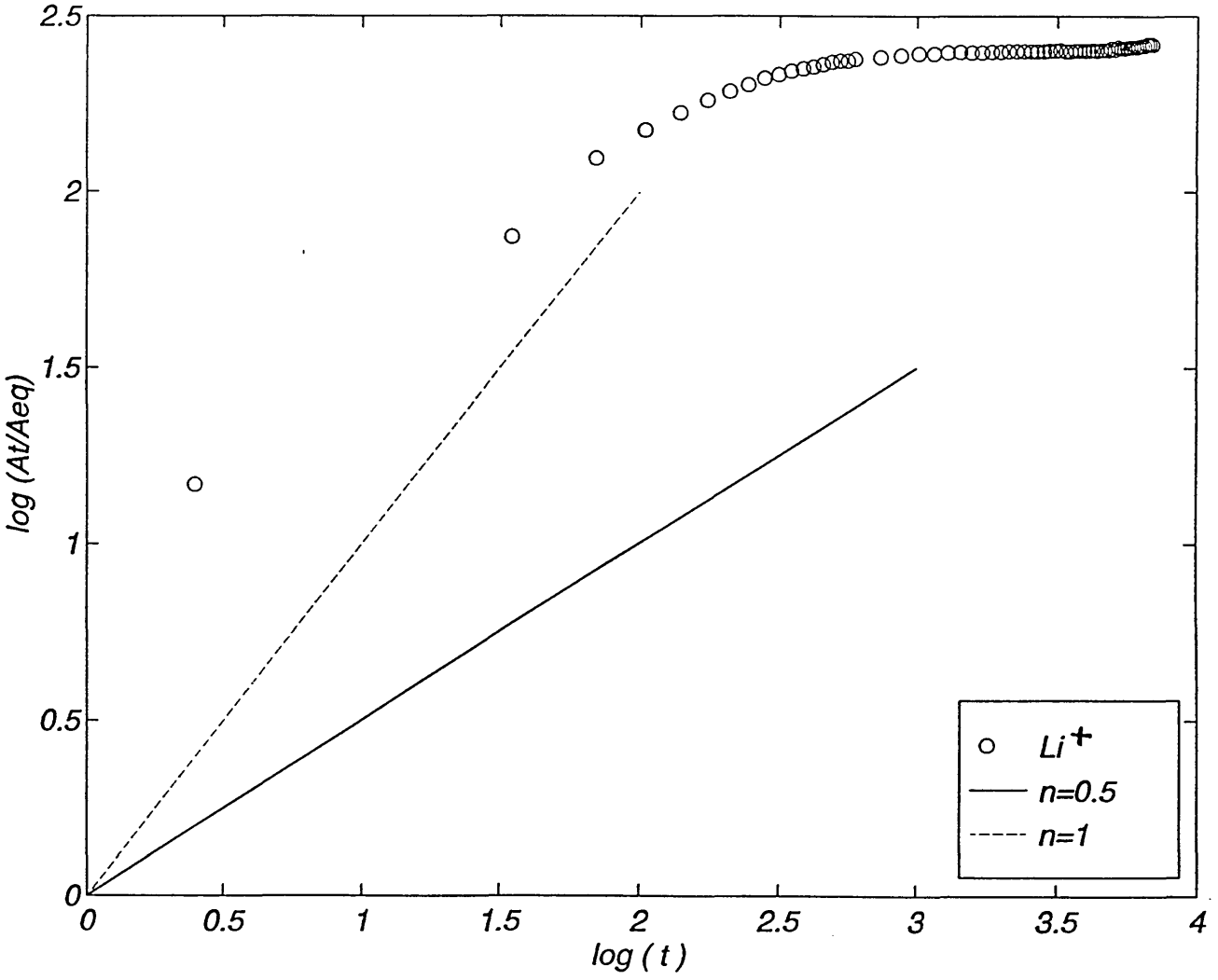

Figure 7.5: Plot of $\log(A_t/A_\infty)$ Versus log(t) for diffusion of water from aqueous Li^+ solution into SPEES/PES (S8). Solid line: n=0.5 and dashed line: n=1

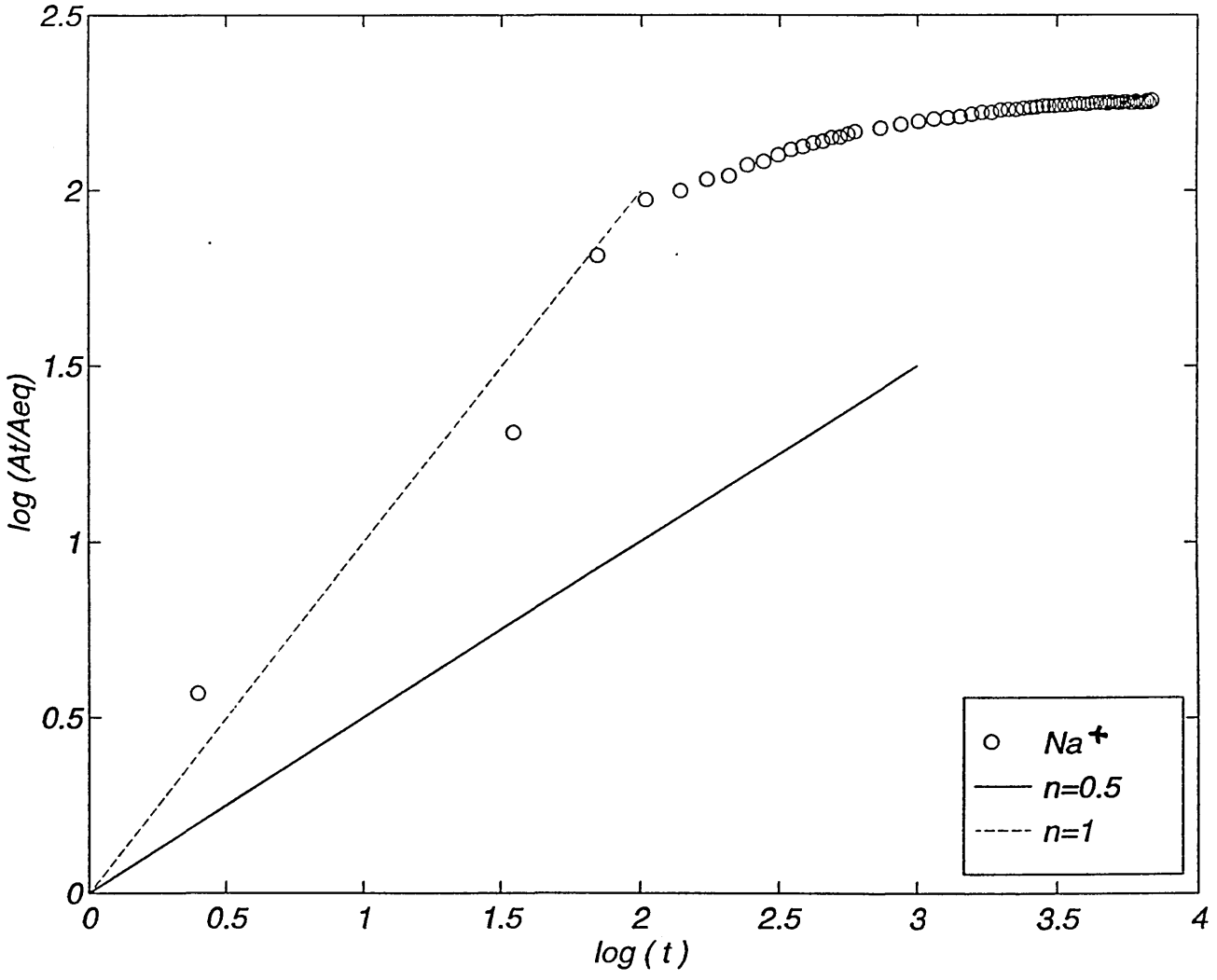

Figure 7.6: Plot of $\log(A_t/A_\infty)$ Versus log(t) for diffusion of water from aqueous Na^+ solution into SPEES/PES (S8). Solid line: n=0.5 and dashed line: n=1

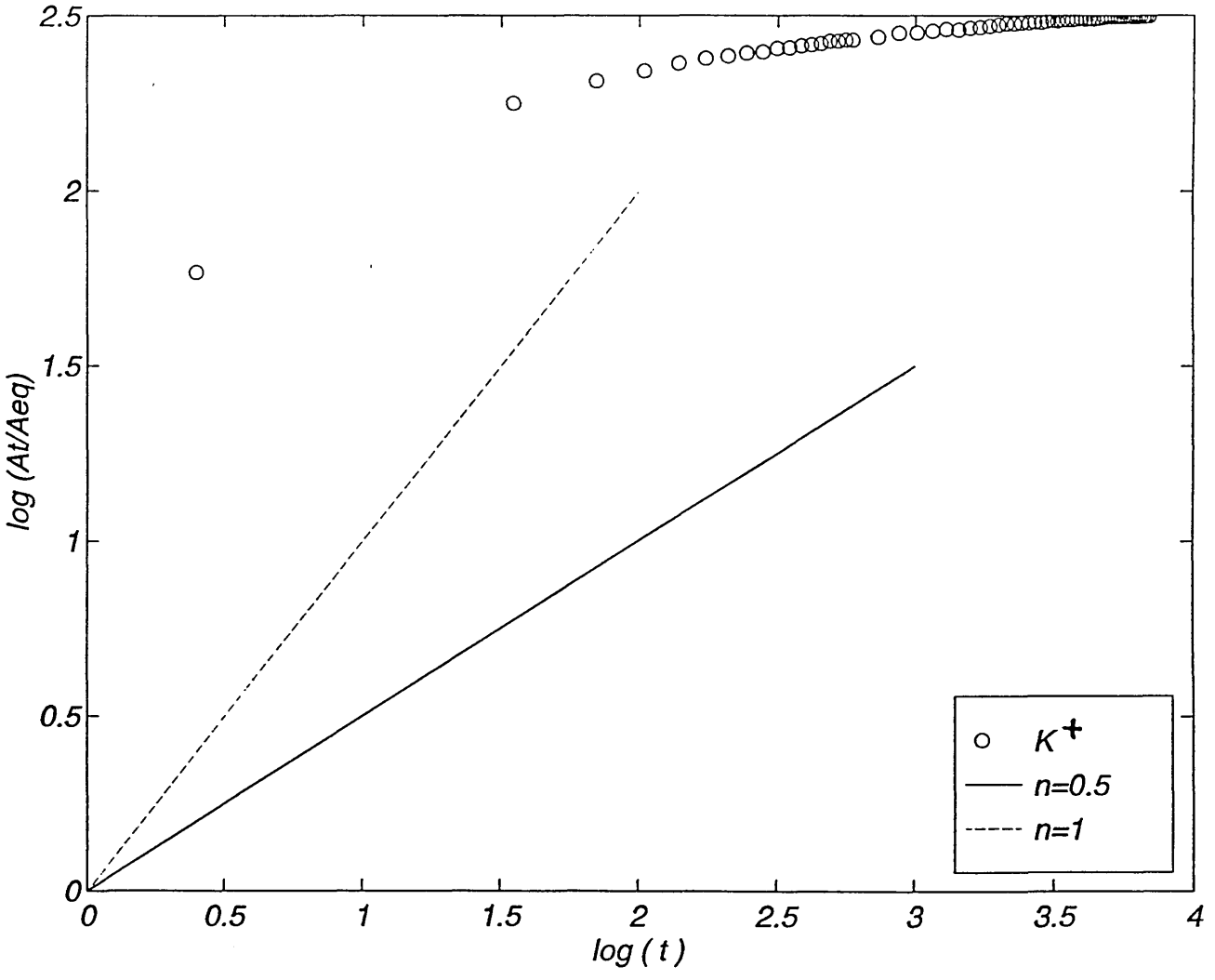

Figure 7.7: Plot of $\log(A_t/A_\infty)$ Versus log(t) for diffusion of water from aqueous K^+ solution into SPEES/PES (S8). Solid line: n=0.5 and dashed line: n=1

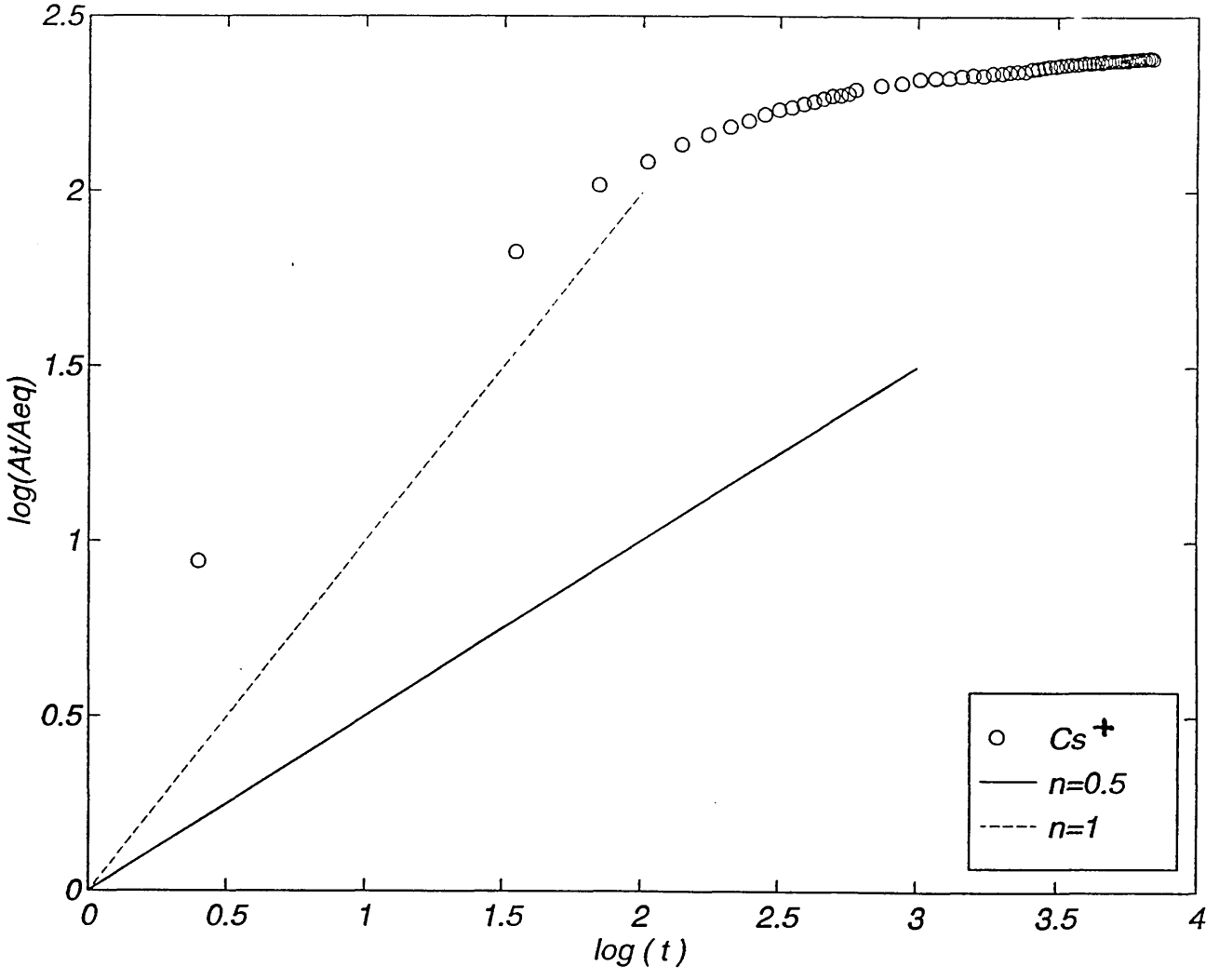

Figure 7.8: Plot of $\log(A_t/A_\infty)$ Versus log(t) for diffusion of water from aqueous Cs^+ solution into SPEES/PES (S8). Solid line: n=0.5 and dashed line: n=1

Quezado et al [7.1] characterised the water-anion-cation interactions at low water contents by studying the infrared spectra of Nafion membranes (see chapter 5) in twenty different cationic forms. Spectra in the OH stretching region and in the H-O-H bending region allowed the distinction between hydrogen bonded and non-hydrogen-bonded water molecules. This gave information on the mode of attachment of water molecules to the cation-anion pairs.

When there is a good match between the Lewis acid strength of the cation and the Lewis base strength of the anion, ion pairs are relatively stable and water molecules tend to attach themselves to the polymer surface. When the acid strength of the cation and the base strength of the anion are mismatched, as is the case for small cations of high charge or for large cations of low charge, water molecules tend to be inserted between the ion pairs even at the lowest water contents. Their study of the OH stretching (3520 cm^{-1}) and H-O-H bending (1630 cm^{-1}) bands showed that, at low water content, the attachment of water molecules to cations and anions in Nafion membranes may have the following three modes (See figure 7.9).

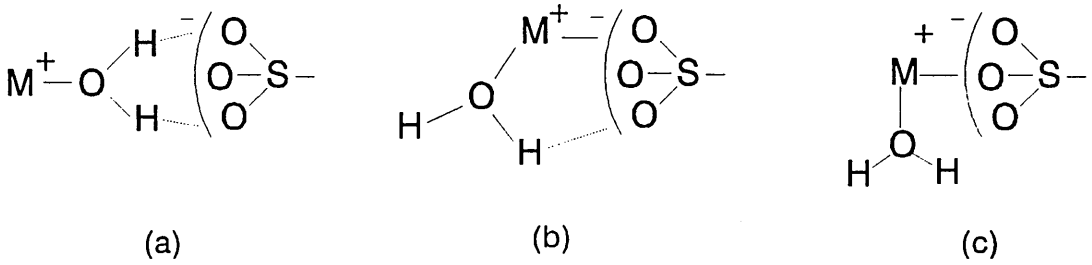

Figure 7.9: *various modes of attachment of water to cations and anionic sites in polymer film*

In mode (a), the water molecules are inserted between the cation and anion, while in modes (b) and (c), the water molecules are attached to the cation-anion pair without disrupting the cation-anion "bond". It would be expected that the interaction between cation and anion in mode (a) would be weaker than that in modes (b) and (c). Quezado et al [7.1] found that alkali metals followed mode (a) primarily, while for alkaline earth metals, modes (b) and (c) were dominant.

In another study, Lowry and Mauritz studied the ionic hydration effects in perfluorosulfonate ionomers by FTIR spectroscopy [7.2] by examining the changes in the $-SO_3^-$ symmetric stretching band which can be used to measure the strength of the interaction between cations and the SO_3^- groups. They showed that the position of the band was almost the same for Li^+, Na^+ and K^+ (1058 cm^{-1}) in hydrated membranes. This may be due to the presence of well developed hydration shells and thus the formation of completely dissociated ion pairs (no strong cation-anion interaction). However, in the case of Rb^+ and Cs^+, there is no well developed hydration shell. These ions can approach the polymer anionic groups ($-SO_3^-$) and form a stronger cation-anion interaction. In our work it was not possible to obtain well resolved $\nu(SO_3^-)$ bands with good S/N ratio in order to study the possible changes in the width and position of this band. This was due to highly absorbing nature of SPEES/PES in the relevant range of the IR spectrum.

A cation with weakly bound hydration shell, such as Cs^+, would be expected to form a relatively strong interaction with polymer anionic sites and in this way it is competing with the water molecules to be absorbed onto these sites. As a result of weaker hydration, more water molecules are present as totally mobile molecules to diffuse into the polymer film and hence give a higher level of water intensity at equilibrium. Whereas for Na^+ with strongly bound hydration shell, with relatively weak interaction with polymer, more water molecules are adsorbed on the anionic sites of the polymer.

In an ionic solution a number of different species are present including (a) hydrated anions and cations, (c) free water molecules, and (b) H_3O^+ ions. Bockris [7.3] suggested that the term 'primary solvation' (primary hydration in the case of water as solvent) be used to refer to the number of solvent molecules near to an ion which have lost their translational degrees of freedom and move as one entity with the ion during its Brownian motion. The size of primary hydration shell of various ions is different and dependent upon the charge/size ratio of the ions. Smaller ions bind more water than larger ions, and cations somewhat more water than anions (since the positive charge is more effective in polarising the negative electronic clouds of the solvent molecules).

There are a number of methods for determining the hydration number. Unfortunately, these methods give different results [7.4]. Data for univalent ions can be divided into two classes: hydration numbers less than ten; and those considerably greater than ten. Methods giving the lower values measure the primary hydration number and those giving higher values, the primary hydration together with an indefinite contribution from the secondary hydration. Table 7.2 shows the hydration number of a number of ions. The heats of hydration and bare ionic radii of the ions used in this work are shown in table 7.3.

Ion	From compressibility	From entropy	From apparent molar volume	From mobility	Most probable integral value
Li^+	5 - 6	5	2.5	6	5 ± 1
Na^+	6 - 7	4	4.8	2.4	4 ± 1
K^+	6 - 7	3	1.0	-	3 ± 2
Cs^+				-	0-1
Mg^{++}	16	13		14	13 ± 1
Ca^{++}	-	10		7.5 - 10.5	9 ± 1
Cl^-	0 - 1	3	0	-	2 ± 1

Table 7.2: *Primary hydration number of individual ions as determined by various methods [7.5]*

Ion	Heat of Hydration (Kcal g ion^{-1})	Bare ionic radius, (nm)
Li^+	-136	0.068
Na^+	-114	0.095
K^+	-94	0.133
Cs^+	-80	0.169
Mg^{++}	-490	0.061
Ca^{++}	-410	0.099
Cl^-	-65	0.181

Table 7.3: *Heat of hydration and bare ionic radius of individual ions [7.6]*

SPEES/PES is an ion exchange polymer. Since, the sulphonation of the copolymer occurs in 98% H_2SO_4, the counter ions are H^+ ions. The counter ions are partially free and can readily be exchanged for others of the same sign from soluble electrolytes. On this basis, as a result of long exposure of the SPEES/PES film to such ionic solutions, an ion exchange process is expected. When the polymer film is exposed to an ionic solution, it is expected that the free water molecules and the hydrated ionic species will be adsorbed on the surface of the polymer film. The polymer contains anionic sites (SO_3^-), and the surface of the polymer will be in contact with the ionic solution containing H_3O^+.

An array of H_3O^+ ions as well as the hydrated ionic species is formed adjacent to the polymer surface (figure 7.10). As a result of adsorption of some of the hydrated ionic species, it is expected that a number of the water molecules are prevented from adsorption on the surface of the polymer and consequently diffusion into the polymer matrix will be affected.

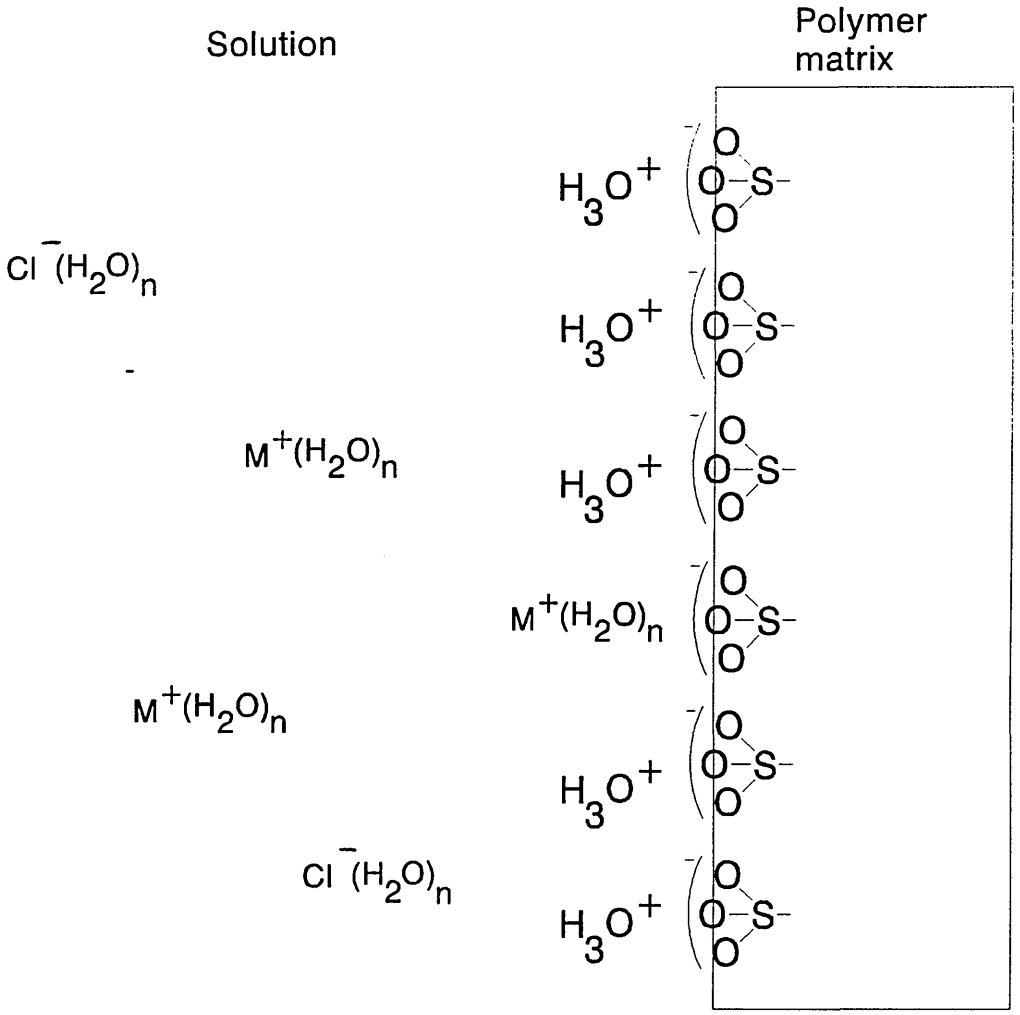

Figure 7.10: *Polymer surface in contact with an ionic aqueous solution*

The nature of these species depend on their hydration number and hydration plays an important role in; (a) the specific adsorption on the polymer ionic sites. In general, the specific adsorption of an ion is enhanced by large size and therefore larger polarisability (charge/size ratio) and by weaker hydration, which itself is a function of ion size. For example, the large I^- ion is the most strongly adsorbed and the small but highly hydrated Na^+ ion is adsorbed least. (b) the larger hydrated ions occupy more space at the surface of the polymer and thus prevent more water molecules being adsorbed and further diffusing into the polymer film.

On this basis, it is expected that the diffusion of water molecules from various cationic solutions to be different. From table 7.1, it is clear that the diffusion of water into SPEES/PES from Li^+ and Cs^+ solutions have greater diffusion coefficients than those of Na^+ and K^- solutions.

One possible reason for this observation is that strongly hydrated small $Li^+(H_2O)_n$ has weak adsorption via solvent separated interaction. Therefore, there is easy H_2O access to the surface. Weakly hydrated ions like $Cs^+(H_2O)$ have ion-ion interaction but the charge/size ratio is small so the interaction is not strong and water access is still relatively high. Na^+ and K^+ have higher charge/size ratio and can interact via ion-ion interactions and effectively stop water molecules getting to surface. As a result, the diffusion coefficient decreases. This argument is consistent with the data.

SPEES/PES is a reverse osmosis membrane and, on this basis, it is expected that most of the ionic species are prevented from penetrating into the polymer matrix. However, it is reasonable to expect that a number of these species diffuse into the membrane and also carry with them some water molecules (depending on their hydration shell).

The results obtained in this study are in a good agreement with those of Xue et al [7.7]. who studied the interdiffusion of metal ion-hydrogen ion couples in Nafion (see chapter 5) membrane systems by a rotating diffusion cell (RDC) technique. They showed that at high metal concentration (0.1 mol/l), the transport rate is controlled by membrane diffusion and the metal diffusion follows the order $Li^+ < Cs^+ < Rb^+ < Na^+ < K^+$ for alkali metals, and $Y^{3+} < Ca^{2+} < Na^+$ for ions of similar ionic size (0.095-0.099 nm). It is clear that this order of diffusion is the reverse of the order of data obtained in this study. However, it should be noted that they measured the diffusion of metal ions into the polymeric system, whereas in the studies described here the diffusion of water molecules in the presence of the above cations is described. This

implies that maybe there is some degree of competition (and maybe complementarity) between the diffusion of ionic species and water molecules.

It should be noted that in a FTIR-ATR experiment, the amount of those water molecules measured are those detected within the range of the evanescent field (see chapter 1). However, it is clear that there are a number of types of water molecules present during the diffusion process. The major categories include: (a) free water molecules which are totally mobile and can diffuse into the polymeric system freely, (b) water molecules which are surrounding the metal ions (hydration shell) and move with the metal ions, (c) water molecules which are bound to the ionic sites of the polymeric system (ionomer), (d) the H_3O^+ ions, and (e) the water molecules forming water "clusters" possibly in the microvoids within the polymer matrix. In this study we have measured the integrated intensity of the ν(OH) band of diffusing water which results from a combination of of these different types of water molecules. It should be noted that it is more difficult to distinguish a particular diffusion process.

As described earlier, it is known that in aqueous solutions, metal ions are generally surrounded by a layer (or multilayer) of water molecules. The hydration number depends on both ionic radius and charge (charge/size ratio) and the diffusion rate of an ion in aqueous solution depends on the size of its hydration shell.

However, in a polymer matrix the movement of the hydrated ions seems to be different from that in aqueous solutions. Crank and Park [7.8] state that diffusion coefficients in the polymer are always less than those of the same ions in free solution. This is partly due to the obstructing effect of the polymer chains. Alfrey et al [7.9] showed that, at infinite dilution, a high proportion of the counter-ions would always be found within a few Å of the chain. Thus an electrical double layer is formed by the fixed charges and the attendant counter-ions. It is relatively easy for the counter-ions to diffuse in a direction parallel to the chain axes because they then remain within the cylindrical shell

in which their electrostatic potential is low. This mechanism is called "chain diffusion" [7.10] and would lead to very tortuous diffusion paths. In order to jump from the atmosphere around one chain to its neighbour, the counter-ions have to overcome the intervening electrostatic potential barrier in the direction of diffusion. This process which is called [7.10] "volume diffusion", becomes more and more difficult as the separation of the chains is increased by swelling. Both mechanisms of diffusion occur simultaneously in relative amounts which are determined by the swelling, ionic concentration and temperature.

In concentrated polyelectrolyte solutions, the double layers around neighbouring chains overlap considerably and the potential barriers present less hindrance to volume diffusion. In such solutions the obstruction to diffusion is mainly caused by the bulky polymer chains and causes the diffusion coefficient to decrease with increasing concentration. Boyd and Soldano [7.11] have examined the effects of valency and type of counter-ion and have shown that the degree of swelling in the polymers varies and depends on the nature of the counter-ions. It tends to be greater with highly hydrated ions, such as magnesium, than with relatively poorly hydrated ions, such as Cs^+.

Since, the ion diffusing into the membrane carries a number of water molecules (depending on its hydration number) it is expected that, when a cation such as Na^+ or Li^+ with relatively large hydration shell enters the range of the evanescent field, it brings more water molecules into this 'detecting' region than a cation with a poorly bound hydration shell such as Cs^+. On the other hand, the ions a with strongly bound hydration shell, cause greater extent of swelling and are expected to diffuse slower than less hydrated ions due to decreased volume diffusion (jumping from one polymer chain to its neighbour).

Table 7.1 shows the diffusion coefficient for the diffusion of water in aqueous Na^+ and Ca^{++} solutions. These two ions have similar bare ionic sizes (0.095 - 0.099 nm). However, it is clear that diffusion coefficient of water molecules from Ca^{++} solution is lower than that of Na^+ solution.

This observation may also be explained by the effect of charge/size ratio of Ca^{++} and Na^+ ions on adsorption onto polymer anionic sites. Ca^{++} ion, with a similar size to Na^+ but a greater charge/size ratio has a greater ion-surface interaction and competition of these hydrated cations for adsorption on the surface of the polymer film with water molecules and also the metal ion-sulfonate interactions.

All of the aqueous ionic solutions used so far were prepared from the chloride salts and thus Cl^- ion was present as the anion. It was shown that various cations have significant effect on the diffusion of water into the SPEES/PES membrane. In order to study the effect of anions other than Cl^- ion, a $NaNO_3$ solution was prepared and the effect of NO_3^- ion was examined.

Figure 7.11 shows the integrated absorbance of ν(OH) band of diffusing water into SPEES/PES as a function of time from aqueous solution containing NO_3^-. The comparison of the diffusion curve of water from NO_3^- ion solution with that of Cl^- ion solution is shown in figure 7.12. It is clear that the intensity at equilibrium is lower in diffusion of water from Cl^- ion solution than that of NO_3^- ion solution. It is expected that the NO_3^- ion with greater size than Cl^- ion causes greater degree of swelling in the polymer. As a result, more water molecules will be present in the polymer matrix and thus, greater water intensity at equilibrium.

7.3. Effect of ionic concentration on diffusion of water into SPEES/PES

The effect of various ions on the diffusion of water into SPEES/PES (S8) was described in section 7.2. However, it is important to know whether the concentration of these ions in the aqueous solution has any significant effect on diffusion of water.

7.3.1. Experimental

A variety of Na+ aqueous solutions were prepared with different concentrations. NaCl (99.99%) was obtained from Aldrich Chemical Company. The polymer films were SPEES/PES (S8) and were cast from a NMP solution on ZnSe ATR prism and annealed at 65 °C. The infrared spectra were collected using a Mattson Polaris spectrometer. The FTIR-ATR technique was utilised and the spectrometer parameters are summarised in table 6.2. The spectra were manipulated using Mattson FIRST® software.

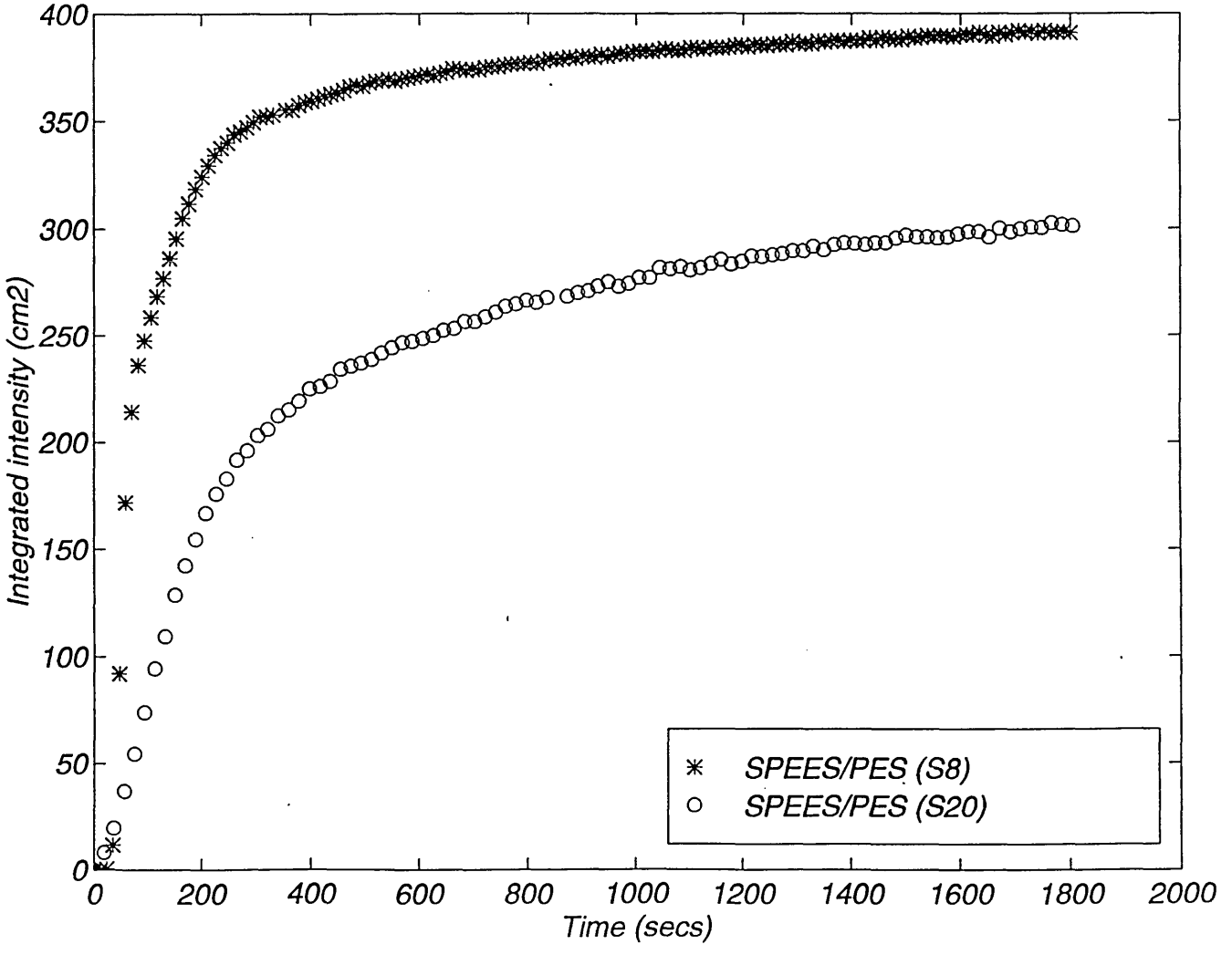

Figure 7.11: *A plot of integrated absorbance of ν(OH) band as a function of time for diffusion of water from NO_3^- ion solution in SPEES/PES (S8) and (S20)*

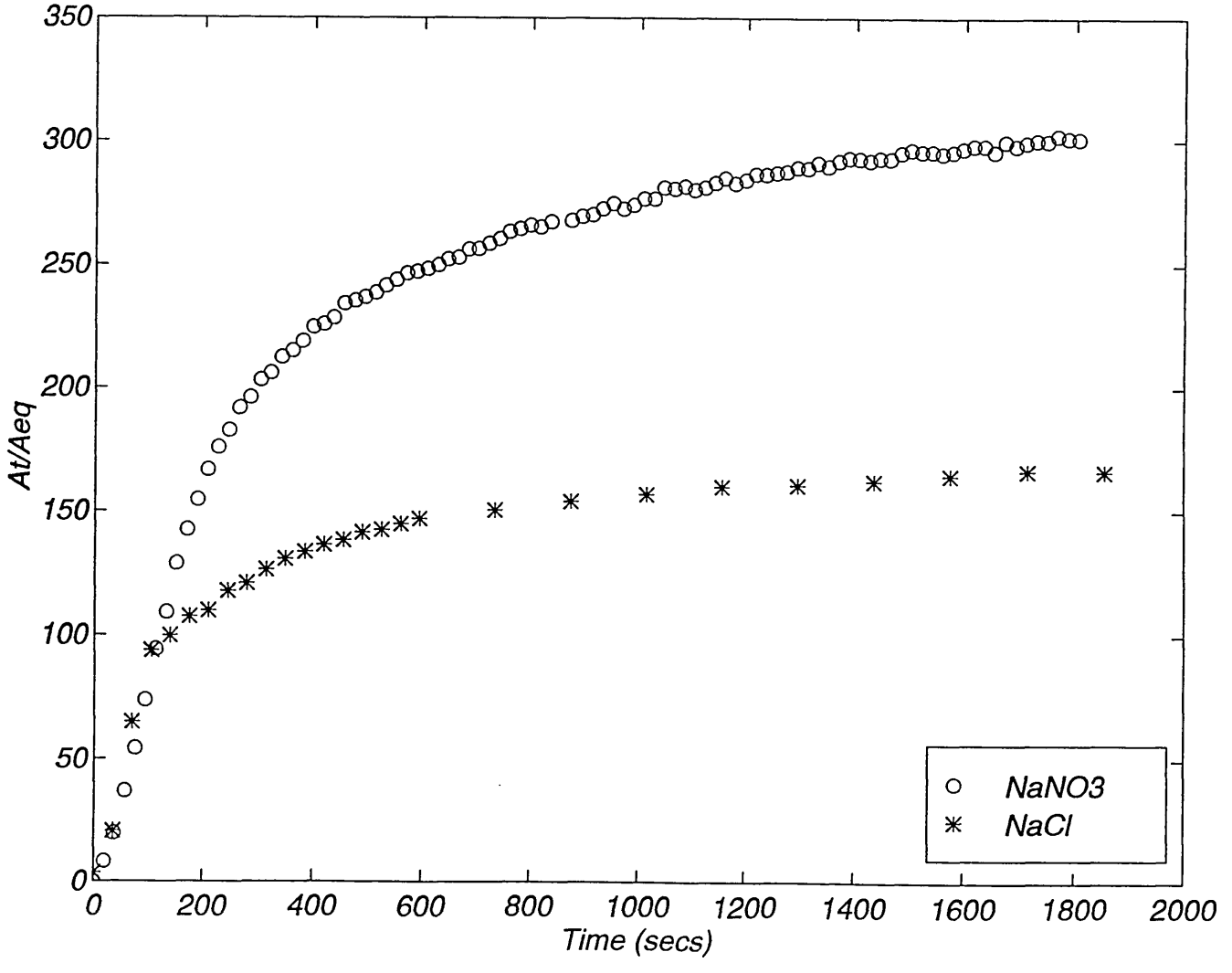

Figure 7.12: A plot of integrated absorbance of v(OH) band as a function of time for diffusion of water from NO_3^- ion and Cl^- solutions into SPEES/PES (S8)

7.3.2. Results and Discussion

Table 7.4 shows the values of diffusion coefficients for diffusion of water from sodium chloride solutions with different concentrations into SPEES/PES (S8). It is clear that both diffusion coefficients; D_1 and D_2 decrease with increasing Na^+ ion concentration.

One possible explanation for these variation in value of diffusion coefficients is the effect of hydrated Na^+ ion on adsorption of water molecules on the surface of the polymer film.

Concentration (mole)	D_1 (cm^2/sec)	D_2 (cm^2/sec)	X_a
Pure Water	$(1.80 \pm 0.27) \times 10^{-8}$	$(5.96 \pm 0.24) \times 10^{-9}$	0.76 ± 0.03
0.2	$(6.76 \pm 0.08) \times 10^{-9}$	$(5.21 \pm 0.09) \times 10^{-10}$	0.81 ± 0.04
0.6	$(4.69 \pm 0.1) \times 10^{-9}$	$(2.66 \pm 0.08) \times 10^{-10}$	0.71 ± 0.03
0.85	$(2.27 \pm 0.1) \times 10^{-9}$	$(1.45 \pm 0.1) \times 10^{-10}$	0.66 ± 0.04

Table 7.4: *Diffusion of water from Na^+ aqueous solutions with various concentration into SPEES/PES (S8).*

As was described in section 7.2., upon exposing the SPEES/PES (S8) polymer surface containing anionic sites (SO_3^-) to an aqueous Na^+ solution, a double layer analogous to an electrode double layer is formed. The hydrated Na^+ ions as well as the water molecules are adsorbed on the surface of the polymer. It is clear that in this way the higher concentration of the ions in the solution, the greater the surface of the polymer film which will be occupied by the ions. On this basis, it is clear that the diffusion of water molecules into the polymer matrix will be slower and thus a lower diffusion coefficient. It is also for this reason that, as can be seen from table 7.4, the diffusion of water molecules from pure bulk water is much faster than that of aqueous ionic solutions.

Increasing the Na^+ ion concentration can also increase the swelling of the polymer matrix. Since the polymer chains have to accommodate more ions in the matrix, thus more water molecules will be present in the polymer at the equilibrium state. This is manifested as a greater intensity of the ν(OH) band at the equilibrium (see figures 7.13 and 7.14).

A plot of $\log(A_t/A_\infty)$ as a function of log(t) for diffusion of water from Na^+ ion solution with various concentrations is shown in figure 7.15. It is clear that the exponent 'n' again takes a value between 0.5 and 1. This indicates an anomalous diffusion behaviour and the need for a 'dual' mode diffusion model.

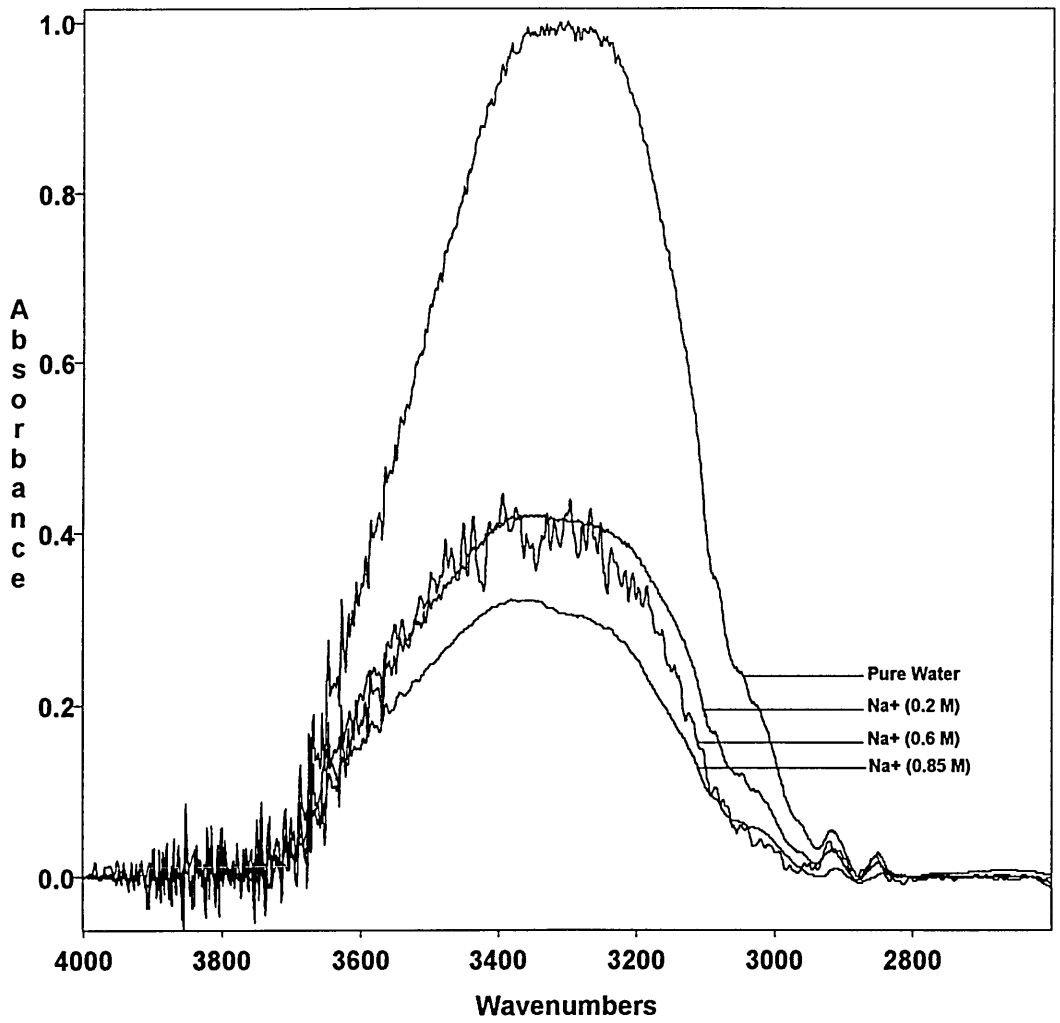

Figure 7.13: *A comparison of ν(OH) band of water at equilibrium in SPEES/PES (S8) from aqueous Na+ solutions with different concentrations*

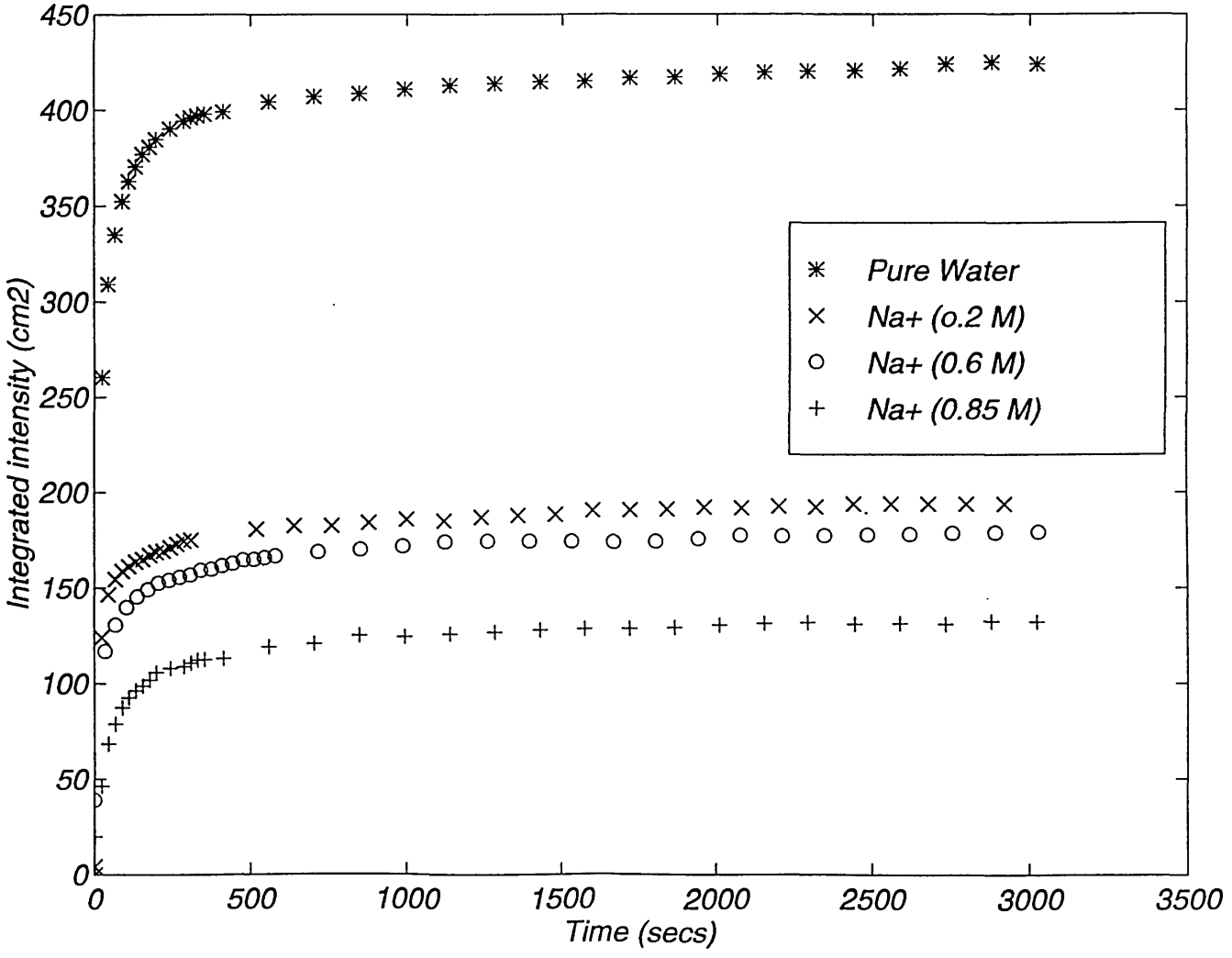

Figure 7.14: A plot of the integrated intensity of v(OH) band versus time for diffusion of water into SPEES/PES (S8)

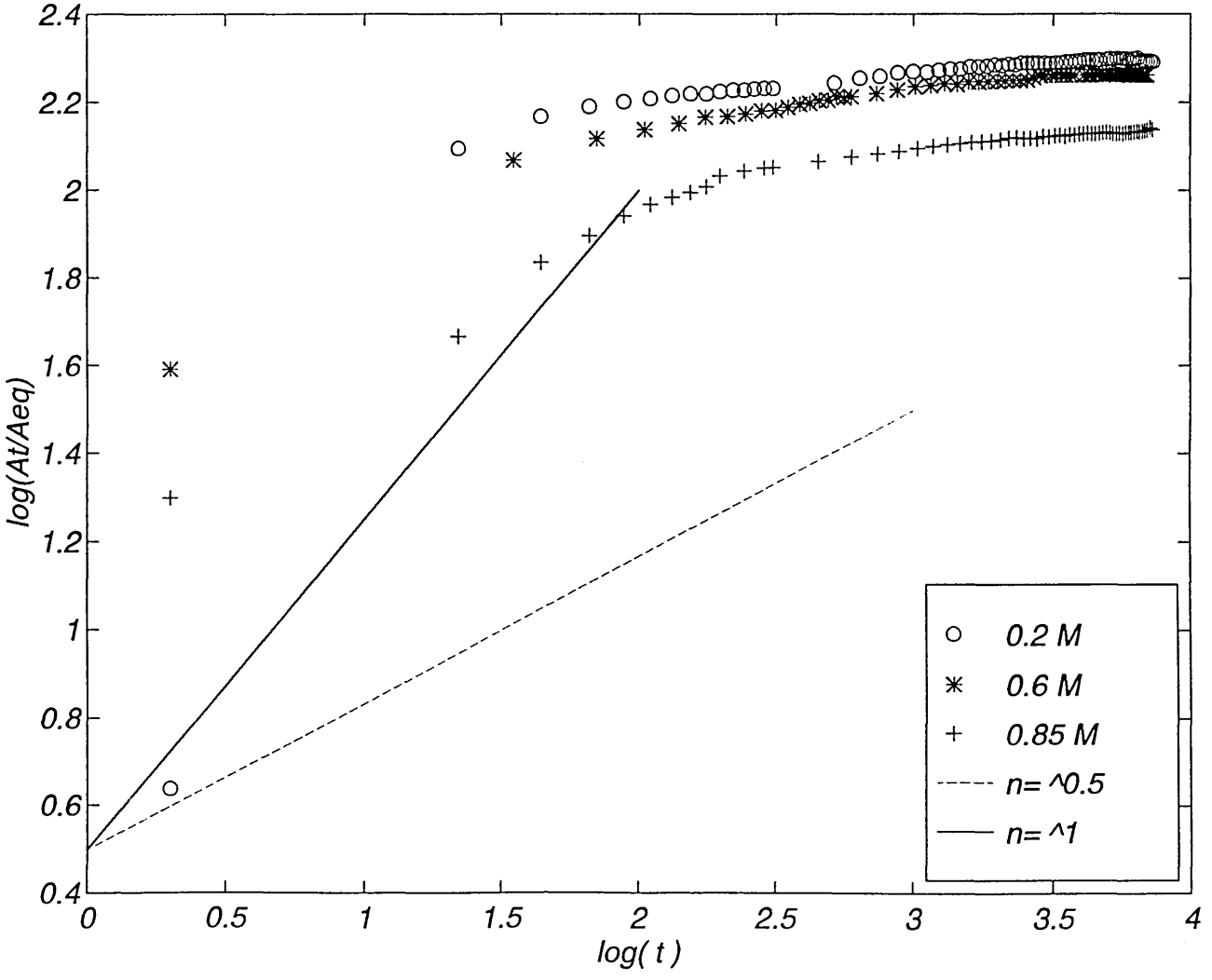

Figure 7.15: A plot of $\log(A_t/A_\infty)$ versus log(t) in diffusion of water from Na+ ion solutions with various concentrations

7.4. SPEES/PES-PVOH laminate

A polymer membrane used for desalination purposes consist of various layers. These include: (a) an ultra fine membrane with honeycomb structure for supporting the fragile sulphonated polyetherethersulphone/ polyethersulphone (SPEES/PES) layer, (b) a layer of SPEES/PES, and (c) a layer of insoluble polyvinylalcohol.

So far, the study of the diffusion of water into a single layer of SPEES/PES has been described. However, in order to examine the diffusion of water into a multilayer film, a two-layered model sample consisted of a top layer of PVOH and a bottom layer of SPEES/PES (S8) was prepared.

The possible changes at the interface between the constituent layers before and after diffusion of water was studied by Raman confocal microspectroscopy (see section 2.4.2.) and a depth profile of the laminate was obtained. The diffusion of water into the laminate was studied using FTIR-ATR spectroscopy technique.

7.4.1. Experimental

(a) Sample preparation

PVOH was purchased from Aldrich Chemical Company Ltd and SPEES/PES (S8) was obtained from NWW Acumem Limited.

The SPEES/PES (S8) layer (bottom layer) of laminate films was deposited onto a ZnSe ATR prism from N-methyl-2-pyrrolidonone, NMP (99+%, HPLC grade) using the dip coating procedure [3.22]. A PVOH film was then deposited onto the SPEES/PES (S8) layer as a 'coating' by the same technique with water as solvent, to produce a laminate. At each stage samples were dried in the oven at 65 ^{o}C for 24 hours.

In previous depth profiling experiments, the laminate was deposited onto a quartz slide in order to prevent interfering fluorescence from the substrate in Raman spectroscopy. However in this study, the laminate was deposited on a ZnSe ATR prism. In this way it is possible to obtain a depth profile of the laminate before and after diffusion of water into the film from the same point on the laminate film.

Figure 7.16 shows a schematic diagram of such polymer laminates. The thickness of PVOH and SPEES/PES layers were determined to be 3 and 7 μm (within 5% and 2 % accuracy), respectively, with the use of a surface profiler (Laser Form Talysurf).

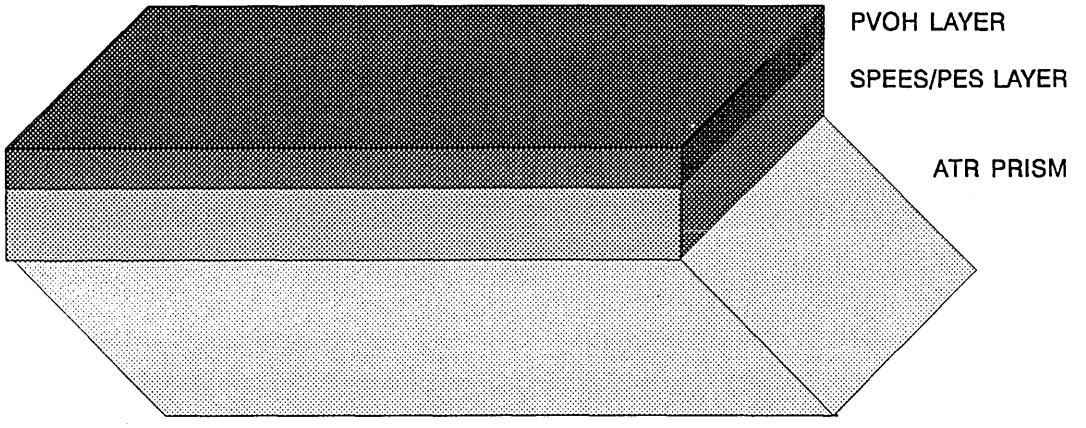

Figure 7.16: *The quartz slide and the deposited polymer laminate of PVOH-SPEES/PES.*

(b) Raman confocal microspectroscopy procedure

Raman spectra were recorded on a Renishaw Ramascope© spectrometer (system 2000). The Ramascope was set up in confocal mode using a 100x short-working-length objective (NA value of 0.95), a slit width of about 15 μm and a CCD area of 4 x 576 pixels. The long axis (576 pixels) defines the spectral dimension and the short axis describes the height of the image. The arrangement of the CCD and the slit width acts as the pinhole for blocking out-of-focus signals. This confocal arrangement provides the depth resolution of about 2.5 ± 0.3 μm.

A depth profile of each laminate was then obtained by focusing the microscope stepwise (1 μm) through the polymer laminate and recording a spectrum at each step. The position, area and the full width at half height (FWHH) of the important bands were determined as a function of the depth using the Renishaw curve-fitting programme.

(c) FTIR-ATR procedure

The diffusion of water into the laminate was studied by FTIR-ATR technique. A Mattson Polaris FTIR spectrometer was utilised and the instrumental parameters are summarised in table 6.2. The temperature of the diffusing water was 25 ^{o}C.

7.4.2. Results and Discussion

(a) Depth profiling

Figure 7.17a shows a Raman depth profile of the laminate before diffusion of water. The bands at 854 and 917 cm^{-1} correspond to PVOH and the bands at 1071 and 1146 cm^{-1} correspond to SPEES/PES. Since the depth resolution of the confocal Raman technique used in this is 2.5 ± 0.3 μm, it is expected that the characteristic bands of the bottom layer to be observed in this spectrum. However, it is the spectra corresponding to the depths of 2 - 6 μm which show evidence of a laminate interface between the two layers. All of the characteristic bands at a depth of 9 μm correspond to pure SPEES/PES.

After the depth profile of the dry laminate has been collected, the film was subjected to diffusion of pure water. In order to examine any changes to the interface layer as a result of water diffusion, the depth profile of the wet film at the same point (where the depth profile of dry film has been collected) was obtained. Figure 7.17b shows the corresponding Raman spectra.

A comparison of the spectra corresponding to the interfacial region of the laminate before and after diffusion shows no changes to the position or the shape of the bands corresponding to PVOH or SPEES/PES. This may indicate that there are no significant interactions between these two polymers at the interface or only weak interactions of water with polymer. However, it should be noted that the spectral resolution of the Raman confocal technique using a Renishaw Ramascope is 2 ± 0.2 cm^{-1}. Thus, spectral changes smaller than this cannot be accurately determined.

(b) Diffusion of water

Figure 7.18 shows a plot of integrated intensity of ν(OH) band of diffusing water as a function of time. A comparison of the curves corresponding to the diffusion of water in a SPEES/PES film with that of SPEES/PES-PVOH laminate shows that the intensity at the equilibrium is lower in the case of laminate than a single film of SPEES/PES. Table 7.5 shows the values of diffusion coefficient corresponding to water diffusion into a SPEES/PES film and a SPEES/PES-PVOH laminate.

Membrane	D_1 (cm^2/sec)	D_2 (cm^2/sec)	X_a
SPEES/PES (S8)	$(1.52 \pm 0.27) \times 10^{-8}$	$(1.47 \pm 0.24) \times 10^{-9}$	0.76 ± 0.03
SPEES/PES-PVOH	$(3.95 \pm 0.08) \times 10^{-8}$	$(3.91 \pm 0.09) \times 10^{-10}$	0.70 ± 0.04

Table 7.5: *Diffusion coefficient corresponding to diffusion of water into SPEES/PES and SPEES/PES-PVOH laminate*

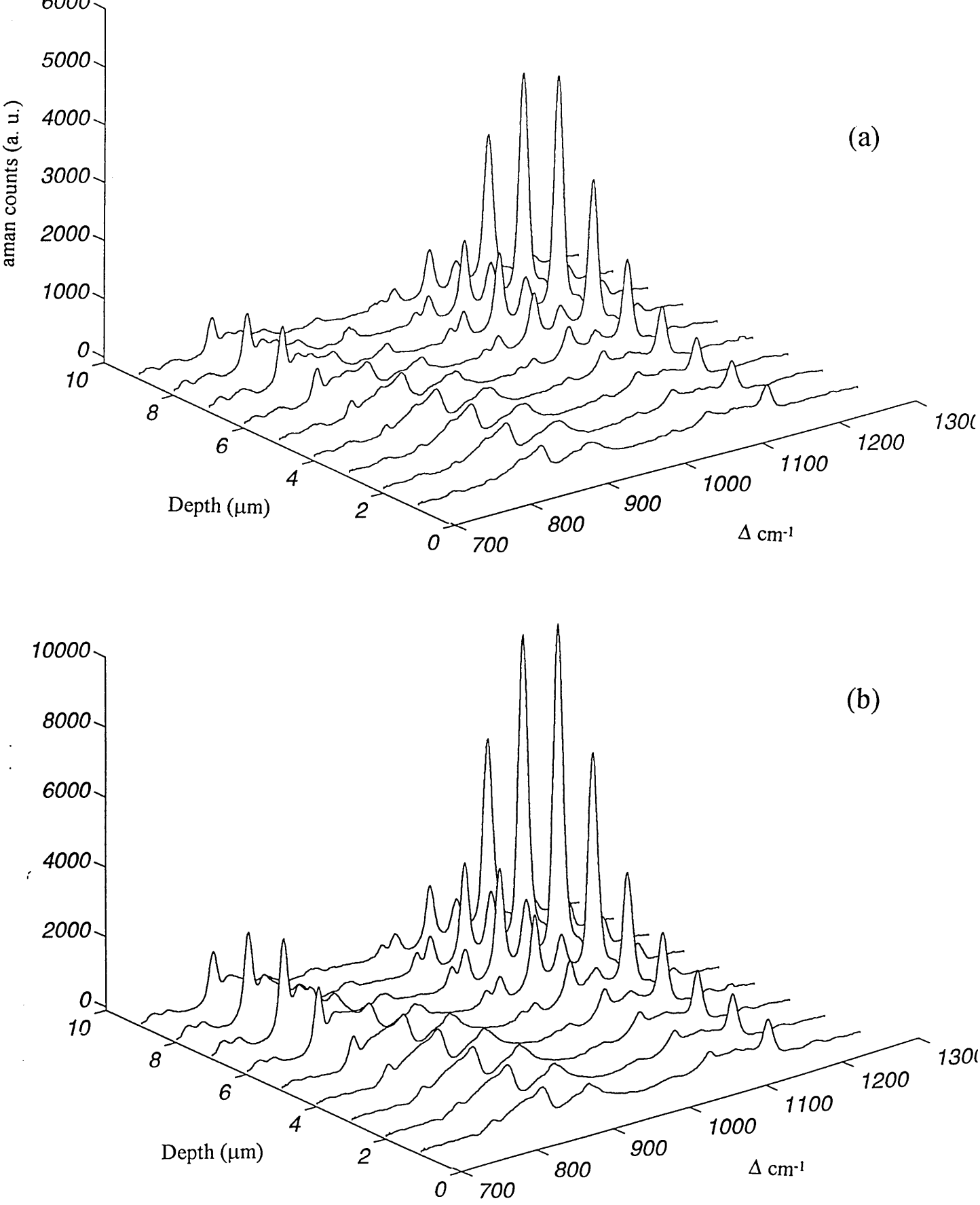

Figure 7.17: *Depth profile of (Raman spectra) a SPEES/PES - PVOH laminate (a) before diffusion of water, (b) after diffusion of water*

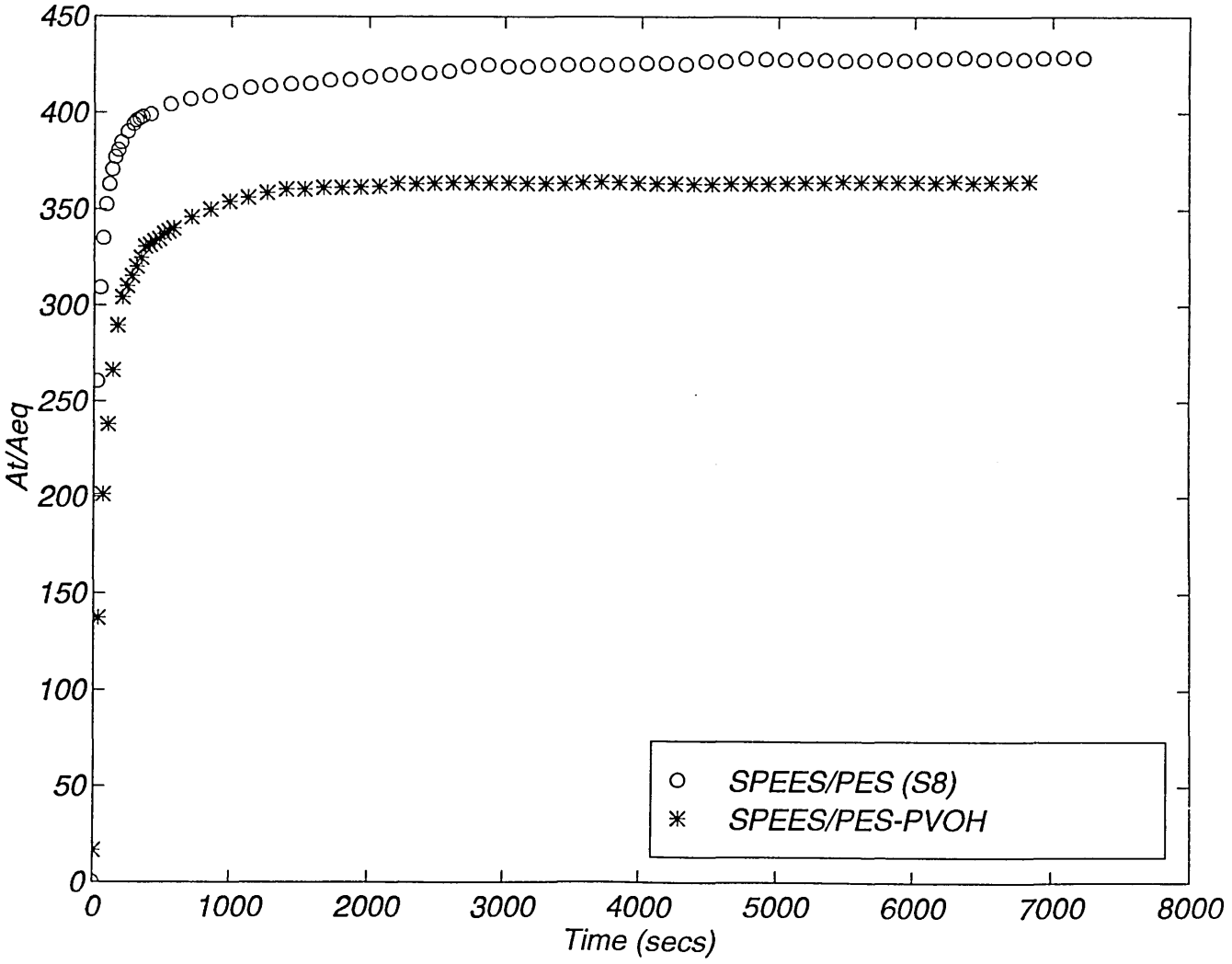

Figure 7.18: Integrated intensity of ν(OH) versus time in diffusion of water into SPEES/PES (S8) and SPEES/PES-PVOH laminate

Table 7.5 shows that the diffusion coefficient (D_1) corresponding to the Langmuir sorption of the water is greater in the case of the laminate. On the other hand the diffusion coefficient (D_2) corresponding to long term diffusion of water described by Henry's Law is lower in the case of the laminate.

Another factor controlling the rate of diffusion is the concentration of the water molecules in contact with the surface of the SPEES/PES layer. In the case of SPEES/PES film, water diffuses into the polymer matrix from a reservoir of pure bulk water. Whereas in the case of a the laminate, water molecules have to first penetrate into the PVOH (top layer) before diffusing into the SPEES/PES layer. It is clear that the concentration of the water molecules for diffusion from a PVOH film in the case of the laminate is lower than the bulk water diffusion into SPEES/PES.

Figure 7.19 shows a plot of $\log(A_t/A_\infty)$ as a function of log(t). It is clear from this figure that the slope of the experimental diffusion curves is greater than that of corresponding to n=0.5. This indicates an anomalous diffusion behaviour.

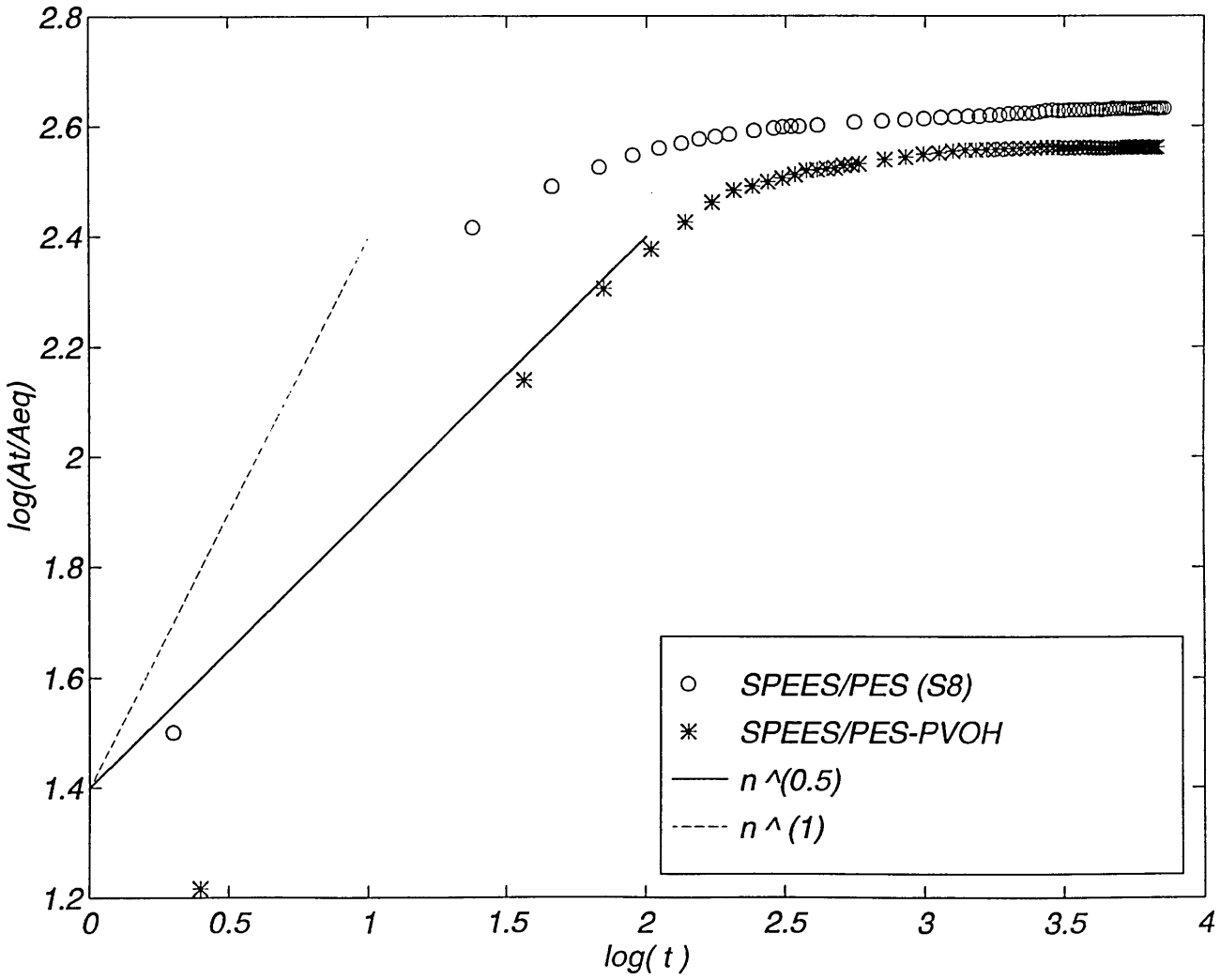

Figure 7.19: *A plot of log(At/At) versus log(t) for diffusion of water into SPEES/PES and SPEES/PES-PVOH*

7.5. Annealing temperature

All of the polymer films used in the diffusion studies described in previous sections were prepared by annealling at 65 °C. However, in order to investigate the effect of annealing temperature on the diffusion of pure water, a number of SPEES/PES films were prepared at different temperatures. It is shown that the changes in polymer morphology brought about by the thermal history can influence the diffusion process.

7.5.1. Experimental

The polymer films were SPEES/PES (S12) and cast from a NMP solution onto a ZnSe ATR prism. The films were then annealed at various temperatures (65, 89 and 98 °C) for 24 hours. The FTIR-ATR spectroscopy procedure was carried out using a Mattson Polaris spectrometer. The infrared spectra were collected at room temperature using the parameters presented in table 6.2. A Mattson FIRST® software was used for manipulating the data.

7.5.2. Results and Discussion

Figure 7.20 shows a comparison of the ν(OH) band of diffusing water into SPEES/PES. The significant difference between the spectra is the intensity of the band. The intensity of the ν(OH) band is lower for the films annealed at higher temperatures. Figure 7.21 shows a plot of integrated absorbance of ν(OH) band as a function of time for diffusion of water in polymer films annealed at 65, 89, and 98 °C. Table 7.6 shows the values of diffusion coefficient for the above films.

Annealing Temperature (°C)	D_1 (cm²/sec)	D_2 (cm²/sec)	X_a
65	$(1.29 \pm 0.1) \times 10^{-8}$	$(1.39 \pm 0.08) \times 10^{-9}$	0.83 ± 0.1
89	$(1.51 \pm 0.09) \times 10^{-9}$	$(1.08 \pm 0.1) \times 10^{-9}$	0.71 ± 0.09
98	$(8.72 \pm 0.1) \times 10^{-10}$	$(6.81 \pm 0.08) \times 10^{-10}$	0.64 ± 0.09

Table 7.6: *Diffusion of water into SPEES/PES (S12) films annealed at various temperatures*

It is apparent from figure 7.21 and table 7.6 that:

1- Diffusion in the films annealed at lower temperatures reach an equilibrium state faster than ones annealed at higher temperatures.

2- The intensity at equilibrium is greater for the diffusion in the films annealed at lower temperature.

3- As the annealing temperature increases, the curves become more sigmoidal in shape. This means a slow initial (induction time) diffusion and after a time delay the rate of diffusion increases significantly.

4- The diffusion coefficients are greater for the films annealed at lower temperatures.

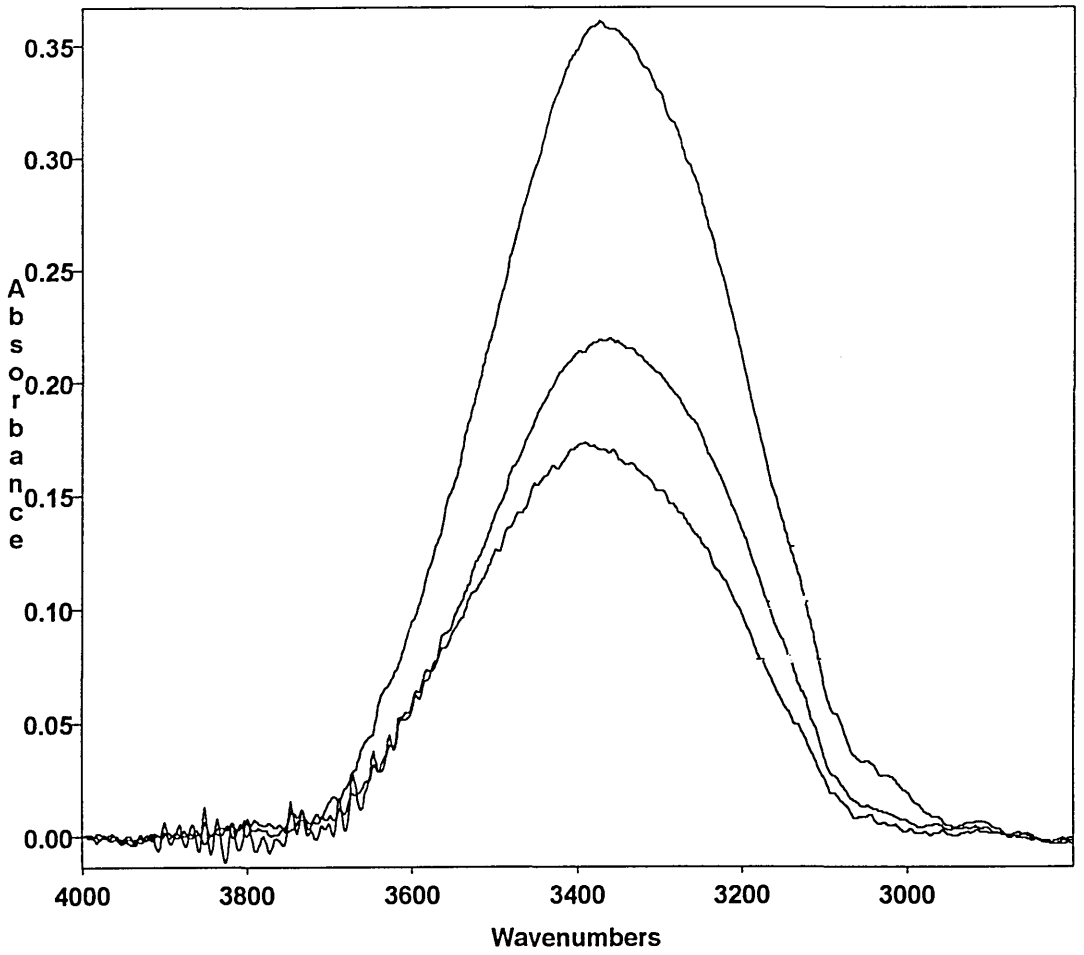

Figure 7.20: A comparison of ν(OH) band of water in SPEES/PES annealed at different temperatures

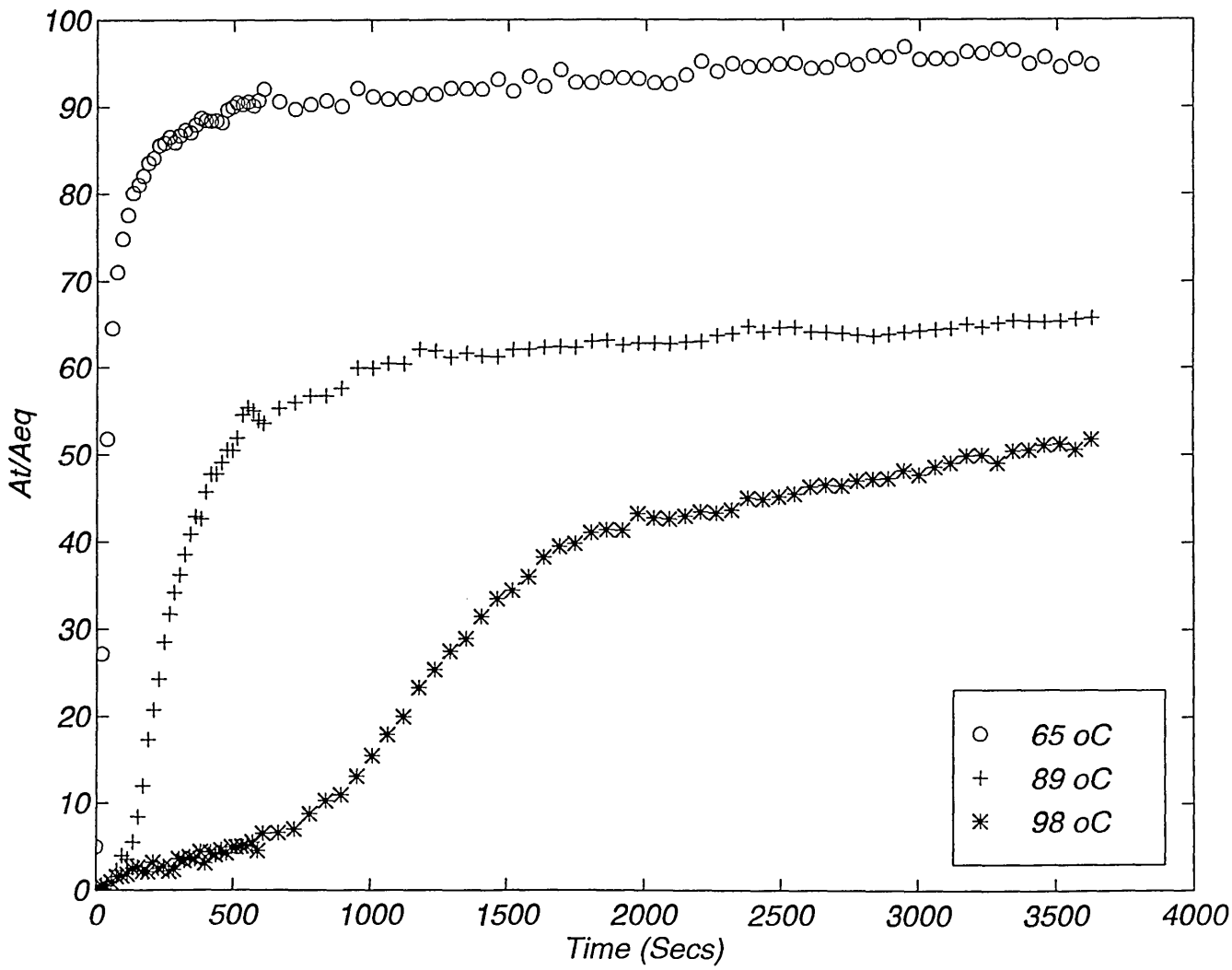

Figure 7.21: Plot of integrated absorbance versus time for diffusion of water into SPEES/PES (S8) annealed at various temperatures

The above observations are due to the morphological changes of the polymer matrix as a result of annealing at high temperatures. The diffusion of small molecules moving through the polymer matrix is dependent in part, on the polymer morphology. This controls the propagation of a molecule from one site to another and the flexibility of the polymer chains required to cooperate with the movement. The diffusivity of the molecule can be influenced by any factor that changes either the structure or the flexibility of the polymer. It is thought [5.51] that the diffusion pathways will be in the amorphous regions.

There are two major factors controlling the polymer morphology. These are (a) the processing history and (b) the defect content. The surface perfection and thickness of crystalline lamellae are modified by the number of random branches which occur during the crystal growth process as the defects are excluded to the lamellar surfaces. The number of defects moved to the surface of lamellae are determined by the thermal history, and the lamellar thickness is determined by the annealing temperature and time.

A number of researchers [7.12 - 7.15] have investigated the surface orientation effect in melt crystallised PE which occurs because thermal cooling first causes nucleation at the surface, which then induces spherulitic growth normal to the surface. On this basis, the time delay for diffusion in the films annealed at high temperatures can be due to existence of some surface skin [5.16]. This can also explain the lower diffusion coefficient for highly annealed films which indicates a slower diffusion of water into the polymer matrix.

Subjecting any glassy polymer film to high annealing will act to increase the packing density of the film dependent on time and temperature. Gas and vapour sorption in glassy polymers such as SPEES/PES takes place by a dual-mode mechanism in which there are two categories of sorption sites: Small Henry's mode sites which correspond

to d-spacing (average interchain-separation) and larger Langmuir sites which represent excess free volumes which have been frozen into the glass as a result of the inability of the macromolecules to undergo maximum close packing during quenching. The lower equilibrium intensity level observed in the diffusion in the films annealed at higher temperatures can be explained by greater close packing (denser packing) of the polymer matrix. Thus, a smaller free volume is present in the matrix for diffusion of water.

Chapter 8

Introduction
Summary and conclusion
Future work

8.1. Introduction

The main aim of this chapter is to summarise the results and discussions in the rest of the thesis and to draw a conclusion. Some future work will also be suggested.

8.2. Summary and conclusion

It was shown that confocal Raman microspectroscopy may be employed to obtain depth profiles of polymer laminates. The advantage of this technique is that it can provide information about the physical and chemical interactions of various layers of a polymer laminate. This is due to a higher degree of depth resolution (2μm) in confocal Raman microspectroscopy in comparison with non-confocal Raman spectroscopy.

In chapter 3, the effects of three different parameters on the nature of chemical and physical interactions at the interface were discussed. In order to investigate the effect of molecular weight, a PVOH/PMMA laminate was chosen. Three different laminates with various PMMA molecular weights were examined, with a view to studying hydrogen bonding interaction between the alcohol and ester groups of PVOH and PMMA layers. The ν(C=O) band showed no apparent frequency shift due to hydrogen bonding interactions between the ester and alcohol groups. Dilution of PMMA carbonyl lone pair dipoles in the interfacial region (with a band shift opposite to that associated with hydrogen bonding interaction) may be responsible for the absence of observable ν(C=O) band shift. However, considerable broadening of the ν(C=O) band has been observed in the interfacial region. This confirms the existence of hydrogen bonding interactions. It was

difficult to study variations in the ν(O-H) band of PVOH layer, due to the very low intensity of the hydroxyl group vibration. It was also demonstrated that (as expected) for a given annealing time, PMMA films with lower molecular weight show a greater degree of interdiffusion compared to those with higher molecular weights.

In order to study the effect of annealing temperature, a PVOH/PAN laminate was chosen. Some degree of hydrogen bonding between the constituent polymers in this laminate was also expected between the nitrile group of PAN and the hydroxyl group of PVOH. It was demonstrated that increase in annealing temperature resulted in an increase in interdiffusion. However, the observed data showed that the degree of hydrogen bonding reduced if the polymer laminate is annealed at a higher temperature than the glass transition temperature, Tg of both of the constituent polymers. At temperatures higher than Tg. mobility of the polymer chains will increase significantly. Thus, some hydrogen bonding breakage and consequently phase separation due to dissociation of intermolecular hydrogen bonding resulted.

In order to examine whether the changes in the band width of the nitrile band in PVOH/PAN are due to hydrogen bonding, a system with no known hydrogen bonding interaction was studied. The system for this experiment was PAA/PAN. Although PAA contains hydroxyl group in its structure, the system did not show great degree of hydrogen bonding to PAN. This may be due to hydrogen bonding interactions (intra and intermolecular) between the carbonyl and hydroxyl groups of various PAA chains. Thus, the formation of intermolecular hydrogen bonds with PAN is hindered. However, the interfacial region of the PAA/PAN laminate seems to be broader than that of PVOH/PAN laminate because of the lower molecular weight of PAA in comparison to PVOH.

It was also observed that the polymer systems that have been annealed at higher temperatures show a greater degree of fluorescence. The background fluorescence makes the collection of the spectra with well resolved bands increasingly difficult.

The effect of annealing time was studied using a PVOH/PMMA laminate. No significant change was observed as a result of annealing the laminate at various lengths of time. One possible explanation for this is that the interdiffusion processes reached the equilibrium state in the initial stages of annealing process. However, it should be noted that the small changes in the interdiffusion process after rapid initial one is difficult to detect with confocal Raman microspectrometry. This is due to the limitations of this method with approximately 2 μm resolution along the optical axis, z.

In chapter 4, it was demonstrated that information about the possible physical and chemical interactions in a polymer blend can be investigated using Raman imaging with global illumination and confocal Raman mapping of the surface.

Point by point confocal Raman mapping provides better resolution in the lateral direction and as such can be used to determine the changes in the Raman spectra due to physical and chemical interactions at the interfacial borders between different constituents in a heterogeneous polymer blend. However, the long time needed to obtain such Raman maps can be a disadvantage. On the other hand, Raman imaging with global illumination is much faster technique, but only can provide information about the distribution of various phases.

The Raman map of a PMMA-PAN blend shows the variations in intensity of the Raman band corresponding to characteristic Raman band of each component. It is clear that PAN particles are embedded in a PMMA matrix.

The Raman map corresponding to band width of $\nu(C\equiv N)$ shows that no significant changes has occurred and as such no interactions between PMMA and PAN phases is seen. This has been rationalised by probable absence of any compatible functional groups in these two polymers for interactions such as hydrogen bonding.

However, the Raman map of PAN-PVOH blend shows significant changes in the band width of the nitrile band of PAN. This band broadening is expected to be a result of hydrogen bonding interactions between the hydroxyl group of PVOH and the nitrile band of PAN. The Raman map of interfacial region in a PMMA/PVOH laminate has also been obtained. It shows a uniform distribution of constituent polymers at the interface.

The results of studies corresponding to the diffusion of pure water into sulphonated polyetherethersulphone/polyethersulphone, SPEES/PES was discussed in chapter 6. It was shown that the state of water in the polymer matrix is different from that of liquid water. The $\nu(OH)$ band of water in the polymer has shifted to higher frequency. This could be due to a shift in equilibrium between strongly and weakly hydrogen bonded water molecules. This is in accordance with the continum model, describing water as having essentially complete hydrogen bonding, at least at low temperatures, but as having a distribution of angles, distances, and bond energies.

However, the $\nu(OD)$ band of HDO in SPEES/PES shows no apparent shift in position. However, this band is broader in SPEES/PES than pure water. The possible reason is the effect of the environment around the $\nu(OH)$ and $\nu(OD)$ vibrations. In an 18% solution of D_2O/H_2O, $\nu(OH)$ or $\nu(OD)$ vibrations are surrounded predominantly by hydrogen atoms and as such OD species are well separated, and thus oscillate in an OH 'diluted' environment. This results in a narrower range of environments and thus, a narrower $\nu(OD)$ band.

It was shown that the diffusion process is not Fickian nor case II. SPEES/PES is a glassy polymer with high degree of homogeneity. It was found that the diffusion of water into SPEES/PES is best described by a dual mode sorption model. Other researchers have also found that dual mode sorption model can describe the diffusion processes in glassy polymers.

The degree of sulphonation of SPEES/PES has significant effect on the diffusion coefficient. The diffusion coefficients was greater for water diffusion into SPEES/PES with higher sulphonation level. This is due to greater tendency of SPEES/PES with higher number of hydrophilic sulphone groups. It was also determined that the absorption level at equilibrium increased significantly from the first sorption process. In addition the time taken to reach the equilibrium state is very rapid in the first sorption. The desorption process seemed to be different than sorption. i.e. the rate of desorption was different than sorption. This implies a hysteresis effect.

In chapter 7, the results of diffusion of water from aqueous ionic solutions into SPEES/PES was presented. It was shown that the rate of diffusion of water from various ionic solutions (Li^+, Na^+, K^+, Cs^+) is different. The order of the equilibrium intensity and diffusion coefficient is: $Li^+ > Cs^+ > Na^+ > K^+$. In order to explain the data, it is thought that a number of factors have to be considered. However, it should be noted that, it is difficult to draw a definite conclusion based on the present data.

One possible reason for this observation is that the small, strongly hydrated $Li^+(H_2O)_n$ has weak adsorption at the polymer interface via solvent separated interaction. Therefore, this improves ease of H_2O access to surface. Weakly hydrated ions like $Cs^+(H_2O)$ have ion-ion polymer interactions but the charge/size ration is small so interaction is not strong. Na^+ and K^+ have higher charge/size ratio and can interact via ion-ion interactions and

effectively stop water molecules getting to surface. As a result, the diffusion coefficient decreases. This argument is at best consistent with data.

It was shown that the concentration of the ionic solutions has a significant effect on the diffusion process. The diffusion coefficient of water from Na^+ solution with higher concentration is smaller than that of lower concentration. The hydrated Na^+ ions as well as the water molecules are adsorbed on the surface of the polymer. It is clear that in this way, the higher the concentration of the ions in the solution is, the greater the surface of the polymer film which will be occupied by the ions. On this basis, it is clear that the diffusion of water molecules into the polymer matrix will be slower and thus give a lower diffusion coefficient. It is also for this reason that, as can be seen from table 7.4, the diffusion of water molecules from pure bulk water is much faster than that of aqueous ionic solutions.

The depth profiling study of a laminate PVOH-SPEES/PES shows no significant interaction between the constituent layers. In addition a study of diffusion of pure water into the laminate shows a greater diffusion coefficient than the diffusion of pure water into a single layer of SPEES/PES. This implied that the PVOH layer can facilitate the diffusion process.

It was also found that the diffusion of water into SPEES/PES annealed at lower temperature reached an equilibrium state faster than ones annealed at higher temperatures, and as the annealing temperature increases, the plot of diffusion curves become more sigmoidal in shape. This is due to morphological changes of the polymer matrix as a result of annealing at high temperatures. The diffusion of small molecules moving through the polymer matrix is dependent in part, on the polymer morphology. This controls the propagation of a molecule from one site to another and the flexibility of the polymer chains required to cooperate with the movement. The diffusivity of the molecule can be

influenced by any factor that changes either the morphology or the flexibility of the polymer. It is thought that the diffusion pathways are in the amorphous regions.

8.3. Future work

There are a number of areas of study which could be carried out in order to help better understanding of the interdiffusion and diffusion processes discussed in this thesis.

These include:

(a) The *in situ* study of molecular interactions at the interfacial region during interdiffusion in a polymer laminate. One of the areas of work presented in this thesis was the effect of annealing temperature on the degree of interdiffusion. The polymer laminates first were annealed at a particular temperature and then after cooling, a depth profile of the laminate was obtained. However, this gave no information about the rate of interdiffusion in such laminates. Confocal Raman microspectroscopy could be utilised to determine the rate of interdiffusion by focusing onto the interfacial region. The subsequent analysis of the spectra collected at regular time intervals should, in principle, give information about the molecular interactions between the constituent polymer layers during the interdiffusion process.

(b) The further study of state of water in SPEES/PES. The work presented in this thesis is corresponding to diffusion of water into SPEES/PES. The shift in the position of ν(OH) band of water was reported. However, in order to give a better understanding of molecular interactions between the water molecules and the SO_3^- sites of the polymer, the study could be carried with low water content.

(c) The effect of various ionic forms of SPEES/PES (e. g. Li^+, Na^+, K^+, Cs^+, Ca^{++}, Mg^{++}) on the diffusion of pure water. SPEES/PES material used in the work presented in this thesis was in H^+ form. However, it is important to determine whether other forms of SPEES/PES have any significant effect on the rate of diffusion of pure water. FTIR-ATR spectroscopy can be used *in situ* to provide information about the molecular interactions between SO_3^- sites and H_2O molecules in the presence of various counter ions.

(d) The diffusion of hydrated ionic species into SPEES/PES. In chapter 7 the results of diffusion of water from an aqueous NO_3^- solution was presented. However, due to high absorbance of SPEES/PES in the region of spectra which NO_3^- bands appear, it was difficult to obtain reliable information about the rate diffusion of this hydrated ion into the polymer matrix. However, it is expected that other ionic species (e.g. SCN^-) could be selected for such this study providing that they have infrared bands in the a region of spectrum which does not interfere with highly absorbing SPEES/PES bands.

REFERENCES

1.1 E. Bright Wilson. JR, J. C. Decius, and P. C. Cross, *Molecular Vibrations*, McGraw-Hill, London, 1955.

1.2 B. Schrader (Ed), *Infrared and Raman Spectroscopy*, VCH, Cambridge, 1995.

1.3 P. R. Griffiths and J. A. de Haseth, *Fourier Transform Infrared Spectroscopy*, John Wiley & Sons, New York (1986).

1.4 N. J. Harrick, *Internal Reflection Spectroscopy*, Harrick Scientific Corporation, New York(1987).

1.5 F. M. Mirabella, Jr., *Internal Reflection Spectroscopy*: Theory and Applications, Vol 15, Marcel Dekker, New York (1993).

2.1 D. J. Gardiner, *Practical Raman Spectroscopy*, D. J. Gardiner and P. R. Graves (Eds), 1989, Springer-Verlag, Berlin.

2.2 T. R. Gilson and P. J. Hendra, *Laser Raman Spectroscopy*, 1972, Wiley-Interscience, London.

2.3 G. W. Chantry, *The Raman Effect*, Vol I, Chap 2, 1971, Marcel Dekker, New York.

2.4 R. J. H. Clark, *Advances Infrared and Raman Spectroscopy*, 1, 1975, p143.

2.5 D. A. Long, *Raman Spectroscopy*, 1977, McGraw-Hill, UK.

2.6 J. P. Meier and B. J. Kip, Microbeam Analysis, 3, 1994, p61.

2.7 N. -T. Yu, D. C. Denagel, D. Jui-Yuan Ho and J. F. R. Kuck, Biological Application of Raman Spectroscopy, T. G. Spiro (Ed), John Wiley & Sons, New York, Vol 1, 1987, p47.

2.8 A. Z. Genack, Analytical Chemistry, 56, 1984, p2957.

2.9 T. Hirschfeld, J. Opt. Soc. Am, 63, 1973, p476.

2.10 G. J. Rosasco, E. S. Etz and W. A. Cassatt, IVth International Conference on Raman Spectroscopy, Brunswick, Maine, U.S.A., 1974.

2.11 G. J. Rosasco, E. S. Etz and W. A. Cassatt, Applied Spectroscopy, 29, 1975, p396

2.12 M. Delhaye and P. Dhamelincourt, IVth International Conference on Raman Spectroscopy, Brunswick, Maine, U.S.A., 1974.

2.13 M. Delhaye and P. Dhamelincourt, Journal of Raman Spectroscopy, 3, 1975, p33.

2.14 G. J. Rosasco and E. S. Etz, Res. Dev, 28, 1977, p20.

2.15 P. Dhamelincourt and P. Bisson, Microsc. Acta, 79, 1977, p267.

2.16 P. Dhamelincourt, Laser in Chemistry (M. West, ed), Elsevier, Amesterdam, 1977, p48.

2.17 P. Dhamelincourt, Thesis, Université de Lille, France, 1979.

2.18 M. Delhaye, E. A. Dasilva and G. S. Hayat, Am. Lab, 83 (April 1977).

2.19 I. M. Robinson, M. Zakikhani, R. J. May and R. J. Young, Journal of Materials Science, 6, 1987, p1212.

2.20 H. Sakata, G. Dresselhaus, M. S. Dresselhaus and M. Endo, Journal of Applied Physics, 63, 1988, p2769.

2.21 J. W. Ager. III, K. D. Veirs, J. Shamir and G. M. Rosenblatt, Journal of Apllied Physics, 68, 1990, p3598.

2.22 N. Everall and J. Lumsdon, Journal of Materials Science, 26, 1991, p5269.

2.23 N. Everall, J. Lumsdon and D. J. Christopher, Carbon, 29, 1991, p133.

2.24 G. J. Rosasco, Advances in Infrared and Raman Spectrocopy, R. Clark and R. E. Hester (Eds), Vol 7, Heyden and Son, London, 1980, p223.

2.25 J. W. Lichtman, *Scientific American*, p 30, August 1994.

2.26 C. S. Foote, *Free Radicals in Biology*, Vol II, W. A. Pryor (ed), Academic Press, New York, 1976, p85-133.

2.27 C. J. H. Brennan and I. W. Hunter, *Applied Spectroscopy*, 49, 1995, p1373.

2.28 C. J. H. Brennan and I. W. Hunter, *Applied Spectroscopy*, 49, 1995, p1086

2.29 C. J. H. Brennan and I. W. Hunter, *Applied Spectroscopy*, 49, 1995, p971

2.30 A. Feofanov, S. Sharonov, P. Valisa, E. Dasilva, I. Nabiev and M. Manfait, *Review of Scientific Instruments*, 66, 1995, p3146

2.31 S. Sharonov, I. Nabiev, I. Chourpa, A. Feofanov, P. Valisa and M. Manfait, *Journal of Raman Spectroscopy*, 25, 1994, p699

2.32 K. P. J. Williams, G. D. Pitt, B. J. E. Smith. A. Whitley, D. N. Batchelder and I. Hayward, *Journal of Raman Spectroscopy*, 25, 1994, p131

2.33 A. Govil, D. M. Pallister and M. D. Morris, *Applied Spectroscopy*, 47, 1993, p75

2.34 C. M. Stellman, K. S. Booksh, J. E. Reddic and M. L. Myrick, *Review of Scientific Instruments*, 67, 1996, p79

2.35 N. Everall, H. Owen and J. Salter, *Applied Spectroscopy*, 49, 1995, p610

2.36 B. Schrader, G. Baranovic, S. Keller and J. Sawatzki, *Fresenius Journal of Analytical Chemistry*, 349, 1994, p4

2.37 J. Andrews, Spectroscopy Europe, 7, 1995, p8.

2.38 J. Barbillat, P. Dhamelincourt, M. Delhaye and E. Dasilva, *Journal of Raman Spectroscopy*, 25, 1994, p3

2.39 T. G. Spiro (Editor), *Biological Applications of Raman spectroscopy, Vol. I-III*, Wiley, New York, 1987-1988.

2.40 T. W. Patapoff, G. A. Thomas, Y. Wang and W. L. Peticolas, *Biopolymers*, 27, 1988, p493.

2.41 C. Otto, F. F. M. de Mul, B. J. M. Harmsen and J. Greve, J. *Nucleic Acids Res*, 15, 1987, p7605.

2.42 G. L. Puppels, C. Otto and J. Greve, *Trens in Analytical Chemistry*, Vol 10, No 8, 1991, p 249.

2.43 G. L. Puppels, F. F. M. de Mul, C. Otto, J. Greve, M. Robert-Nicoud, D. J. Arndt-Jovin and T. M. Jovin, *Nature*, Vol 347, 1990, p301.

2.44 G. L. Puppels, W. Colier, J. H. F. Olminkhof, C. Otto, F. F. M. de Mul and J. Greve, *J. Raman. Spec*, 22, 1991, p217.

2.45 W. L. Kubasek, Y. Wang. G. A. Thomas, T. W. Patapoff, K. H. Schoenwaelder, J. H. Van der Sande and W. L. Peticolas, *Biochemistry*, 25, 1986, p7440.

2.46 G. J. Thomas, Jr., J. M. Benevides and B. Prescott, in R. H. Sarma and M. H. Sarma (Editors), *Biomolecular Stereo-dynamics IV*, Adenine Press, 1986, p. 227.

2.47 R. W. Wartell and J. T. Harrell, *Biochemistry*, 25, 1986, p.2664.

2.48 T. O'Connor, S. Mansy, M. Bina, D. R. McMillin, M. A. Bruck and R. S. Tobias, *Biophys. Chem.*, 15, 1981, p53.

2.49 J. L. Lippert, D. Tyminski and P. J. Desmeules, *J. Am. Chem. Soc.*, 98, 1976, p7075.

2.50 M. N. Siamwiza, R. C. Lord and M. C. Chen, *Biochemistry*, 14, 1975, p4870.

2.51 T. Kitagawa, T. Azuma and K. Hamaguchi, *Biopolymers*, 18, 1979, p451.

2.52 G. L. Puppels, *PhD-thesis*, University of Twente, Enchede, 1991.

2.53 H. Hayashi, Y. Nishimura, M. Katahira and M. Tsuboi, *Nucleic Acids Res.*, 14, 6, 1986, p2583.

2.54 R. J. Erckens, F. H. M. Jongsma, J. P. Wicksted, M. Motamedi, F. Hendrikse and W. F. March, *Vision Research*, 35, 1995, p3316.

2.55 L E. Jurdana, K. P. Ghiggino, K. W. Nugent and I. H. Leaver, *Textile Research Journal*, 65, 1995, p593.

2.56 H. J. Duindam, G. F. J. M. Vrensen, C. Otto, G. J. Puppels and J. Greve, *Journal of Lipid Research*, 36, 1995, p1139.

2.57 C. L. Dekorte, A. F. W. Vandersteen. J. M. Thijssen, J. J. Duindam, C. Otto and G. J. Puppels, *Experimental Eye Research*, 59, 1994, p617

2.58 I. V. Yaroslavsky, A. N. Yaroslavsky, C. Otto, G. J. Puppels, G. F. J. M. Vrensen, H. Duindam and J. Greve. *Experimental Eye Research*, 59, 1994, p393.

2.59 S. Sharonov, I. Chourpa, H. Morjani, I. Nabiev, M. Manfait and A. Feofanov, *Analytica Chemica Acta*, 290, 1994, p40.

2.60 M. H. Sweets, G. F. J. M. Vrensen, K. Otto, G. J. Puppels and J. Greve, *Biochemica Et Biophysica Acta*, 1164, 1993, p236.

2.61 G. J. Pupples, H. S. P. Garritsen, G. M. J. Segersnolten, F. F. M. Demul and J. Greve, *Biophysical Journal*, 60, 1991, p1046.

2.62 M. H. Vanderveen and J. J. Tenbosch, *Caries Research*, 1, 1996, p93

2.63 S. M. Grimes, S. R. Johnstone and D. N. Batchelder, *Analyst*, 120, 1995, p2741

2.64 I. P. Hayward, K. j. Baldwin, D. M. Hunter, D. N. Batchelder and G. D. Pitt, *Diamond and Related materials*, 4, 1995, p617

2.65 M. Delhye, M. C. Dhamelincourt and E. Dasilva, *Revue De L Institute Francais Du Petrole*, 48, 1993, p183

2.66 B. J. Palys, G. J. Pupples, D. Vandenham and D. Feil, *Journal of Electroanalytical Chemistry*, 326, 1992, p105

2.67 S. Hajatdoost and J. Yarwood, *Applied Spectroscopy*, 50, 1996, p558.

2.68 R. Evans, T. Kasteliner, S. Hajatdoost, R. Banga and J. Yarwood, *Journal of Raman Spectroscopy*, 27, 1996, p695

2.69 L. Markwort, B. Kip, E. Dasilva and B. Roussel, *Applied Spectroscopy*, 49, 1995, p1411

2.70 A. M. Radder, J. A. Vanloon, G. J. Pupples and C. A. Vanblitterswijk, *Journal of Materials Science-Materials in Medicine*, 6, 1995, p510

2.71 M. Claybourn, A. Luget and K. P. J. Williams, *ACS Symposium Series*, 598, 1995, p41

2.72 A. Garton, D. N. Batchelder and C. W. Cheng, *Applied Spectroscopy*, 47, 1993, p922

2.73 P. Dhamelincourt, J. Barbillat and M. Delhaye, *Spectroscopy Europe*, 5, 1993, p16.

2.74 R. Tabaksblat, R. J. Meier and B. J. Kip, *Applied Spectroscopy*, 46, 1992, p60.

2.75 K. P. J. Williams, G. D. Pitt, D. N. Batchelder and B. J. Kip, *Applied Spectroscopy*, 48, 2, 1994, p232.

2.76 A. Boivin and E. Wolf, *Phys. Rev*, 138, 1965, p1561.

2.77 M. Born and E. Wolf, *Principles of Optics*, Pergamon Press, Oxford (1980), 6th ed, p435.

2.78 D. N. Batchelder, Chunwei Cheng and G. D. Pitt, Advanced Materials, 3, 1991, p566.

2.79 K. P. J. Williams and D. N. Batchelder, Spectroscopy Europe, 6, 1994, p19.

2.80 G. J. Pupples, M. Grond and J. Greve, Applied Spectroscopy, 47, 1993, p1256.

2.81 P. J. Treado, I. W. Levin and E. Neil Lewis, Applied Spectroscopy, 46, 1992, p1211.

2.82 H. R. Morris, C. C. Hoyt and P. J. Treado, Applied spectroscopy, 48, 1994, p857.

2.83 P. J. Treado and M. D. Morris, Applied Spectroscopy, 44, 1990, p1.

2.84 P. J. Treado, A. Govil, M. D. Morris, K. D. Sternnitzke and R. L. McCreery, Applied Spectroscopy, 44, 1990, 1270.

2.85 P. J. Treado and M. D. Morris, Spectrochim. Acta Rev, 13, 1990, p355.

2.86 K. L. K. Liu, L. H. Chen, R. S. Sheng and M. D. Morris, Applied Spectroscopy, 45, 1991, p1717.

2.87 Confocal microscopy, T. Wilson (Ed), Academic Press, London, 1990.

2.88 Handbook of Biological Confocal Microscopy, J. B. Pawley (Ed), Plenum press, New York, 1990.

2.89 A. Govil, D. M. Pallister, L. Heng Chen and M. D. Morris, Applied Spectroscopy, 45, 1991, p1604.

2.90 A. Govil, D. M. Pallister and M. D. Morris, Applied Spectroscopy, 47, 1993, p 331

2.91 S. Nakashima, NATO ASI Ser, Ser B, 273, 1991, p291.

2.92 G. Abstrelter, Applied Surface Science, 50, 1991, p73.

2.93 W. C. Tang, H. J. Rosen, Microbeam Anal, 26th, 1991, p101.

2.94 J. Jimenez, E. Martin, P. A. Carmelo and A. Torres, Semicond. Sci. Tech, 7(1A), 1992, A288.

2.95 J. Jimenez, E. Martin and A. C. Prieto, Mater. Lett, 12(3), 1991, p132.

2.96 A. Hashimoto, T. Kamujoh and N. Watanabe, Jpn Journal of Applied Physics, 26, 1987, p1128.

2.97 K. Mizoguchi, S. Nakashima, A. Fuju, A. Mitsuishi, H. Morimoto, H. Onoda and T. Kato, Jpn Journal of Applied Physics, 26, 1987, p903.

2.98 J. B. Hopkins and L. A. Farrow, Journal of Applied Physics, 59, 1986, p1103.

2.99 P. D. Wang, C. Cheng, C. M. Sotomayor Torres and D. N. Batchelder, Journal of Applied Physics, 74, 1993, p5907.

2.100 L. S. Grigoryan, H. D. Birt, S. Sathaiah, S. V. Sharma, H. Clara and A. K. Majumdar, Journal of Raman Spectroscopy, 23, 1992, p127.

2.101 K. Niwase, K. Nakamura. I. Tanaka, Y. Miyamoto and T. Tanabe, J. Nucl. Mater, 179-181(part A), 1991, p214.

2.102 I. P. Hayward, K. J. Baldwin, D. M. Hunter, D. N. Batchelder and G. D. Pitt, Diamond and Related Materials, 4, 1995, p617.

2.103 H. Boyer, Microbeam analysis, 1983, p265.

2.104 S. W. Lee, K. S. Hong, R. A. Condrate, R. P. Hapanowicz and R. F. Speyer, Journal of materials Science, 27, 1992, p4961.

2.105 M. Bowden, N. M. Dixon, D. J. Bardiner and S. F. Carter, J. Mater. Sci. Mat. in Electronics, 1990, p34.

2.106 G. J. Rosasco, E. Roedder, In international Geology Congress, 1976, 25th Abstr, 3, p812.

2.107 J. Dubessy, M. C. Boiron, A. Moisette, C. Monnin and N. Stretenskaya, Eur. J. Mineral, 4, 1992, p885.

2.108 P. Dhamelincourt, H. J. Schubnel, Rev Gemnol, 52, 1977, p11.

2.109 J. D. Pasteris, J. C. Seitz and B. Wopenka, Microbeam Analysis, 1985, p25.

2.110 B. Wopenka and J. D. Pasteris, Applied Spectroscopy, 40, 1986, p144.

2.111 K. L. Higgins, C. L. Stein, Microbeam Analysis, 1986, p31.

2.112 H. Boyer and D. C. Smith, Microbeam Analysis, 1984, p107

2.113 F. J. Purcell and W. B. White, Microbeam Analysis, 1983, p28

2.114 T. Jawhari, J. C. Merino, J. C. Rodriguez-Cabello and M. Pastor, Polymer, 33, 1992, p4199.

2.115 D. N. Batchelder, C. Cheng and G. D. Pitt, Advanced Materials, 3, 1991, p566.

2.116 L. Markwort, B. Kip, E. Da Silva and B. Russel, Applied Spectroscopy, 49, 1995, p1411.

2.117 A. Garton, D. N. Batchelder and C. Cheng, Applied Spectroscopy, 47, 1993, p922.

2.118 M. D. Schaeberle, C. G. Karakatsanis, C. J. Lau and P. J. Treado, Analytical Chemistry, 67, 1995, p4316.

2.119 C. Galiotis, R. J. Young and D. N. Batchelder, Journal of polymer Science, Polym. Phys. Ed, 21, 1983, p2483.

2.120 R. J. Young, D. Lu and R. J. day, Polymer International, 24, 1991, p71.

2.121 R. J. day, I. M. Robinson, M. Zakikhani and R. J. Young, Polymer, 28, 1987, p1833.

2.122 R. J. Young, R. J. Day and M. Zakikhani, Journal of Material Science, 25, 1990, p127.

2.123 G. Wu, K. Tashiro, M. Kobayashi, T. Komatsu and K. Nakagawa, Macromolecules, 22, 1989, p758.

2.124 K. Prasad and D. T. Grubb, Polymer Physics, B27, 1989, p381.

2.125 K. Prasad and D. T. Grubb, Polymer Physics, B28, 1990, p2199.

2.126 D. T. Grubb and Z. -F. Li, Polymer, 33, 1991, p2587.

2.127 M. C. P. Van Eijk, P. J. R. Leblans, R. J. Meier and B. J. Kip, J. Matter. Sci. Lett, 9, 1990, p1263.

2.128 B. J. Kip, M. C. P. Van Eijk and R. J. Meier, Integration of Fundamental Polymer Science and Technology-5.c, (Rolduc Polymer Meeting 1990), P. J. Lemstra and L. A. L. Kleintjens (Eds), Elsevier Applied Science, London, 1991, p183-187.

2.129 B. J. Kip, M. C. P. Van Eijk and R. J. Meier, Journal of polymer Science, B29, 1991, p99.

2.130 J. A. H. Moonen, W. A. C. Roovers, R. J. Meier and B. J. Kip, Journal of Polymer Science, Polym. Phys. Ed, B30, 1992, p361.

2.131 C. Galiotis, R. J. Young, P. H. J. Yeung and D. N. Batchelder, Journal of Material Science, 19, 1984, p3640.

2.132 I. M. Robinson, R. J. Young, C. Galiotis and D. N. Batchelder, Journal of Materials Science, 22, 2987, p3642.

2.133 P. K. Kim, Y. Y. Xu, C. Cheng and S. L. Hsu, Polymer, 27, 1986, p1547.

2.134 H. Jahankhani, C. Vlattas and C. Galiotis, Proc. Interfacial Phenomena in composite Materials 1989, F. R. Jones (Ed), Butterworths, London, 1989, p125-131.

2.135 H. Jahankhani and C. Galiotis, J. Compos. Mater, 25, 1991, p609.

2.136 L. Boogh, R. J. Meier, H. H. Kausch and B. J. Kip, Journal of Polymer Science, Polym Phys. Ed B30, 1992, p325.

2.137 D. J. Gardiner and M. Bowden, Microscopy and analysis, November issue, 1990, p27.

2.138 X. Hu, R. J. day, J. L. Stanford and R. J. Young, Journal of material Science, 27, 1992, p5958.

2.139 T. Jawhari, J. C. Merino, J. C. Rodriguez-Cabello and J. M. Pastor, Polymer, 33, 1992, p4199.

2.140 T. Jawhari, J. C. Merino and J. M. Pastor, Journal of material Science, 27, 2992, p2231.

2.141 T. Jawhari, J. C. Merino and J. M. Pastor, Journal of material Science, 27, 2992, p2237.

2.142 M. Bowden, J. W. Bradley, D. J. Gardiner and B. J. Kip, Proc. 13th Int Conf. on Raman Spectroscopy 1992, p1046.

2.143 R. H. Duaskardt, D. K. Viers and R. O. Ritchie, J. Am. Ceram. Soc, 72, 1989, p1124.

2.144 R. H. Duaskardt, W. C. Carter, D. K. Viers and R. O. Ritchie, Acta. Metal. Mater, 38, 1990, p2327.

2.145 M. Bowden, G. D. Dickson, D. J. Gardiner and D. J. Wood, Applied Spectroscopy, 44, 1990, p1679.

2.146 S. B. Best, R. J. H. Clark and R. Withnall, Proceedings XIIIth ICORS, W. Kiefer (Ed), John Wiley & Sons, Chichester and New York, 1992, p1042.

2.147 E. S. Etz, B. B. Thomazic and W. E. Brown, Microbeam Analysis, 1986, p39.

2.148 S. Zheng and A. T. Tu, Apllied Spectroscopy, 40, 1986, p8.

2.149 G. J. Puppels, T. C. B. Schut, N. M. Sijtsema, M. Grond, F. Maraboelf, C. G. Degrauw, C. G. Figdor and J. Greve, Journal of Molecular Structure, 347, 1995, p477.

2.150 R. Le Ny, C. Fiaud and A. T. Nguyen, J. de. Physique, C2 2 45, 1984, p148.

2.151 D. J. Gardiner, A. C. Govin, C. Gutteridge and E. S. Raper, Corrosion Science, 25, 1985, p1019.

2.152 T. E. Doyle, J. L. Alvarez, Microbeam Analysis, 1983, p277.

3.1 H. Younes and D. Cohn, J. Biomed. Mater. Res. 21, 1987, p1301.

3.2 M. Bender, *Interfacial phenomena in biological systems* (Marcel Dekker, New York, 1991).

3.3 G. Gillberg, J. Adhes. 21, 1987, p129.

3.4 T. C. Wang and L. J. Boutman, Polym. Eng. Sci. 25, 521, 1985, p529.

3.5 Q. Deng, C. S. Sundar, and Y. C. Jean, J. Phys. Chem. 96, 1992, p492.

3.6 J. H. Ramsden, J. Phys. Chem. 96, 1992, p3388.

3.7 M. Shimonura, J. F. Rabolt, and K. Song, Langmuir. 8, 1992, p877.

3.8 N. E. Schlotter and P. Y. Furlan, Vib. Spec. 3, 147 (1992).

3.9 J. K. F. Tait, J. Yarwood, N. M. Dixon, N. Everall, G. Davis, and R. Melntyre, J. Raman. Spec, 24, 1993, p511.

3.10 G. Boven, R. H. G. Brinkhuis, E. J. Vorenkamp, G. Challa, and A. J. Schouten, Polymer. 33, 6, 1992, p1150.

3.11 M. R. Pereira and J. Yarwood, J. Polym. Sci: Part B: Polym Phys. 32, 1994, p1881.

3.12 F. P. Price, P. T. Gilmore, E. L. Thomas, and R. L. Laurence, J. Polym. Sci: Polym Symp. 63, 1978, p33.

3.13 R. S. Raghava and R. W. Smith, J. Polym. Sci: Polym. Phys. 27, 1989, p2525.

3.14 S. Koizumi, H. Hasegawa, and T. Hashimoto, Macromolecules. 23, 1990, p2955.

3.15 E. Jabbari and N. A. Peppas, Polymer Bulletin. 27, 1991, p305.

3.16 J. Kramer, P. Green, and J. Palmstrom, Polymer. 25, 473 (1984).

3.17 R. W. Garbella and J. H. Wendorff, Makromol. Chem. 189, 1988, p2459.

3.18 T. Finerman and B. Crist, Polymer. 28, 1987, p375.

3.19 S. J. Whitlow and R. P. Wool, Macromolecules. 22, 1989, p2648.

3.20 J. Klein and B. J. Briscoe, Polymer. 17, 1976, p48.

3.21 M. L. Fernandez, J. S. Higgins, J. Penfold, R. C. Ward, C. Shackelton, and D. J. Walsh, Polymer. 29, 1988, p1923.

3.22 P. Groenveld, J. Paint. Techn, 43, 1971, p50.

3.23 J. Yarwood, in *Spectroscopy and Structure of Molecular Complexes*, J. Yarwood, Ed. (Plenum, New York, 1973), p. 180.

3.24 V. M. Shelley, A. Talintyre, J. Yarwood, and R. Buchner, Faraday Discuss. Chem. Soc. 85, 1988, p211.

3.25 M. S. Bradley, and V. Buch, J. Chem. Phys. 99, 1993, p2332.

3.26 H. Deng, J. Zheng, J. Burgner, and R. Callender, J. Phys. Chem. 93, 1989, p4710.

3.27 N. Tanaka, K. Ito, and H. Kitano, Macromolecules. 27, 1994, p540.

3.28 Z. Bashir, S. P. Church and D. Waldron, Polymer, 35, 1994, p967.

3.29 G. Socrates, Infrared Characteristic Group Frequencies, John Wiley and Sons, New York, 1980.

3.30 X. Zhang, K. Takegoshi and K Hikichi, Polymer, 35, 1994, p718.

3.31 N. Tanaka, K. Ito and H. Kitano, Macromolecules, 27, 1994, p540.

4.1 J. Lyngaae-Jorgensen, *Polymer Blends and Alloys*, M. J. Folkes and P. S. Hope (Eds), 1993, Blackie Academic & Professional, p75.

4.2 A. Garton, Infrared Spectroscopy of Polymer Blends, Composites and Surfaces, Hahser Publishers, New York, 1992.

4.3 L. A. Utracki, Polymer Blends, Hanser Publishers, New York, 1991.

4.4 H. J. Teh, J. Appl. Polym. Sci, 28, 1983, p605.

4.5 J. Korger-Kocsis, A. Kalo and V. Kuleznev, Polymer, 25, 1984, p279.

4.6 N. C. Billingham and P. D. Calvert, Inst. Phys. Conf. Ser, 98, 1989, p571.

4.7 D. Hemsley (Ed), Applied Polymer Light Microscopy, Elsevier Science Publishers, 1989.

4.8 R. Gelles and C. W. Frank, Macromolecules, 16, 1983, p1448.

4.9 D. J. Walsh, J. S. Higgins and S. Rostami, Macromolecules, 16, 1983, p388.

4.10 L. C. Chan, J. K. Gillham, A. J. Kinloch and S. J. Shaw, Rubber toughened epoxies. Advances Chem. Ser, 209, 1984.

4.11 D. L. Hadlin and E. L. Thomas, Macromolecules, 16, 1983, p1514.

4.12 D. Vesely and D. S. Finch, Macromol. Chem. Symp, 16, 1988, p329.

4.13 D. Vesely, D. S. Finch and G. E. Cooley, Polymer, 29, 1988, p1402.

4.14 G. Z. Li, Y. Jin, L. H. Shi, M. L. Ye and F. L. Bai, Journal of Polymer Science Part B Polymer Physics, 34, 1996, p1079.

4.15 P. S. Brown and A. J. Tinker, Kautschuk Gummi Kunststoffe, 48, 1995, p606.

4.16 M. Mansfeld, A. Flour and W. S. Veeman, Applied magnetic Resonance, 8, 1995, p573.

4.17 K. Takegoshi, K. Tsuchiya and K. Hikichi, Polymer Journal, 27, 1995, p284.

4.18 T. Nomura, T. Nishio, M. Akiyama, E. Sugihara and K. Tanaka, Kobunshi Ronbunshu, 52, 1995, p83.

4.19A. Asano, K. Takegoshi and K. Hikichi, Polymer, 35, 1994, p5630.

4.20 B. Boutevin, M. Khamlichi, Y. Pietrasanta and J. J. Robin, Polymer Bulletin, 34, 1995, p117.

4.21 P. A. Mirau, J. L. White and S. A. Heffner, Macromolecular Symposia, 86, 1994, p181.

4.22 X. Q. Zhang, M. Shimoda and A. Toyoda, Polymer, 35, 1994, p4280.

4.23 W. Y. Zheng, K. Levon, T. Taka, J. Laakso and J. E. Osterholm, Journal of Polymer Science Part B Polymer Physics, 33, 1995, p1289.

4.24 H. E. Simmons, W. R. Hertler and B. B. Sauer, Journal of Applied Polymer Science, 52, 1994, p727.

4.25 M. Okamoto and T. Inoue, Polymer Engineering and Science, 33, 1993, p445.

4.26 S. A. Schwarz, B. J. Wilkens, M. A. A. Pudensi, M. H. Rafailovich, J. Sokolov, X. Zhao, W. Zhao, X. Zheng, T. P. Russel and R. A. L. Jones, Molecular Physics, 76, 1992, p937.

4.27 I. V. Yermakov, T. L. Lebedeva, A. D. Litmanovich and N. A. Plate, Vysokomolekulyarnye Soedineniya Seriya A, 34, 1992, p84.

4.28 Z. Osawa and Y. Fukuda, Polymer degradation and stability, 32, 1991, p285.

4.29 V. Abetz, G. Muller, R. Stadler and S. Schlick, Macromolecular Chemistry and Physics, 196, 1995, p3845.

4.30 M. T. Razzak, S. Sudiro, A. Sudradjat, A. Waskito and M. F. Djamili, Radiation Physics and Chemistry, 46, 1995, p1263.

4.31 C. G. Pitt, J. Wang, S. s. Shah, R. Sik and C. F. Chignell, Macromolecules, 26, 1993, p2159.

4.32 D. D. Deshpande, C. Basu and M. Panday, Journal of Applied Polymer Science, 43, 1991, p1701.

4.33 M. C. Davies, K. M. Shakesheff, A. G. Shard, A. Domb and C. J. Roberts, Macromolecules, 29, 1996, p2205.

4.34 D. M. Bielinski, S. Affrossman, M. Hartshorne and R. A. Pethrick, Polymer, 36, 1995, p4899.

4.35 J. L. Angulosanchez and R. D. Short, Polymer, 36, 1995, p1559.

4.36 W. K. Lee, W. J. Cho, A. Takahara and T. Kajiyama, Polymer, 36, 1995, p1229.

4.37 P. Sakellariou, Polymer, 34, 1993, p3408.

4.38 A. J. Pertsin, M. M. Gorelova, V. Y. Levin and L. I. Makarova, Journal of Applied Polymer Science, 45, 1992, p1195.

4.39 M. C. Davies, K. M. Shakesheff, A. G. Shard, A. Domb, C. J. Roberts, S. J. B. Tendler and P. M. Williams, macromolecules, 29, 1996, p2205.

4.40 K. M. Shakesheff, X. Y. Chen, M. C. Davies, A. Domb, C. J. Roberts, S. J. B. Tendler and P. M. Williams, Langmuir, 11, 1995, p3921.

4.41 K. Tanaka, J. S. Yoon, A. Takahara and T. Kajiyama, Macromolecules, 28, 1995, p934.

4.42 S. K. S. Roy and C. K. Das, Polymers and Polymer Composites, 3, 1995, p403.

4.43 J. R. Isasi, E. Meaurio, C. Cecteros and I. Katime, Macromolecular Chemistry and Physics, 197, 1996, p641.

4.44 C. C. Su and E. M. Woo, Macromolecules, 28, 1995, p6779.

4.45 P. Jannasch and B. Wesslen, Journal of Applied Polymer Science, 58, 1995, p753.

4.46 A. Sanchis, M. G. Prolongo, R. G. Rubio and R. M. Masegosa, Polymer Journal, 27, 1995, p10.

4.47 X. Q. Zhang and D. H. Solomon, Macromolecules, 27, 1994, p4919.

4.48 H. Rawal and S. Devi, Polymer Journal, 25, 1993, p1215.

4.49 M. Sargent and J. L. Koenig, Advances in Chemistry Series, 236, 1993, p191.

4.50 R. A. L. Jons and E. J. Kramer, Polymer, 34, 1993, p115.

4.51 R. Mani, T. Mani and J. R. Stevens, Journal of Polymer Science Part A Polymer Chemistry, 30, 1992, p2025.

4.52 K. Kugo, T. Kitaaura and J. Nishino, Kobunshi Ronbunshu, 4, 1992, p327.

4.53 D. E. Bhagwagar, P. C. Painter, M. M. Coleman and T. D. Krizan, Journal of Polymer Science Part B Polymer Physics, 29, 1991, p1547.

4.54 M. B. Clark, C. A. Burkhardt and J. A. Gardella, Macromolecules, 24, 1991, p799.

4.55 S. Kawahara and S. Akiyama, Polymer Journal, 23, 1991, p7.

4.56 P. P. Hong, F. J. Boerio and S. D. Smith, Macromolecules, 27, 1994, p596.

4.57 P. P. Hong, F. J. Boerio and S. D. Smith, Macromolecules, 26, 1993, p1460.

4.58 M. D. Schaeberle, C. G. Karakatsanis, C. J. Lau and P. J. Treado, Analytical Chemistry, 67, 1995, p4316.

5.1 E. Kongold, K. Kock and H. Strathmann, Desalination, 24, 1978, p129.

5.2 J. R. Bontha and P. N. Pintauro, Chemical Engineering Science, 49, 1994, p3835.

5.3 P. Meares, European Polymer Journal, 2, 1966, p241.

5.4 R. E. Kesting and A. K. Fritzsche, *Polymeric Gas Separation Membranes*, John Wiley & Sons Inc, 1991.

- R. E. Kesting, Synthetic Polymeric membranes, John Wiley & Sons Inc, 1985.

5.5 K. A. Mauritz and A. J. Hopfinger, *Modern Aspects of Electrochemistry*, J.O'M. Bockris, D. E. Conway, and R. E. White (Eds), No 14, Plenum Press, London, 1982.

5.6 F. H. Stillinger, Water in Polymers, ACS Symposium Series, S. P. Rowland (ed), No 127, American Chemical Society, Washington, D. C. 1980.

5.7 A. R. Haly and J. W. Snaith, Biopolymers, 10, 1971, p1681.

5.8 M. Falk, Canadian Journal of Chemistry, 58, 1980, p1495.

5.9 F. G. Donnan, Z. Elekrtochem, 17, 1911, p572.

5.10 F. G. Donnan, Chemical Review, 1, 1924, p73.

5.11 K. A. Mauritz and S. R. Lowry, Polym. Prep. Am. Chem. Soc. Div. Polym. Chem, 19, 1978, p336.

5.12 S. R. Lowry and K. A. Mauritz, Journal of American Chemical Society, 102, 1980, p7665.

5.13 R. A. Komoroski, Polym. Prep. Am. Chem. Soc. Div. Polym. Chem, 19, 1978, p341.

5.14 R. A. Komoroski and K. A. Mauritz, Journal of American Chemical Society, 100, 1978, p7487.

5.15 P. W. Atkins, Physical Chemistry, 3rd Ed, Oxford University Press, Oxford, 1988.

5.16 A. Alfrey, E. F. Gurnee and W. G. Lloyd, Journal of Polymer Science, C12, 1966, p249.

5.17 J. Crank, *The Mathematics of Diffusion*, 2nd Ed, Clarendon Press, Oxford, 1994.

5.18 M. J. Reimers and T. A. Barbari, Journal of Polymer Science: Part B: Polymer Physics, Vol 32, 1994, p131.

5.19 R. M. Barrer, J. A. Barrier and J. Slater, Journal of Polymer Science, 27, 1958, p177.

5.20 S. S. Kasargod, F. Adib and P. Neogi, Journal of Chemical Physics, 103, 1995, p7114.

5.21 J. H. Petropoulos, Journal of Polymer Science, A-2, 8 1980, p1797.

5.22 W. J. Koros, D. R. Paul, Journal of Polymer Science: Part B: Polymer Physics, 14, 1976, p687.

5.23 W. J. Koros, D. R. Paul, Journal of Polymer Science: Part B: Polymer Physics, 14, 1976, p1903.

5.24 W. R. Vieth, J. M. Howell and J. H. Hsieh, Journal of Membrane Science, 1 1976, p177.

5.25 T. Uragami, H. B. Hopfenberg, W. J. Koros, D. K. Yang, V. T. Stannett and R. T. Chern, Journal of Applied Polymer Science, 24, 1986, p779.

5.26 R. T. Chern, W. J. Koros, E. S. Sanders and R. Yui, Journal of Membrane Science, 15, 1983, p157.

5.27 R. J. Hernandez, J. R. Giacin and E. A. Grulke, Journal of Membrane Science, 65, 1992, p187.

5.28 W. J. Koros, D. R. Paul and A. A. Rocha, Journal of Polymer Science: Polymer Physics Ed, 14, 1976, p687.

5.29 H. Hachsuka. H. Takizawa, Y. Tsujita, A. Takizawa and T. Kinoshita, Polymer, 32, 1991, p2382.

5.30 H. Kumazawa, J. Wang and E. Sada, Journal of Polymer Science: Part B: Polymer Physics, 31, 1993, p881.

5.31 K. Toi, T. Ito, I. Ikemoto and T. Kasai, Journal of Polymer Science: Part B: Polymer Physics, 30, 1992, p497.

5.32 K. Toi, T. Ito, T. Shirakawa and I. Ikemoto, Journal of Polymer Science: Part B: Polymer Physics, 30, 1992, p549.

5.33 T. Shibusawa, Journal of Polymer Science: Part B: Polymer Physics, 31, 1993, p29.

5.34 G. R. Mauze and A. Stern, Polymer Engineering and Science, 23, 1983, p548.

5.35 W. R. Vieth, J. M. Howell and J. H. Hsieh, Journal of Membrane Science, 5, 1976, p177.

5.36 D. R. Kemp and D. R. Paul, Journal of Polymer Science, 12, 1974, p485.

5.37 J. Komiyama and T. Iijima, Journal of Polymer Science: Part A-2, 12, 1974, p1465.

5.38 T. Shibusawa and Y. Chigira, Journal of Polymer Science: Part B: Polymer Physics, 30, 1992, p563.

5.39 W. R. Vieth, S. S. Wang and S. G. Gilbert, Biotechnology and Bioengeenring Symposiom, 3, 1972, p285.

5.40 W. J. Koros, M. R. Coleman and D. R. B. Walker, Annual Review of Materials Science, 22, 1992, p47.

5.41 Y. Chen, T. Mityano, A. Found and T. Matsuura, Journal of Membrane Science, 48, 1990, p203.

5.42 J. Crank and G. S. Park, *Diffusion in Polymers*, Academic Press: London, 1968.

5.43 C. H. Rhee and J. D. Ferry, Journal of Applied Polymer Science, 21, 1977, p773.

5.44 G. S. Park and T. V. Hoang, European Polymer Journal, 15, 1979, p817.

5.45 C. Y. Hui, K. C. Wu, R. C. Laskey and J. Kramer, Applied Physics, 61, 1987, p5137.

5.46 R. W. Kosmeyer, Von. E. Mierwell and N. A. Peppas, Journal of Polymer Science. Part B, 24, 1986, p409.

5.47 H. M. Tong, K. L. Saenger and C. J. Durning, Journal of Polymer Science. Part B, 27, 1989, p689.

5.48 C. A. Pawlisch, A. Macris and R. L. Laurence, Macromolecules, 20, 1987, p1564.

5.49 N. L. Thomas and A. H. Windle, Polymer, 18, 1977, p1195.

5.50 N. L. Thomas and A. H. Windle, Polymer, 19, 1978, p255.

5.51 N. L. Thomas and A. H. Windle, Polymer, , 22, 1981, p627.

5.52 N. Schlotter and P. V. Furlan, Polymer, 33, 1992, p3332.

5.53 G. T. Fieldson and T. A. Barbari, Polymer, 34, 1993, p1146.

5.54 G. T. Fieldson and T. A. Barbari, AIChE Journal, 41, 1995, p795.

5.55 K. Hemmelmann, and V. H. Brandt, Exp. Tech. Phys, 34, 1986, p439.

5.56 V. H. Brandt, K. Hemmelmann, Exp. Tech. Phys, 35, 1987, p349.

5.57 K. Cogan Farinas, L. Doh, S. Venkatraman, and R. O.Pottas, Macromolecules, 27, 1994, p5220.

5.58 J. R. Xu and C. M. Balik, Applied Spectroscopy, 42, 1988, p1543.

5.59 D. E. Wurster, V. Buraphacheep, and J. M. Patel, Pharm. Res, 10, 1993, p616.

5.60 M. R. Pereira and J. Yarwood, Journal of Chemical Society, Faraday Trans, 92, 1996, p2737.

5.61 D. J. Kuzmenka and S. Granick, Colloids and Surfaces, 31, 1988, p105.

5.62 E. Rosenberg and R. Kellner, 8th International Conference on Fourier Transform Spectroscopy (1991), p346.

5.63 M. .R. Pereira, PhD thesis, University of Durham, 1994.

5.64 W. H. Press, B. P. Flannery, S. A. Teukosky, W. T. Vetterling, *Numerical Recipies in Pascal*, Cambridge University Press, 1990.

6.1 G. Zundel, Hydration and Intermolecular Interaction, Academic Press, New York (1969).

6.2 W. Kujawski and J. Null, Journal of Applied Polymer Science, 44, 1992, p951.

6.3 A. Einsenberg, and M. Pineri, Structure and Properties of Ionomers, NATO ASI Series, Vol 198, D. Reidel Publishing Company, Holland (1986).

6.4 M. R. Pereira, PhD Thesis, Durham University (1994).

6.5 B. Curnutte and D. Williams, Structure of Water and Aqueous Solutions, Werner A. P. Luck (Ed), Verlug chemie and Physik Verlag, Weinheim/Bergstr (1974).

6.6 M. J. Reimers and T. A. Barbari, Journal of Polymer Science: Part B: Polymer Physics, Vol 32, 1994, p131.

6.7 R. M. Comforti and T. A. Barbari, Macromolecules, 26, 1993, p5209.

6.8 G. K. Fleming and W. J. Koros, Macromolecules, 19, 1986, p2285.

6.9 B. Dé Nevè,and M. E. R. Shanahan, Polymer, 34, 1993, p5099.

6.10 C. Vergelati, A. Perwuelz, L. Volvelle, M. A. Romero and Y. Holl, Polymer, 35, 1994, p262.

6.11 B. D. Ratner and S. C. Yoon, Polymer Surface Dynamics', J. D. Andrade (Ed), Plenum, New York (1988).

6.12 L. Lavielle and J. J. Schultz, Colloid Interface Science, 106, 1985, p438.

6.13 H. Yasuda, B. Sherry, M. A. El Nokaly and S. E. Friberg, Journal of Applied Polymer Science, 27, 1982, p1735.

6.14 E. Ruckenstein and S. V. Gourieankar, Journal of Colloid Interface Science, 109, 1986, p557.

7.1 S. Quezado, J. C. T. Kwak and M. Falk, Can. J. Chem, 62, 1984, p958.

7.2 S. R. Lowry and K. A. Mauritz, J. Am. Chem. Soc, 102, 1981, p4665.

7.3 J. O'M. Bockris, Quart. Rev. Chem. Soc., London, 3, 1949, p173.

7.4 B. E. Conway and J. O'M. Bockris, Modern Aspects of Electrochemistry, J. O'M. Bockris (Ed), No 1, London, Butterworths (1968).

7.5 J. O'M. Bockris and A. K. N. Reddy, Modern Electrochemistry, Vol 1, London, Macdonald (1970).

7.6 Bernal and Fowler, Journal of Chemical Physics, 1, 1933, p515.

7.7 T. Xue, R. B. Longwell and K. Osseo-Asare, Journal of Membrane Science, 58, 1991, p175.

7.8 J. A. Crank, G. S. Park, Diffusion in polymers, J. A. Crank and G. S. Park (Eds), B. L. L. D., 1968.

7.9 T. Alfrey, P. W. Berg and H. Morawetz, Journal of Polymer Science, 7, 1951, p543.1

7.10 A. O. Jakubovic, G. J. Hills and J. A. Kitchener, Trans. Faraday Soc, 55 1959, p263.

7.11 G. E. Boyd and B. A. Soldano, J. Am. Chem. Soc, 75, 1953, p6091.

7.12 J. Muccigrosso and P. J. Phillips, IEEE Tran. Electr. Insul, EI-13, 1978, p172.

7.13 A. S. Michaels, H. J. Bixler and H. L. Fein, Journal of Applied Polymer Science, 35, 1964, p3165.

7.14 R. K. Eby, Journal of Applied Physics, 35, 1964, p2720.

7.15 P. N. Lowell and N. G. McCrum, Journal of Polymer Science, Part A-2, 9, 1971, p1935.

Appendix I

CONFERENCES ATTENDED

1- Infrared and Raman Discussion Group: Martin and Willis Prize Meeting
University of Nottingham, Nottingham, UK
12-13 April 1994

Poster presented: "Depth Profiling of Polymer Laminates Using Confocal Raman Microspectroscopy"

2- Faraday Discussion 98: Polymers at Surface and Interfaces
University of Bristol, Bristol, UK
12-14 September 1994

Poster presented: "Depth Profiling of Polymer Laminates Using Confocal Raman Microspectroscopy"

3- Polymat 94
Imperial College, London, UK
19-22 September 1994

4- Infrared and Raman Discussion Group: 143rd Meeting
Renishaw plc, Wotton-Under-Edge, UK
12 October 1994

5- Infrared and Raman Discussion Group: Martin and Willis Prize Meeting
Rutherford Appleton laboratory, Chilton, UK
5-6 April 1995

Talk presented: "Depth Profiling of Polymer laminates"

6- MSG/MAG/IRDG: Imaging/Mapping using Vibrational Spectroscopy-Microscopy
St. Catherine's College Oxford University, Oxford, UK
7 June 1995

7- Advances in Microscopy of Polymers
The Institute of Physics, London, UK
28 September 1995

8- Microspectroscopy Application Group: Food & Packaging Applications, Advanced Techniques and Complementary Microscopies
Unilever Research, Port Sunlight Laboratory, Bebington, UK
8 November 1995

9- Faraday Discussion 103: Hydration Process in Biological and Macromolecular Systems
Sheffield Hallam University, Sheffield, UK
1-3 April 1996

Poster presented: "Study of Diffusion of Water into Sulphonated polyetherethersulphone/polyethersulphone"

10- XVth International Conference on Raman Spectroscopy, ICORS 96
University of Pittsburgh, Pittsburgh, USA
11-16 August 1996

Poster presented: "Depth Profiling of Polymer Laminates Using Confocal Raman Microspectroscopy"

Appendix II

PAPERS PUBLISHED

1- S. Hajatdoost and J. Yarwood, " Depth Profiling of Poly(methyl methacrylate), Poly(vinyl alcohol) Laminates by Confocal Raman Microspectroscopy ". Applied Spectroscopy, Vol 50, No 5 (1996) p558.

2- S. Hajatdoost, M. Olsthoorn and J. Yarwood, ".Study of Multilayer Polymer Film Laminates Using Vibrational Spectroscopy ". To be submitted

3- S. Hajatdoost and J. Yarwood, " Diffusion of Water into Sulphonated Poly etherethersulphone/polyethersulphone, SPEES/PES Membrane ". To be submitted

4- S. Hajatdoost and J. Yarwood, " Diffusion of Water From Ionic Aqueous Solutions into Sulphonated Poly etherethersulphone/polyethersulphone, SPEES/PES Membrane ". To be submitted

alcohol) Laminates by Confocal Raman Microspectroscopy

SOHAIL HAJATDOOST and JACK YARWOOD*

Sheffield Hallam University, Materials Research Institute, Pond Street, Sheffield S1 1WB, U.K.

We report a molecular depth profiling study of a PMMA/PVOH laminate on quartz using confocal Raman microspectroscopy. It is demonstrated that this technique can be successfully employed to study the hydrogen-bonding interaction between the ester and alcohol groups near the interfacial region. The carbonyl, ν(C=O), band of PMMA shows significant broadening in the interfacial region. Various PMMA/PVOH laminates with different PMMA molecular weights have been studied, and it is demonstrated that the PMMA layers with lower molecular weight show a greater degree of interpenetration for a given annealing time.

Index Headings: **Confocal Raman microspectroscopy; Poly(vinyl alcohol); Poly(methyl methacrylate); Polymer laminate; Depth profiling.**

INTRODUCTION

Polymer laminates, formed by the combination of several polymers to form multilayer structures, are used, for instance, as food packaging materials and are important in connection with areas such as biocompatibility,[1,2] adhesion,[3] and diffusion.[4–8] Such laminates may be a combination of two or more layers. The properties of these polymeric layers at the interface are affected by polymer/polymer interdiffusion, and, in all applications, the properties of the laminate are determined by the concentration profile of the two polymers across the interface.

A number of techniques have been used to study the polymer laminates. These techniques include waveguide Raman spectroscopy,[9] external reflection and attenuated total reflection infrared spectroscopy (FT-IR/ATR),[10,11] scanning electron microscopy combined with energy-dispersive spectroscopy (SEM/EDS),[12] transmission electron microscopy (TEM),[13,14] and transmission electron microscopy combined with energy-dispersive spectroscopy (TEM/EDS).[15] Furthermore, several techniques have been utilized to measure the concentration profile across the interface. These include Rutherford backscattering spectroscopy (RBS),[16] small-angle X-ray scattering (SAXS),[17] small-angle neutron scattering (SANS),[18] secondary ion mass spectrometry (SIMS),[19] IR microdensitometry,[20] and neutron reflectometry.[21]

The polymer laminate used in this work was a two-layered model sample consisting of a top layer of poly(vinyl alcohol) (PVOH) and a base layer of poly(methyl methacrylate) (PMMA). Figure 1 shows the schematic diagram of the deposited polymer laminate on a quartz slide. This experimental system was chosen for two reasons: (1) it was possible to find a solvent that dissolves the PVOH but not the PMMA, and (2) it is not unreasonable to expect interfacial interactions by hydrogen bonding between these two polymers.

Received 30 June 1995; accepted 7 January 1996.

* Author to whom correspondence should be sent.

Pereira and Yarwood[11] have used FT-IR/ATR spectroscopy with the barrier film technique to obtain a depth profile of a PMMA/PVOH laminate. However, this technique requires preparation of many laminates with PMMA layers of different thicknesses. Tait et al.[9] have used waveguide Raman spectroscopy to obtain a depth profile of a PVOH/PMMA laminate. This technique is limited by difficulties found in achieving a viable waveguide.

In this work, we have used confocal Raman microspectroscopy to study the variations in the interfacial region in model polymer laminates as a function of polymer molecular weight. This technique does not provide the information on as small a scale as in the case of neutron total reflection or TEM, but it does have advantages—for example, (1) the need for little sample preparation, (2) the nondestructive nature of the technique, and (3) the ease of use of the technique.

Tabaksblat et al.[22] have given a detailed assessment of confocal Raman microscpectroscopy. Because of the use of a pinhole, this technique provides good spatial resolution along the optical axis, Z, of the microscope and also good spatial resolution in the lateral direction, XY (perpendicular to the optical axis). The high resolution achieved by this technique is due to the use of a pinhole (see Fig. 2).

The light reflected from a selected plane in a laminate is focused to a point and allowed to pass through a pinhole positioned in front of the detector. The rays that are reflected from below and above the plane of focus are mainly (but not totally) blocked by the opaque regions around the pinhole.

EXPERIMENTAL

Polymer Laminate Preparation. Poly(vinyl alcohol) was obtained from Aldrich Chemical Company Ltd.; poly(methyl methacrylate) [PMMA(I) and PMMA (II)] samples were donated by ICI (Wilton); and PMMA(III) was purchased from Fluka Chemicals Ltd. PMMA films were deposited onto a quartz slide from dichloromethane (DCM) of spectroscopic grade by the dip-coating procedure.[23] A PVOH film was then deposited onto the PMMA layer as a "coating" by the same technique, with water as solvent, to produce a laminate (Fig. 1). At each stage, samples were dried in the oven at 70 °C for 24 h. The thicknesses of the PMMA and PVOH layers were determined within 1% and 5% accuracy, respectively, with the use of a surface profiler (Laser Form Talysurf).

Confocal Raman Microspectroscopy. Raman spectra were recorded on a Renishaw Ramascope spectrometer with the 632.8-nm line of a He–Ne laser. This instrument is equipped with a Peltier cooled charge-coupled device

0003-7028/96/5005-0558$2.00/0

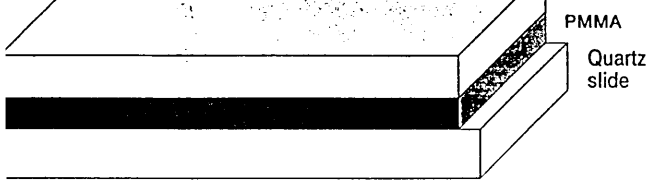

IG. 1. The quartz slide and deposited polymer laminate of PMMA nd PVOH.

CCD) detector, a holographic grating (1800 grooves/mm), nd two Raman holographic edge filters, which prevent he backscattered laser radiation from entering the spectroraph. The stigmatic single spectrograph is attached to an lympus BH2 microscope. The Ramascope was set up in onfocal mode with a 100× short-working-length objecve [numerical aperture (NA) value of 0.95], a slit width f about 15 μm, and a CCD area of 4 × 576 pixels (pixel ize, 22 μm²). The long axis (576 pixels) defines the spec- l dimension, and the short axis describes the height of e image.[24] The arrangement of the CCD and the slit acts s the pinhole for blocking out-of-focus signals. The depth solution of the confocal arrangement was checked by sing a silicon sample as a reference material. In this exriment the focus of the laser was stepwise (1 μm) anned away from the silicon, and the signal intensity of e fundamental vibration at 519 cm^{-1} was recorded. Fige 3 shows a plot of Raman intensity as a function of stance away from silicon surface. The depth resolution as thus determined as 2.0 ± 0.3 μm by the full width at lf-maximum (FWHM) criterion. However, it should be ted that actual depth resolution depends on the specific tical properties (absorption, refraction, and scattering) of ch system that is measured. It is clear from Fig. 3 that, though about 90% of the scattered light is contributed m 2.5 μm below and above the plane of focus, signifant Raman scattering light is also contributed from the gions further above and below this region.

A depth profile of each laminate was then obtained by cusing the microscope stepwise (1 μm) through the

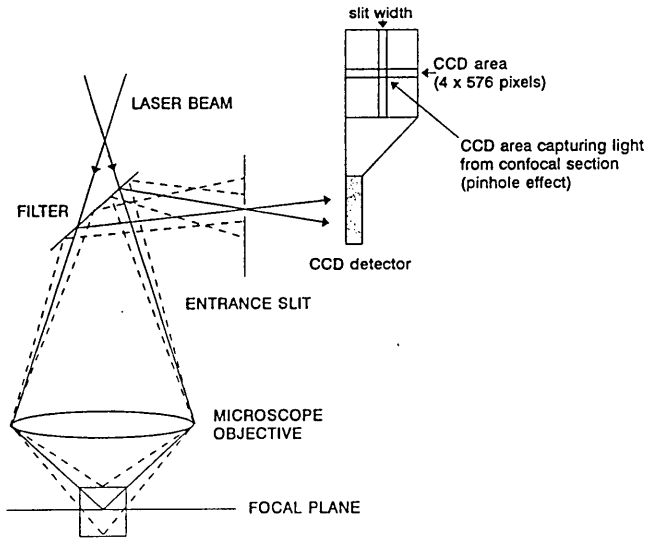

. 2. Schematic diagram of the principle of confocal Raman microctroscopy.

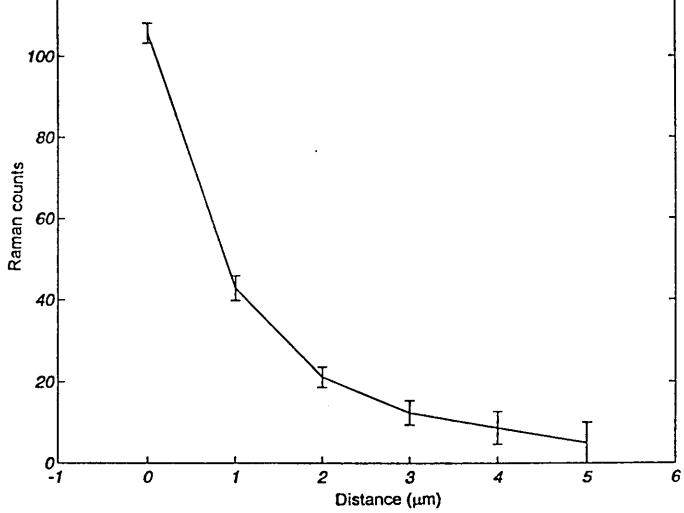

FIG. 3. Plot of the intensity (Raman counts for total exposure time) of the most fundamental vibration of silicon as a function of distance from the surface.

polymer laminate and recording a spectrum at each step. Thus the amount of each polymer signal present in the laminate, as a function of the depth, was determined.

RESULTS AND DISCUSSION

PMMA/PVOH laminates prepared with various molecular weights of PMMA were used for these experiments (see Table I). The thicknesses of the PMMA and PVOH layers were 4.5 ± 0.5 μm and 9.5 ± 0.5 μm, respectively. This system was selected to examine interactions at the interfacial region due to possible hydrogen bonding between the carbonyl group of PMMA and the hydroxyl group of PVOH. Another advantage of this system is that we can deposit the PVOH layer from water on a PMMA substrate, since PMMA is not soluble in water. Spectra of the pure individual films are shown in Fig. 4.

In order to obtain a depth profile of each laminate, the 550–1100 cm^{-1} region of the spectrum was recorded. Figure 5 shows the spectra recorded as a function of depth for the PMMA(III)/PVOH laminate. As expected, the initial spectra show no bands corresponding to PMMA and only PVOH bands at 854 and 917 cm^{-1} (Fig. 5a–5d). The subsequent spectra (Fig. 5e–5j) indicate the presence of PMMA with bands at 813 and 601 cm^{-1} as well as PVOH bands. The important feature of this region, which we call the interfacial region, is that, as we continue recording the spectra through the depth of the laminate, the intensities of the PMMA bands increase as the intensities of the PVOH bands decrease. This result is expected, since, with focusing at the deeper parts of the laminate, spectra are collected closer to the PMMA

TABLE I. Molecular weight of the polymers used.

Polymer	MW (g mol^{-1})
PVOH	50×10^3
PMMA(I)	800×10^3
PMMA(II)	120×10^3
PMMA(III)	34×10^3

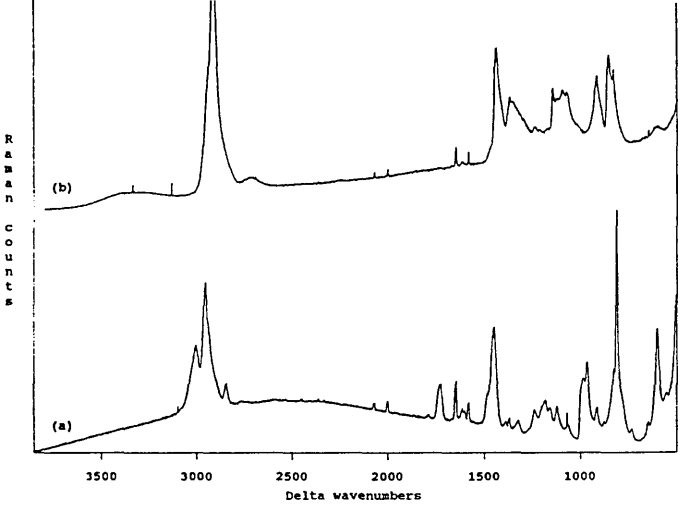

FIG. 4. Raman spectra of (*a*) pure PMMA film and (*b*) pure PVOH film.

layer and further away from the PVOH layer. It is this region which is expected to show some hydrogen-bonding interaction between the ester and alcohol groups of the PMMA and PVOH layers, respectively. Finally, the last spectrum (Fig. 5k) shows only bands corresponding to the pure PMMA. However, the intensity of the PMMA bands shows a decrease on moving into the pure PMMA layer. This phenomenon has been observed for all three cases. The loss of intensity of the PMMA band in the lower regions is probably due to the effects of absorption, scattering, and mismatch of the refractive index of the two polymers at the interface. The details of these processes need further investigation.

It is clear from Fig. 5 that the bands corresponding to both PMMA and PVOH layers appear in some of the spectra. Since both polymers have Raman bands in the

was utilized to distinguish spectra corresponding to the PVOH and PMMA layers. Thus a spectrum of pure PVOH film (see Fig. 4b) was first obtained, and this spectrum was used for spectral subtraction without any intensity weighting. Then the spectrum of pure PVOH film was subtracted from each spectrum. However, in order to remove all the bands corresponding to the PVOH layer, it was necessary to add scale and offset values to each of the input files before they were subtracted. Figure 6 shows the results of the spectral subtraction. It can be seen that the first detectable sign of PMMA band at 813 cm^{-1} has appeared in the plane of focus about 4 μm below the top surface of the upper layer in the PMMA(III)/PVOH laminate. However, it should be noted that this observation does not indicate the position of the upper boundary of the interfacial region. The reason for this condition is that, as mentioned earlier (see Fig. 3), although approximately 90% of the scattered light is collected from about 2.5 μm below and above the plane of focus, significant Raman signals may be contributed by PMMA in the lower regions.

The spectral subtraction method was repeated, as above, to determine the last spectrum which shows any bands corresponding to the upper layer (PVOH). Hence, a spectrum of a pure PMMA film (see Fig. 4a) was first collected, and then this spectrum was used for subtraction without adjustment of the intensity. As mentioned earlier, scale and offset values were added to each of the input files before they were subtracted. Figure 7 shows the results of the subtraction. It is clear that the last detectable sign of the bands corresponding to PVOH at 917 and 854 cm^{-1} appears in the spectrum of the plane of focus about 10 μm below the top surface. For the reasons mentioned above, it should be noted that this observation does not necessarily define the position of the lower boundary of the interfacial region.

In order to determine whether the depth of penetration

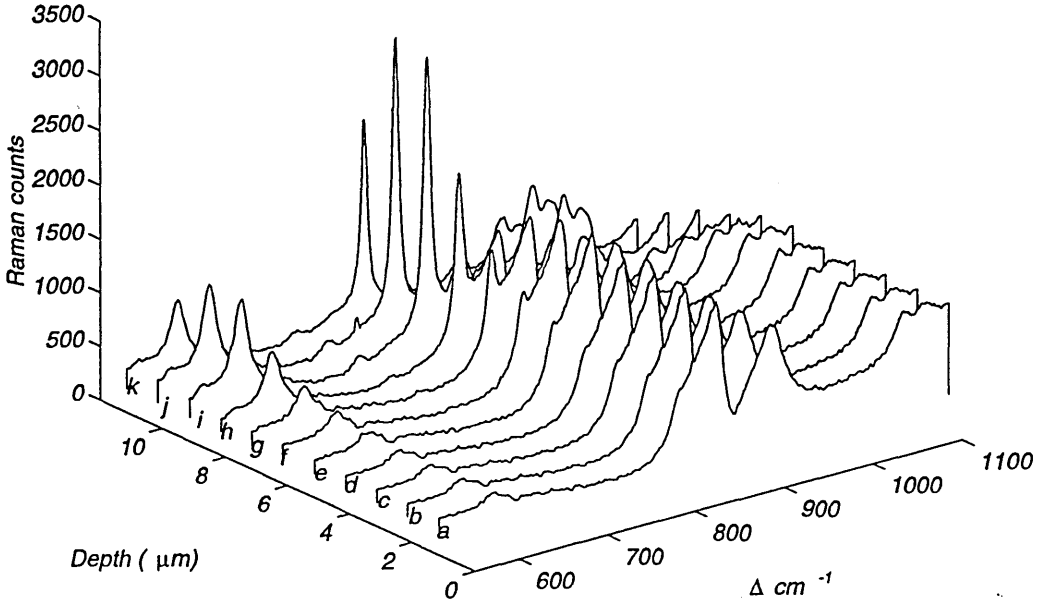

FIG. 5. Three-dimensional representation of the depth profile of PMMA(III)/PVOH/quartz laminate obtained by focusing the microscope stepwise (1 μm) through the laminate.

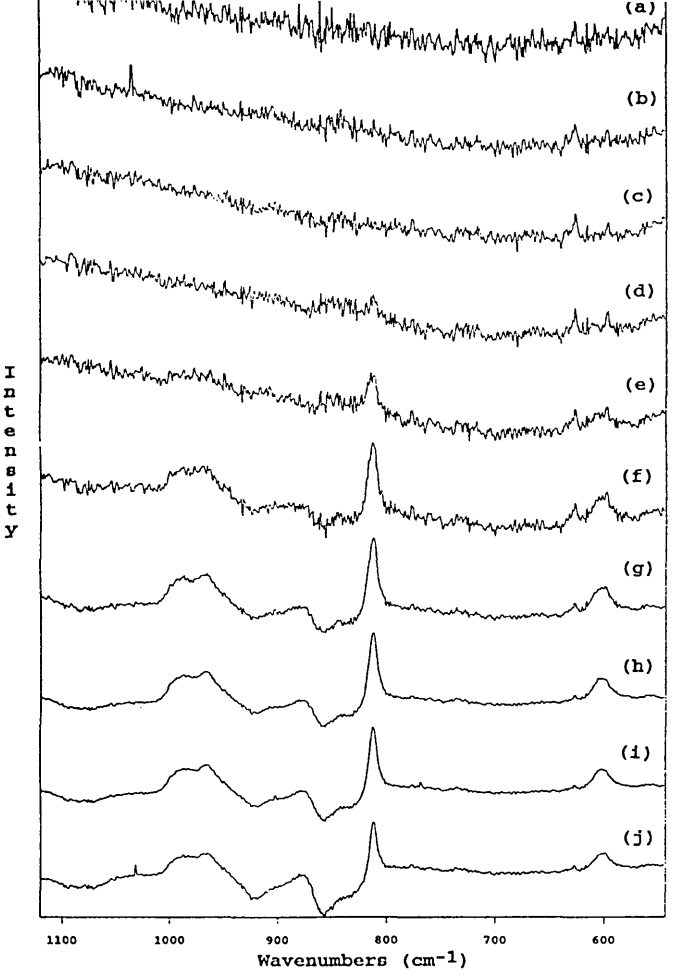

IG. 6. Raman data obtained by subtraction of a pure PVOH film from ach of spectra recorded in the depth of the PMMA(III)/PVOH lamiate.

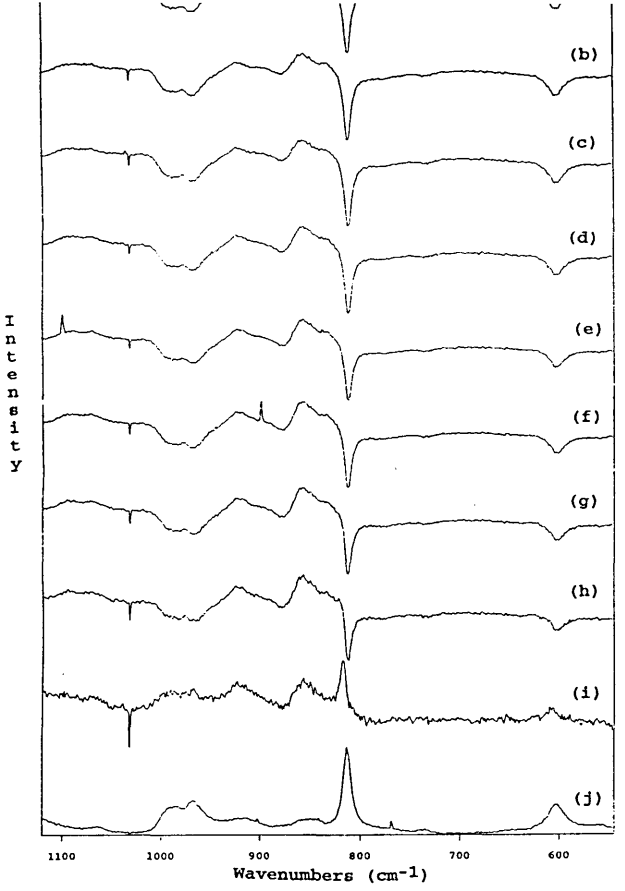

FIG. 7. Raman data obtained by subtraction of a pure PMMA film from each of spectra recorded in the depth of the PMMA(III)/PVOH laminate.

s related to the molecular weight of the PMMA film, we erformed the same experiment and obtained the depth rofiles for the PMMA(II)/PVOH and PMMA(I)/PVOH aminates with PMMA molecular weights of 120,000 and 00,000, respectively. Figure 8 shows the plot of intensity s Raman counts for total exposure time as a function of epth for the all three different PMMA/PVOH systems. t should be noted, however, that in view of the depth esolution of the confocal microscope, we cannot deterine the exact upper and lower boundaries of the interacial region, and thus the limits of each region in Fig. 8 re not as sharp as those presented. In addition to this onsideration, it should be noted that, unlike the case for ne infrared technique, in a Raman experiment the value f intensity (Raman counts) in a fixed time scale may lightly vary because of the effect of various factors such s slight changes in laser intensity or dust particles, and o on. Thus, this degree of uncertainty has been corrected y adding error bars to each intensity value.

It is clear from Fig. 8 that the degree of interpenetraon is not the same in all three systems. Indeed, although is difficult to determine the exact position of the interacial region, it can be seen that the interfacial region is broader for the laminates with lower PMMA molecular weight.

One possible explanation for the relationship between molecular weight and the degree of interpenetration of PMMA is the effect of molecular weight on the mobility of the polymer chains at a limited annealing time. Boven et al.,[10] using infrared spectroscopy, have shown that the rate of the interdiffusion is dependent on the molecular weight of the polymers used. This means that the polymers with the lower molecular weight reach a completely mixed (equilibrium) system faster than the polymers with higher molecular weight. We believe, therefore, that the PMMA(III)/PVOH laminate with lower PMMA molecular weight has come closer to the completely mixed system than PMMA(I)/PVOH laminate with much higher PMMA molecular weight. However, it should be noted that a full theoretical description of the interdiffusion of polymer species has not yet been elucidated. Nevertheless, this study indicates the potential power of confocal Raman microspectroscopy to study the extent and rate of interdiffusion in polymer laminates.

Interfacial Effects. So far we have shown that the two polymers interpenetrate towards each other at the interfacial region. In this region, the existence of some degree of hydrogen-bonding interaction between PMMA and PVOH films might be expected. It is well known[25] in vibrational spectroscopy that hydrogen bonding is man-

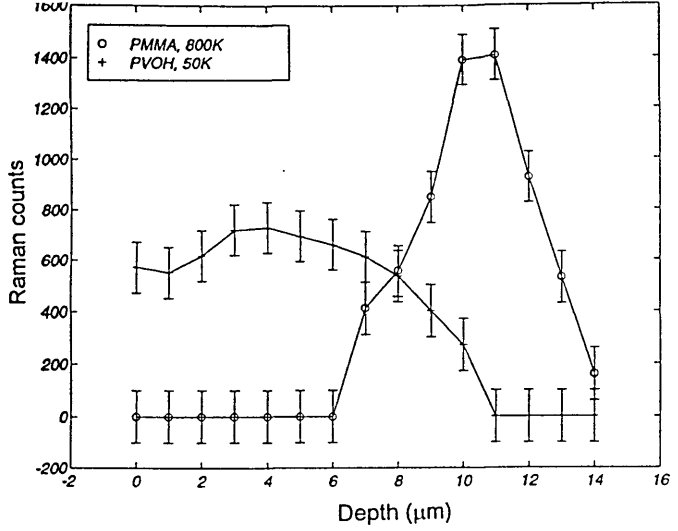

(b)

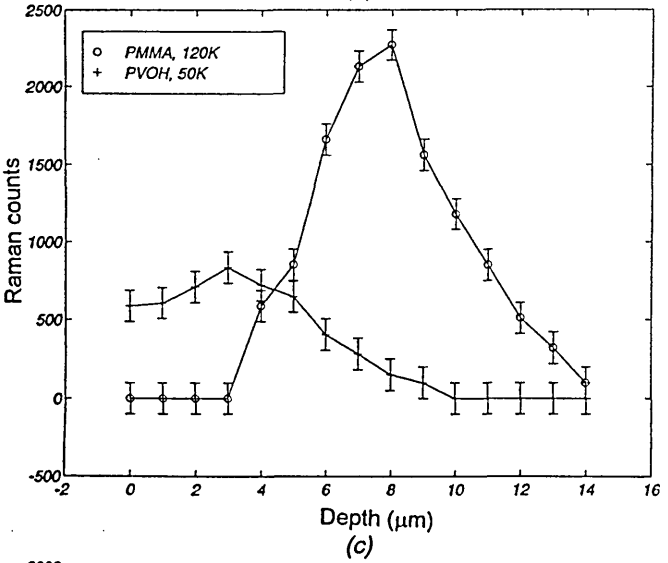

(c)

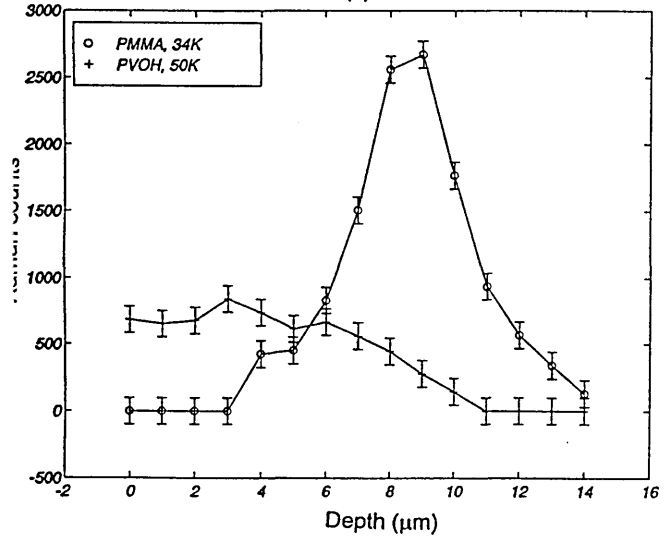

IG. 8. Plot of the intensity (Raman counts for total exposure time) as function of depth for (*a*) PMMA (I)/PVOH laminate, (*b*) PMMA I)/PVOH laminate, and (*c*) PMMA (III)/PVOH laminate.

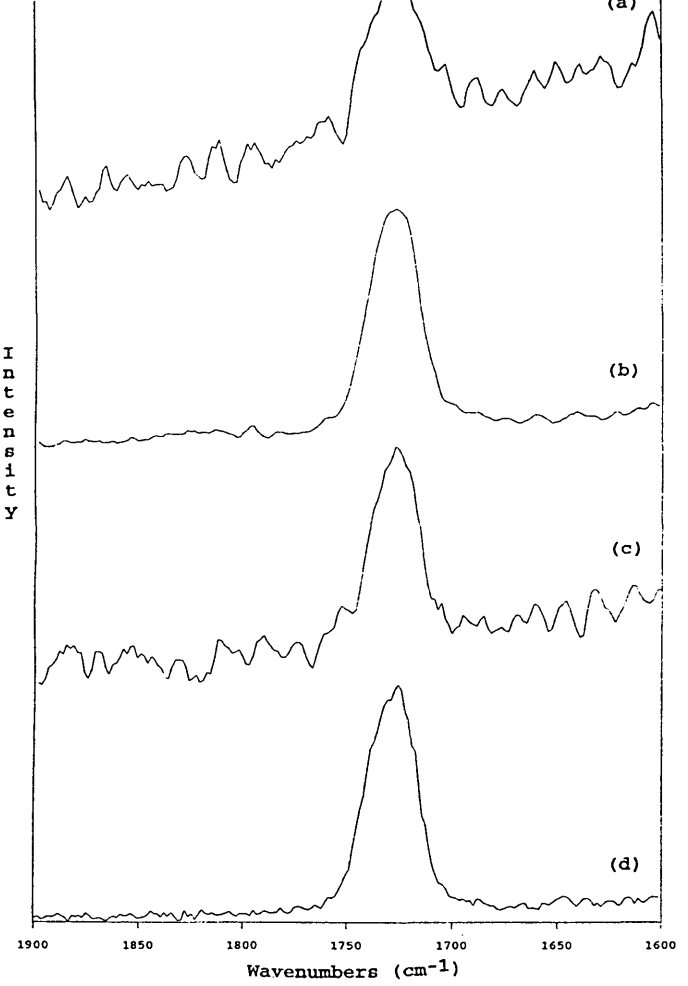

FIG. 9. Raman spectra of carbonyl band of PMMA(III)/PVOH laminate. Carbonyl band corresponding to (*a*) upper part of the interfacial region; (*b*) middle of the interfacial region; (*c*) PMMA layer; and (*d*) a pure PMMA film.

ifested by frequency shifts, band broadening, and intensity changes in the carbonyl, ν(C=O), and hydroxyl, ν(O–H), bands of the ester and alcohol groups of the polymers. Unfortunately the ν(O–H) band (at about 3400 cm^{-1}), which is very strong in the infrared spectrum, does not have a very high Raman cross section (see Fig. 4b). However, the ν(C=O) band is clearly visible in the Raman spectrum, and the possible changes in this band at the interfacial region can be studied. Figure 9 shows the Raman spectra recorded at the 1600–1900 cm^{-1} region for the various depths of the PMMA(III)/PVOH laminate. It is clear that the carbonyl band is broader near the upper part of the interfacial region (Fig. 9a) than in the PMMA layer (Fig. 9c), even allowing for a relatively low signal-to-noise ratio.

Since the PVOH film has been deposited on the PMMA film from a water solution, one should consider whether hydrogen bonding between the hydroxyl group of water and carbonyl group of the ester (PMMA) may be responsible for the ν(C=O) band broadening. In order to check this, a pure PMMA film was coated with a water layer and then was dried in an oven for the same drying temperature and time (70 °C, 24 h) used for the laminates.

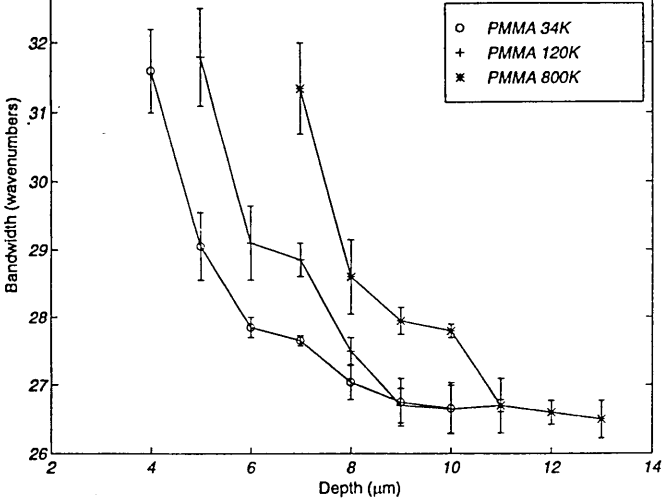

FIG. 10. Plot of ν(C=O) bandwidth changes as a function of depth through the PMMA/PVOH laminate.

A comparison of the spectra of the PMMA film before and after a few hours of exposure to water shows a (C=O) band broadening. However, the spectrum of PMMA after complete drying shows no ν(C=O) band roadening. This result indicates that all the hydrogen onding due to water–PMMA association has been re- ıoved after complete drying. Thus it can be concluded hat the ν(C=O) band broadening in the laminate after omplete drying is due to hydrogen bonding between the ydroxyl group of the PVOH and the carbonyl group of he PMMA.

Figure 10 shows a plot of full width at half-height FWHH) of the ν(C=O) band as a function of the dis- ınce, Z, from the top surface focal plane of the laminate. he error bars have been determined on the basis of un- ertainty caused by the noise level in the spectra for mea- uring the exact FWHH. As expected, for the hydrogen- onding interaction, the bandwidth is much broader at ıe interfacial region and decreases as it approaches the MMA layer. Indeed the bandwidth measured for the (C=O) band of pure PMMA region (Fig. 9c) of the ıminate is in a good agreement with that measured for PMMA film (Fig. 9d). However, there was no obvious hift of the ν(C=O) band, as might also be expected for hydrogen-bonded interaction. One possible explanation ›r this result is the effect of the dilution phenomena in ıe interfacial region. In this region the PMMA carbonyl roup may interact via dipolar interaction with other MMA carbonyls or via hydrogen bonding with sur- ›unding PVOH molecules. Shelley et al.[26] have explored ıe variation in Raman isotropic ν(C=O) band position ıd half-width (FWHH) for DMF as a function of con- ɛntration in carbon tetrachloride, CCl_4. They have ıown that the ν(C=O) band shifts to higher frequency ·ith band broadening as the mole fraction of DMF de- ·eases. It is also known[27–29] that the ν(C=O) band shifts › lower frequency with band broadening due to inter- ıolecular hydrogen bonding. A close examination of the ›ectra of PMMA/PVOH laminate shows that the con- ɛntration of PMMA decreases from the pure PMMA yer to the upper sections of the interfacial region. It is interactions with other PMMA carbonyls in the PMMA layer compared to the interfacial region. This dilution effect is expected to lead to a blue shift with band broadening of the ν(C=O) mode in the interfacial layer. On the other hand, the degree of hydrogen-bonding interaction between PMMA and PVOH molecules is higher in the interfacial region compared with that in pure PMMA. This condition is expected to lead to a red shift with band broadening of the ν(C=O) band. Thus, the overall result of these two effects on the ν(C=O) band is expected to be little or no frequency shift with band broadening. In this sense our observations may be rationalized.

SUMMARY AND CONCLUSION

We have shown that confocal Raman microspectroscopy may be employed to obtain depth profiles of polymer laminates. The system chosen for this detailed investigation was PMMA/PVOH. Three different laminates with various PMMA molecular weights were examined, with a view to studying hydrogen-bonding interactions between the alcohol and ester groups of PVOH and PMMA layers. The ν(C=O) band shows no apparent frequency shift due to hydrogen-bonding interactions between the ester and alcohol groups. We believe that dilution of PMMA carbonyl lone pair dipoles in the interfacial region (with a band shift opposite to that associated with hydrogen-bonding interaction) may be responsible for the absence of an observable ν(C=O) band shift. However, considerable broadening of the ν(C=O) band has been observed at the interfacial region, which confirms the existence of hydrogen-bonding interactions. We have not been able to study variations in the ν(O–H) band of the PVOH layer because of the very low intensity of the hydroxyl group vibration. We have also demonstrated that, for a given annealing time, PMMA films with lower molecular weight show a greater degree of interdiffusion compared to those with higher molecular weights. This observation points to the possibility of studying the extent and rate of interdiffusion in polymer laminates with confocal Raman microspectroscopy.

ACKNOWLEDGMENTS

We thank Dr. Neil Everall of ICI (Wilton) for supplying us with PMMA samples of different molecular weights. Valuable discussions with Prof. Julia Higgins, FRS, are gratefully acknowledged.

1. H. Younes and D. Cohn, J. Biomed. Mater. Res. **21,** 1301 (1987).
2. M. Bender, *Interfacial Phenomena in Biological Systems* (Marcel Dekker, New York, 1991).
3. G. Gillberg, J. Adhes. **21,** 129 (1987).
4. T. C. Wang and L. J. Boutman, Polym. Eng. Sci. **25,** 521, 529 (1985).
5. Q. Deng, C. S. Sundar, and Y. C Jean, J. Phys. Chem. **96,** 492 (1992)
6. J. H. Ramsden, J. Phys. Chem. **96,** 3388 (1992).
7. M. Shimonura, J. F. Rabolt, and K. Song, Langmuir **8,** 887 (1992).
8. N. E. Schlotter and P. Y. Furlan, Vib. Spectrosc. **3,** 147 (1992).
9. J. K. F. Tait, J. Yarwood, N. M. Dixon, N. Everall, G. Davis, and R. McIntyre, J. Raman Spectrosc. **24,** 511 (1993).
10. G. Boven, R. H. G. Brinkhuis, E. J. Vorenkamp, G. Challa, and A. J. Schouten, Polymer **33,** 6, 1150 (1992).
11. M. R. Pereira and J. Yarwood, J. Polym. Sci.: Part B: Polym. Phys. **32,** 1881 (1994).
12. F. P. Price, P. T. Gilmore, E. L. Thomas, and R. L. Laurence, J. Polym. Sci.: Polym. Symp. **63,** 33 (1978).

14. S. Koizumi, H. Hasegawa, and T. Hashimoto, Macromolecules **23,** 2955 (1990).
15. E. Jabbari and N. A. Peppas, Polymer Bulletin **27,** 305 (1991).
16. J. Kramer, P. Green, and J. Palmstrom, Polymer **25,** 473 (1984).
17. R. W. Garbella and J. H. Wendorff, Makromol. Chem. **189,** 2459 (1988).
18. T. Finerman and B. Crist, Polymer **28,** 375 (1987).
19. S. J. Whitlow and R. P. Wool, Macromolecules **22,** 2648 (1989).
20. J. Klein and B. J. Briscoe, Polymer **17,** 48 (1976).
21. M. L. Fernandez, J. S. Higgins, J. Penfold, R. C. Ward, C. Shackelton, and D. J. Walsh, Polymer **29,** 1923 (1988).
23. P. Groenveld, J. Paint Techn. **43,** 50 (1971).
24. K. P. J. Williams, G. D. Pitt, D. N. Batchelder, and B. J. Kip, Appl. Spectrosc. **48,** 232 (1994).
25. J. Yarwood, in *Spectroscopy and Structure of Molecular Complexes,* J. Yarwood, Ed. (Plenum, New York, 1973), p. 180.
26. V. M. Shelley, A. Talintyre, J. Yarwood, and R. Buchner, Faraday Discuss. Chem. Soc. **85,** 211 (1988).
27. M. S. Bradley and V. Buch, J. Chem. Phys. **99,** 2332 (1993).
28. H. Deng, J. Zheng, J. Burgner, and R. Callender, J. Phys. Chem. **93,** 4710 (1989).
29. N. Tanaka, K. Ito, and H. Kitano, Macromolecules **27,** 540 (1994).